UCGE Reports

Number 20296

Department of Geomatics Engineering

Development of Combined GPS L1/L2C Acquisition and
Tracking Methods for Weak Signals Environments

(URL: http://www.geomatics.ucalgary.ca/links/GradTheses.html)

by

Cyrille Gernot

October 2009

SCHULICH
School of Engineering

UNIVERSITY OF
CALGARY

UNIVERSITY OF CALGARY

DEVELOPMENT OF COMBINED GPS L1/L2C ACQUISITION AND TRACKING

METHODS FOR WEAK SIGNALS ENVIRONMENTS

by

Cyrille Gernot

A THESIS

SUBMITTED TO THE FACULTY OF GRADUATE STUDIES

IN PARTIAL FULFILMENT OF THE REQUIREMENTS FOR THE

DEGREE OF DOCTOR OF PHILOSOPHY

DEPARTMENT OF GEOMATICS ENGINEERING

CALGARY, ALBERTA

OCTOBER, 2009

Abstract

Acquiring and tracking signals such as legacy GPS L1 C/A can prove challenging under adverse conditions. Increasing the processing gain by 20 dB usually requires long coherent integrations which remain limited by the 50 Hz data bits transmitted. Fortunately, the GPS has been modernized with the addition of a civil signal, namely L2C, on the L2 frequency band.

In this research, new acquisition methods making use of both the L1 C/A and L2C signals in a combined manner are developed and tested. Several different methods are investigated through their probabilities of detection and false alarm. The three best-performing methods are then described theoretically. The first method implies a non-coherent summation of L1 and L2 correlator outputs. The second method implements an independent differential summation of L1/L2 correlator outputs and the third method represents a non-coherent plus dependent differential summation. While each method is shown to increase the detection performance compared to a standard GPS receiver, the non-coherent plus dependent differential summation method outperforms all the others.

Next a Kalman filter based tracking method combining the L1 C/A and L2C signal energy is presented. One of the main difficulties when combining these signals arises due to inter-frequency biases (ionospheric delay, satellite and receiver instrumental biases) which cannot be neglected. In order to solve this problem, the output of the code and phase discriminators are combined through a Kalman filter estimating the relative delay

between L1 and L2, the L2 code and phase errors, the L2 frequency error and the L2 phase acceleration error. Results are shown in terms of sensitivity compared to standard single frequency tracking. It is also shown that estimates of the vertical Total Electron Content (TEC) can be derived from the Kalman filter outputs and that they match the TEC value provided by the International GNSS Service (IGS).

Acknowledgements

The author would like to acknowledge the following persons for their help and support which permitted the success of this research:

Table of Contents

List of Tables

List of Figures and Illustrations

xi

xiii

List of Symbols, Abbreviations and Nomenclature

PRN..Pseudo-Random Noise
QPSK .... Ground Based Augmentation Systems
RF...Radio Frequency
ROC .... Receiver Operating Characteristics
SBAS.. Quadrature Phase Shift Keying
STEC.. Slant Total Electron Content
TCXO... Temperature Controlled Crystal Oscillator
TEC...Total Electron Content
TECU .... Total Electron Content Unit = 10^{16} el/m^2
THSS.. Time Hopping Spread Spectrum
VTEC..Vertical Total Electron Content
WAAS.. Wide Area Augmentation System

Symbols ....**Definition**

$F(\bullet)$...Fourier transform
$F^{-1}(\bullet)$.. Inverse Fourier transform

A .... Signal amplitude
B ....Front-end bandwidth
C_X .... Covariance matrix of X
C/N_0...Carrier to noise density ratio
c...Speed of light
$c(t)$...Code chip at time t
c_{local} .... Local replica of the ranging code
$d(t)$... Data bit at time t
dt ....Code misalignment
E ....Satellite elevation angle
ΔF...Doppler residual
f_0 ....Carrier wave frequency
f_1 or f_{L1}... L1 center frequency
f_2 or f_{L2}... L2 center frequency
f_c .... Chipping rate
f_D .... Doppler frequency
F_S...Sampling frequency
I ....In-phase correlator output
I_D .... In-phase component after Doppler removal
I_{IF}.. IF in-phase component
K...modified Bessel function of the second kind
k... k^{th} correlator output
M ....Number of correlator outputs
$M(E)$ .... Ionosphere mapping function
P_d...Probability of detection
P_{fa}...Probability of false alarm

xvii

Chapter One: Introduction

Positioning and navigation face an ever-increasing need for accuracy and reliability. Global Navigation Satellite Systems (GNSS) provide their users with a useful means to obtain precise position, velocity and time through the transmitted signals. In order to make up for the strong market that is the navigation field (pedestrian navigation, indoor applications, geomatics and other civil and military applications), several countries have started to develop or modernize their own systems. For instance, the European Union is currently developing Galileo which will transmit on four different frequencies and China is designing Compass which will include three geostationary satellites (Dong et al 2007). On the other hand, the Global Positioning System, which is already in place and transmits on two frequencies for civil applications (L1 and L2), is one of the most accurate and reliable positioning systems currently operational (e.g. Cannon 2005) and is being modernized through the addition of a third frequency band (L5) for aviation and new civilian signals on L1 and L2. The civil signal present on the L1 frequency band namely L1 C/A standing for Coarse Acquisition has been transmitted since the beginning of the system. The signal present on the L2 frequency band namely L2C was first transmitted in 2005. However, acquiring and tracking GPS signals has proven to be extremely difficult in harsh environments such as indoors or urban canyons, which represents a major market for novel applications such as pedestrian navigation and safety of life (USA Federal Communications Commission Enhanced-911 mandate). To this end, extensive research has been orientated toward this specific field of activity in order to improve the achieved

performance. Due to the recent availability of L2C and the fact that very little research has targeted the possibility of inter-frequency combination of L1 C/A and L2C for weak signal acquisition and tracking, this subject is a strong source of interest. The potential improvement due to the presense of two civil signals in terms of acquisition and tracking is the subject of this thesis.

1.1 Background and Motivation

The Global Positioning System (GPS) is currently the only fully operational GNSS available. Officially named NAVSTAR GPS, the system is operated by the United States Department of Defense and reached full operational capability on July 17, 1995. Using a constellation of at least 24 satellites, it allows a user anywhere on the Earth to obtain precise time, position, and velocity 24 hours a day regardless of weather conditions. GPS receivers are able to obtain the aforementioned information by calculating the distance to at least four satellites and solving for the three spatial unknowns and the receiver time offset. User velocity is obtained from Doppler frequency or carrier phase observations (Kaplan et al 2006). The achieved accuracy varies from several metres to several centimetres depending on the positioning method utilized (e.g. Lachapelle 2006). In order to achieve high precision, the receiver has to use carrier phase observables. This causes an ambiguity problem created by the fact that the GPS receiver is only able to access the residual phase information. That is to say, the integer number of cycles separating the receiver from the satellite remains unknown. Therefore, centimetre level accuracy can not be achieved without solving for the ambiguities (Lachapelle 2006). Moreover, GPS signals are present on L1 and L2 at 1575.42 Mhz and 1227.6 MHz. However, until

recently, the only signal present on L2 was the so-called L2P signal (P standing for precision code). To prevent spoofing, the P-code is encrypted by the United States Department of Defence using the so-called Y code (Wiederholt & Kaplan 2006). As a result, the L2P signal is not available for authorized use by civilian users. This severely affects rapid carrier phase ambiguity resolution needed for survey, carrier phase differential or kinematic users because these applications often require the difference between the L1 and L2 phase measurements, resulting in a wavelength 4.5 times larger than L1 only (so-called widelane technique). This has been a strong area of research for the past 30 years (MacDoran 1985, Keegan 1990, Woo 1999). As one does not have access to the Y code, semi-codeless or codeless techniques are used to reconstruct the L2 carrier phase. Common techniques are squaring, cross-correlation, P-code aided L2 and Z-tracking (Woo 1999). As the Y code is unknown and the various squaring and cross-correlation techniques result in signal power loss with respect to increased noise, these techniques, despite their added complexity, perform poorly compared to an ideal phase lock loop.

Even if the algorithms used to solve for the ambiguities do provide fairly good performance, the main drawback of carrier phase positioning remains the inability to maintain phase lock under harsh conditions or even acquire and track the signal in weak signal environments. Since position can only be achieved if four satellites are tracked at the same time, weak signals have become a major concern for the navigation community. To place things in context, the minimum received power guaranteed by the Interface Control Document (ICD) is -158.5 dBW, or 1.4×10^{-16} W, for L1 C/A. This does not

include any external source of attenuation. Therefore, acquiring or tracking the L1 C/A signals has proven to be very challenging indoors and in urban canyon environments. To this end extensive research has been conducted to improve the performance obtained from acquisition and tracking techniques. Common techniques include the use of High Sensitivity GPS (HS GPS) receivers relying on data bit estimation and Assisted-GPS receivers making use of external information to perform data wipe-off techniques. However, the availability and the reliability of assistance data or data bit estimation techniques still remains a problem.

The GPS system itself is currently in a modernization phase. Actually, one could even claim that this modernization started much earlier than it is commonly thought through the development of augmentation systems supporting the GPS L1 signal (GPS I). These external systems were designed to provide additional information in order to increase availability, reliability and accuracy through the transmission of corrections parameters. These systems can be separated into two main categories: Satellite-Based Augmentation Systems (SBAS) and Ground-Based Augmentation Systems (GBAS). The first one remains much more widely known by the civilian community than the second one. The ability of a receiver to obtain corrections from the US WAAS system (Wide Area Augmentation System) or the European EGNOS system (European Geostationary Navigational Overlay Service) is one of the most common specifications of today's civilian GPS receivers. However, even though these complementary systems are especially attractive in terms of positioning and navigation, they still remain restricted by the technical limitations inherent to the common GPS L1 C/A signal: the inability of the

receiver to acquire and track the signals indoors or in urban environments. Note that these limiting factors include attenuation, obstructions and multipath. Whereas attenuation and obstructions can hardly be mitigated, numerous studies were directed toward multipath detection and suppression (Ries et al 2003, Nunes et al 2005, Braasch 1997, Pany et al 2005).

Due to these specific limitations and the recent growth of the civilian market regarding positioning and navigation applications (one would only have to cite precision farming, pedestrian navigation, and car navigation as examples), the GPS system has recently experienced and is still under modernization. Indeed, the so-called GPS II and GPS III developments were already investigated by the US Department of Defense during the 1990's (Crews 2008). GPS II improves signal availability and reliability through the addition of two new signals L2C (BPSK modulation) and L5 (QPSK modulation) respectively transmitted at 1227.6 MHz and 1176.45 MHz. Finally, Block III GPS modernized satellites currently scheduled for 2013 should add a new L1 civil signal named L1C. Broadcast at 1575.42 MHz at 1.5 dB higher than L1 C/A, L1C will be composed of a data channel and a pilot channel. Whereas it has the same chipping rate as L1 C/A, L1C is formed through a completely different type of code called Binary Offset Carrier modulation BOC(1,1) (Avellone et al 2007, Gerein et al 2004, Betz 2002) for the data channel and time-multiplexed BOC(1,1) and BOC(6,1) for the pilot channel. L1C having a different frequency than L2 or L5, it will further assist in ionospheric effect estimation through multi-frequency combination (Skone 2007).

As of today, the GPS II L2C signal is great interest (for civilian applications) as it is the major new signal currently available. Moreover with the launch of the Block IIR-M satellites carrying the L2C signal, a considerable effort directed to overcome the legacy GPS L1 C/A signal's limitations has been done (Fontana et al 2001). In particular, the new L2C signal has brought the following points of interest to the scientific community:

- Being designed to overcome the limitations experienced by the legacy L1 C/A, it features better cross-correlation properties, up to 44 dB protection (Fontana et al 2001).

- The presence of the CL code (standing for long ranging code) which is a pilot channel (dataless signal) allows for longer coherent integration as no sign flips due to data bits are experienced by a receiver using the pilot channel. Such a novelty is especially important in term of receiver sensitivity and improves acquisition and tracking in attenuated environments such as indoors (Mongrédien 2008).

- The presence of the new civilian signal on L2 allows for better correction of the ionospheric effect thanks to dual-frequency correction methods (Skone 2007).

- The data channel ranging code period (CM code, CM standing for moderate ranging code) is the same as a data bit period. The need for data bit synchronization is removed. This last point is especially important given that L1 C/A signal and L2C signal have their data bits synchronized. As such, a dual frequency receiver does not need to perform data bit synchronization on L1 either.

Due to the presence and availability of the new L2C signal, numerous studies have already been conducted to assess its potential. For instance, regarding acquisition performance, Lim et al (2006) proposed a fast acquisition scheme of L2C signals through the aid of L1 to accelerate CM code phase and frequency offset estimation. Psiaki (2004) developed a FFT-based acquisition scheme to acquire L2 CM and CL codes under weak signal conditions whereas Yang (2005) investigated acquisition techniques on L2 CM alone, L2 CL alone and possible joint acquisition of CM/CL. Regarding tracking algorithms, combination of the L2C pilot and data channel and assessment of performance had been proposed by Muthuraman et al (2007, 2008). Finally, single channel tracking through the use of a Kalman filter was proposed and performance has shown an increase in sensitivity over various constant loop bandwidths (Psiaki 2001, Psiaki & Jung 2002, Humphreys et al 2005, Petovello & Lachapelle 2006, Yu et al 2006). Different implementations of the filter were investigated and their capabilities were compared for different signals (Mongrédien et al 2007, Petovello & Lachapelle 2006). The development of ultra-tight GPS receivers combining the benefits of L1 C/A and L2C GPS with IMU (Inertial Measurement Units) also proved to increase the overall performance compared to a standard receiver (Gebre-Egziabher et al 2005, Landis et al 2006, Ohlmeyer 2006, Petovello et al 2008).

Even though all these improvements are of great help to increase sensitivity, limitations still exist. For instance, L2C data and pilot channel being time multiplexed, using the pilot channel only causes a 3 dB loss in terms of signal power. However, GPS signals can be attenuated by 20 dB or more under adverse conditions (Lachapelle 2006). In degraded

signal environments, enhancing the processing gain by 20 dB or more requires a significant increase of the coherent integration time. Such extension would then be limited by the local oscillator stability. Indeed, in terms of mass-market users, the cost of the GPS receiver integrated in cellular phones, PDAs or even car navigation systems must be kept low and a trade-off has to be made on the oscillator performance. Consequently, one would need to improve the receivers' sensitivity without significantly increasing the coherent integration time. This last point could be done using both L2C data and pilot channels. However, the coherent integration time will then be limited by the presence of the 50 Hz navigation message on the data channel. Note that in terms of acquisition, the CL code can hardly be used without assistance due to its length (Fontana et al 2001). As such, acquisition is commonly done by zeroing the CL code which is equivalent to trying to acquire a 3 dB lower signal.

At this point, it is worth to mention that the performance of different acquisition schemes should be evaluated through the probability of false alarm and the probability of correct detection. A good introduction to these concepts is given in Kay (1993) and Schnidman (1989), and as applied to radar technologies (Shnidman 1995). It is common in the literature to use the deflection coefficient to compare different acquisition schemes. However, the very nature of the deflection coefficient supposes that the evaluation is done in the presence of Gaussian noise only (Borio et al 2008). This is not the case when using non-coherent or differential types of acquisition inherent to inter-frequency acquisition schemes. As such, the deflection coefficient provides a rather poor evaluation

under these conditions. Note that a thorough analysis of several acquisitions performance through the probabilities metric was performed by Borio (2008).

1.2 Objectives and Thesis Contributions

The addition of the new L2C signal has brought the number of unencrypted signals available to civilian users to two and increased the total usable signal power. As such, new receiver algorithms performing the combination of L1 C/A and L2C signals can be considered. However, whereas the development of numerous new signals at different frequencies offers a great number of possibilities of combining the signals, only the combinations of pilot and data channel on the same frequency have really been investigated (e.g. Yang et al 2004, Muthuraman et al 2007). Therefore, inter-frequency combination has become important to investigate to enhance acquisition and tracking sensitivity. The research performed herein focuses on novel detection and tracking schemes that collectively utilize the signals from the same system with more than one frequency. Specific interests will be directed toward L1/L2C combination due to immediate availability of real signals. Even if inter-frequency L1/L5 combination has already been investigated by Ioannides (2007), this work had been limited to simulation and tremendously lacks details.

The central interest of this document is the development of acquisition algorithms and new tracking techniques permitting the combination of two signals transmitted at different frequencies to increase performance in weak signal environments. The work performed herein investigates the combinations performance in terms of acquisition and

tracking compared to common techniques making use of only one frequency. Special concerns are directed toward attenuated signals.

The primary novelties brought forth by this thesis are the combinations of already transmitted signals through

- A detailed analysis of the common non-coherent acquisition technique used for single frequency including the parameters involved and cell probabilities of false alarm and detection

- A presentation and simple analysis of the common tracking techniques used for single frequency including details on the parameters used in a PLL and DLL and on error sources when using inter-frequency signal feeding or aiding

- The development and testing of new acquisition schemes combining L1 C/A and L2C including a detailed analysis of the limiting factors and the computation of cell probabilities of false alarm and detection

- The development and testing of a new Kalman filter based tracking scheme combining L1 C/A and L2C, focusing on the advantages arising from the inter-frequency combination over single frequency tracking

- The testing of the proposed Kalman filter combining L1 and L2 under mild ionospheric scintillation events.

All the algorithms proposed are tested using real data as well as simulated data to provide a controlled environment. Note that a strong point of interest of this thesis is the

immediate availability of real signals therefore allowing the immediate implementation of such algorithms for commercial use.

1.3 Thesis Outline

Chapter 2 focuses on the presentation of the GPS signal structure. The L1 C/A and L2C signals are introduced and the main differences between them are highlighted. A first introduction to the acquisition process is also provided in this chapter. Prior to the combination of any signal transmitted at different frequencies, specific considerations have to be directed toward the relative time delay that can occur between those signals. Even if the tropospheric effect is independent of the frequency and therefore should not play any role in a possible relative delay, it is well known that other delays can be introduced due to the ionosphere and the receiver and satellite antennas and electronics. The quantification of this time delay will be investigated throughout this chapter as well as its degradation on the proposed acquisition schemes. Moreover, the Doppler relation between signals transmitted at different frequencies is not entirely represented by the simple ratio of the two frequencies. Similarly, the phase difference between L1 C/A and L2C signals can only be known if the distance between the satellite antenna and the receiver antenna phase centers is perfectly known and no phase disturbances is to occur on the signal path (ionospheric effects). Therefore, the initial phase relation between the two signals cannot possibly be known prior to signal tracking. As such, a detailed analysis of these three parameters is provided in this chapter. Finally, this chapter also includes the derivation of the signal model used throughout this research for both L1 C/A and L2C signals.

Chapter 3 is divided in two main parts. First, several combined L1 / L2 acquisition methods presenting specific interests are introduced. A simulation process based on the signal model provided in Chapter 2 is then presented and used to assess the performance of each of these methods. The second part of this chapter details the results obtained for each of the proposed combined L1 / L2 acquisition schemes. Estimated probabilities of detection and false alarm are used to compare the combining methods to the commonly used non-coherent acquisition on L1 only. The three error sources inherent to the acquisition process mentioned in Chapter 2 (relative code delay, Doppler shifts and relative phase between L1 and L2) are investigated further in term of their effects on each combined acquisition performance.

Chapter 4 is also divided in two parts and follows a similar plan to Chapter 3. First, the theoretical probability density functions of the best combined L1/L2 acquisition techniques investigated in Chapter 3 are derived. The derivation proposed is based on the signal model presented in Chapter 2 and provides the characteristics and probability density functions of the combined methods when the L1 and L2 signals are present and when the L1 and L2 signals are absent. Based on the derived probability density functions, the theoretical probabilities of false alarm and detection of each combining method are calculated. As a means of comparison, the theoretical probability density function of the single frequency non-coherent acquisition is also provided. The second part of this chapter presents the results obtained in terms of theoretical and estimated probabilities of false alarm and detection. The effect of the coherent integration time of

the combining method is also assessed. Finally, conclusions and recommendations for each combining methods are drawn.

Chapter 5 is the logical extension of Chapter 4 and introduces the concept of tracking using a Kalman filter. Indeed, the use of a Kalman filter in the tracking loop has proven to be an enormous advantage throughout the last few years (Petovello et al 2008). The ultimate purpose of a Kalman filter being to use several sources of information to obtain an optimal estimator, it could be of tremendous help in the combination of signals transmitted at different frequencies. As mentioned earlier, L1 C/A and L2C reception is corrupted by the presence of a time delay, and a Doppler shift and phase offset between them. However, these three parameters are of ultimate importance for tracking signals under harsh conditions while wanting to obtain accurate carrier phase measurements. The combination of the signals through a Kalman filter can permit access to these unknowns and the ability to track them over time. Macchi (2009) proposed a Kalman filter capable to track three signals transmitted at the same frequency simultaneously. Megahed (2009) developed a Kalman filter combining L1 C/A and L5 to estimate the L1 and L5 signal amplitudes, phases and code delays and L5 frequency error and phase acceleration that does not account for ionospheric effects. In this thesis an improved model that accounts for the ionospheric effect is developed.

Chapter 6 provides the results of the above Kalman filter based combined tracking method. Once again, results are presented through the comparison of the combined method against the commonly used single frequency tracking technique. Special considerations are directed toward the tracking sensitivity of each method. As a by-

product, the proposed Kalman filter based combined tracking also provides the user with an estimate of the ionospheric conditions. The estimated ionospheric parameters are compared to the ionospheric parameters obtained through external source of data and discussed. Finally, the effect of ionospheric scintillation on the combined tracking method is assessed.

Chapter 7 presents the conclusions of this research and provides recommendations regarding future work.

Chapter Two: L1 & L2 Signal Model and Ionospheric Effect

This chapter introduces the Global Positioning System and provides details on the type of signals it uses and their modulations. Once the signals transmitted by GPS are described, the acquisition process corresponding to the detection of the incoming signals and taking place at the receiver level is presented. Finally, as the purpose of the work herein is to combine GPS signals transmitted from the same satellite but at different frequencies, an analysis of the possible sources of divergence of these signals is provided.

2.1 Introduction to Spread Spectrum and CDMA

2.1.1 Spread Spectrum

In telecommunications, spreading the spectrum of a signal is a technique where a signal is transmitted using a bandwidth larger than required to contain the payload (Ward 2006). A sequential noise-like signal structure is generally used in the process of spreading the initial narrow band information over a wide band of frequencies. In order to retrieve the desired information, the end-user receiver "de-spreads" the spectrum by correlating the incoming signal with the same noise-like sequence used at the encoding transmitter. The purpose of a spread-spectrum signal is to protect against potential interference. The original use of this technique was military as it would not only resist against enemy jamming but also hide the fact that any communication is taking place at all. Indeed, once

spread across a wide frequency range, the transmitted signal is located under the ambient noise level.

Spread spectrum techniques include Frequency Hopping Spread Spectrum (FHSS), Chirp Spread Spectrum (CSS), Time Hopping Spread Spectrum (THSS) and Direct Sequence Spread Spectrum (DSSS). GPS uses DSSS; this technique is described in more detail in the following (Borio 2008).

2.1.2 Direct Sequence Spread Spectrum

DSSS is a technique based on the multiplication of the data to be transmitted by a "noise-like" signal. Its purpose is to spread the energy of the original information over a wider band. The noise signal which is a pseudorandom sequence of 1 and -1 usually has a higher frequency than the initial signal. Once applied, the DSSS technique results in a signal resembling white noise. Provided that the end-user receiver has knowledge of the pseudorandom sequence used during the spreading process, it can use it to multiply the received signal and as such, retrieve the original data. This last point mathematically corresponds to a correlation of the transmitted pseudorandom sequence with the pseudorandom sequence stored locally in the receiver and is called "de-spreading".

However, for the "de-spreading" process to work properly, it is necessary for both locally generated and incoming sequences to be synchronized. Whereas this could seem challenging and a drawback of the DSSS technique, this synchronization process is actually the basis of most satellite navigation systems such as GPS, Galileo and Compass. Indeed, if one has access to the time of transmission of the signal, the correlation process

directly provides the time of reception through the synchronization process. The difference between the time of transmission and the time of reception represents the transit time from the transmitter to the satellite and can be used to determine the distance separating them. Provided that the receiver has a synchronized clock and has access to three signals and the transmitters' positions, it can then deduce its position in a three dimensional space. In the case that the receiver clock is not synchronized, the receiver clock offset, which is common to all satellites observations, can be determined by observing a fourth signal.

2.1.3 Code Division Multiple Access

Based on DSSS, the Code Division Multiple Access method (CDMA) is a channel access method used in particular by GPS. Its principle is that each transmitter possesses a different pseudorandom sequence. Indeed, as several transmitters are located on the same frequency band, an end-user receiver needs to be able to differentiate between them. Therefore, a different pseudo-random noise sequence (PRN) is needed for each transmitter. As mentioned earlier, by correlating the incoming PRNs with locally generated PRNs, the time needed for the signal to transit from one specific satellite identified through its PRN to the receiver can be deduced and used to determine the receiver's position.

2.2 Introduction to L1 and L2 GPS signals

2.2.1 L1 C/A

GPS L1 C/A makes use of the Direct Sequence/Code Division Multiple Access technique through a Binary Phase Shift Keying (BPSK) modulation. The L1 C/A PRN codes used during the spreading process are so called Gold codes and were chosen for their good cross-correlation and auto-correlation properties (about 24 dB protection) as explained by Ward (2006). As such, the different PRNs are almost orthogonal. The PRN sequences are 1023 chips long and clocked at 1.023 MHz. Figure 2-1 and Figure 2-2 shows the auto-correlation function for GPS L1 C/A PRN 31. Note that PRN 31 was only taken as an example and that all other PRN numbers have similar correlation properties. From these figures, it is clear that the auto-correlation properties of the GPS L1 C/A codes are good and that for each code, the correlation peak, in the absence of noise, is a triangle that is two chips wide at the base (see Figure 2-1 and Figure 2-2).
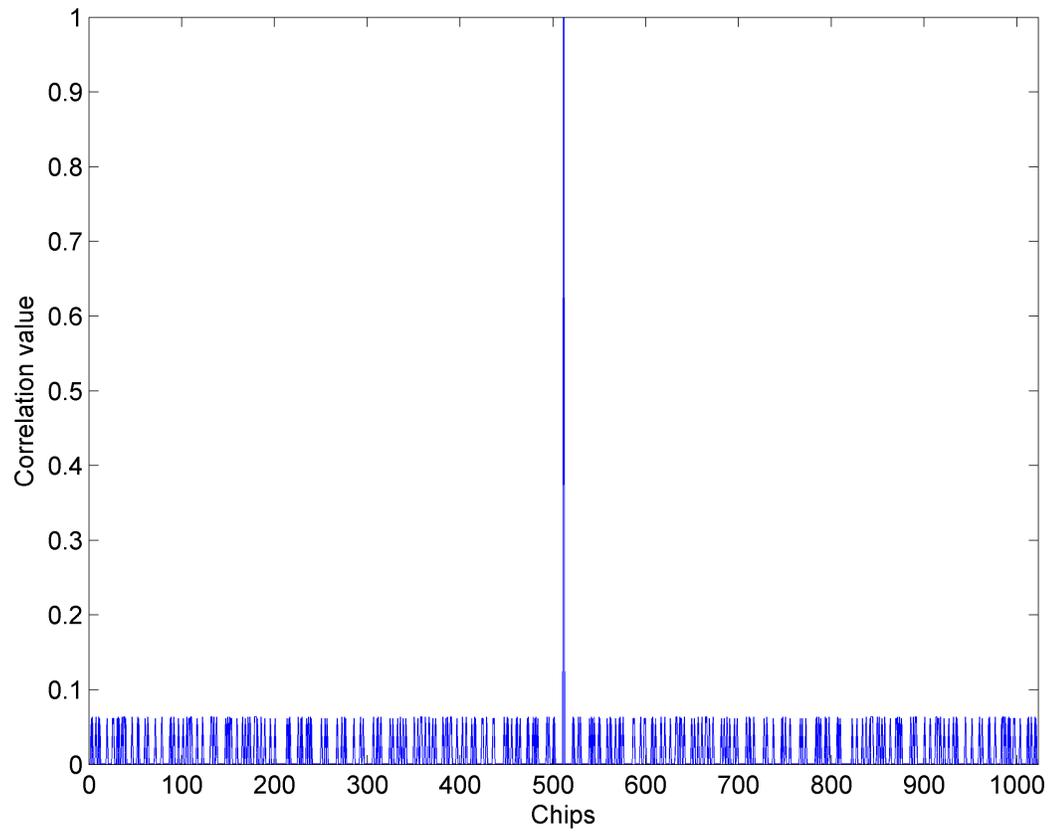
Figure 2-1: Normalized auto-correlation of GPS L1 C/A PRN 31
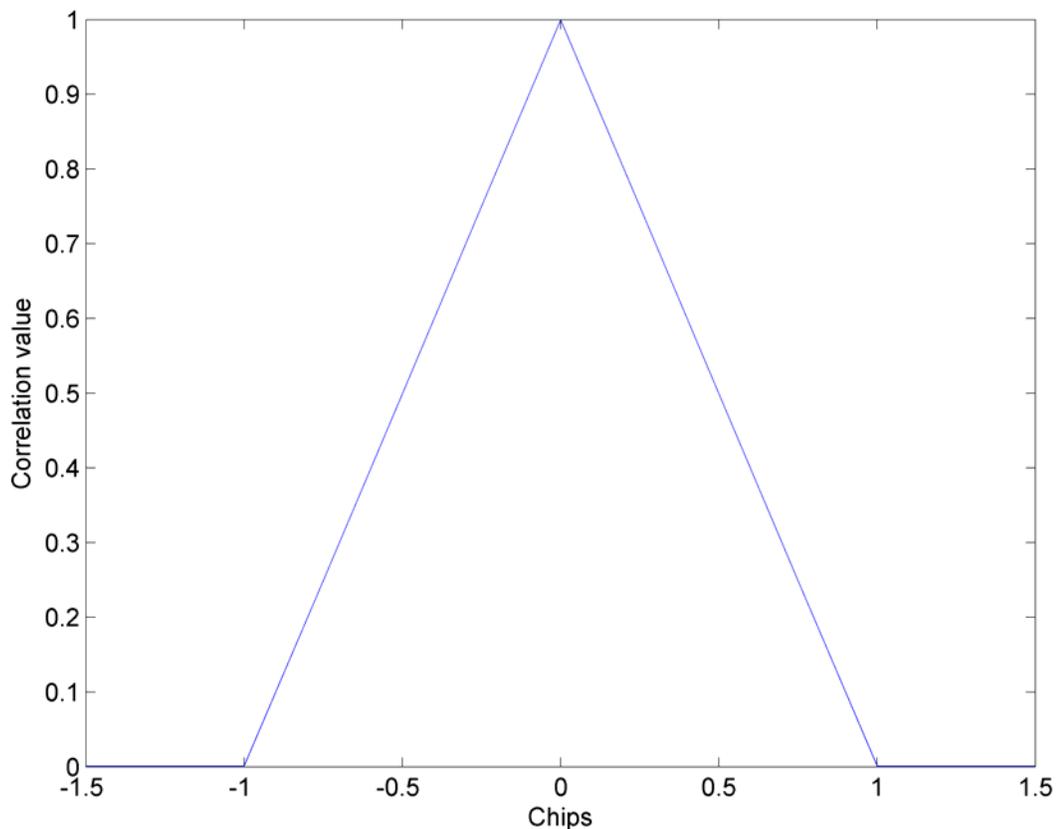
Figure 2-2: Detailed view of the normalized correlation peak of GPS L1 C/A PRN 31 auto-correlation function

The PRN sequence is used to spread the initial signal which is a sinusoid with a frequency of 1575.42 MHz modulated by a 50 Hz navigation message used to transmit the satellites position to the receiver. The data bits transmitted are synchronized with the L1 C/A pseudo-ranging code. However, as the PRN sequence used is shorter than a data bit (1 ms versus 20 ms), the synchronization obtained via the correlation process does not contain information about the data bits boundaries. As such, it is necessary to perform a data bit synchronization after the initial correlation. Figure 2-3 shows the application of

the DSSS process for PRN 31. For the sake of the illustrations provided in Figure 2-3, the

carrier signal considered is not the one used by GPS but is set to a frequency of 1 MHz.
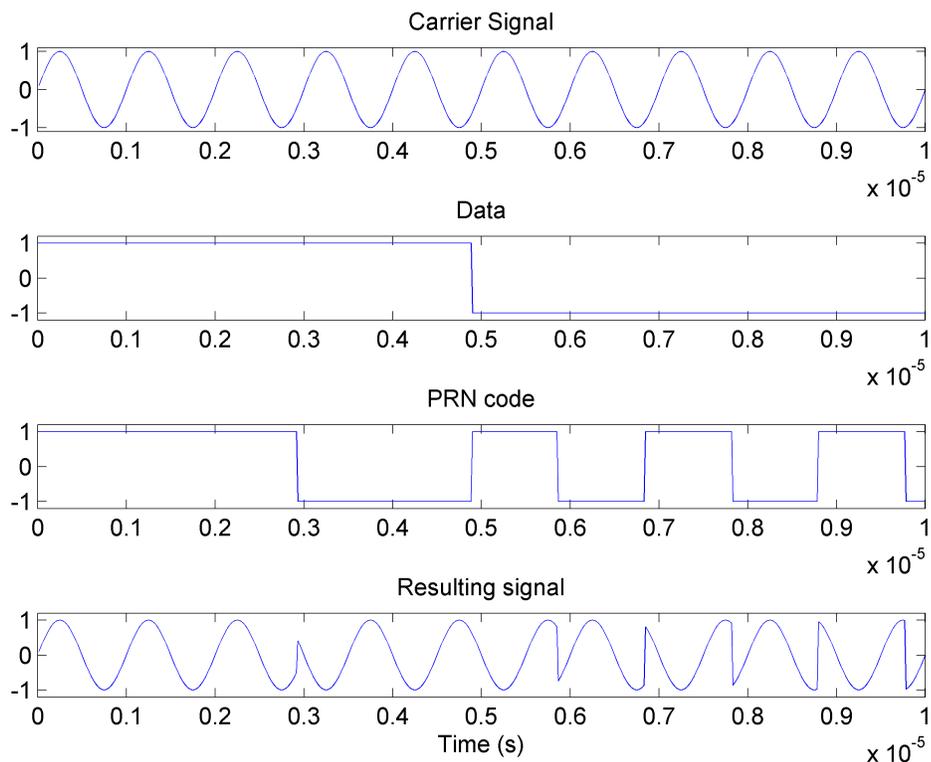
Figure 2-3: Application of the DSSS process to the GPS signal.

Finally, the GPS L1 C/A minimum received power as measured at the output of a 3 dB$_i$

linearly polarized user antenna is -158.5 dBW. Its power spectral density is shown in

Figure 2-4. As it was mentioned earlier the GPS signal is buried under the thermal noise

due to the DSSS process.
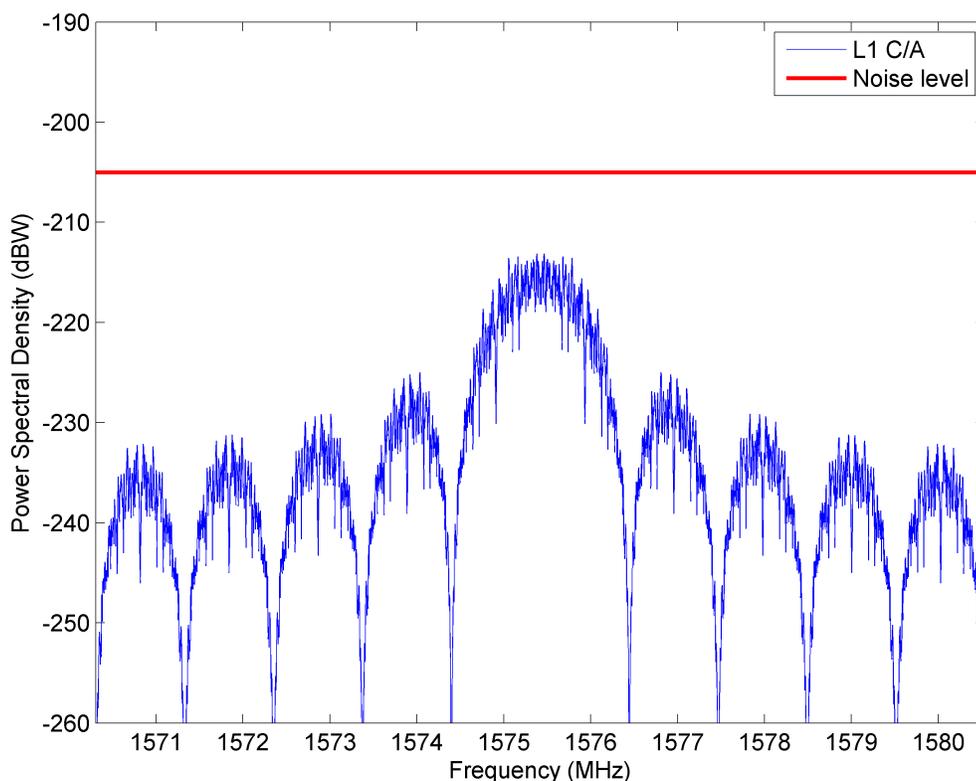
Figure 2-4: Power Spectral Density of the GPS L1 C/A signal and typical thermal noise level

2.2.2 Introduction to GPS L2C signal

During the past decade, the U.S. Department of Defense has worked on the development of two new civilian signals, namely L2C and L5, respectively designed for civilians and aviation purposes. As the following work focuses on L1 C/A and its combination with L2C, only the L2C structure is described herein.

The first Block IIR-M satellite transmitting L2C was launched on September 26, 2005 and uses the PRN sequence number 17. Since then, several satellites namely PRNs 31, 12, 15, 29, 07 and 01 were launched chronologically. At the time of writing, these seven

satellites were transmitting L2C signals without the navigation message. Indeed, the L2C and L5 navigation messages are scheduled to be implemented as part of Operational Control Segment (OCS) upgrades scheduled for 2011 $^{+}$/- one year (Hahn & Powers 2007).

L2C is located at 1227.60 MHz and transmitted 1.5 dB lower than the legacy GPS L1 C/A itself located at 1575.42 MHz and received with a nominal power of -158.5 dBW. Unlike L1 C/A, the L2C signal contains two pseudo-ranging codes namely the CM and CL codes, standing for moderate ranging code and long ranging code respectively, and representing the data and the pilot channel. The data channel is formed by the 10230 chip CM code clocked at 511.5 kHz and modulated by a 50 Hz navigation message. Note that as the CM code and the data bits of the navigation message last 20 ms and are synchronized, the need for data bit synchronization arising with the legacy L1 C/A (data bits lasting 20 ms and C/A code lasting 1 ms) is removed. At this point, it is also important to note that whereas both the L1 C/A and L2C CM codes are modulated by a navigation message, these messages are different for the L1 and L2 signals. The L2 CL code contains 767,250 chips and is clocked at 511.5 kHz. Unlike the CM code, the CL code is not modulated by any navigation message. Moreover, the CL code has an excellent 45 dB cross-correlation protection provided by its extreme length (1.5 s). Note that the CL code being dataless, it allows for coherent integration longer than the 20 ms limit imposed on L1 C/A and L2 CM by the data bit transmitted.

Since the L2 frequency of 1227.6 MHz also carries the military P(Y) signal, the development of L2C was limited to a single bi-phase carrier. Therefore the two channels

(CM and CL) are time multiplexed at 1.023 MHz, the resulting signal being used to BPSK modulate the 1227.6 MHz carrier signal. The time-multiplexed representation of the CM and CL codes is shown in Figure 2-5.
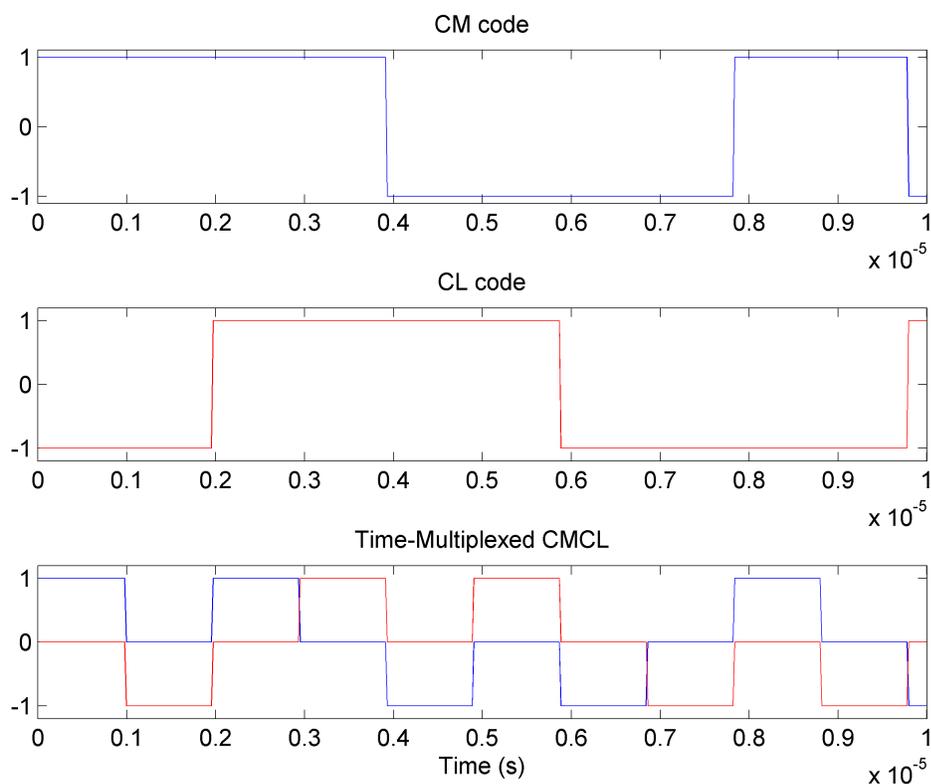
Figure 2-5: CM and CL codes time-multiplexed representation

Note that the fact that CM and CL codes are time multiplexed also implies that they share the total L2C power of -160 dBW equally. This last point is especially important as the extreme length of the CL code makes it very difficult to use during the acquisition process. Therefore, the CL code is usually zeroed, which leads to a signal degradation of 3 dB pushing L2C 4.5 dB lower than L1 C/A in terms of acquisition.
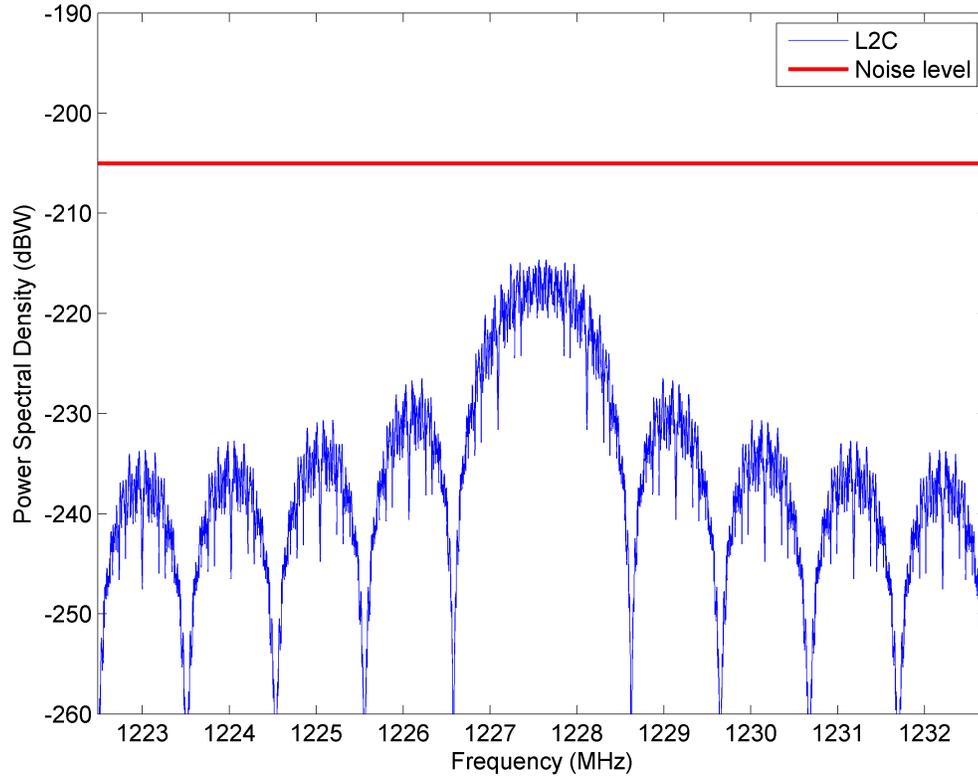
Figure 2-6: Power Spectral Density of the L2C signal

The power spectral density of L2C is represented in Figure 2-6. Note that, for both the L1 C/A and L2C signals, the power spectral density of the signal is usually represented as its envelope defined by (Julien 2005):

$$PSD_E\left(f\right)=\frac{1}{f_c}\left(\frac{\sin\left(\dfrac{\pi}{f_c}(f-f_{L1/L2})\right)}{\dfrac{\pi}{f_c}(f-f_{L1/L2})}\right)^2$$ **2-1**

with f_c being the chipping rate of 1.023 MHz and $f_{L1/L2}$ the carrier frequency of L1 C/A or L2C.

2.3 Acquisition process

The acquisition process represents the process during which signal detection takes place. Due to the relative motion between the satellite and the receiver, a Doppler frequency affects the carrier frequency. Therefore in order to properly remove the carrier wave, a Doppler removal process must take place over a specific range of Doppler frequencies. The relation between the Doppler frequency and the relative satellite-receiver motion is (neglecting the oscillator effects and ionospheric effect):

$$f_D = \frac{v_{r,s}}{c} f_0 \qquad \qquad \textbf{2-2}$$

with f_D being the Doppler effect, $v_{r,s}$ the relative satellite-receiver velocity, c the speed of light and f_0 the carrier wave frequency.

Moreover, the receiver needs to synchronize the locally generated PRN code with the incoming PRN code during the correlation process. As such, the acquisition process has a two dimensional search space, one dimension corresponding to the PRN code delay, the other to the Doppler frequency. Once the carrier wave and pseudo-ranging code are properly found, the "de-spreading" process corresponding to the correlation makes the signal "come out" of the noise (Figure 2-7).
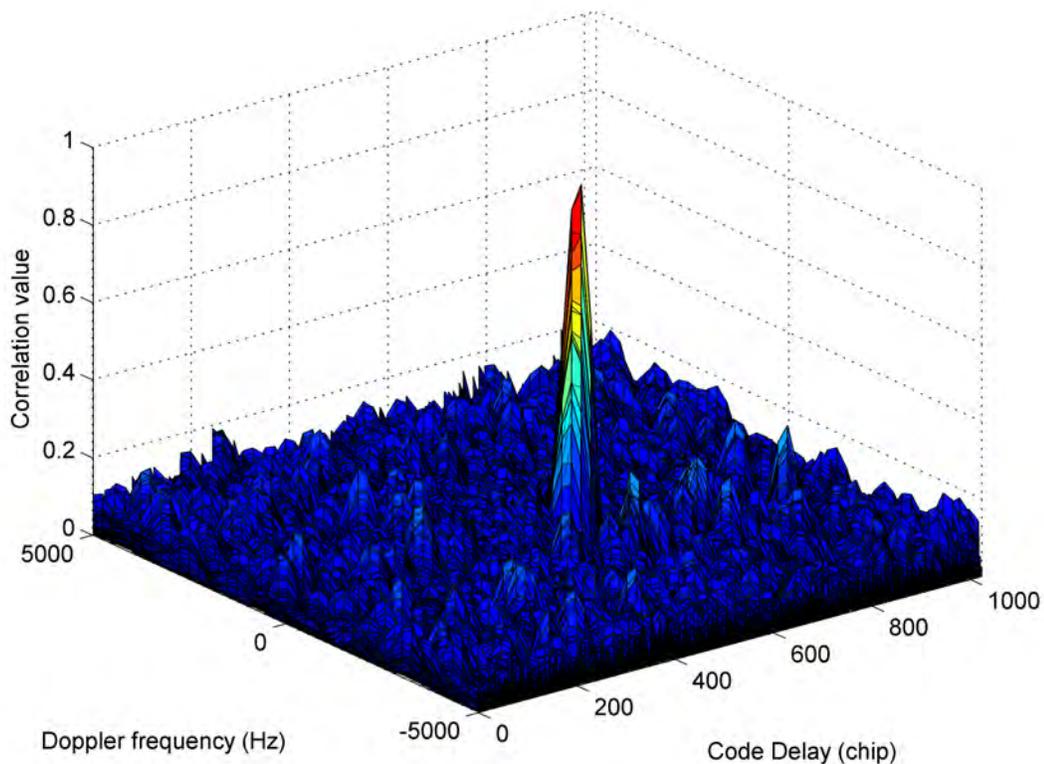
Figure 2-7: Correlation of the GPS L1 C/A signal over the two-dimensional search space necessary for acquisition
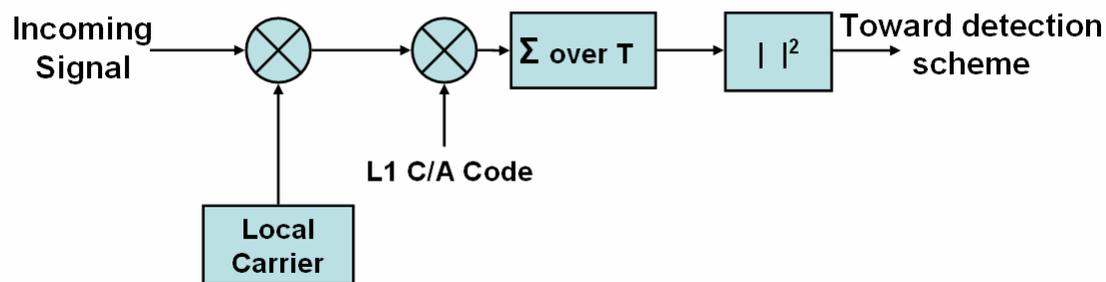
Figure 2-8: Block diagram of a basic acquisition scheme

The block diagram representation of the basic acquisition scheme is shown in Figure 2-8.

The enhancement of the signal-to-noise ratio through the correlation is called the process

gain and is dependent on the time T used for the correlation summation. This last point will be described in the following section.

2.4 Signal Model and Correlator Outputs

2.4.1 Signal Model

This section introduces the signal model which will be used in all the following sections. The proposed model applies to both the GPS L1 C/A and GPS L2C signals.

At the input of the receiver antenna, the GPS L1 C/A signal is the summation of all signals transmitted by the different satellites in view. This is written as (Borio 2008):

$$s_{RF,total} = \sum_{i=1}^{N} A_i \cdot d_i(t-\tau_i) \cdot c_i(t-\tau_i) \cdot \cos\left(2\pi\left(f_{L1} + f_{D,i}\right)t + \theta_i\right)$$ **2-3**

where A_i is the signal amplitude, d_i is the data bit, c_i is the PRN sequence, τ_i is the delay introduced by the signal transit time, $f_{D,i}$ is the Doppler frequency and θ_i is the phase offset of the ith satellite.

Due to the additive Gaussian noise quality of the surrounding environment, this signal is corrupted by zero-mean independent identically distributed Gaussian noise w_{RF} of power spectral density $\frac{N_0}{2}$ (Borio 2008).

As the different PRN codes can be considered orthogonal (Borio 2008), each satellite's signal is treated independently by the receiver. Therefore, in the following analysis only one signal is considered:

$$s_{RF,total} = A \cdot d(t-\tau) \cdot c(t-\tau) \cdot \cos\left(2\pi\left(f_{L1} + f_D\right)t + \theta\right)\right) + w_{RF}(t).$$

2-4

For the sake of simplification, it is assumed that conversion to the working space intermediate frequency f_{IF} is done in one stage only by multiplying the RF signal by $2 \cdot \cos\left(2\pi(f_{L1} - f_{IF})t\right)$ and $2 \cdot \sin\left(2\pi(f_{L1} - f_{IF})t\right)$ followed by a low-pass filter.

This process converts the incoming signal to in-phase and quadra-phase components still modulated by the intermediate plus Doppler frequency:

$$I_{IF}(t) = A \cdot d(t-\tau) \cdot c(t-\tau) \cdot \cos\left(2\pi(f_{IF} + f_D)t + \theta\right) + w_{IF,I}(t)$$

$$Q_{IF}(t) = A \cdot d(t-\tau) \cdot c(t-\tau) \cdot \sin\left(2\pi(f_{IF} + f_D)t + \theta\right) + w_{IF,Q}(t).$$

2-5

Note that as the cosine and sine functions are orthogonal, the noise component can be considered uncorrelated.

From this point forward, the signal is converted to the digital domain. As such, if one neglects the quantization losses, the in-phase and quadra-phase components can be expressed as:

$$I_{IF}(nT_S) = A \cdot d(nT_S - \tau) \cdot c(nT_S - \tau) \cdot \cos\left(2\pi(f_{IF} + f_D)nT_S + \theta\right) + w_{IF,I}(nT_S)$$

$$Q_{IF}(nT_S) = A \cdot d(nT_S - \tau) \cdot c(nT_S - \tau) \cdot \sin\left(2\pi(f_{IF} + f_D)nT_S + \theta\right) + w_{IF,Q}(nT_S).$$

2-6

In order to simplify the notation, nT_s is simply noted as n from now on and the signals considered are discrete signals sampled with a frequency F_s equal to twice the front-end bandwidth B:

$$F_S = \frac{1}{T_S} = 2 \cdot B .$$

<div align="right">**2-7**</div>

As such, the noise components $w_{IF,I}$ and $w_{IF,Q}$ have a variance $\sigma_{IF}^2 = \frac{N_0 F_S}{2}$.

2.4.2 Computation of the correlator outputs

The Doppler removal process is then performed by multiplying $I_{IF}(n)$ and $Q_{IF}(n)$ by

$\sqrt{2} \cos\left(2\pi(f_{IF} + \hat{f}_D)nTs + \theta_{LO}\right)$ and $\sqrt{2} \sin\left(2\pi(f_{IF} + \hat{f}_D)nTs + \theta_{LO}\right)$ respectively:

$$I_D(n) = I_{IF}(n) \cdot \sqrt{2} \cos\left(2\pi(f_{IF} + \hat{f}_D)nTs + \theta_{LO}\right)$$

<div align="right">**2-8**</div>

$$Q_D(n) = Q_{IF}(n) \cdot \sqrt{2} \sin\left(2\pi(f_{IF} + \hat{f}_D)nTs + \theta_{LO}\right).$$

Note that, as the receiver does not have any external information, an estimated Doppler is used and the phase θ_{LO} represents the random initial phase of the local oscillator. Once the Doppler removal process is applied, a local replica of the ranging code c_{local} is generated with an estimated code delay and multiplied with the $I_D(n)$ and $Q_D(n)$ output by the Doppler removal process. The results of these multiplications are then respectively summed over the coherent integration time T (N_S being the number of samples during a coherent integration) desired during the "integrate and dump" process. The resulting real and imaginary parts are named I and Q for the sake of simplicity:

$$I = \frac{1}{N_S} \sum_{n=0}^{N_S - 1} I_D(n) \cdot c_{local}(n - \hat{\tau})$$

<div align="right">**2-9**</div>

$$Q = \frac{1}{N_S} \sum_{n=0}^{N_S-1} Q_D(n) \cdot c_{local}(n-\hat{\tau}).$$

Therefore, assuming that the local and incoming code delays are aligned to less than 1 chip, the useful signal at this point can be expressed at the kth coherent integration as:

$$S(k) = I(k) + j \cdot Q(k) = \frac{1}{N_S} \cdot \frac{A}{\sqrt{2}} \cdot d(k) \cdot R(dt) \sum_{n=(k-1)N_S}^{kN_S-1} e^{j \cdot (2\pi \cdot \Delta F T_S + \varphi)} \qquad \textbf{2-10}$$

with ΔF being the Doppler residual, dt the code misalignment in chips, R the auto-correlation function and φ the phase difference between the incoming signal and local oscillator at the beginning of the first coherent integration ($k = 1$).

By rearranging the terms defining the summation of the above equation and noticing that $N_S \cdot T_S = T$, the summation term can be expressed as (by changing the range of the summation index):

$$\sum_{n=(k-1)N_s}^{kN_s-1} e^{j(2\pi\Delta FnT_S + \varphi)} = e^{j(2\pi\Delta FT_D(k-1)+\varphi)} \sum_{n=0}^{N_s-1} e^{j(2\pi\Delta FnT_S)}. \qquad \textbf{2-11}$$

At this point one can recognize a geometric progression and simplify Equation 2-11 as follows:

$$\sum_{n=0}^{N_s-1} e^{j(2\pi\Delta FnT_S)} = \frac{1-e^{j(2\pi\Delta FT)}}{1-e^{j(2\pi\Delta FT_S)}} = \frac{\sin(\pi\Delta FT)}{\sin(\pi\Delta FT_S)} e^{j(\pi\Delta F(T-T_S))} \qquad N_S \frac{\sin(\pi\Delta FT)}{\pi\Delta FT} e^{j(\pi\Delta F(T-T_S))}.$$

Therefore, it is now possible to obtain a closed form solution for the real and imaginary parts of the correlator output at the kth coherent integration:

$$I(k) = \frac{A}{\sqrt{2}} \cdot d(k) \cdot R(dt) \cdot \frac{\sin(\pi \Delta FT)}{\pi \Delta FT} \cos\left(\pi \Delta FT(2k-1) + \varphi\right)$$

2-12

$$Q(k) = \frac{A}{\sqrt{2}} \cdot d(k) \cdot R(dt) \cdot \frac{\sin(\pi \Delta FT)}{\pi \Delta FT} \sin\left(\pi \Delta FT(2k-1) + \varphi\right).$$

Note that the independent Gaussian noise present at the receiver input is also modified by the Doppler removal and integrate and dump process. The noise present at the output of the correlators remains independent and identically distributed for the real and imaginary part:

$$w_I \quad w_Q \quad N(0, \sigma^2) \text{ with } \sigma^2 = \frac{\sigma_{IF}^{\;2}}{N_S}.$$

Finally, the above derivation is independent of the signal considered and, as such is valid for both L1 and L2C, real and imaginary correlator outputs.

Note that the expected amplitude of the correlator outputs has an attenuation factor in the form of a sinc function dependent on the parameters T, the coherent integration time and ΔF, the residual Doppler frequency. Therefore, for a given T, the farther the estimated Doppler frequency is from the true frequency, the more the signal is going to be attenuated (Figure 2-9).
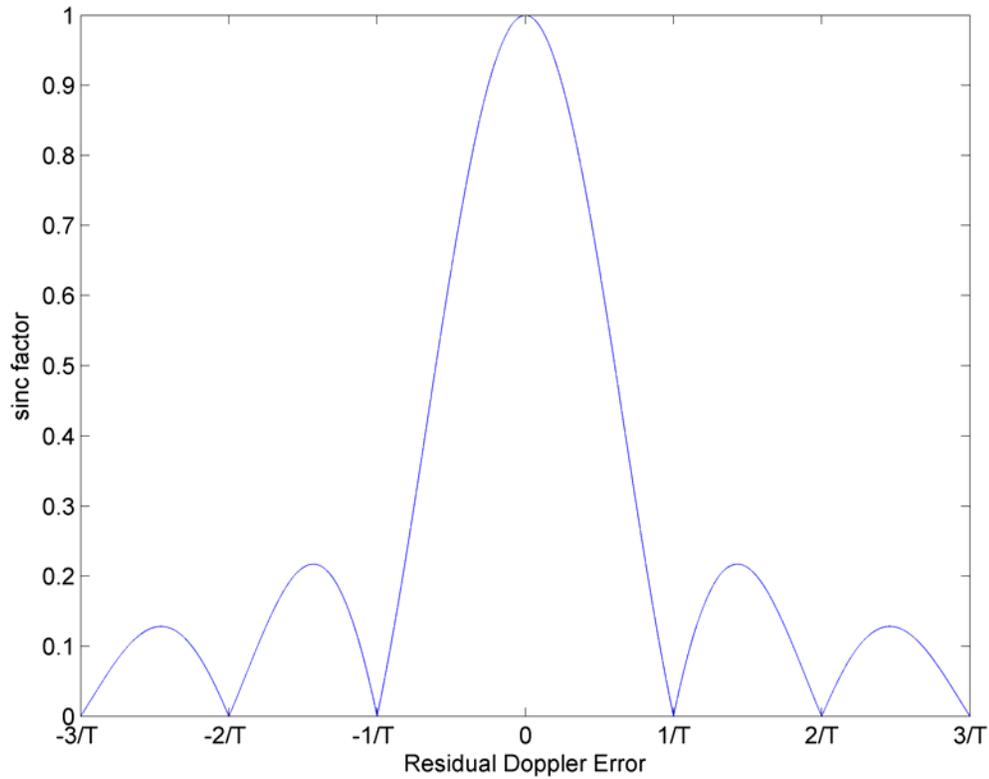
Figure 2-9: Sinc function attenuation factor as a function of the residual frequency error and *T*

Due to the relation between the sinc function attenuation factor and the Doppler estimate used by the receiver during the Doppler removal process, if a longer coherent integration was to be used, the number of Doppler bins defining the acquisition such space would need to be increased. A commonly used function defining the relation between the Doppler bin size and the coherent integration time *T* is

$$BinSize = \frac{2}{3 \cdot T} \ . \qquad\qquad \textbf{2-13}$$

This insures a maximal attenuation factor of 0.82 as the maximum error is limited to half the Doppler bin size. As the Doppler bin size is decreased, the number of Doppler bins defining the acquisition search space is increased and so is the acquisition computation load (Figure 2-10).
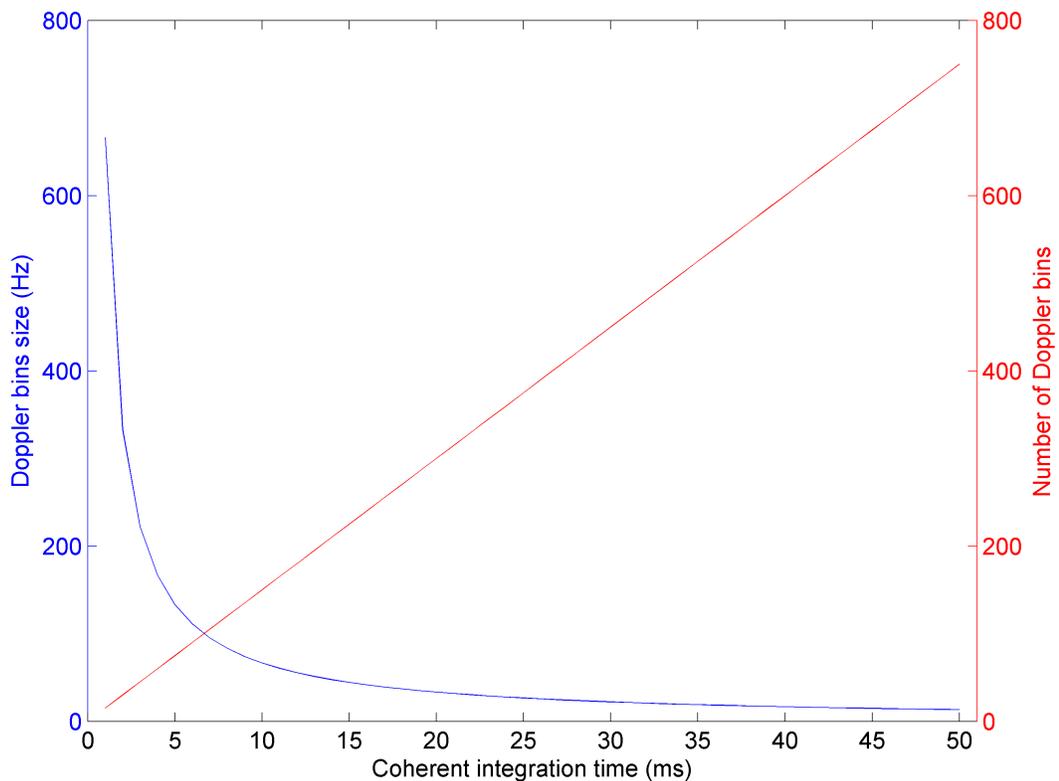
Figure 2-10: Doppler bins size and number of Doppler bins needed to cover the search space as a function of the coherent integration time

Another limitation of long coherent acquisition is the fact that, without external information, the data bits boundaries are unknown. As such, if one was to perform a coherent acquisition across a change of data bits with sign inversion, the process gain brought by the coherent summation would be reduced or cancelled depending on the position of the data bit change with respect of the coherent integration interval.

L2C was developed in order to help the end user to perform long coherent integration with the final purpose of improving the receiver detection performance. This was done by providing the availability of a dataless channel (CL code) and making the CM code duration equal to the data bit duration. However, if one were to use the complete L2C CM code during the acquisition process, the handling of long coherent integration times would be simplified with regard to the L1 C/A long coherent integration at the expense of the number of Doppler bins needed to cover all possible Doppler frequencies created by the relative user/satellite motion. Such an increase would lead to an extended search space and therefore a longer processing time.

A total number of 300 Doppler bins would be needed to cover the entire Doppler search space for a stationary receiver (-5000 Hz to 5000 Hz) if one were to use the 20 ms CM code. This represents 20 times more bins than what is needed for a 1 ms coherent integration. Making use of the complete CL code would be completely unreasonable as it would require a Doppler bins size of 0.44 Hz for a total of 22,500 Doppler bins. This implies that the receiver is capable to estimate the signal true Doppler with a precision better than 0.44 Hz, which would require no or few dynamics as well as an accurate Doppler model for the satellite. Even if the user was to try to make use of sub-sections of the CL code during the acquisition process, it would be extremely challenging to properly align them with the incoming signal without using external timing information or any other GPS signal. Due to these reasons, and as mentioned earlier, the CL code is commonly zero-padded and left unused during a direct acquisition process of L2C.

2.5 Divergence between L1 and L2 signals

Both L1 C/A and L2C are synchronized when they are generated. However the signals transit through the satellite hardware, the atmosphere and the receiver hardware can desynchronize them.

The instrumental relative group delay defines the relative group delay induced by the satellite or receiver hardware. This effect is on the order of the nanoseconds, which is negligible (Coco et al 1991, Sasibhushana Rao 2007) in terms of L1/L2 inter-frequency acquisition but must be considered during the tracking process. Regarding the ionosphere effect, a more detailed analysis is presented below.

As an example, the TEC (Total Electron Content) values across North America (United States and Canada, latitude 30° to 90°) ranged from 10 TECU to 60 TECU on a typical quiet day in 2001, during solar maximum (Fedrizzi et al 2004). During solar storm activity, the TEC value can reach 200 TECU or more (Fedrizzi et al 2004). Moreover, as the ionosphere can be represented by a layer stretched between GPS satellites and the user's receiver, the signal path when transiting through this layer will be directly dependent on the elevation angle. As such, a mapping function is used to link the Slant TEC (STEC) which is the TEC encountered on the signal path to the elevation angle of the satellite and the Vertical TEC (VTEC) (Skone 2007) with E being the elevation angle, h being the average ionosphere layer height and R_e being the earth radius):

$$STEC = M(E) \cdot VTEC$$

$$M(E) = \frac{1}{\sqrt{1 - \left(\dfrac{\cos(E)}{1 + h/R_e}\right)^2}} \cdot$$

2-14

Using the above formula, one can express the time difference between L1 C/A and L2C correlation peaks in seconds:

$$\Delta t_{L1-L2} = \frac{40.3}{c} \cdot \left(\frac{1}{f_2^{\,2}} - \frac{1}{f_1^{\,2}}\right) \cdot STEC = 1.34 \cdot 10^{-7} \cdot STEC \cdot \frac{f_1^{\,2} - f_2^{\,2}}{f_1^{\,2} f_2^{\,2}}$$

2-15

with f_1 and f_2 being the L1 and L2 frequencies and c being the speed of light. From Equation 2-15, the signal degradation observed if one signal were tracked and its delay used to acquire the other can be easily expressed by converting the time distance in seconds to unit of chips.
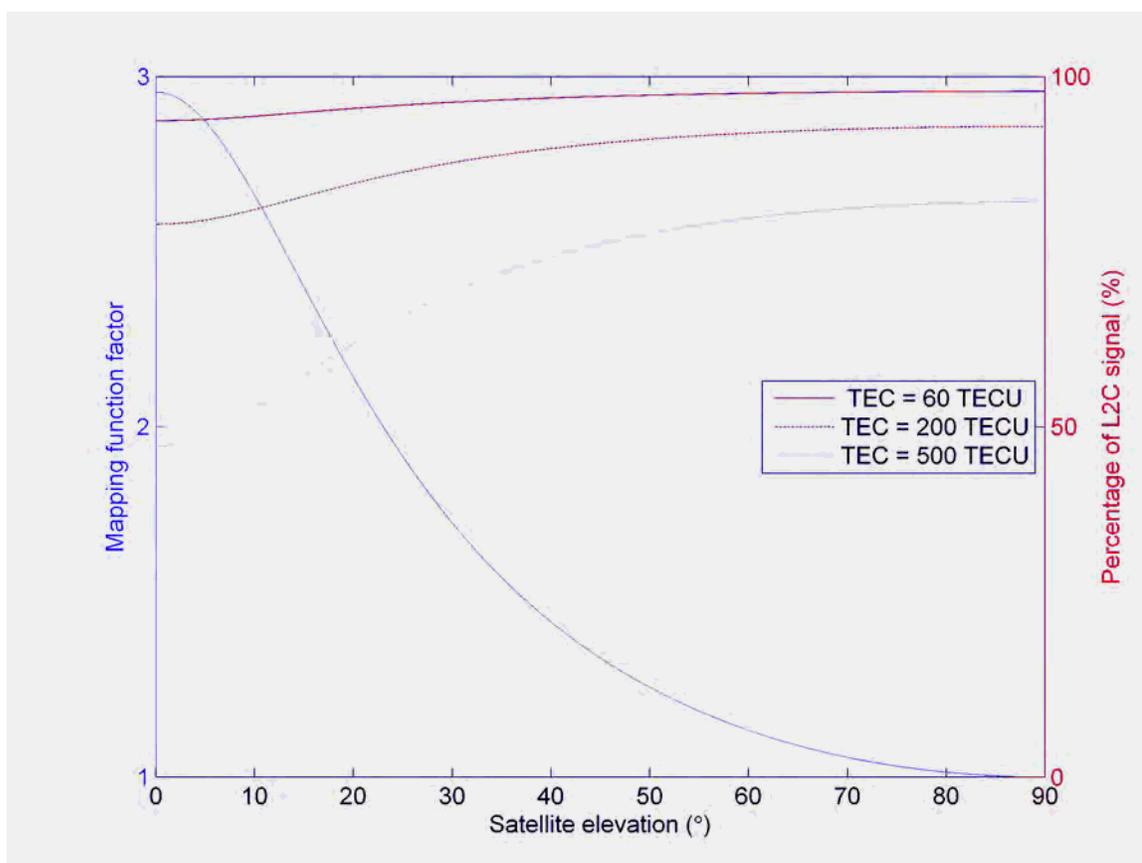
Figure 2-11: Percentage of L2C signal left when locked on L1

Figure 2-11 clearly shows that the expected signal degradation is about 7 % for a satellite located at the horizon for high value of VTEC encountered on a normal day (60 TECU). Note that even during an ionospheric storm increasing the VTEC to 200 TECU, a satellite located at the horizon would only be degraded by about 20 % but, under such adverse conditions, tracking of the signals would be challenging if not impossible due to the ionosphere's activity. Given these results, the combined acquisition of L1/L2 signals can be performed without external information regarding the relative code delay. Finally, it is important to note that the following direct relation exists between the Doppler effect of L1 f_{D1} and the Doppler effect on L2 f_{D2} as this effect is mainly due to the relative user / satellite motion:

$$f_{D1} = \frac{f_1}{f_2} f_{D2} \,.$$

The relative group delay between L1 and L2 remains unknown without external information. It is small enough to be ignored during the acquisition process combining the incoming signals. Chapter 5 shows a combined tracking method estimating the ionosphere for better performance.

From the above results, it is clear that the time delay induced by the ionosphere between L1 C/A and L2C is small enough to be overlooked. As such, the next chapter will present several acquisition techniques combining L1 and L2 signals. The proposed methods are first tested through simulations of the correlator outputs based on the equations presented earlier in this chapter.

Chapter Three: A first approach to combined acquisition methods

In this chapter, five post-correlation acquisition methods combining L1 C/A and L2C signals are presented. Their performance is evaluated using a simulation process. Details and further theoretical analysis of the best methods are then presented in the following chapter.

3.1 Combined acquisition methods investigated

The proposed acquisition methods are post-correlation methods. As such, they use the output of the correlators as input and differ only after the integrate-and-dump process takes place as illustrated in Figure 3-1.
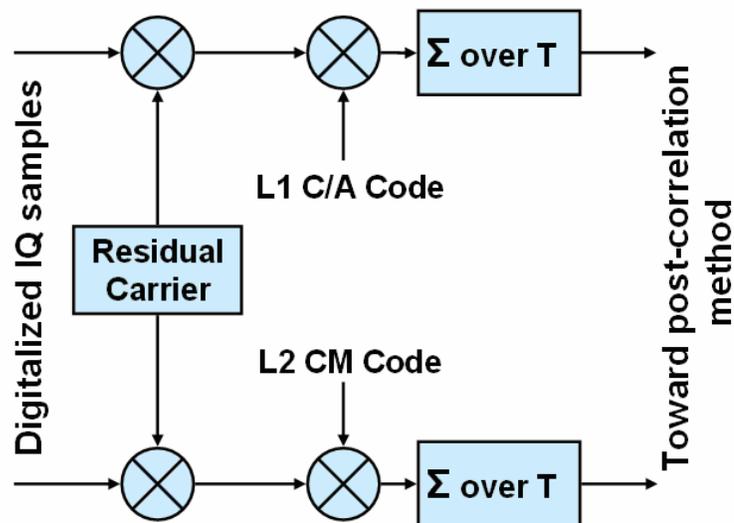
Figure 3-1: Doppler removal, code removal and integrate and dump process performed prior to the proposed acquisition methods

Note that summation over *T* represents the coherent integration time considered. The output signal sent toward the post-correlation methods is equivalent to $I_1(k) + j.Q_1(k)$ for L1 and $I_2(k) + j.Q_2(k)$ for L2. The expressions of *I(k)* and *Q(k)* can be found in the previous chapter, Equation 2-12.

After the coherent summation is performed, the outputs of the correlators are sent toward the post-correlation methods. Note that as the L2C signal has a smaller broadcast power (resulting in a smaller carrier-to-noise density ratio C/N_0 assuming no fading is occurring); it is weighted by a weighting factor *W*. The method used to obtain this weighting factor is described in Section 3.3.1.

The first method called NC_{L1L2} represents the summation of non-coherent acquisition performed on L1 and L2 (Figure 3-2). Its mathematical representation is

$$S_{NCL1L2} = \sum_{k=1}^{M}\left(I_{k,L1}^{2} + Q_{k,L1}^{2}\right) + W^{2} \cdot \sum_{k=1}^{M}\left(I_{k,L2}^{2} + Q_{k,L2}^{2}\right). \qquad \textbf{3-1}$$

This method is the simplest combining method proposed and was chosen due to its low computation load.
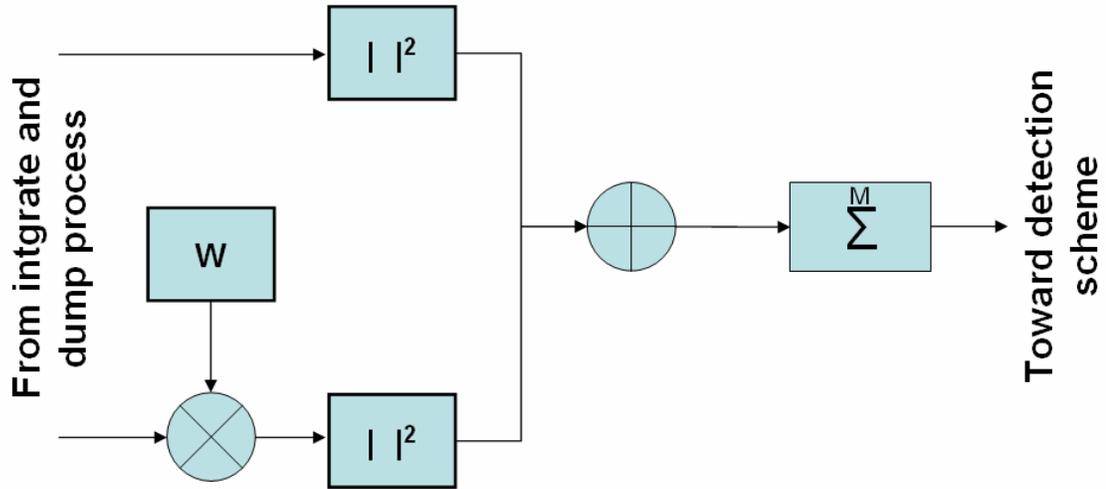
Figure 3-2 : NC$_{L1L2}$ method represented as a block diagram

The second method, named Diff$_{L1L2}$, performs a summation of differential acquisitions done on L1 and L2 (shown in Figure 3-3 with the symbol * standing for complex conjugate). Its mathematical expression is

$$S_{DiffL1L2} = \sum_{k=1}^{M/2}\left(I_{2k,L1} \cdot I_{2k-1,L1} + Q_{2k,L1} \cdot Q_{2k-1,L1}\right) + W^2 \cdot \sum_{k=1}^{M/2}\left(I_{2k,L2} \cdot I_{2k-1,L2} + Q_{2k,L2} \cdot Q_{2k-1,L2}\right). \qquad \textbf{3-2}$$
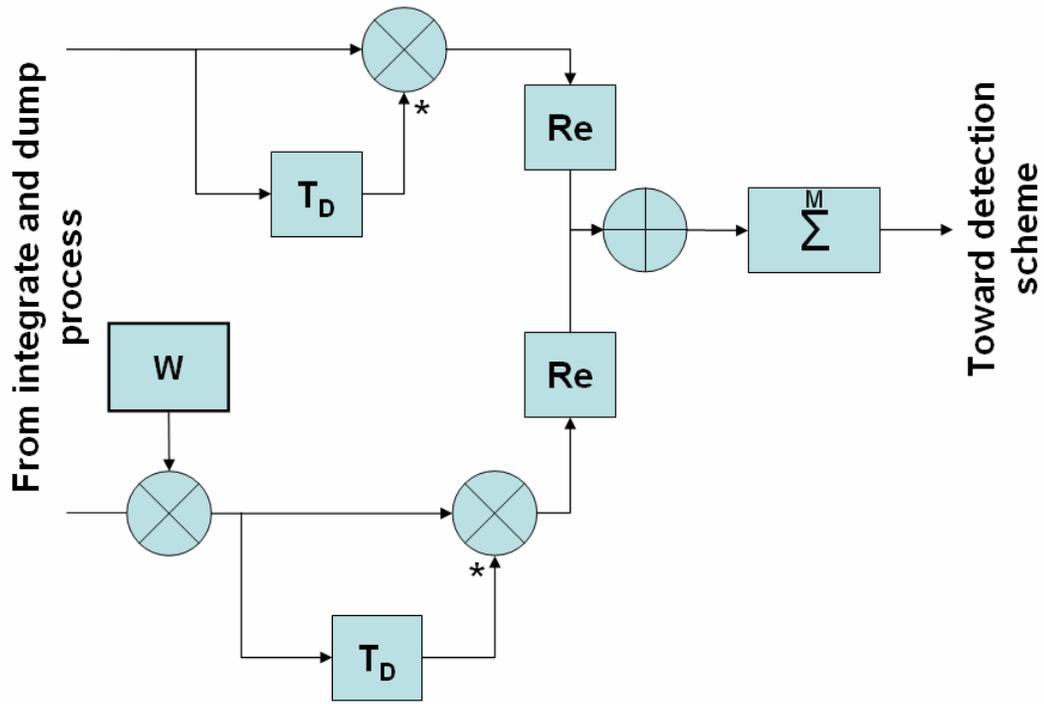
Figure 3-3 : Diff$_{L1L2}$ represented as a block diagram

This method avoids the noise squaring involved in the NC$_{L1L2}$ method while remaining low in terms of computational needs. Note that successive correlator outputs are not multiplied. Each correlator output is present only once in the summation. As such, the noise is not correlated as independent pairs are used.

The third method investigated, named NCDiff$_{L1L2}$, is the summation of the non-coherent and differential acquisitions on L1 and L2 (Figure 3-4). Its mathematical representation is

$$S_{NCDiffL1L2} = \left[\begin{array}{c} \sum_{k=1}^{M} \left(I_{k,L1}{}^2 + Q_{k,L1}{}^2 \right) \\ + \sum_{k=1}^{M-1} \left(I_{k,L1} \cdot I_{k+1,L1} + Q_{k,L1} \cdot Q_{k+1,L1} \right) \end{array} \right] + W^2 \cdot \left[\begin{array}{c} \sum_{k=1}^{M} \left(I_{k,L2}{}^2 + Q_{k,L2}{}^2 \right) \\ + \sum_{k=1}^{M-1} \left(I_{k,L2} \cdot I_{k+1,L2} + Q_{k,L2} \cdot Q_{k+1,L2} \right) \end{array} \right]. \qquad \textbf{3-3}$$
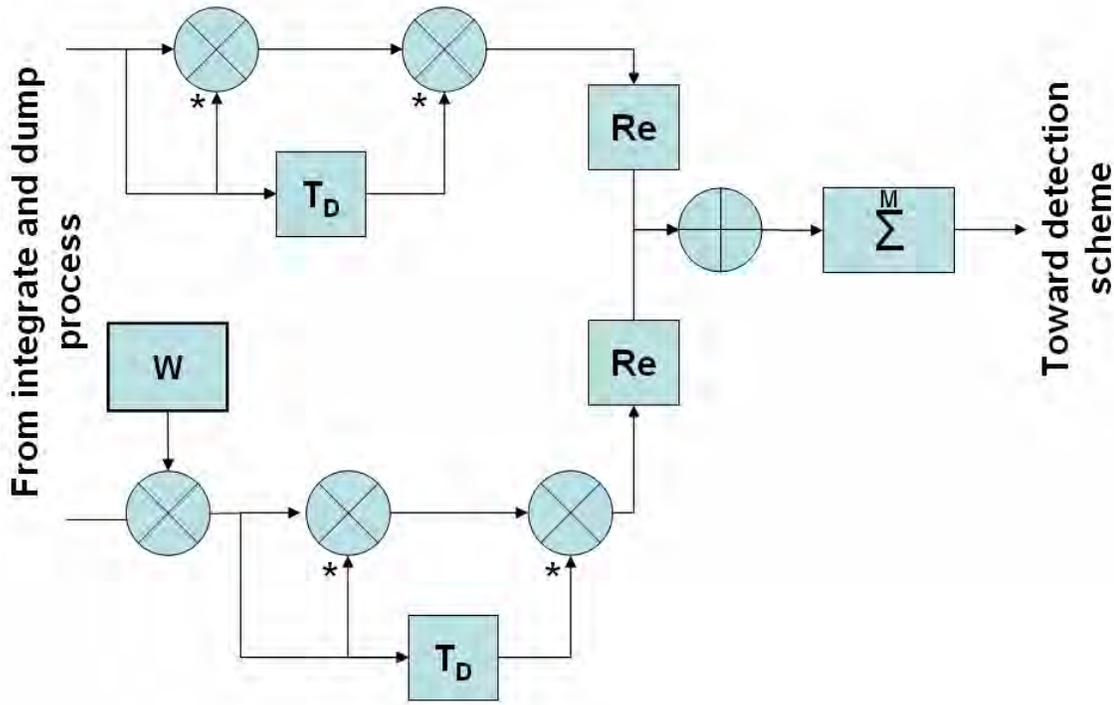
Figure 3-4 : NCDiff$_{L1L2}$ represented as a block diagram

The difference between the differential methods Diff$_{L1L2}$ and NCDiff$_{L1L2}$ comes from the fact that Diff$_{L1L2}$ uses each correlator output only once during the differential summation whereas NCDiff$_{L1L2}$ uses a same correlator output several times during the differential summation (see Equations 3-2 and 3-3). As such, the terms of the NCDiff$_{L1L2}$ method's summation are correlated.

The next method is the addition of the multiplication of the real parts and imaginary parts of L1 and L2 correlator outputs (Figure 3-5). Its mathematical representation is

$$S_{NCML1L2} = \sum_{k=1}^{M} \left(W \cdot I_{k,L1} \cdot I_{k,L2} \right)^2 + \left(W \cdot Q_{k,L1} \cdot Q_{k,L2} \right)^2 . \qquad \textbf{3-4}$$
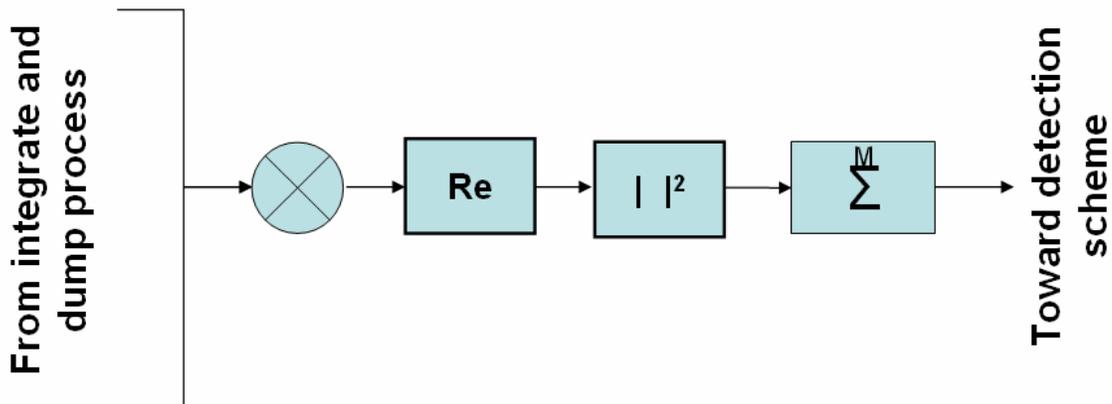
Figure 3-5: NCM$_{L1L2}$ represented as a block diagram

This method was chosen due to its potential for multipath mitigation. As the multipath, present on L1 and L2 are potentially uncorrelated, this method can avoid acquisition of a multipath signal. Moreover, as the correlation peak of L1 and L2 are multiplied, the overall peak is narrowed and the estimate of code delay is more accurate. Figure 3-6 shows the normalized correlation peak of L1 C/A only and L1 C/A times L2 CM.
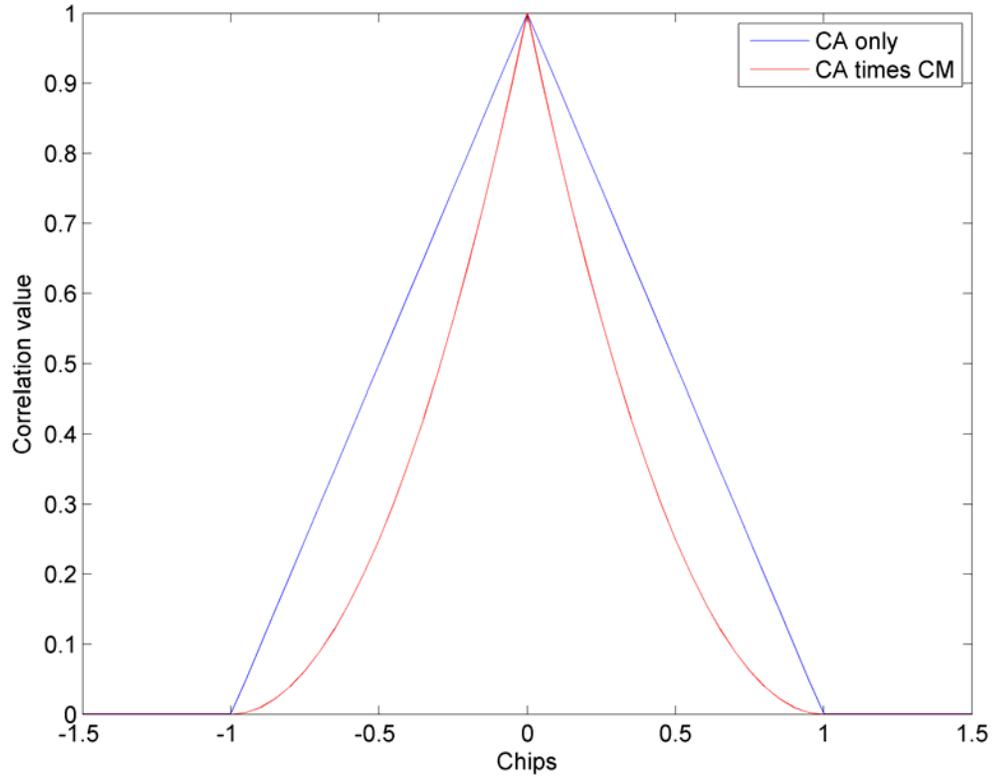
Figure 3-6: Normalized correlation peaks of L1 C/A only and L1 C/A times L2 CM codes

This method has two drawbacks:

- Multiplying L1 and L2 correlator outputs not only multiplies the output noise but remove the effect of the weight *W* applied on L2

- The overall L1 L2 correlation peak is smaller than the correlation peak on L1 only as shown in Figure 3-7.
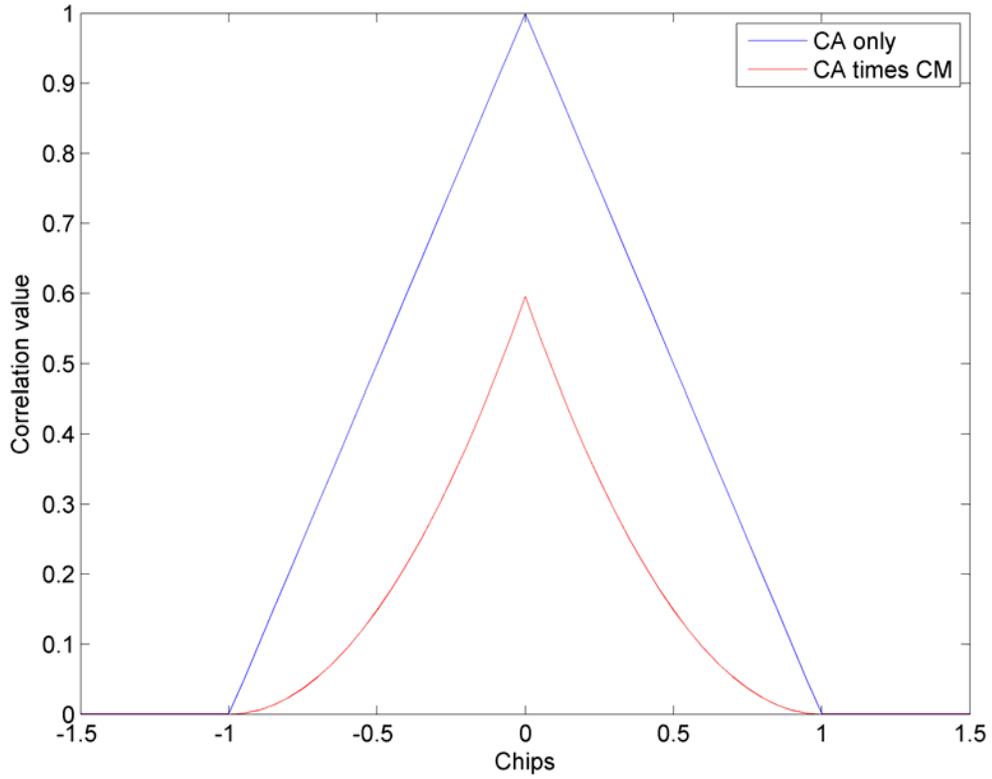
Figure 3-7: Normalized correlation peaks of L1 C/A only compared to L1 C/A times L2 CM correlation peak. L1 C/A times L2C correlation is normalized by the correlation peak of L1 C/A

The last combining method investigated represents a coherent summation of L1 and L2 correlator outputs (Figure 3-8) and is named COH_{L1L2}. Its mathematical expression is

$$S_{COHL1L2} = \sum_{k=1}^{M} \left(I_{k,L1} + I_{k,L2} \right)^2 + \left(Q_{k,L1} + Q_{k,L2} \right)^2 .$$

3-5
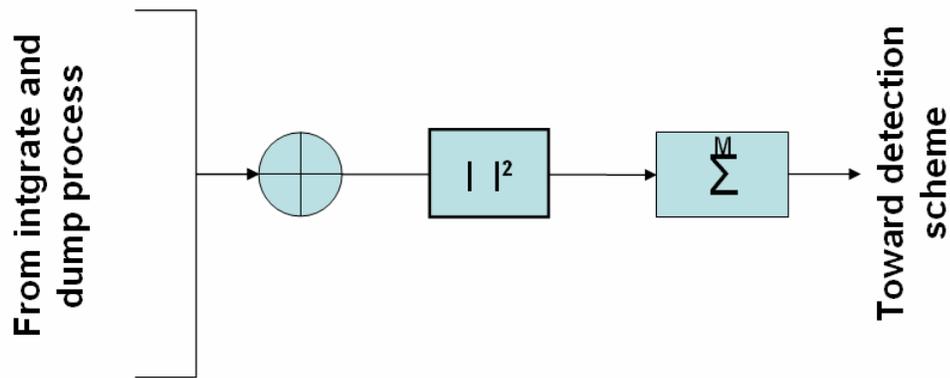
Figure 3-8: Non-coherent summation of the L1 C/A plus the L2C over M post-correlation outputs

3.2 Details on the simulation process

In order to investigate the performance of each method and compare them to the common non-coherent acquisition method of L1 C/A only, a statistical analysis has been conducted.

As each method differs from the others only after the integrate and dump process of L1 and L2 signals, special consideration was given toward the possibility to simulate the L1 and L2 correlator outputs directly. The expression of the real and imaginary parts of the correlator outputs were derived in Chapter 2 and are repeated here for convenience:

$$I(k) = \frac{A}{\sqrt{2}} \cdot d(k) \cdot R(dt) \cdot \frac{\sin(\pi\Delta FT)}{\pi\Delta FT} \cos\left(\pi\Delta FT(2k-1)+\varphi\right) + w_I(k)$$

3-6

$$Q(k) = \frac{A}{\sqrt{2}} \cdot d(k) \cdot R(dt) \cdot \frac{\sin(\pi\Delta FT)}{\pi\Delta FT} \sin\left(\pi\Delta FT(2k-1)+\varphi\right) + w_Q(k)$$

with w_I w_Q $N(0,\sigma^2)$ with $\sigma^2 = \dfrac{\sigma_{IF}^{\,2}}{N_S}$.

Based on Equation 3-6, the correlator outputs are dependent on known parameters and unknown parameters. Indeed, the coherent integration time T is defined by the user and the signal amplitude A is a direct function of the carrier-to-noise density ratio C/N_0 according to

$$\frac{C}{N_0} = \frac{A^2}{2} \cdot \frac{1}{N_0} = \frac{A^2}{2} \cdot \frac{F_s}{2\sigma_{IF}^2}.$$

3-7

Therefore, either by fixing the C/N_0 and A or σ_{IF}, it is possible to simulate the real and imaginary part of the correlator outputs with the correct amplitude and noise statistics. However, Equation 3-6 is also composed of unknown parameters: the time error dt on the synchronization of the local and incoming codes, the data bit modulating the kth millisecond $d(k)$, the residual frequency error ΔF and the initial phase error φ both due to the misalignment of the locally generated carrier with the incoming carrier signal. Note that all of these parameters are unknown to the user but bounded with respect to their definition. For instance, the Doppler frequency bins size defined in Equation 2-13 limits the residual frequency error to 333.33 Hz for a 1 ms coherent integration, the code step size limits dt, φ ranges between 0 and 2π and the data bit can only take values of +1 or -1. Therefore, the L1 correlator outputs can be simulated by defining the known parameters and keeping the unknown ones random but bounded according to the parameters shown in Table 3-1.

Table 3-1: Parameters used to simulate the L1 correlator outputs

Known Parameters	
$C/N_{0\,L1}$	Defined by user
T	1 ms
σ_1^2	equal to σ^2
Unknown parameters	
$d_1(k)$	Random 1 or -1
dt_1	Uniformly distributed
ΔF_1	Uniformly distributed
φ_1	Uniformly distributed

Once the parameters for simulation of the L1 correlator outputs have been defined, the L2 correlator outputs can be simulated as well. Indeed, the L2 signal power is 1.5 dB lower than L1 and an additional 3 dB attenuation is applied due to the zero-padding technique (Fontana et al 2001). This last point can either be performed by assuming that the L2 C/N_0 is 4.5 dB lower than L1 C/N_0 or by assuming that the L2 C/N_0 is 1.5 dB lower than L1 but the noise variance at the output of the L2 correlator is twice that at the output of the L1 correlator due to the zero-padding, which is equivalent to performing the integration over half of the samples. In the following, the second solution was chosen. The residual frequency error on L2 is directly related to the residual frequency error on L1 by the factor f_2 / f_1 as the Doppler estimate used on L1 is converted by this factor and used on L2 to perform the Doppler removal process. It is assumed that the same code step size is used on L1 and L2, therefore the code error related to the code step size is

identical on L1 and L2. However, the time error affecting the auto-correlation peak on L2 is also dependent on the ionospheric effect. As such, this effect is also simulated based on a uniform distribution between 0 and 90° satellite elevation angle to define the mapping factor and a uniform distribution between 10 TECU and 60 TECU Vertical TEC. These two parameters are then used to define the relative code delay between L1 and L2 according to

$$\Delta t_{L1-L2} = 1.34 \cdot 10^{-7} \cdot M(E) \cdot VTEC \cdot \frac{f_1^2 - f_2^2}{f_1^2 f_2^2} \qquad \textbf{3-8}$$

$$M(E) = \frac{1}{\sqrt{1 - \left(\dfrac{\cos(E)}{1 + \dfrac{h}{R_e}}\right)^2}} . \qquad \textbf{3-9}$$

Δt_{L1-L2} is in turn added to the code error due to the code step size. Finally, as no external information is used and since the L1 navigation message differs from the L2 navigation message, the initial phase error on L2 is kept random as well as the data bit applied, as shown in Table 3-2.

Table 3-2: Parameters used to simulate the L2 correlator outputs

Known Parameters	
$C/N_{0\,L2}$	$C/N_{0\,L1} - 1.5$
T	1 ms
$\sigma_1{}^2$	equal to twice σ^2
Unknown parameters	
$d_2(k)$	Random 1 or -1
dt_2	$dt_1 + d_{iono}$
d_{iono}	Dependent on VTEC and Map
VTEC	Uniformly distributed
Map	Dependent on elevation angle E
E	Uniformly distributed
ΔF_2	$\Delta F_1 \times f_2 / f_1$
φ_2	Uniformly distributed

3.3 Expression of the acquisition outputs as quadratic forms

First of all, the simulation performed aimed to assess the performance of the combined acquisition techniques using 1 ms coherent integration with four non-coherent summations (M=4).

Considering the vector of correlator output on L1 and on L2 as:

$$V = \begin{bmatrix} I_{1,L1} & Q_{1,L1} & \cdots & I_{M,L1} & Q_{M,L1} & W \cdot I_{1,L2} & W \cdot Q_{1,L2} & \cdots & W \cdot I_{M,L2} & W \cdot Q_{M,L2} \end{bmatrix}^T.$$

The output of each combined acquisition is denoted as S. For all the combined acquisitions this can then be expressed through the following quadratic form:

$$S = V^H A V \qquad\qquad\qquad \textbf{3-10}$$

where H standing for Hermitian conjugate and A represents the design matrix of the acquisition method of interest. The use of the matrix A defining the acquisition method to investigate is especially interesting when one tries to assess the method performance statistically. Indeed, obtaining N outcomes of the acquisition method under investigation can be done in parallel using the following formula:

$$S_N = \sum_{over\ columns} \left(V_N^T \cdot A \otimes V_N^T \right)$$

with V_N^T being a $2M \times N$ matrix of correlator outputs (each columns representing the vector V used to generate each outcome of the acquisition method investigated), A representing the design matrix defined by the quadratic form mentioned above, $\otimes$ representing a term by term multiplication and S_N being a $N \times 1$ matrix containing N outcomes of the acquisition method under investigation. Using a parallel implementation is especially interesting as it tremendously reduces the time necessary to conduct a statistical analysis.

3.3.1 Quadratic form of NC$_{L1L2}$

The NC$_{L1L2}$ method output is expressed as:

$$S_{NCL1L2} = \sum_{k=1}^{M} \left(I_{k,L1}^{2} + Q_{k,L1}^{2} \right) + W^{2} \cdot \sum_{k=1}^{M} \left(I_{k,L2}^{2} + Q_{k,L2}^{2} \right).$$

As such, it can be put in a quadratic form by considering the vector V defined earlier and the matrix A$_{NCL1L2}$:

$$A_{NC_{L1L2}} = \begin{bmatrix} 1 & 0 & \cdots & 0 & 0 & \cdots & \cdots & 0 \\ 0 & \ddots & \ddots & \vdots & \vdots & \ddots & \ddots & \vdots \\ \vdots & \ddots & \ddots & 0 & \vdots & \ddots & \ddots & \vdots \\ 0 & \cdots & 0 & 1 & 0 & \cdots & \cdots & 0 \\ 0 & \cdots & \cdots & 0 & W^{2} & 0 & \cdots & 0 \\ \vdots & \ddots & \ddots & \vdots & 0 & \ddots & \ddots & \vdots \\ \vdots & \ddots & \ddots & \vdots & \vdots & \ddots & \ddots & 0 \\ 0 & \cdots & \cdots & 0 & 0 & \cdots & 0 & W^{2} \end{bmatrix}$$

3-11

which has the form of a block matrix with two matrices forming the diagonal and corresponding to a non-coherent acquisition on L1 and L2 only respectively.

3.3.2 Quadratic form of Diff$_{L1L2}$

The Diff$_{L1L2}$ method output is expressed as:

$$S_{DiffL1L2} = \sum_{k=1}^{M/2} \left(I_{2k,L1} \cdot I_{2k-1,L1} + Q_{2k,L1} \cdot Q_{2k-1,L1} \right) + W^{2} \cdot \sum_{k=1}^{M/2} \left(I_{2k,L2} \cdot I_{2k-1,L2} + Q_{2k,L2} \cdot Q_{2k-1,L2} \right).$$

As such, it can be put in a quadratic form by considering the vector V defined earlier and the matrix A$_{DiffL1L2}$:

$$A_{Diff_{L1L2}} = \begin{bmatrix} \tilde{A}_{Diff_{L1L2}} & 0 \\ 0 & W^2 \cdot \tilde{A}_{Diff_{L1L2}} \end{bmatrix}$$

3-12

with:

$$\tilde{A}_{Diff_{L1L2}} = \begin{bmatrix} 0 & Id_2 & 0 & 0 & 0 & 0 & 0 & \cdots \\ 0 & \ddots & 0 & \ddots & \ddots & \ddots & \ddots & \ddots \\ 0 & \ddots & \ddots & Id_2 & \ddots & \ddots & \ddots & \ddots \\ 0 & \ddots & \ddots & \ddots & 0 & \ddots & \ddots & \ddots \\ 0 & \ddots & \ddots & \ddots & \ddots & Id_2 & \ddots & \ddots \\ 0 & \ddots & \ddots & \ddots & \ddots & \ddots & 0 & \ddots \\ 0 & \ddots & \ddots & \ddots & \ddots & \ddots & \ddots & \ddots \\ \vdots & \ddots & \ddots & \ddots & \ddots & \ddots & \ddots & \ddots \end{bmatrix}, \ Id_2 = \begin{bmatrix} 1 & 0 \\ 0 & 1 \end{bmatrix}$$

$\tilde{A}_{Diff_{L1L2}}$ being a $M \times M$ matrix.

3.3.3 Quadratic form of NCDiff$_{L1L2}$

The NCDiff$_{L1L2}$ method output is expressed as:

$$S_{NCDiffL1L2} = \begin{bmatrix} \sum_{k=1}^{M}\left(I_{k,L1}{}^2 + Q_{k,L1}{}^2\right) \\ + \sum_{k=1}^{M-1}\left(I_{k,L1} \cdot I_{k+1,L1} + Q_{k,L1} \cdot Q_{k+1,L1}\right) \end{bmatrix} + W^2 \cdot \begin{bmatrix} \sum_{k=1}^{M}\left(I_{k,L2}{}^2 + Q_{k,L2}{}^2\right) \\ + \sum_{k=1}^{M-1}\left(I_{k,L2} \cdot I_{k+1,L2} + Q_{k,L2} \cdot Q_{k+1,L2}\right) \end{bmatrix} .$$

As such, it can be put in a quadratic form by considering the vector V defined earlier and

the matrix A$_{NCDiffL1L2}$:

$$A_{NCDiff_{L1L2}} = \begin{bmatrix} \tilde{A}_{NCDiff_{L1L2}} & 0 \\ 0 & W^2 \cdot \tilde{A}_{NCDiff_{L1L2}} \end{bmatrix}$$

3-13

with:

$$\tilde{A}_{NCDiff_{L1L2}} = \begin{bmatrix} 1 & 0 & 1 & 0 & 0 & \cdots & 0 \\ 0 & \ddots & \ddots & \ddots & \ddots & \ddots & \vdots \\ \vdots & \ddots & \ddots & \ddots & \ddots & \ddots & 0 \\ \vdots & \ddots & \ddots & \ddots & \ddots & \ddots & 0 \\ \vdots & \ddots & \ddots & \ddots & \ddots & \ddots & 1 \\ \vdots & \ddots & \ddots & \ddots & \ddots & \ddots & 0 \\ 0 & \cdots & \cdots & \cdots & \cdots & 0 & 1 \end{bmatrix}$$

being an $M \times M$ matrix.

3.3.4 Quadratic form of NCM_{L1L2}

The NCM_{L1L2} method, being expressed as

$$S_{NCML1L2} = \sum_{k=1}^{M} \left(W \cdot I_{k,L1} \cdot I_{k,L2} \right)^2 + \left(W \cdot Q_{k,L1} \cdot Q_{k,L2} \right)^2 ,$$

needs a slight modification of the V vector as V_m:

$$V_m = \begin{bmatrix} I_{1,L1} \cdot I_{1,L2} & Q_{1,L1} \cdot Q_{1,L2} & \cdots & I_{M,L1} \cdot I_{M,L2} & Q_{M,L1} \cdot Q_{M,L2} \end{bmatrix}^T .$$

As such, it can be put in a quadratic form by considering the vector V_m and the matrix $A_{NCML1L2}$:

$$A_{NCM_{L1L2}} = \begin{bmatrix} W^2 & 0 & \cdots & 0 \\ 0 & \ddots & \ddots & \vdots \\ \vdots & \ddots & \ddots & 0 \\ 0 & \cdots & 0 & W^2 \end{bmatrix} = W^2 \cdot Id_M$$

being an $M \times M$ matrix equals to W^2 times the $M \times M$ identity matrix Id_M.

3.3.5 Quadratic form of COH_{L1L2}

The COH_{L1L2} method, being expressed as

$$S_{COHL1L2} = \sum_{k=1}^{M} \left(I_{k,L1} + I_{k,L2} \right)^2 + \left(Q_{k,L1} + Q_{k,L2} \right)^2 ,$$

needs a slight modification of the V vector as V_c:

$$V_m = \begin{bmatrix} I_{1,L1} + I_{1,L2} & Q_{1,L1} + Q_{1,L2} & \cdots & I_{M,L1} + I_{M,L2} & Q_{M,L1} + Q_{M,L2} \end{bmatrix}^T.$$

As such, it can be put in aquadratic form by considering the vector V_m and the matrix $A_{COHL1L2}$:

$$A_{COH_{L1L2}} = \begin{bmatrix} 1 & 0 & \cdots & 0 \\ 0 & \ddots & \ddots & \vdots \\ \vdots & \ddots & \ddots & 0 \\ 0 & \cdots & 0 & 1 \end{bmatrix}$$

being an $M \times M$ matrix.

3.4 Results

In this section, the Receiver Operating Characteristics (ROC) curve is used. It is defined as the probability of detection P_d as a function of the probability of false alarm P_{fa}. In the specific case investigated herein, the probability of detection is defined as the probability to detect the presence of the signal under the H_1 hypothesis (signal is actually present). On the other hand, the probability of false alarm is defined as the probability to detect the presence of the signal under the hypothesis H_0 (signal is actually absent). As it is customarily the case, P_{fa} is fixed and used to determine a threshold β such that the integral of the noise PDF (PDF obtained under H_0) from β to infinity is equal to P_{fa}. The same threshold β is then used to compute P_d, which is the integral of the PDF obtained under H_1 from β to infinity:

$$P_{fa} = \int_{\beta}^{+\infty} f_{S/H_0}(s) ds \qquad \qquad \textbf{3-14}$$

$$P_d = \int_\beta^{+\infty} f_{S/H_1}(s)\, ds \,.$$

$$\text{3-15}$$

Figure 3-9 and Figure 3-10 illustrate graphically P_d and P_{fa} under Gaussian noise conditions.
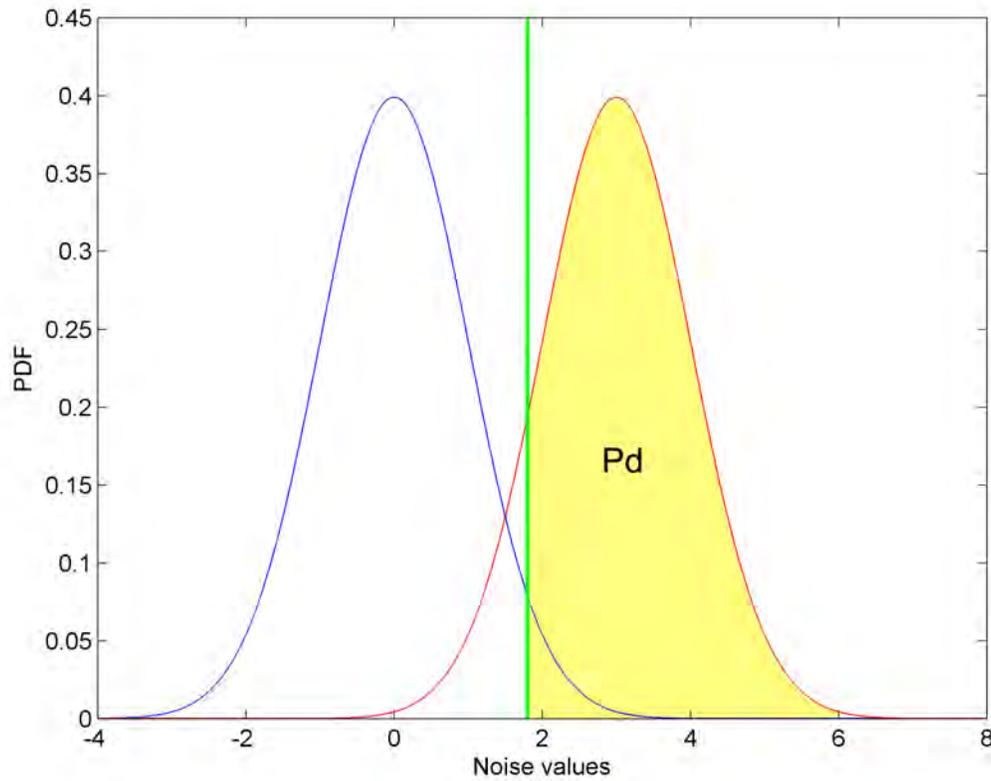
Figure 3-9: Illustration of the probability of detection under Gaussian noise
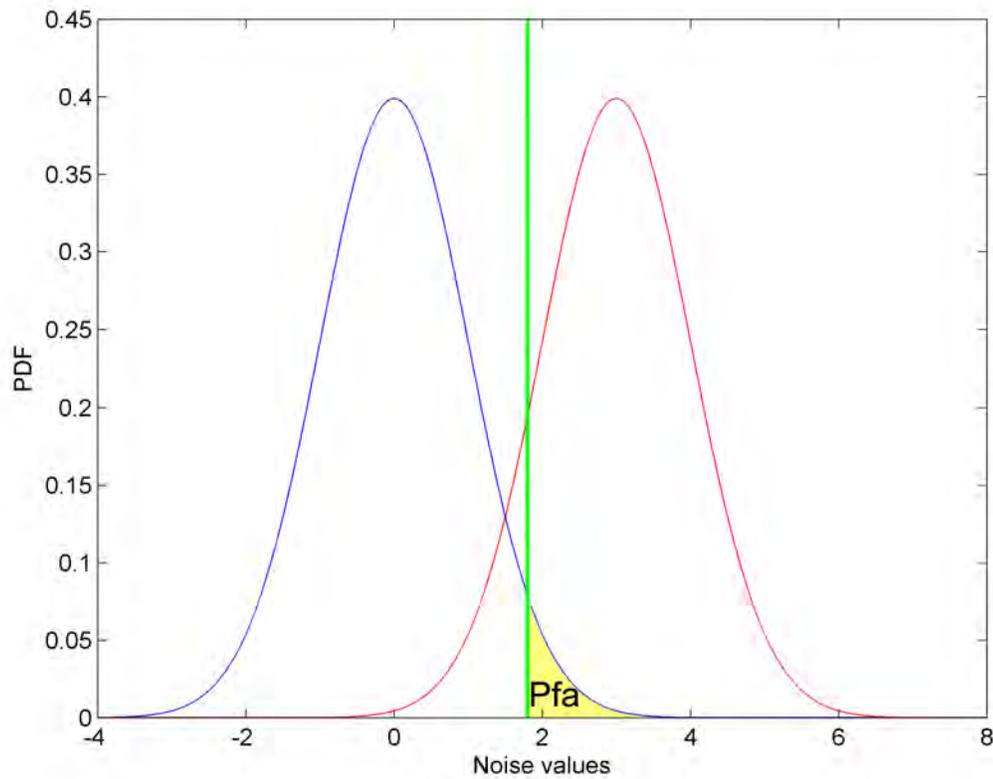
Figure 3-10: Illustration of the probability of false alarm under Gaussian noise

3.4.1 Overall performance

First the overall performance of the proposed acquisition schemes are investigated using the simulation parameters described in Table 3-3.

Table 3-3: Parameters used to assess the post-correlation methods performance

$C/N_{0\,L1}$	30 dB-Hz
$C/N_{0\,L2}$	28.5 dB-Hz
Noise Variance on L2	Twice the Noise Variance on L1
T_D	1 ms
Code phase step	0.25 chip
ΔF_1	Uniform on [-333.33 ; 333.33] Hz
ΔF_2	ΔF_1 x f_2 / f_1
$\theta_1\,\theta_2$	Uniformly distributed on [0 2π]
Data bit	{-1 ; 1}
Number of trials	100,000

As mentioned earlier, the signal power of L1 C/A is 1.5 dB above that of L2C. Moreover, the L2 CL code is usually zero-padded during the acquisition process. This last point results in the coherent integration on L2 to behave as if it was done over half the incoming samples. The noise variance on L2 is then twice as large as the noise variance on L1. Therefore, one has to be careful when trying to combine L1 C/A and L2 CM signals. Indeed as more signal power is present on L1 C/A than L2 CM, the latter should have less weight than the former. Assuming a weight of 1 on L1 C/A, a rule of thumb leading to the theoretical L2 CM weight to apply is directly related to the relative power $R_{C/N0}$ of the two signals as follows:

$$W_e = \sqrt{10^{-R_{C/N_0}/10}} \approx 0.59$$

As the two noise variances must be considered equal when using the above formula, the value of $R_{C/N0}$ is of 4.5 dB.

The effect of applying a different weight W to the output of the L2 correlators is illustrated in Figure 3-11 for each method investigated. The probability of detection P_d is computed as a function of the probability of false alarm P_{fa} of 0.001. As a means of verification, the effect of weighting L2 when using a non-coherent acquisition on L1 only (NC_{L1}) is also provided. Obviously, NC_{L1} acquisition is not affected by W. Note that the mathematical expression of NC_{L1} is:

$$S_{NCL1} = \sum_{k=1}^{M} \left(I_{k,L1}^{2} + Q_{k,L1}^{2} \right).$$
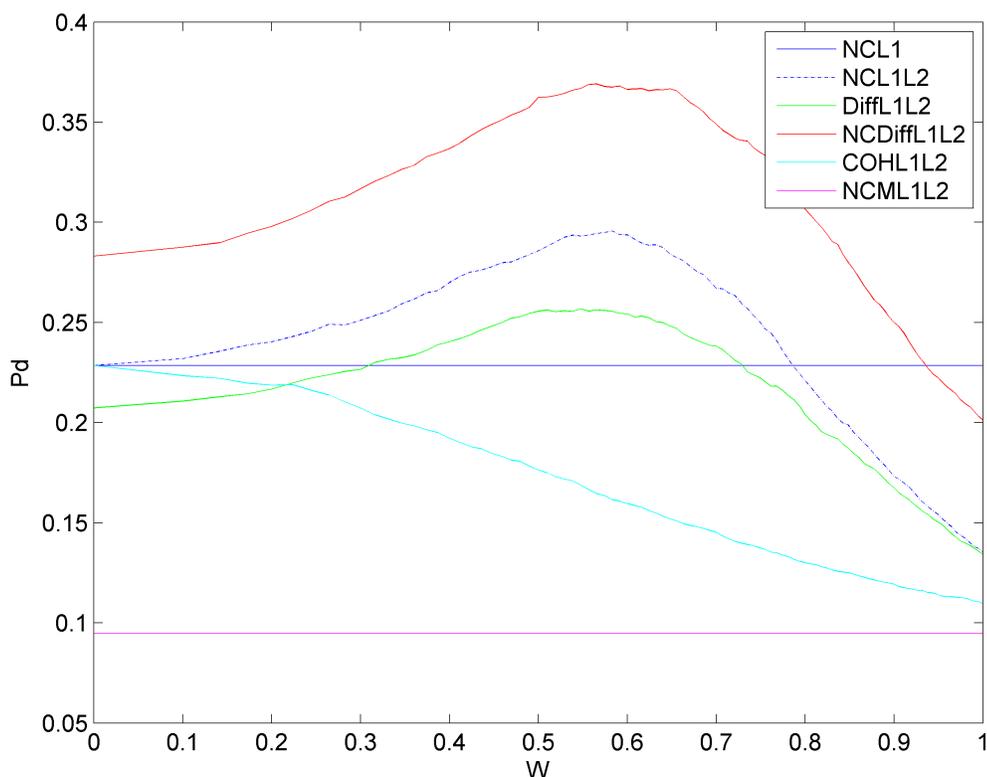
Figure 3-11: Probability of detection obtained by applying different weights to the L2 post-correlation outputs for P_{fa}=1e-3

As is clearly shown in Figure 3-11, the theoretical weight of 0.59 does not exactly correspond to the optimal one of 0.55 found numerically. Indeed, the probability of detection observed using a weight of 0.55 is above all the ones obtained with a different weight. This can be easily explained by the fact that the theoretical weight found did not take into account the ionospheric delay which behaves in this case like an additional signal attenuation on L2 and as such calls for a smaller weight than the synchronized L1 and L2 signals case. Note that the optimal weight is therefore dependent on the ionospheric activity but will be kept at 0.55 in the following, assuming the end user has no external information available.

Figure 3-11 also shows that the NC_{L1} acquisition does not depend on the weight applied on L2 as it was expected. The NCM_{L1L2} acquisition does not depend either on W. Indeed, given the mathematical expression of this method,

$$S_{NCML1L2} = \sum_{k=1}^{M} \left(W \cdot I_{k,L1} \cdot I_{k,L2} \right)^2 + \left(W \cdot Q_{k,L1} \cdot Q_{k,L2} \right)^2 ,$$

it is clear that by applying W on L2, it also affects L1. As such, the effect of weighting L2 is cancelled. Note that the NC_{L1L2} and COH_{L1L2} methods have the same performance as the NC_{L1} acquisition if W is set to zero. This was expected as both the COH_{L1L2} and NC_{L1L2} mathematical expressions are reduced to the NC_{L1} mathematical expressions if W is equal zero. Finally, COH_{L1L2} shows lower performance than NC_{L1} if W is set above zero. This phenomenon is explained by the fact that the phase offset between L1 and L2 is unknown. The coherent summation of L1 C/A and L2 CM can then be destructive if the phase offset is equal to π, and details on this point are provided later in this section.

Once the optimal weight of 0.55 has been determined, the overall performances of all the proposed methods are assessed using the parameters presented in Table 3-3. At this point, results are presented through the Receiver Operating Curve (ROC), defined earlier. Note that the ROC curve obtained is the equivalent of the one a receiver would have if it had no access to any external information.

Figure 3-12 shows the results obtained for each acquisition method. It clearly shows the advantage of combining L1 and L2 signal using the NC_{L1L2}, the $NCDiff_{L1L2}$ or the $Diff_{L1L2}$ methods. Note that whereas the $Diff_{L1L2}$ method seems to show worse

performance than the NC_{L1} method, it actually offers better probabilities of detection for small probabilities of false alarm which represents an important area of interest. Indeed, all of these methods outperform the probability of detection obtained using a non-coherent acquisition on L1 only. However, the COH_{L1L2} and NCM_{L1L2} methods have an overall probability of detection worse than the NC_{L1} method.
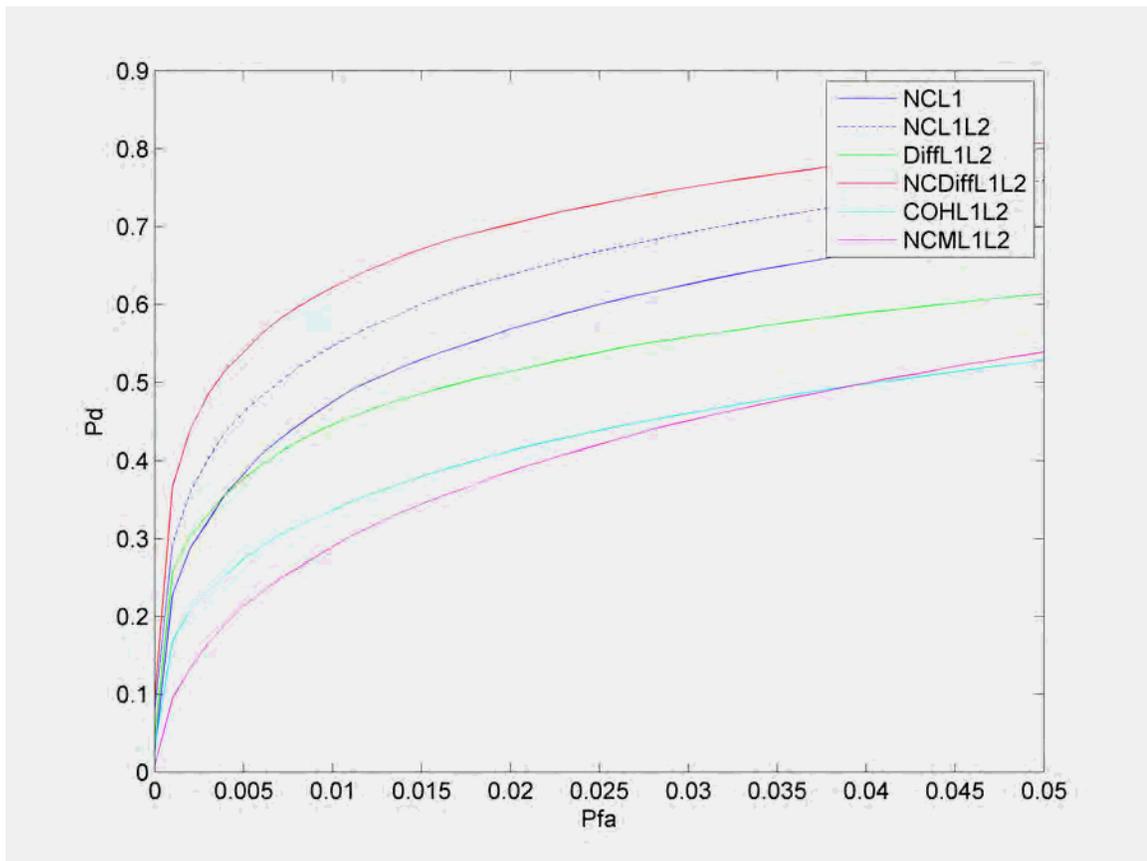
Figure 3-12: Receiver Operating Curve (ROC) for the different methods proposed.

In the case of the COH_{L1L2} method, the degradation observed is explained by the fact that no information on the signal phase or the data bit boundaries was available to the receiver. As such, if both signals had the same initial phase but the data bits transmitted on L1 were of the opposite sign to those transmitted on L2, adding the two signals

coherently would destroy the signal component. Similarly, if both signals have the same data bit sign but are out of phase by π, the coherent summation will result in a degradation of the total signal power. Finally, even if both signals have the same data bit and initial phase error, the different residual Doppler frequency will result in a phase shift between the two signals over time, which itself will result in a signal degradation during the coherent summation of the L1 and L2 correlator outputs. Figure 3-13 illustrates the degradation that will be observed for each non-coherent summation M as a function of the residual Doppler frequency error. Note that the relative initial phase difference between L1 and L2 signals was set to zero.
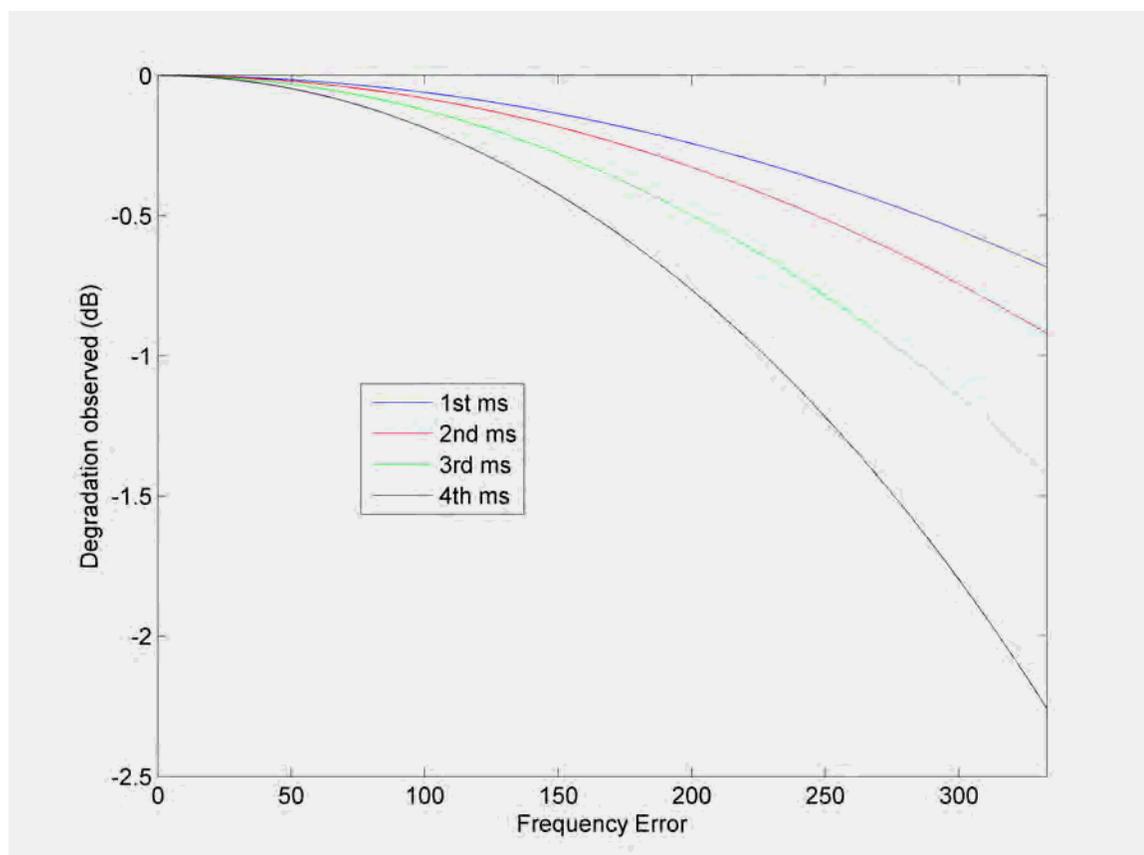
Figure 3-13: Degradation observed on the coherent summation of L1 and L2 post-correlation outputs for each millisecond as a function of L1 Doppler residual

The NCM$_{L1L2}$ method is also dependent on the frequency error through the multiplication of the two sinc functions. However, the greatest bottleneck of this method does not come from any remaining errors on the signals. Indeed, due to the multiplication, weighting the L2 post-correlation output is useless therefore it cannot take advantage of the fact that the L2 signal has a signal power 1.5 dB lower than L1 C/A and twice its noise variance at the correlator output.

3.4.2 Effect of the residual Doppler frequency error

In order to confirm the above results and explanations, another series of simulations was performed using the parameters listed in Table 3-4. In this case, assessing the effect of the residual Doppler frequency on the acquisition schemes was attempted. In order to do so, all of the data bit transitions and any initial phase errors were manually removed.

Table 3-4: Simulation parameters used to assess the effect of the frequency error on the acquisition schemes

$C/N_{0\,L1}$	30 dB-Hz
$C/N_{0\,L2}$	28.5 dB-Hz
Noise Variance onL2	Twice the Noise Variance on L1
T_D	1 ms
Code phase step	0.25 chip
ΔF_1	From -333.33 to 333.33 Hz
ΔF_2	$\Delta F_1 \times f_2 / f_1$
θ_1	0
θ_2	0
Data bits	1
Pfa	0.001
Number of trials	100,000

Figure 3-14 illustrates the results obtained as a function of the residual Doppler frequency error on L1. Note that, as mentioned earlier, the Doppler errors on L2 are related to the Doppler errors on L1 by the ratio f_2 / f_1. It is observed that the two methods that are the most affected by a residual Doppler error are the $Diff_{L1L2}$ and the $NCDiff_{L1L2}$. This last point can be surprising as both the non-coherent method and differential method taken separately aim to get rid of the residual dynamics. As such, they are only dependent on the Doppler error term through the sinc function. However, a simple rearrangement of the $NCDiff_{L1L2}$ equation can easily explain this behaviour, namely

$$S_{NCDiffL1L2} = \left[\begin{array}{c} \sum_{k=1}^{M} \left(I_{k,L1}{}^2 + Q_{k,L1}{}^2 \right) \\ + \sum_{k=1}^{M-1} \left(I_{k,L1} \cdot I_{k+1,L1} + Q_{k,L1} \cdot Q_{k+1,L1} \right) \end{array} \right] + W^2 \cdot \left[\begin{array}{c} \sum_{k=1}^{M} \left(I_{k,L2}{}^2 + Q_{k,L2}{}^2 \right) \\ + \sum_{k=1}^{M-1} \left(I_{k,L2} \cdot I_{k+1,L2} + Q_{k,L2} \cdot Q_{k+1,L2} \right) \end{array} \right]$$

$$= \left\{ \begin{array}{c} \dfrac{I_{1,L1}{}^2 + Q_{1,L1}{}^2}{2} \\ + \sum_{k=1}^{M-1} \left[\dfrac{\left(I_{k,L1} + I_{k+1,L1} \right)^2}{2} + \dfrac{\left(Q_{k,L1} + Q_{k+1,L1} \right)^2}{2} \right] \\ + \dfrac{I_{M,L1}{}^2 + Q_{M,L1}{}^2}{2} \end{array} \right\}$$

$$+ \left\{ \begin{array}{c} \dfrac{W^2 \cdot I_{1,L1}{}^2 + W^2 \cdot Q_{1,L1}{}^2}{2} \\ + \sum_{k=1}^{M-1} \left[\dfrac{W^2 \cdot \left(I_{k,L1} + I_{k+1,L1} \right)^2}{2} + \dfrac{W^2 \cdot \left(Q_{k,L1} + Q_{k+1,L1} \right)^2}{2} \right] \\ + \dfrac{W^2 \cdot I_{M,L1}{}^2 + W^2 \cdot Q_{M,L1}{}^2}{2} \end{array} \right\}$$

From the above equation, it is clearly evident that the NCDiff$_{L1L2}$ implies a coherent summation of two successive post-correlation outputs on the same frequency. As such, the coherent integration time for this summation is 2 ms and so the resulting Doppler bin size must be divided by two compared to the one millisecond case to avoid large signal degradation. The maximum Doppler residual error should then be reduced to about 165 Hz. Note that, if the maximum Doppler error on L1 is 165 Hz then the maximum Doppler error on L2 is only 128 Hz. Similarly, a maximum Doppler error of 165 Hz on L2 corresponds to a maximum Doppler error on L1 of 211 Hz. With 165 Hz and 211 Hz Doppler errors on L2 and L1 respectively, both L1 and L2 coherent summations show a strong degradation resulting from the combined acquisition proposed. Figure 3-14 clearly illustrates this effect as the NCDiff$_{L1L2}$ method begins to experience the strongest

degradation in the probability of detection once the residual Doppler error on L1 is about

215 Hz and performs worse than the NC_{L1} once the residual Doppler error of L1 is about

285 Hz.
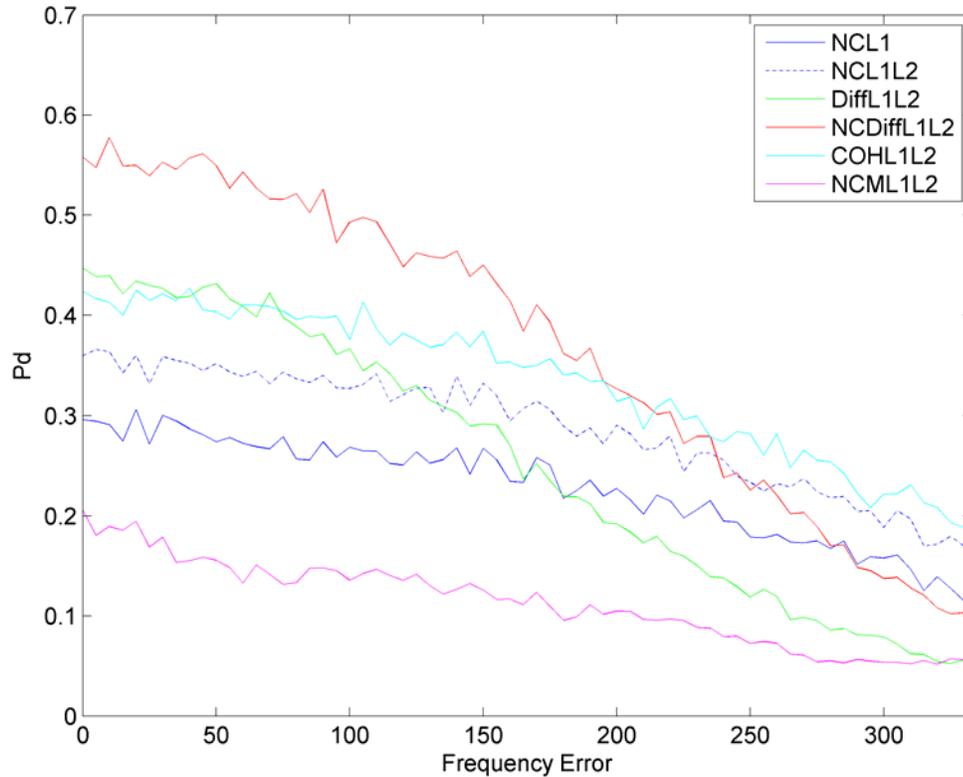
Figure 3-14: Effect of residual Doppler errors on the different acquisition methods

A simple mathematical derivation can easily explain the behaviour of the $Diff_{L1L2}$

method. Recalling, that

$$I(k) = \frac{A}{\sqrt{2}} \cdot d(k) \cdot R(dt) \cdot \frac{\sin(\pi \Delta FT)}{\pi \Delta FT} \cos\left(\pi \Delta FT(2k-1) + \varphi\right)$$

$$Q(k) = \frac{A}{\sqrt{2}} \cdot d(k) \cdot R(dt) \cdot \frac{\sin(\pi \Delta FT)}{\pi \Delta FT} \sin\left(\pi \Delta FT(2k-1) + \varphi\right)$$

and that

$$S_{DiffL1L2} = \sum_{k=1}^{M/2} \left(I_{2k,L1} \cdot I_{2k-1,L1} + Q_{2k,L1} \cdot Q_{2k-1,L1} \right) + W^2 \cdot \sum_{k=1}^{M/2} \left(I_{2k,L2} \cdot I_{2k-1,L2} + Q_{2k,L2} \cdot Q_{2k-1,L2} \right),$$

it can be shown that for a specific value of k, the summation $I_{2k,L1} \cdot I_{2k-1,L1} + Q_{2k,L1} \cdot Q_{2k-1,L1}$

becomes

$$I_{2k,L1} \cdot I_{2k-1,L1} + Q_{2k,L1} \cdot Q_{2k-1,L1} = \left(\frac{A}{\sqrt{2}} \cdot d(k) \cdot R(dt) \cdot \frac{\sin(\pi\Delta FT)}{\pi\Delta FT} \right)^2 \cdot X$$

with

$$X = \cos\left(\pi\Delta FT(2 \cdot (2k) - 1) + \varphi \right) \cdot \cos\left(\pi\Delta FT(2 \cdot (2k-1) - 1) + \varphi \right)$$
$$+ \sin\left(\pi\Delta FT(2 \cdot (2k) - 1) + \varphi \right) \cdot \sin\left(\pi\Delta FT(2 \cdot (2k-1) - 1) + \varphi \right).$$

Therefore,

$$X = \cos\left(\pi\Delta FT(2 \cdot (2k) - 1) + \varphi - (\pi\Delta FT(2 \cdot (2k-1) - 1) + \varphi) \right)$$
$$= \cos\left(2\pi\Delta FT \right)$$

and $Diff_{L1L2}$ is dependent on the frequency error.

3.4.3 Effect of the initial phase difference between L1 and L2

In order to verify that the initial phase difference between L1 and L2 affects only the COH$_{L1L2}$ method, a final simulation was performed using the parameters listed in Table 3-5. Note that in order to analyze the effect of the relative phase offset only, residual Doppler errors and data bits were removed from the simulation.

Table 3-5: Simulation parameters used to assess the effect of the initial relative phase error between L1 and L2 on the acquisition schemes

$C/N_{0\ L1}$	30 dB-Hz
$C/N_{0\ L2}$	28.5 dB-Hz
Noise Variance on L2	Twice the Noise Variance on L1
T_D	1 ms
Code phase step	0.25 chip
ΔF_1	0
ΔF_2	$\Delta F_1 \times f_2 / f_1$
θ_1	0
θ_2	From 0 to 2π
Data bits	1
Pfa	0.001
Number of trials	100,000

Figure 3-15: Effect of the relative phase offset between L1 and L2 signals on the different acquisition methods

Results obtained are shown in Figure 3-15. As was expected and explained previously, the COH_{L1L2} method is strongly affected by the relative phase offset as it implies the coherent summation of the post-correlation outputs of the L1 and L2 signals. A relative phase of π implies that the COH_{L1L2} method becomes destructive. Indeed, the summation involved becomes a subtraction. The fact that the probability of detection for a relative phase of π is not null is due to the weight *W* of 0.55 applied on L2 and the fact that L1 has more signal power than L2.

On the other hand, none of the other methods involved such a summation and, as such, they are not similarly affected by the relative phase offset between the signals.

Obviously, the NC_{L1L2}, $Diff_{L1L2}$ and $NCDiff_{L1L2}$ methods involving either a non-coherent or differential summation or both are not affected by the relative phase offset.

Somewhat surprisingly, the NCM_{L1L2} method is affected by the relative phase offset. In order to explain this phenomenon, a short derivation is performed. The mathematical expression of NCM_{L1L2} is

$$S_{NCML1L2} = \sum_{k=1}^{M} \left(W \cdot I_{k,L1} \cdot I_{k,L2} \right)^2 + \left(W \cdot Q_{k,L1} \cdot Q_{k,L2} \right)^2 .$$

As it has been shown that weighting L2 has no effect on the probabilities, the term W is dropped from the equation for simplicity as

$$S_{NCML1L2} = \sum_{k=1}^{M} \left(I_{k,L1} \cdot I_{k,L2} \right)^2 + \left(Q_{k,L1} \cdot Q_{k,L2} \right)^2 .$$

As the residual Doppler frequency error was kept null during this simulation, the correlator outputs are reduced to:

$$I_{k,L1} = \frac{A_1}{\sqrt{2}} \cdot R(dt) \cdot \cos(0) \text{ and } Q_{k,L1} = \frac{A_1}{\sqrt{2}} \cdot R(dt) \cdot \sin(0) \text{ on L1}$$

and

$$I_{k,L2} = \frac{A_2}{\sqrt{2}} \cdot R(dt_2) \cdot \cos(\varphi) \text{ and } Q_{k,L2} = \frac{A_2}{\sqrt{2}} \cdot R(dt_2) \cdot \sin(\varphi) \text{ on L2}.$$

As such, the NCM_{L1L2} mathematical expression is reduced to

$$S_{NCML1L2} = \sum_{k=1}^{M} \left(I_{k,L1} \cdot I_{k,L2} \right)^2 .$$

Using the expressions above, it is readily shown that

$$I_{k,L1} \cdot I_{k,L2} = \frac{A_1}{\sqrt{2}} \cdot R(dt) \cdot \cos(0) \cdot \frac{A_2}{\sqrt{2}} \cdot R(dt_2) \cdot \cos(\varphi)$$

and

$$S_{NCML1L2} = \sum_{k=1}^{M} \left(I_{k,L1} \cdot I_{k,L2} \right)^2 = M \cdot \left(\frac{A_1 \cdot A_2}{2} \cdot R(dt) \cdot R(dt_2) \cdot \cos(\varphi) \right)^2 \text{ is maximum for}$$

$$\varphi = \begin{cases} 0 \\ \pi \\ 2\pi \end{cases} \text{ and minimal for } \varphi = \begin{cases} \pi/2 \\ 3\pi/2 \end{cases}.$$

As shown by the simulations results obtained above, three L1/L2 combining methods (namely NC_{L1L2}, $Diff_{L1L2}$ and $NCDiff_{L1L2}$) prove to outperform the classic non-coherent acquisition performed on L1 only. The following chapter investigates each of these methods in detail in terms of their theoretical probability density functions and ROC curves. The theoretical results are compared to the probability density functions and ROC curves obtained using simulated and real data.

Chapter Four: Theoretical analysis of the NC_{L1L2}, $Diff_{L1L2}$, and $NCDiff_{L1L2}$ combining methods

This chapter aims to analyze in detail the three best combining methods presented in Chapter 3. As such, a theoretical analysis is conducted for the NC_{L1L2}, $Diff_{L1L2}$ and $NCDiff_{L1L2}$ methods. First, results are presented with 4 ms of incoming data and 1 ms of coherent integration. Then, conclusions are presented for 4 ms of incoming data but 2 ms of coherent integration time. This last point shows the effect of the coherent integration time used on the methods investigated.

4.1 Theoretical performance

The theoretical probability density functions under the hypotheses

- H_0 : signal is not present
- H_1: signal is present

are derived herein. These are then used in Section 4.4 to derive the probabilities of false alarm and detection as well as the Receiver Operating Curves used to evaluate the performance of each method.

Based on Equation 2-12, the correlator outputs for L1 C/A can be expressed as:

$$I_{k,L1} = A_1(k) \cdot \cos\left(\pi \Delta F_1 T (2k-1) + \varphi_1\right) + w_{k,L1}^I$$

$$Q_{k,L1} = A_1(k) \cdot \sin\left(\pi \Delta F_1 T (2k-1) + \varphi_1\right) + w_{k,L1}^Q$$

with

$$A_1(k) = \frac{A_1}{\sqrt{2}} d_1(k) \cdot R(dt_1) \cdot \frac{\sin(\pi \Delta F_1 T)}{\pi \Delta F_1 T}$$

and

$$w^I_{k,L1} \quad w^Q_{k,L1} \quad N(0, \sigma^2).$$

Similarly, the L2C correlator outputs can be expressed as:

$$I_{k,L2} = A_2(k) \cdot \cos\left(\pi \Delta F_2 T (2k - 1) + \varphi_2\right) + w^I_{k,L2}$$

$$Q_{k,L2} = A_2(k) \cdot \sin\left(\pi \Delta F_2 T (2k - 1) + \varphi_2\right) + w^Q_{k,L2}$$

with

$$A_2(k) = \frac{A_2}{\sqrt{2}} d_2(k) \cdot R(dt_2) \cdot \frac{\sin(\pi \Delta F_2 T)}{\pi \Delta F_2 T}$$

and

$$w^I_{k,L2} \quad w^Q_{k,L2} \quad N(0, 2\sigma^2).$$ Note that all the noise components are uncorrelated.

4.1.1 NC$_{L1L2}$ method

Equation 3-1 can be reformulated as:

$$S_{NCL1L2} = X + Y$$

with

$$X = \sum_{k=1}^{M} \left(I_{k,L1}^{2} + Q_{k,L1}^{2} \right)$$

and

$$Y = \sum_{k=1}^{M} \left((W \cdot I_{k,L2})^{2} + (W \cdot Q_{k,L2})^{2} \right).$$

Determination of the PDF under H$_0$

The noise corrupting the output of the correlators being independent, it is evident that both X and Y are chi-square distributed random variables with *2M* degrees of freedom. As such, the PDF of X under H$_0$ is

$$p(x) = \frac{1}{2\sigma^{2}\Gamma(M)} \left(\frac{x}{2\sigma^{2}} \right)^{M-1} \exp\left(\frac{-x}{2\sigma^{2}} \right) \tag{4-1}$$

where Γ is the Gamma function. Similarly, the PDF of Y under H$_0$ is

$$p(y) = \frac{1}{2\sigma_{2}^{2}\Gamma(M)} \left(\frac{y}{2\sigma_{2}^{2}} \right)^{M-1} \exp\left(\frac{-y}{2\sigma_{2}^{2}} \right) \tag{4-2}$$

with $\sigma_{2}^{2} = 2 \cdot W^{2} \cdot \sigma^{2}$.

Therefore the PDF of the NC$_{L1L2}$ method under H$_0$ can be expressed as a summation of independent chi-square random variables (Simon 2006) as:

$$p(s) = \frac{1}{2\sigma^2}\exp\left(\frac{-s}{2\sigma^2}\right)\frac{1}{(M-1)!}\left(\frac{\sigma^2}{\sigma^2-\sigma_2^2}\right)^M \cdot \sum_{i=0}^{M-1}\frac{(2(M-1)-i)!}{i!(M-1-i)!}\left(\frac{\sigma_2^2}{\sigma_2^2-\sigma^2}\right)^{M-1-i}\left(\frac{s}{2\sigma^2}\right)^i$$

$$+\frac{1}{2\sigma_2^2}\exp\left(\frac{-s}{2\sigma_2^2}\right)\frac{1}{(M-1)!}\left(\frac{\sigma_2^2}{\sigma_2^2-\sigma^2}\right)^M \cdot \sum_{i=0}^{M-1}\frac{(2(M-1)-i)!}{i!(M-1-i)!}\left(\frac{\sigma^2}{\sigma^2-\sigma_2^2}\right)^{M-1-i}\left(\frac{s}{2\sigma_2^2}\right)^i$$

4-3

and its characteristic function is:

$$\Psi_S(\omega) = \left(\frac{1}{\left(1-2j\omega\sigma^2\right)\cdot\left(1-2j\omega\sigma_2^2\right)}\right)^M.$$

4-4

Determination of the PDF under H$_1$

The random variables X and Y become non-central chi-square distributed with *2M* degrees of freedom and non-central parameters λ_1 and λ_2 respectively. As such, the PDF of X is expressed as

$$p(x) = \frac{1}{2\sigma^2}\left(\frac{x}{\lambda_1}\right)^{\frac{M-1}{2}}\exp\left(-\frac{x+\lambda_1}{2\sigma^2}\right)I_{M-1}\left(\sqrt{\frac{\lambda_1 x}{\sigma^4}}\right)$$

4-5

and the PDF of Y as

$$p(y) = \frac{1}{2\sigma_2^2}\left(\frac{y}{\lambda_2}\right)^{\frac{M-1}{2}}\exp\left(-\frac{y+\lambda_2}{2\sigma_2^2}\right)I_{M-1}\left(\sqrt{\frac{\lambda_2 y}{\sigma_2^4}}\right)$$

4-6

with

$$\lambda_1 = \sum_{k=1}^{M}A_1(k)^2 \approx \frac{M\cdot A_1^2}{2} \quad\text{and}\quad \lambda_2 = \sum_{k=1}^{M}A_2(k)^2 \approx \frac{M\cdot A_2^2}{2}\quad\text{assuming }\Delta F,\ dt_1\ \text{and}\ dt_2\ \text{are}$$

small.

From this, one can deduce that the PDF of the NC_{L1L2} under H_1 is a summation of two independent non-central Chi-Square variables as

$$p(s) = \frac{1}{2\sigma^2}\left(\frac{\sigma}{\sigma_2}\right)^{2M}\left(\frac{s}{\lambda_1}\right)^{M-\frac{1}{2}}\exp\left(\frac{-s}{2\sigma^2}\right)\cdot\exp\left(-\frac{1}{2}\left(\frac{\lambda_1}{\sigma^2}+\frac{\lambda_2}{\sigma_2^2}\right)\right)$$

$$\cdot\sum_{i=0}^{\infty}\sum_{l=0}^{\infty}\left[\begin{array}{c}\dfrac{\Gamma(M+i+l)}{i!l!\Gamma(M+l)}\left(\dfrac{\sqrt{s}\lambda_2\sigma^2}{2\sqrt{\lambda_1}\sigma_2^4}\right)^l \\ \cdot\left(\dfrac{\sqrt{s}\left(\sigma_2^2-\sigma^2\right)}{\sqrt{\lambda_1}\sigma_2^2}\right)^i I_{2M+i+l-1}\left(\dfrac{\sqrt{s}\lambda_1}{\sigma_1^2}\right)\end{array}\right]$$

4-7

and its characteristic function is:

$$\Psi_s(\omega) = \left(\frac{1}{\left(1-2j\omega\sigma^2\right)\left(1-2j\omega\sigma_2^2\right)}\right)^M\cdot\exp\left(\frac{j\omega\lambda_1}{1-2j\omega\sigma^2}\right)\cdot\exp\left(\frac{j\omega\lambda_2}{1-2j\omega\sigma_2^2}\right).$$

4-8

4.1.2 Diff$_{L1L2}$ method

Once again, the Diff$_{L1L2}$ mathematical expression shown in Equation 3-2, is broken down into two sub-terms according to the two summations it contains:

$$S_{DiffL1L2} = X + Y$$

4-9

$$X = \sum_{k=1}^{M/2}\left(I_{2k,L1}\cdot I_{2k-1,L1}+Q_{2k,L1}\cdot Q_{2k-1,L1}\right)$$

4-10

$$Y = W^2\cdot\sum_{k=1}^{M/2}\left(I_{2k,L2}\cdot I_{2k-1,L2}+Q_{2k,L2}\cdot Q_{2k-1,L2}\right).$$

4-11

The following derivation, regarding the one frequency only differential acquisition, namely for the X or Y random variable only, is based on Avila-Rodriguez et al (2005). Note that in Equation 4-10 and 4-11, *M* is even therefore *M/2* is an integer.

The noise corrupting the output of the correlators is independent over time. The real part of the L1 correlator output at the kth millisecond is independent to the real part of the L1 correlator outputs at the (k+1)[th] millisecond.

Determination of the PDF under H$_0$

The product $I_{2k,L1} \cdot I_{2k+1,L1}$ is a product of independent and identically distributed zero-mean Gaussian random variables. The PDF of $I_{2k,L1} \cdot I_{2k+1,L1}$ and $Q_{2k,L1} \cdot Q_{2k+1,L1}$, according to Simon (2006), is

$$f_{I_{2k,L1} \cdot I_{2k+1,L1}}(z) = f_{Q_{2k,L1} \cdot Q_{2k+1,L1}}(z) = \frac{K_0 \left(\frac{\|z\|}{\sigma^2} \right)}{\pi \sigma^2} \qquad \textbf{4-12}$$

where *K* represents the modified Bessel function of the second kind.

Defining

$$\gamma_k = I_{2k,L1} \cdot I_{2k+1,L1} + Q_{2k,L1} \cdot Q_{2k+1,L1},$$

it is clear that γ is a summation of products of independent and identically distributed Gaussian variables. As such, the PDF of γ can be expressed as

$$f_{\gamma_k}(z) = \frac{1}{2\sigma^2} \exp\left(\frac{-|z|}{\sigma^2}\right).$$

4-13

Additionally, X can now be expressed as:

$$X = \sum_{k=1}^{M/2} \gamma_k.$$

4-14

At this point, one makes use of the following propriety of the PDF when confronted to a sum of independent random variables: "Given X_1 and X_2, two independent random variables of PDF f_{X1} and f_{X2}, the PDF of the sum $X1+X2$ is the result of the convolution of the f_{X1} with f_{X2}."

Moreover, a convolution in the time domain is equivalent to a multiplication in the frequency domain. As such, it is now possible to express the PDF of X through the Fourier transform of the PDF of γ_k :

$$f_X(x) = F^{-1}\left[\prod_{i=1}^{M/2} F\left(f_{\gamma_k}(x)\right)\right].$$

4-15

From the classic Fourier formula:

$$F\left(e^{-\alpha|t|}\right) = \frac{2\sigma}{\alpha^2 + \omega^2},$$

the Fourier transform of the PDF of γ_k is derived as

$$F\left(f_{\gamma_k}(z)\right) = F\left(\frac{1}{2\sigma^2} \exp\left(\frac{-|z|}{\sigma^2}\right)\right) = \frac{1}{1+\sigma^4\omega^2}.$$

4-16

Therefore, the PDF of X can be expressed as

$$f_X(x) = F^{-1}\left[\left(\frac{1}{1+\sigma^4\omega^2}\right)^{\frac{M}{2}}\right].$$

4-17

Similarly, it is shown that the PDF of Y is

$$f_Y(y) = F^{-1}\left[\left(\frac{1}{1+\sigma_2^4\omega^2}\right)^{\frac{M}{2}}\right].$$

4-18

Therefore, the PDF of $S_{DiffL1L2} = X + Y$ is easily shown to be

$$f_{S_{DiffL1L2}}(s) = F^{-1}\left[\left(\frac{1}{1+\sigma^4\omega^2}\right)^{\frac{M}{2}}\left(\frac{1}{1+\sigma_2^4\omega^2}\right)^{\frac{M}{2}}\right].$$

4-19

From that point forward, one needs to show that it is possible to perform a partial fraction expansion of Equation 4-19:

$$\left(\frac{1}{1+\sigma^4\omega^2}\right)^K\left(\frac{1}{1+\sigma_2^4\omega^2}\right)^K = \sum_{i=1}^{K}\left[\frac{a_{K,i}}{\left(1+\sigma^4\omega^2\right)^i} + \frac{b_{K,i}}{\left(1+\sigma_2^4\omega^2\right)^i}\right]$$

with $K = \dfrac{M}{2}$. The above is performed using a development similar to Borio (2008) and it

is shown that the coefficient $a_{K,i}$ and $b_{K,i}$ can be determined using the following

recurrence relationship (where δ represents the Dirac function):

$$a_{K,K-i} = \theta_1 a_{K-1,K-i-1} + \theta_2 a_{K,K-i+1} + B_{K-1,i}$$ **4-20**

$$b_{K,K-i} = \theta_2 b_{K-1,K-i-1} + \theta_1 b_{K,K-i+1} + A_{K-1,i}$$ **4-21**

$$A_{K-1,i} = \left[\sum_{n=1}^{K-1} \theta_2^{n+1} a_{K-1,n} \right] \delta(i - K + 1)$$ **4-22**

$$B_{K-1,i} = \left[\sum_{n=1}^{K-1} \theta_1^{n+1} b_{K-1,n} \right] \delta(i - K + 1)$$ **4-23**

$$\theta_1 = a_{1,1} = \frac{\sigma^2}{\sigma^2 - \sigma_2^2}$$ **4-24**

$$\theta_2 = b_{1,1} = \frac{\sigma^2}{\sigma_2^2 - \sigma^2}.$$ **4-25**

Equation 4-19 can then be rewritten as follows:

$$f_{S_{DiffL1L2}}(s) = \sum_{i=1}^{K} a_{K,i} \cdot F^{-1}\left[\left(\frac{1}{1 + \sigma^4 \omega^2} \right)^i \right] + \sum_{i=1}^{K} b_{K,i} \cdot F^{-1}\left[\left(\frac{1}{1 + \sigma_2^4 \omega^2} \right)^i \right].$$ **4-26**

At this point, it is possible to compute the inverse Fourier transform required in Equation 4-26 using the following derivation:

$$F^{-1}\left[\left(\frac{1}{1 + \sigma^4 \omega^2} \right)^i \right] = \frac{1}{2\pi} \int_{-\infty}^{+\infty} \frac{e^{j\omega t}}{\left(1 + \sigma^4 \omega^2\right)^i} d\omega$$

$$= \frac{1}{2\pi} \left[\int_{-\infty}^{0} \frac{e^{j\omega t}}{\left(1 + \sigma^4 \omega^2\right)^i} d\omega + \int_{0}^{+\infty} \frac{e^{j\omega t}}{\left(1 + \sigma^4 \omega^2\right)^i} d\omega \right]$$

$$= \frac{1}{2\pi} \left[\int_0^{+\infty} \frac{e^{-j\omega t}}{\left(1+\sigma^4\omega^2\right)^i} d\omega + \int_0^{+\infty} \frac{e^{j\omega t}}{\left(1+\sigma^4\omega^2\right)^i} d\omega \right]$$

$$= \frac{1}{2\pi} \int_0^{+\infty} \frac{2\cos(\omega t)}{\left(1+\sigma^4\omega^2\right)^i} d\omega .$$ **4-27**

In order to compute the above integral, the following property of the modified Bessel function of the second kind is used (Abramowitz & Stegun 1964):

$$K_\nu(x \cdot z) = \frac{\Gamma\left(\nu+\frac{1}{2}\right)\cdot(2z)^\nu}{x^\nu \sqrt{\pi}} \cdot \int_0^{+\infty} \frac{\cos(x \cdot t) dt}{\left(t^2+z^2\right)^{\nu+\frac{1}{2}}} .$$ **4-28**

By rewriting Equation 4-27 as follows, it is finally possible to compute the inverse Fourier transform desired:

$$F^{-1}\left[\left(\frac{1}{1+\sigma^4\omega^2}\right)^i\right] = \frac{1}{2\pi} \int_0^{+\infty} \frac{2\cos(\omega t)}{\left(1+\sigma^4\omega^2\right)^i} d\omega$$

$$= \frac{1}{2\pi} \int_0^{+\infty} \frac{2\cos(\omega t)}{\sigma^{4i}\left(\frac{1}{\sigma^4}+\omega^2\right)^i} d\omega$$

$$= \frac{\sigma^{-4i}\sqrt{\pi}\,\|t\|^\nu\, K_\nu\left(\frac{\|t\|}{\sigma^2}\right)}{\pi\cdot\Gamma\left(\nu+\frac{1}{2}\right)\cdot\left(\frac{2}{\sigma^2}\right)^\nu} \quad \text{with } i=\nu+\frac{1}{2} .$$

Therefore, the desired inverse Fourier transform, which also represents the PDF of X that is the differential summation performed on L1 only, can be expressed as:

$$F^{-1}\left[\left(\frac{1}{1+\sigma^4\omega^2}\right)^i\right] = \frac{\sigma^{-(2i+1)}2^{-i+\frac{1}{2}}\|t\|^{i-\frac{1}{2}}K_{\left(i-\frac{1}{2}\right)}\left(\frac{\|t\|}{\sigma^2}\right)}{\sqrt{\pi}\cdot\Gamma(i)}.$$

4-29

Similarly, the differential summation performed on L2 only is expressed as

$$F^{-1}\left[\left(\frac{1}{1+\sigma_2^4\omega^2}\right)^i\right] = \frac{\sigma_2^{-(2i+1)}2^{-i+\frac{1}{2}}\|t\|^{i-\frac{1}{2}}K_{\left(i-\frac{1}{2}\right)}\left(\frac{\|t\|}{\sigma_2^2}\right)}{\sqrt{\pi}\cdot\Gamma(i)}.$$

4-30

Finally, the complete PDF under H_0 for the $\text{Diff}_{\text{L1L2}}$ method is shown to be

$$f_S(s) = \sum_{i=1}^{K}\frac{2^{-i+\frac{1}{2}}\|s\|^{i-\frac{1}{2}}}{\sqrt{\pi}\cdot\Gamma(i)}\cdot\left[a_{K,i}\sigma^{-(2i+1)}K_{\left(i-\frac{1}{2}\right)}\left(\frac{\|t\|}{\sigma^2}\right)+b_{K,i}\sigma_2^{-(2i+1)}K_{\left(i-\frac{1}{2}\right)}\left(\frac{\|t\|}{\sigma_2^2}\right)\right].$$

4-31

Noticing that the characteristic function of X that is the differential acquisition on L1 is the characteristic function of a summation of the product of independent and identically distributed zero-mean Gaussian variables, one can express it as (Simon 2006)

$$\Psi_X(\omega) = \left(\frac{1}{1+\sigma^4\omega^2}\right)^{M/2}.$$

4-32

Similarly, the characteristic function of Y is shown to be

$$\Psi_X(\omega) = \left(\frac{1}{1+\sigma_2^4\omega^2}\right)^{M/2}.$$

4-33

Therefore, making use of the properties of the characteristic functions (Gelb 1974), the characteristic function of the Diff$_{L1L2}$ method under H$_0$ is

$$\Psi_s(\omega) = \left(\frac{1}{1+\sigma^4\omega^2} \cdot \frac{1}{1+\sigma_2{}^4\omega^2} \right)^{M/2}.$$

4-34

Determination of the PDF under H$_1$

Unfortunately, a closed form solution for the PDF of $S_{DiffL1L2}$ could not be determined. Its characteristic function was used instead in order to derive the probability of false alarm and detection of the Diff$_{L1L2}$ method.

However, given the complexity of the derivation, it is assumed that either the Doppler removal process is performed perfectly or that the Doppler residual is close from one coherent integration to the next, and that the data bit remains unchanged during the acquisition period. As such, the outputs of the L1 and L2 correlators are:

$$I_{k,L1} = \frac{\hat{A}_1}{\sqrt{2}} \cdot \cos(\varphi_1) + w_{k,L1}^I$$

$$Q_{k,L1} = \frac{\hat{A}_1}{\sqrt{2}} \cdot \sin(\varphi_1) + w_{k,L1}^Q$$

with

$$\hat{A}_1 = A_1 \cdot R(dt_1)$$

and

$$I_{k,L2} = \frac{\hat{A}_2}{\sqrt{2}} \cdot \cos(\varphi_2) + w^I_{k,L2}$$

$$Q_{k,L2} = \frac{\hat{A}_2}{\sqrt{2}} \cdot \sin(\varphi_2) + w^Q_{k,L2}$$

with

$$\hat{A}_2 = A_2 \cdot R(dt_2) \, .$$

Note that $\hat{A}_1$ and $\hat{A}_2$ are independent of k.

Equation 3-2 can be broken in four different terms such that $S_{DiffL1L2}$ is expressed as follows:

$$S_{DiffL1L2} = S^I_{L1} + S^Q_{L1} + S^I_{L2} + S^Q_{L2} \qquad\qquad \textbf{4-35}$$

$$S^I_{L1} = \sum_{k=1}^{M/2} \left(I_{2k,L1} \cdot I_{2k-1,L1} \right) \qquad\qquad \textbf{4-36}$$

$$S^Q_{L1} = \sum_{k=1}^{M/2} \left(Q_{2k,L1} \cdot Q_{2k-1,L1} \right) \qquad\qquad \textbf{4-37}$$

$$S^I_{L2} = \sum_{k=1}^{M/2} \left(W \cdot I_{2k,L2} \cdot W \cdot I_{2k-1,L2} \right) \qquad\qquad \textbf{4-38}$$

$$S^Q_{L2} = \sum_{k=1}^{M/2} \left(W \cdot Q_{2k,L2} \cdot W \cdot Q_{2k-1,L2} \right) . \qquad\qquad \textbf{4-39}$$

Each random variable $S^{I/Q}_{L1/2}$ expressed in Equations 4-36 to 4-39 is the summation of products of two Gaussian variables both non-zero-mean and with identical variance.

Therefore, the characteristic function of S_{L1}^I is shown to be (Simon 2006)

$$\Psi_{S_{L1}^I}(\omega) = \frac{1}{\left(1+\sigma^4\omega^2\right)^{M/4}} \cdot \exp\left[\frac{j\omega\hat{\lambda}_1\cos^2(\varphi_1) - \hat{\lambda}_1\cos^2(\varphi_1)\sigma^2\omega^2}{2\cdot\left(1+\sigma^4\omega^2\right)}\right] \qquad \textbf{4-40}$$

with

$$\hat{\lambda}_1 = \frac{M\cdot\hat{A}_1^{\ 2}}{2}$$

and

$$\hat{\lambda}_2 = \frac{M\cdot\hat{A}_2^{\ 2}}{2}.$$

Similarly, the characteristic function of S_{L1}^Q is

$$\Psi_{S_{L1}^Q}(\omega) = \frac{1}{\left(1+\sigma^4\omega^2\right)^{M/4}} \cdot \exp\left[\frac{j\omega\hat{\lambda}_1\sin^2(\varphi_1) - \hat{\lambda}_1\sin^2(\varphi_1)\sigma^2\omega^2}{2\cdot\left(1+\sigma^4\omega^2\right)}\right]. \qquad \textbf{4-41}$$

Making use of the properties of characteristic functions, one can write

$$\begin{aligned}\Psi_{S_{L1}^I+S_{L1}^Q}(\omega) &= \Psi_{S_{L1}^I}(\omega)\cdot\Psi_{S_{L1}^Q}(\omega) \\ &= \frac{1}{\left(1+\sigma^4\omega^2\right)^{\frac{M}{2}}}\cdot\exp\left[\frac{j\omega\hat{\lambda}_1 - \hat{\lambda}_1\sigma^2\omega^2}{2\cdot\left(1+\sigma^4\omega^2\right)}\right].\end{aligned} \qquad \textbf{4-42}$$

Regarding L2, a similar development allows the following derivation:

$$\Psi_{S_{L2}^I + S_{L2}^Q}(\omega) = \Psi_{S_{L2}^I}(\omega) \cdot \Psi_{S_{L2}^Q}(\omega)$$

$$= \frac{1}{\left(1 + \sigma_2^4 \omega^2\right)^{\frac{M}{2}}} \cdot \exp\left[\frac{j\omega\hat{\lambda}_2 - \hat{\lambda}_2 \sigma_2^2 \omega^2}{2 \cdot \left(1 + \sigma_2^4 \omega^2\right)}\right] \cdot \qquad \textbf{4-43}$$

From Equations 4-42 and 4-43, the characteristic function of $S_{DiffL1L2}$ can readily be expressed as

$$\Psi_{S_{DiffL1L2}}(\omega) = \Psi_{S_{L1}^I + S_{L1}^Q}(\omega) \cdot \Psi_{S_{L2}^I + S_{L2}^Q}(\omega)$$

$$= \left[\frac{1}{\left(1 + \sigma^4 \omega^2\right)\left(1 + \sigma_2^4 \omega^2\right)}\right]^{\frac{M}{2}} \cdot \exp\left[\frac{j\omega\hat{\lambda}_1 - \hat{\lambda}_1 \sigma^2 \omega^2}{2 \cdot \left(1 + \sigma^4 \omega^2\right)} + \frac{j\omega\hat{\lambda}_2 - \hat{\lambda}_2 \sigma_2^2 \omega^2}{2 \cdot \left(1 + \sigma_2^4 \omega^2\right)}\right] \cdot \qquad \textbf{4-44}$$

At this point, the characteristic function of $S_{DiffL1L2}$ can be used to numerically determine its probability density function using the following property of the characteristic function:

$$f_{S_{DiffL1L2}}(s) = \frac{1}{2\pi} \int_{-\infty}^{+\infty} \overline{\Psi}_{S_{DiffL1L2}}(\omega) \cdot e^{j\omega s} d\omega. \qquad \textbf{4-45}$$

Note that the numerical inverse Fourier transform involved in Equation 4-45 was done following the method proposed by Requicha (1970).

4.1.3 NCDiff_{L1L2} method

Equation 3-3, representing the non-coherent plus differential L1/L2 combined acquisition (NCDiff_{L1L2}) can be reformulated as follows:

$$S_{NCDiffL1L2} = \left\{ \begin{array}{l} \dfrac{I_{1,L1}{}^2 + Q_{1,L1}{}^2}{2} \\[2ex] + \sum_{k=1}^{M-1}\left[\dfrac{\left(I_{k,L1} + I_{k+1,L1}\right)^2}{2} + \dfrac{\left(Q_{k,L1} + Q_{k+1,L1}\right)^2}{2} \right] \\[2ex] + \dfrac{I_{M,L1}{}^2 + Q_{M,L1}{}^2}{2} \end{array} \right\}$$
$$+ \left\{ \begin{array}{l} \dfrac{W^2 \cdot I_{1,L1}{}^2 + W^2 \cdot Q_{1,L1}{}^2}{2} \\[2ex] + \sum_{k=1}^{M-1}\left[\dfrac{W^2 \cdot \left(I_{k,L1} + I_{k+1,L1}\right)^2}{2} + \dfrac{W^2 \cdot \left(Q_{k,L1} + Q_{k+1,L1}\right)^2}{2} \right] \\[2ex] + \dfrac{W^2 \cdot I_{M,L1}{}^2 + W^2 \cdot Q_{M,L1}{}^2}{2} \end{array} \right\}$$

$$\text{4-46}$$

Equation 4-46 can then be further simplified by defining the following vectors:

$$X_{L1} = \begin{bmatrix} I_{1,L1} \\ Q_{1,L1} \\ I_{1,L1} + I_{2,L1} \\ Q_{1,L1} + Q_{2,L1} \\ \vdots \\ \vdots \\ I_{k,L1} + I_{k+1,L1} \\ Q_{k,L1} + Q_{k+1,L1} \\ \vdots \\ \vdots \\ I_{M-1,L1} + I_{M,L1} \\ Q_{M-1,L1} + Q_{M,L1} \\ I_{M,L1} \\ Q_{M,L1} \end{bmatrix} \qquad X_{L2} = W \cdot \begin{bmatrix} I_{1,L2} \\ Q_{1,L2} \\ I_{1,L1} + I_{2,L2} \\ Q_{1,L1} + Q_{2,L2} \\ \vdots \\ \vdots \\ I_{k,L2} + I_{k+1,L2} \\ Q_{k,L2} + Q_{k+1,L2} \\ \vdots \\ \vdots \\ I_{M-1,L2} + I_{M,L2} \\ Q_{M-1,L2} + Q_{M,L2} \\ I_{M,L2} \\ Q_{M,L2} \end{bmatrix}.$$

The mathematical representation of the output of the NCDiff$_{L1L2}$ becomes:

$$S_{NCDiffL1L2} = \frac{1}{2}X_{L1}{}^T X_{L1} + \frac{1}{2}X_{L2}{}^T X_{L2}.$$

4-47

Note that the vectors X_{L1} and X_{L2} are independent.

Moreover, the covariance matrix of X_{L1} is a $(2 \cdot M + 2) \times (2 \cdot M + 2)$ square matrix and is expressed as

$$C_{X_{L1}} = \begin{bmatrix} \sigma^2 & 0 & \sigma^2 & 0 & 0 & 0 & 0 \\ 0 & \sigma^2 & 0 & \sigma^2 & 0 & 0 & 0 \\ \sigma^2 & 0 & 2\sigma^2 & 0 & \ddots & 0 & 0 \\ 0 & \sigma^2 & 0 & \ddots & 0 & \sigma^2 & 0 \\ 0 & 0 & \ddots & 0 & 2\sigma^2 & 0 & \sigma^2 \\ 0 & 0 & 0 & \sigma^2 & 0 & \sigma^2 & 0 \\ 0 & 0 & 0 & 0 & \sigma^2 & 0 & \sigma^2 \end{bmatrix}.$$

4-48

As $C_{X_{L1}}$ is a real symmetric matrix, it is possible to decompose it using an eigenvector decomposition. The matrix of eigenvectors is then orthogonal. The aforementioned properties of a real symmetric matrix are summarized for X_{L1} and $C_{X_{L1}}$ through (T being the transpose operator):

$$C_{X_{L1}} = Q D_{L1} Q^T$$

4-49

$$Q^T = Q^{-1}$$

4-50

When projecting X_{L1} in the orthogonal basis defined by Q, the resulting vector Y_{L1} has a diagonal covariance matrix. This can easily be derived as follows ($< \cdot >$ standing for expected value):

$$Y_{L1} = Q^T X_{L1} \tag{4-51}$$

$$
\begin{aligned}
C_{Y_{L1}} &= <Y_{L1}Y_{L1}{}^T> \\
&= <Q^T X_{L1} X_{L1}{}^T Q> \\
&= <Q^T C_{X_{L1}} Q> \\
&= D_{L1}
\end{aligned}
\tag{4-52}
$$

Moreover, the norm of Y_{L1} is equal to the norm of X_{L1}:

$$Y_{L1}{}^T Y_{L1} = \left(X_{L1}{}^T Q \right) \cdot \left(Q^T X_{L1} \right) = X_{L1}{}^T X_{L1}.$$

Similarly, the covariance matrix of X_{L2} is

$$
C_{X_{L2}} =
\begin{bmatrix}
\sigma_2{}^2 & 0 & \sigma_2{}^2 & 0 & 0 & 0 & 0 \\
0 & \sigma_2{}^2 & 0 & \sigma_2{}^2 & 0 & 0 & 0 \\
\sigma_2{}^2 & 0 & 2\sigma_2{}^2 & 0 & \ddots & 0 & 0 \\
0 & \sigma_2{}^2 & 0 & \ddots & 0 & \sigma_2{}^2 & 0 \\
0 & 0 & \ddots & 0 & 2\sigma_2{}^2 & 0 & \sigma_2{}^2 \\
0 & 0 & 0 & \sigma_2{}^2 & 0 & \sigma_2{}^2 & 0 \\
0 & 0 & 0 & 0 & \sigma_2{}^2 & 0 & \sigma_2{}^2
\end{bmatrix}
\tag{4-53}
$$

and it can be decomposed as follows:

$$C_{X2} = Q D_{L2} Q^T \tag{4-54}$$

$$Q^T = Q^{-1} \tag{4-55}$$

$$Y_{L2} = Q^T X_{L2} \tag{4-56}$$

$$C_{Y_{L2}} = D_{L2}. \tag{4-57}$$

Once again, $Y_{L2}{}^T Y_{L2} = X_{L2}{}^T X_{L2}$.

The output of the NCDiff$_{L1L2}$ method can be expressed as a function of the vectors Y_{L1} and Y_{L2}:

$$S_{NCDiffL1L2} = \frac{1}{2} Y_{L1}{}^T Y_{L1} + \frac{1}{2} Y_{L2}{}^T Y_{L2}.$$

4-58

Note that Y_{L1} and Y_{L2} are independent of each other and that the elements composing Y_{L1} or Y_{L2} are independent (both vector having a diagonal covariance matrix). Moreover, the variance of the elements of Y_{L1} and Y_{L2} are the elements located on the diagonal of D_{L1} and D_{L2} respectively.

After the above development, the characteristic functions of $S_{NCDiffL1L2}$ can readily be determined.

Determination of the PDF under H$_0$

$S_{NCDiffL1L2}$ is the summation of $(4 \cdot M + 2)$ central Chi-Square random variables with one degree of freedom. Its characteristic function is expressed as

$$\Psi_S(\omega) = \prod_{i=1}^{2M+1} \left(\frac{1}{1 - 2j\omega D_{L1}(i)} \right)^{\frac{1}{2}} \left(\frac{1}{1 - 2j\omega D_{L2}(i)} \right)^{\frac{1}{2}}.$$

4-59

Note that $D_{L1}(i)$ represents ith element of the diagonal of D_{L1}.

Determination of the PDF under H₁

$S_{NCDiffL1L2}$ is the summation of $(4 \cdot M + 2)$ non-central Chi-Square random variables with one degree of freedom and non-centrality parameters the square of the mean of the elements of Y_{L1} and Y_{L2}. Its characteristic function is expressed in Equation 4-60 .

$$\Psi_S(\omega) = \prod_{i=1}^{2M+1} \left(\frac{1}{1 - 2j\omega D_{L1}(i)} \right)^{\frac{1}{2}} \cdot \exp\left(\frac{j\omega \cdot \overline{Y}_{L1}(i)^2}{1 - 2j\omega D_{L1}(i)} \right)$$
$$\cdot \prod_{i=1}^{2M+1} \left(\frac{1}{1 - 2j\omega D_{L2}(i)} \right)^{\frac{1}{2}} \cdot \exp\left(\frac{j\omega \cdot \overline{Y}_{L2}(i)^2}{1 - 2j\omega D_{L2}(i)} \right) \quad \textbf{4-60}$$

4.2 Obtaining simulated and real data correlator outputs

4.2.1 Simulation process

Once again results are first assessed by means of a simulation. The correlator outputs are simulated using a similar process to the one described in Chapter 3. Table 4-1 gives the simulation parameters used to generate the L1 correlator outputs whereas Table 4-2 gives the simulation parameters used to generate the L2 correlator outputs.

Table 4-1: Parameters used to simulate the L1 correlator outputs

Parameter	Value
$C/N_{0\ L1}$	30 dB-Hz
T	1 ms
σ_1^2	equal to σ^2
$d_1(k)$	Random 1 or -1
Code Phase Step	1 / 4 chip
dt_1	Uniformly distributed between 0 and 1 / 8 chip
ΔF_1	Uniformly distributed between -333.33 Hz and 333.33 Hz
φ_1	Uniformly distributed between 0 and 2π

Table 4-2: Parameters used to simulate the L2 correlator outputs

Paramter	Value
$C/N_{0\ L2}$	$C/N_{0\ L1} - 1.5$
T	1 ms
σ_1^2	equal to twice σ^2
$d_2(k)$	Random 1 or -1
dt_2	$dt_1 + d_{iono}$
d_{iono}	Dependent on VTEC and Map
VTEC	Uniformly distributed between 10 TECU and 60TECU
Map	Dependent on elevation angle E
E	Uniformly distributed between 0° and 90°
ΔF_2	$\Delta F_1 \times f_2\ /\ f_1$
φ_2	Uniformly distributed between 0 and 2π

4.2.2 Correlator outputs from real data

To validate the simulation, real data was collected. The two signals were collected using a L1/L2 antenna and passed through a variable attenuator. The signals were then split between a NovAtel L1/L2 RF front end and a NovAtel OEMv3 GPS L1/L2 industrial receiver used for C/N_0 reference. The C/N_0 on L1 during the data collection was 30 dB-Hz. Finally, the L1/L2 IF signals were stored on the PC performing the acquisition methods.
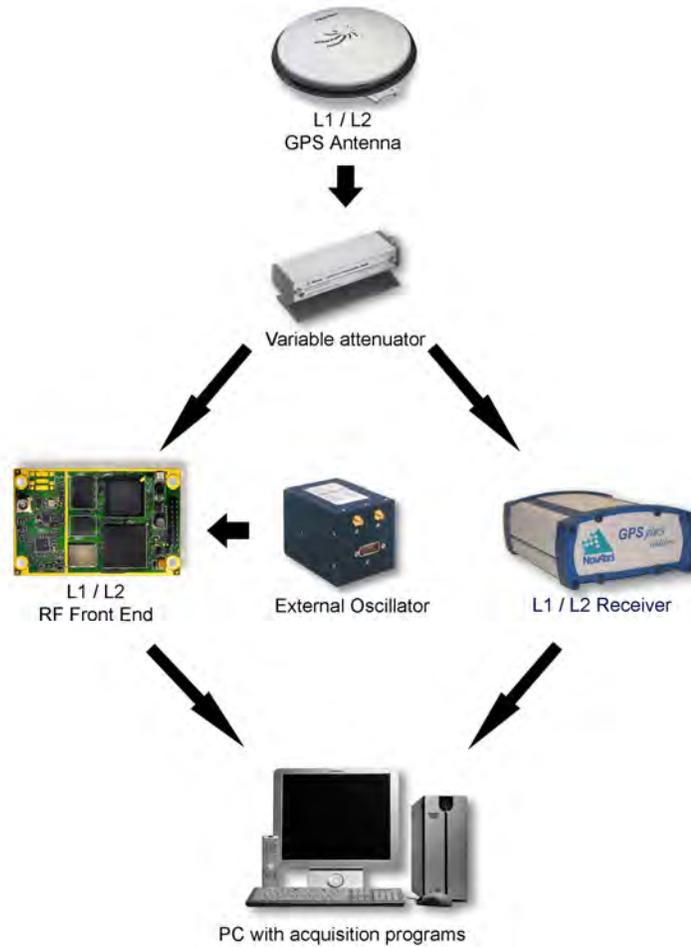
Figure 4-1 : Real data collection scheme

In order to obtain the number of L1/L2 correlator outputs necessary to perform a statistical analysis, it is first required to determine the correct code delay and Doppler frequency needed. Given the amount of attenuation and to ensure the proper correlation peak was found, long coherent integrations were used during this process. Once the initial Doppler frequency and code delay were found, 120,000 1-ms correlator output samples were obtained from two minutes of IF data. Note that the code delay and correct Doppler frequency were followed according to a L1 C/A tracking program running on the side of the correlator output creation program. Finally, as the true Doppler frequency was

known, an artificial offset was created in order for a residual Doppler frequency to corrupt the data.

4.3 Verification of the theory

This section makes use of the theoretical development of the probability density functions under H_0 and H_1 and the probability density function derived from data simulated through Equation 2-12, Table 4-1 and Table 4-2, as well as real data obtained according to Figure 4-1 to verify that theory and practice are coherent.

4.3.1 NC_{L1L2} method

Regarding the NC_{L1L2} method, Figure 4-2 shows the theoretical PDF compared to the simulated PDF. Figure 4-3 shows the theoretical PDF compared to the measured PDF. Note that an arbitrary weight W of 0.6 was chosen during this verification process and the L1 C/N_0 for the simulation chosen was 30 dB-Hz.
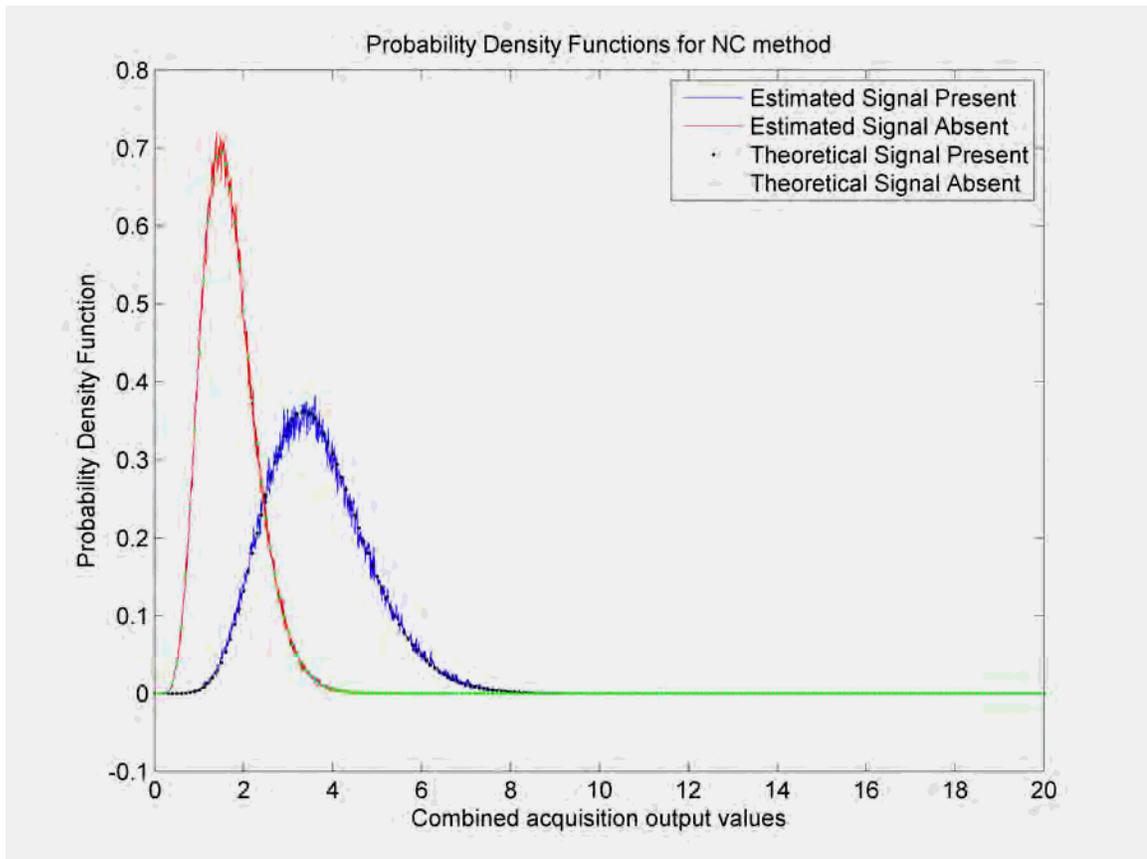
Figure 4-2 : Probability density functions for the NC$_{L1L2}$ method using simulated data
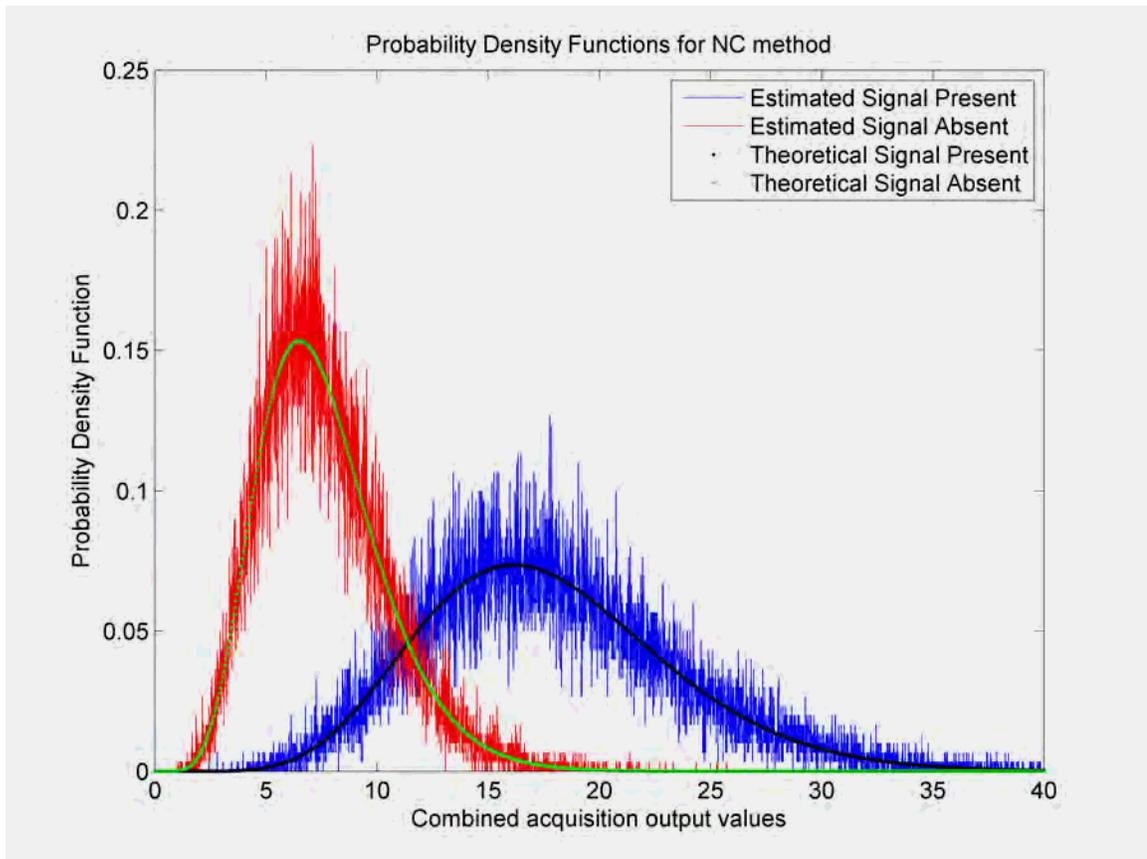
Figure 4-3 : Probability density functions for the NC$_{L1L2}$ method using real data

As shown in the above figures, the theoretical PDFs properly match the PDFs obtained using real and simulated data. As such, one can safely declare the theoretical model verified.

4.3.2 Diff$_{L1L2}$

Regarding the Diff$_{L1L2}$ method, Figure 4-4 shows the theoretical PDF compared to the simulated PDF. Figure 4-5 shows the theoretical PDF compared to the measured PDF. Note that an arbitrary weight W of 0.6 was chosen during this verification process and the L1 C/N$_0$ for the simulation chosen was 30 dB-Hz.
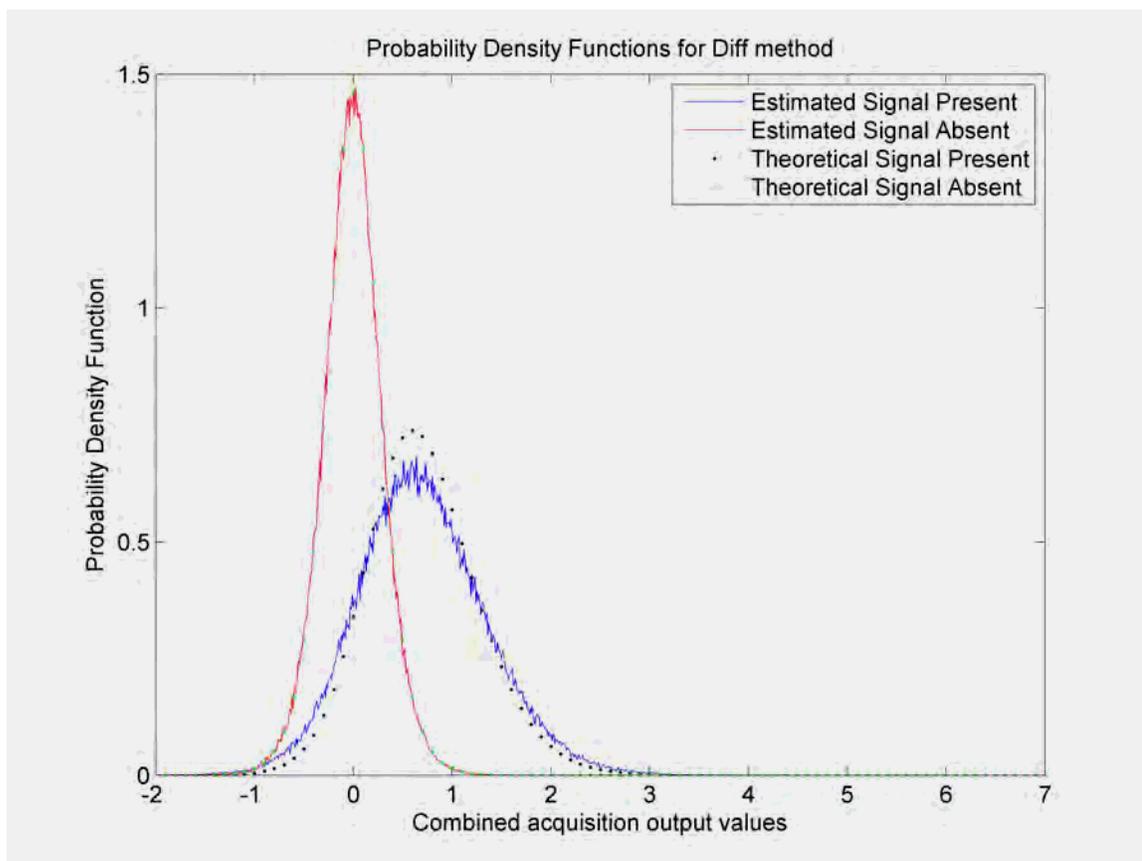
Figure 4-4 : Probability density functions for the Diff$_{L1L2}$ method using simulated data
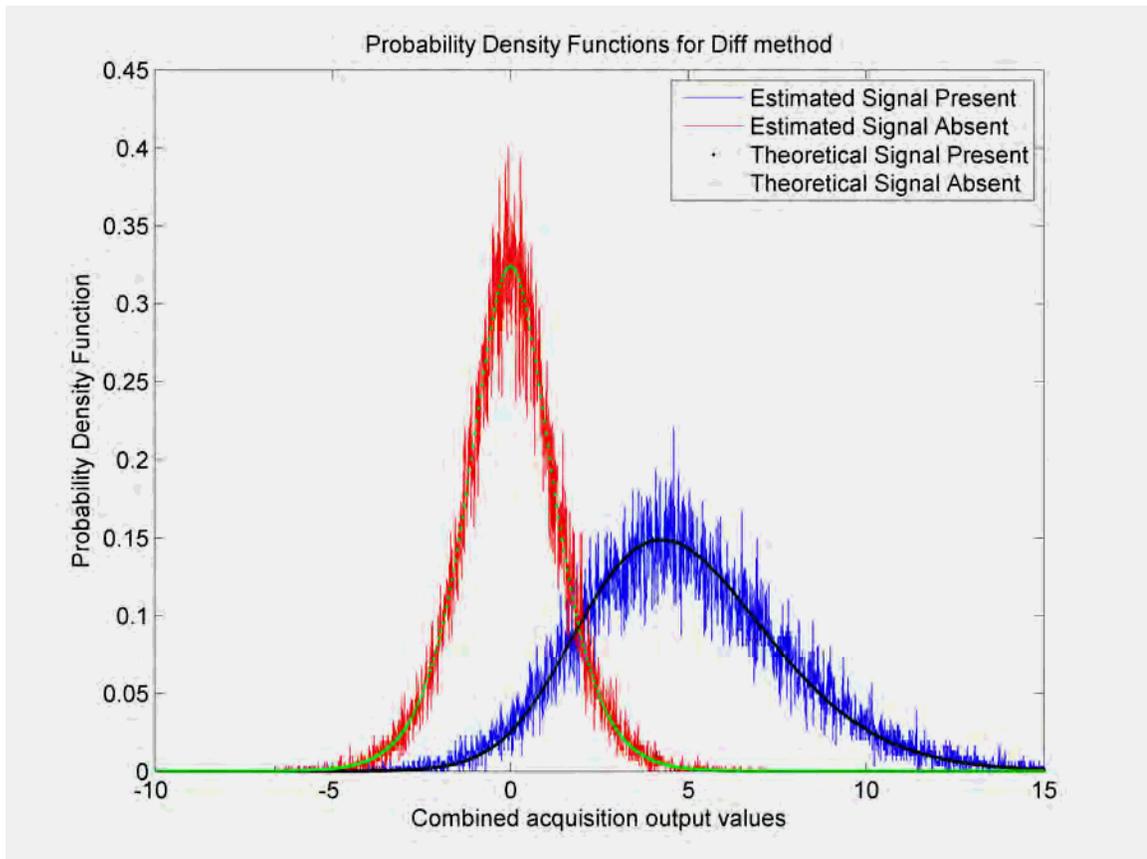
Figure 4-5 : Probability density functions for the Diff$_{L1L2}$ method using real data

Note the presence of small discrepancies between the theory and estimated PDFs under H_1 for the simulated data. These are due to the fact that the theory does not take into account the presence of the residual Doppler. It is shown later that, whereas this does have an important impact on the Receiver Operating Characteristics (ROC), limiting the Doppler error removes the divergence of the theoretical model. As such, the proposed theory remains valid for small residual Doppler frequencies. Regarding real data, the presence of these discrepancies remains but is unseen on the figure. This is due to the fact that the use of real data leads to noisier estimated PDFs and that the Doppler residual was kept small during the real data analysis (about 50 Hz) whereas it ranged from -333.33 Hz

to 333.33 Hz for simulated data. Apart from this minor difference, one can safely declare the theoretical model verified.

4.3.3 NCDiff$_{L1L2}$

Figure 4-6 shows the theoretical PDF compared to the simulated PDF for this method. Figure 4-7 shows the theoretical PDF compared to the measured PDF. Again, an arbitrary weight W of 0.6 was chosen during this verification process and the L1 C/N$_0$ for the simulation chosen was 30 dB-Hz.
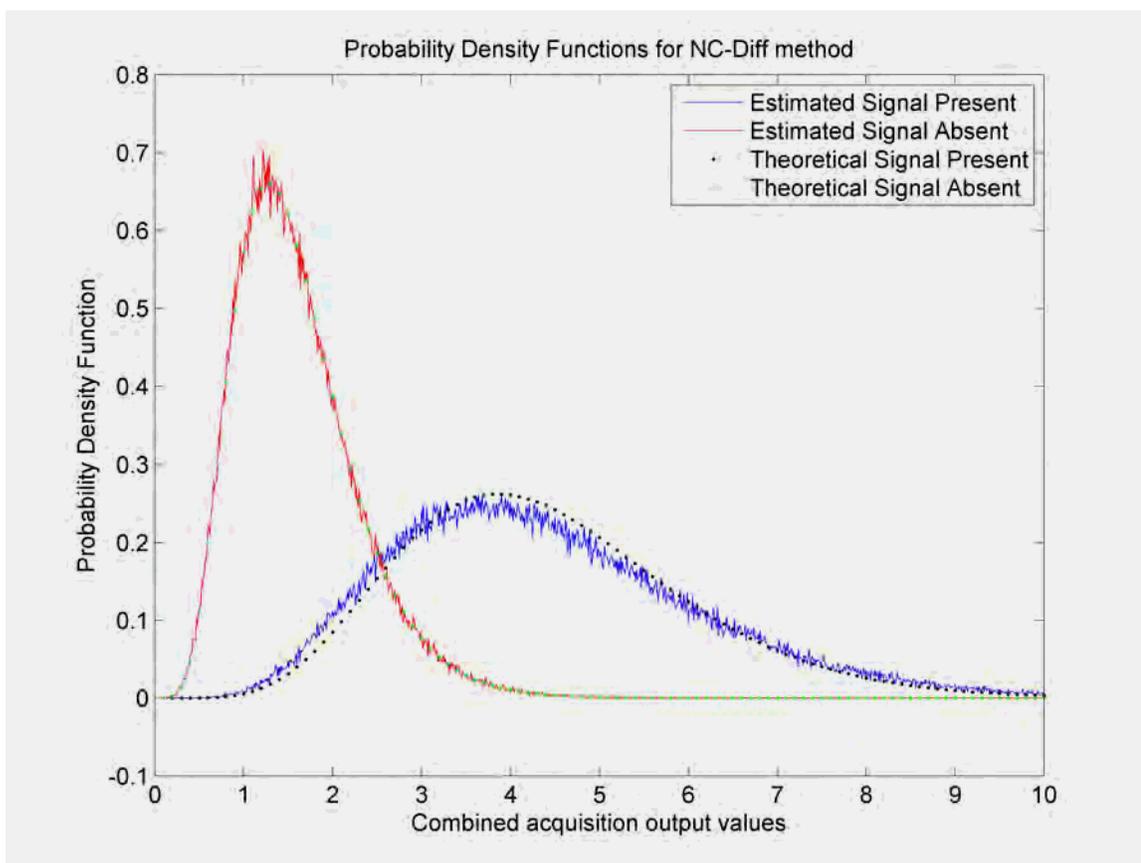
Figure 4-6 : Probability density functions for the NCDiff$_{L1L2}$ method using simulated data
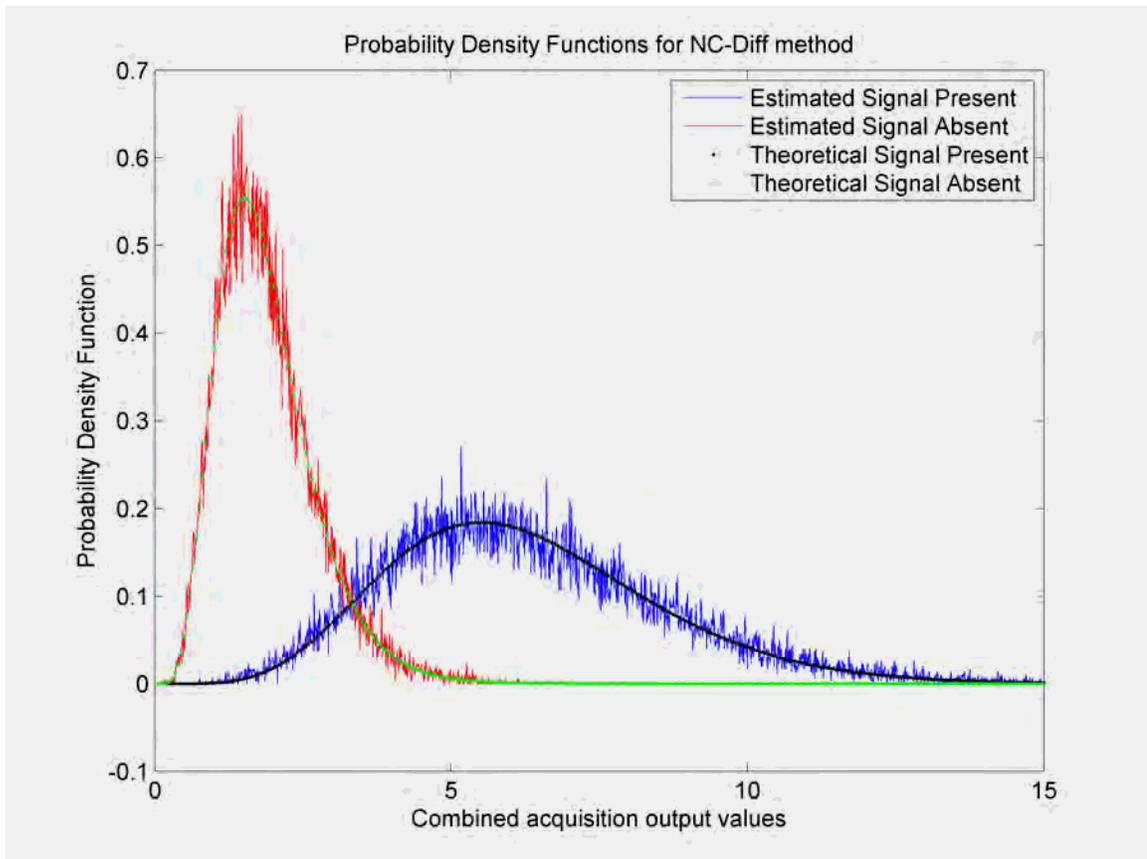
Figure 4-7 : Probability density functions for the NCDiff$_{L1L2}$ method using real data

Once again, the presence of small discrepancies between the theory and estimated PDFs under H_1 is due to the fact that the theory does not take into account the presence of the residual Doppler. However, it is shown later that it does not have an important impact on the Receiver Operating Characteristics (ROC). Regarding real data, the presence of these discrepancies is undetectable due to noisier estimated PDFs and a small Doppler residual (about 30 Hz) ranging from -333 Hz to 333 Hz for simulated data. Apart from this minor difference, one can safely declare the theoretical model verified.

4.4 ROC curves, comparison and analysis

In the following, note that the coherent integration length considered is 1 ms and that the number of coherent integrations to combine is *M=4*.

Prior to any analysis, the optimal weight *W* applied on L2 must be determined for each method. In order to do so, the probability of detection for a fixed probability of false alarm of 0.001 was computed for a set of weight values ranging from 0 to 1. Indeed, as the signal power and noise variance are larger on L2 and the weight applied on L1 is 1, it is expected that the weight to apply on L2 would be smaller than 1.

As such, Figure 4-8, Figure 4-9, and Figure 4-10 show that the optimal weight to apply on L2 for the NC_{L1L2}, the $Diff_{L1L2}$ and the $NCDiff_{L1L2}$ methods, respectively. As seen on these figures, the optimal weight is similar for each method and has a value of 0.55. A weight value of 0 corresponds to the same method performed on L1 only.
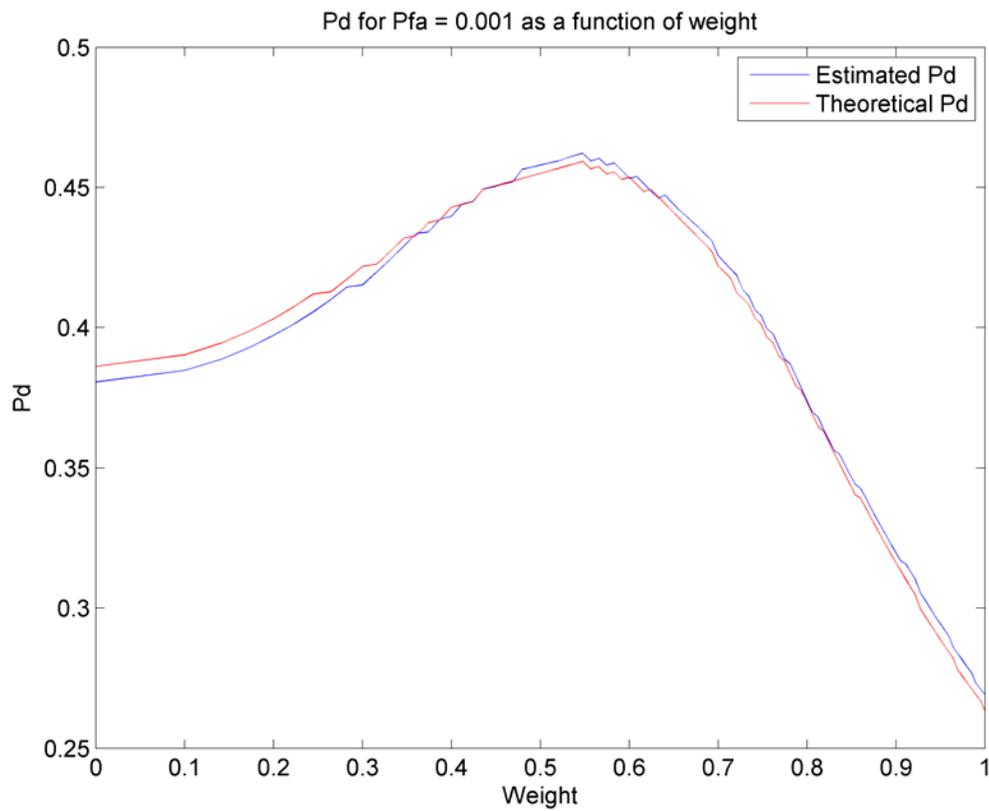
Figure 4-8 : Theoretical probability of detection as a function of the weight applied on L2 for the NC$_{L1L2}$ method
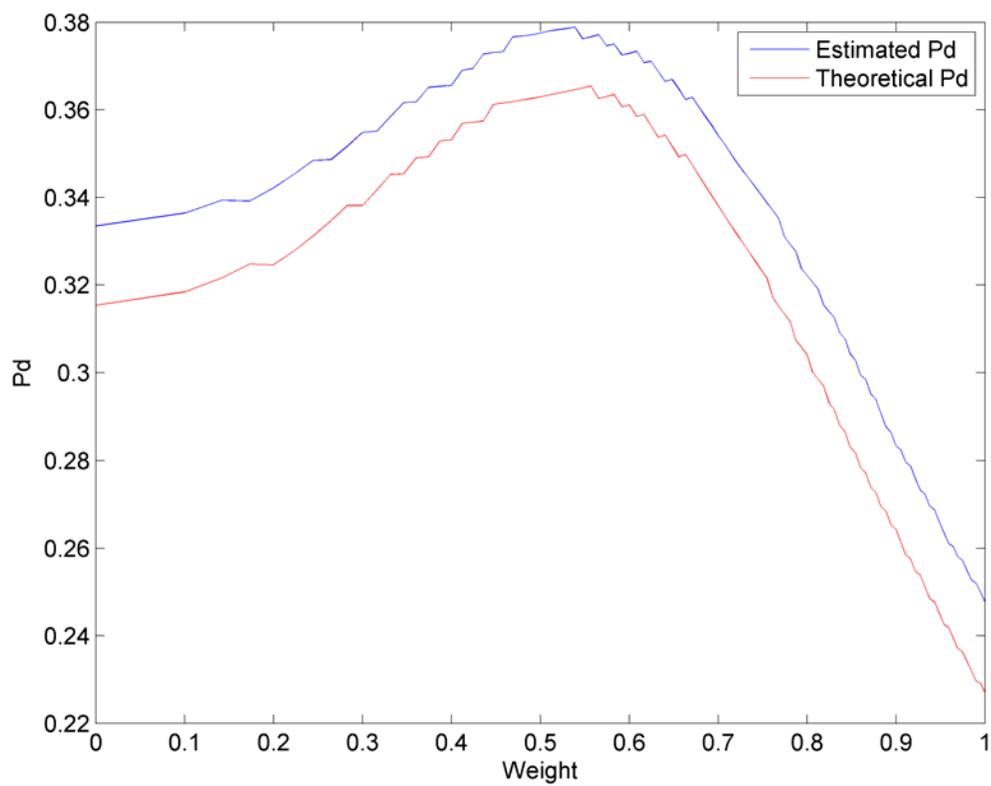
Figure 4-9: Theoretical probability of detection as a function of the weight applied on L2 for the Diff$_{L1L2}$ method
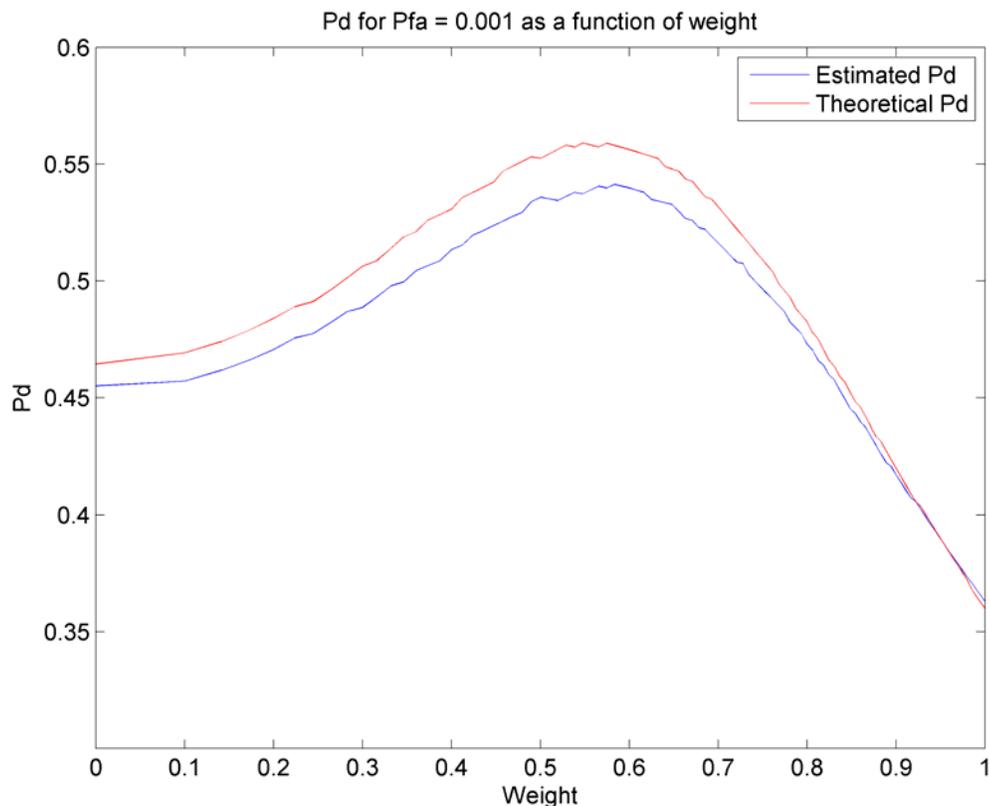
Figure 4-10 : Theoretical probability of detection as a function of the weight applied on L2 for the NCDiff$_{L1L2}$ method

Once the optimal weight is determined, the performance of each method is investigated through comparison of its ROC curve with the ROC curves of a non-coherent acquisition on L1 only using the same number of milliseconds. As the signal power on L2 is smaller than on L1, it is expected that the ROC curves on a non-coherent acquisition on L2 will show poorer performance than a non-coherent acquisition on L1. However, it is still shown here to underline the improvement brought on over an L2 only acquisition, which is most interesting as it removes the need for data bit synchronization.

4.4.1 Results for simulated data

As shown in Figure 4-11 and Figure 4-12, the NC_{L1L2} method outperformed both the non-coherent acquisition on L1 only and the non-coherent acquisition on L2 only methods. When used to determine the ROC curves, the theoretical model developed in Equations 4-3 and 4-7 properly matches the estimated ROC obtained through simulation.
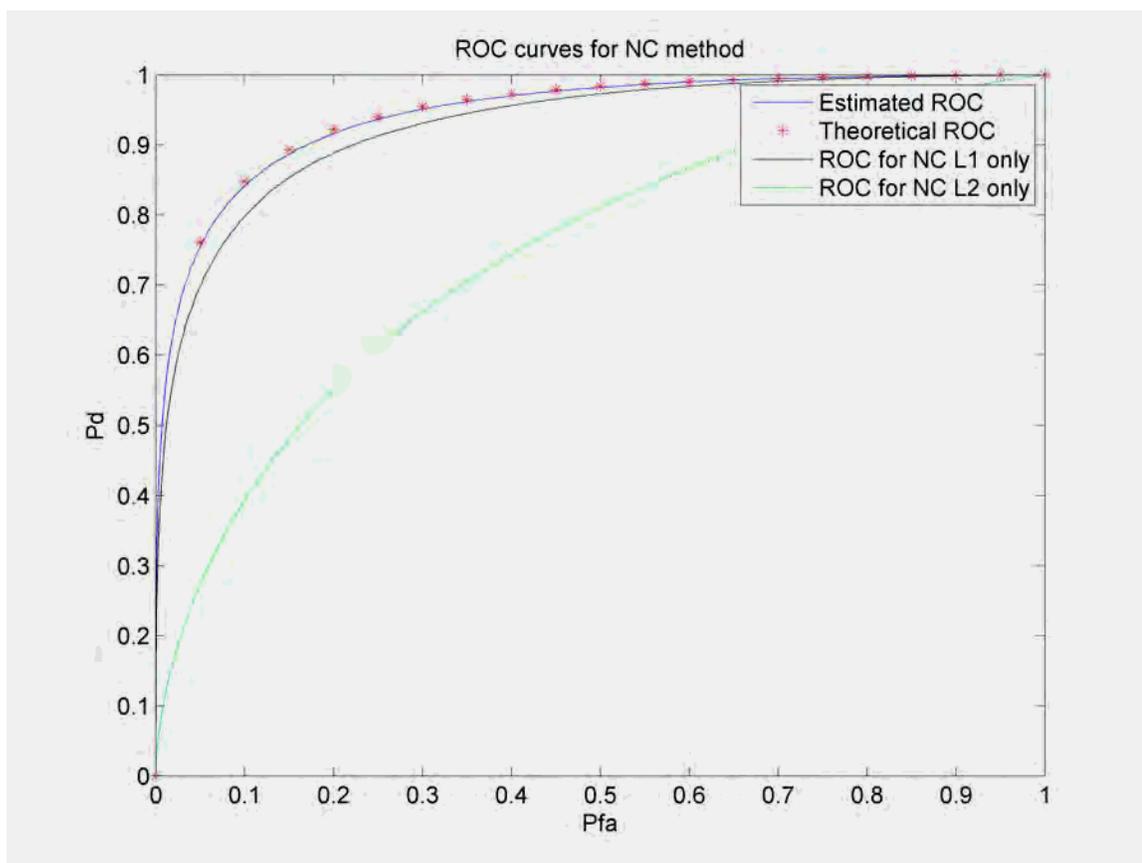
Figure 4-11 : Theoretical and simulation estimated ROC curves for the NC_{L1L2}
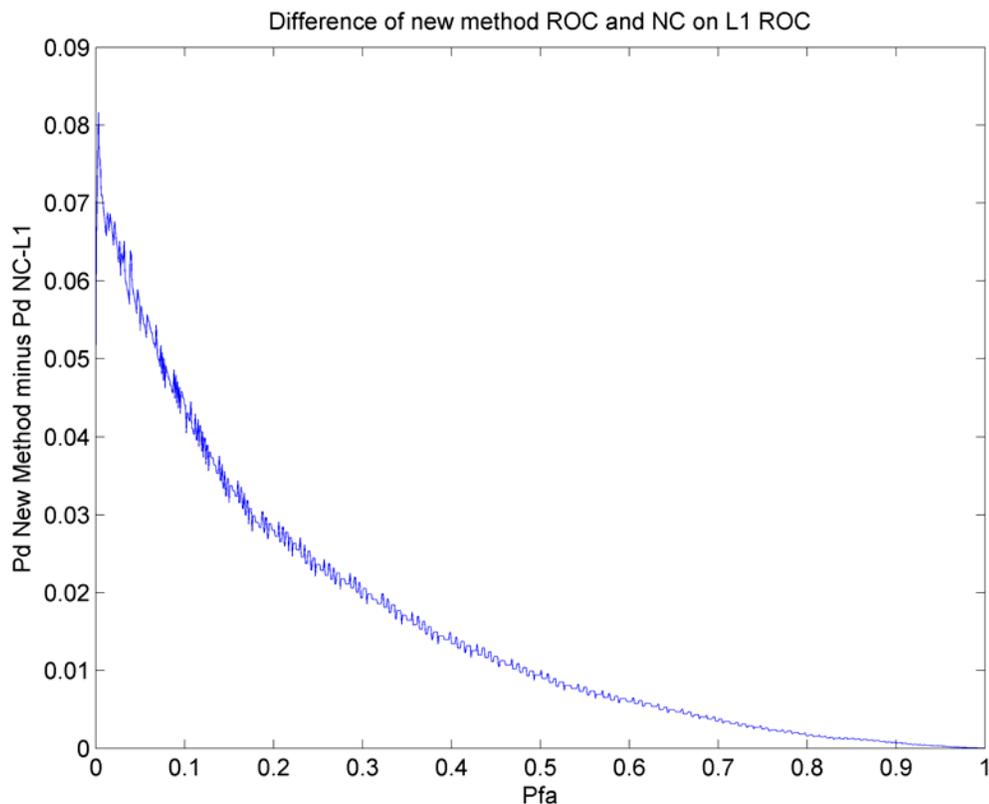
Figure 4-12 : Difference between the NC$_{L1L2}$ ROC and the ROC obtained for a non-coherent acquisition on L1 only using simulated data

Figure 4-13 and Figure 4-14 show the ROC curves obtained through theory and simulation for the Diff$_{L1L2}$. As mentioned earlier, the fact that the Doppler residual (simulated between -333 Hz and 333.33 Hz for a 1 ms coherent integration) was not taken into account in the theoretical model degrades it greatly. As such, the ROC obtained through simulation does not match the ROC obtained through theory. Moreover, the performance of this method, while far above a L2 only non-coherent integration, does not reach the performance of a L1 only non-coherent acquisition.
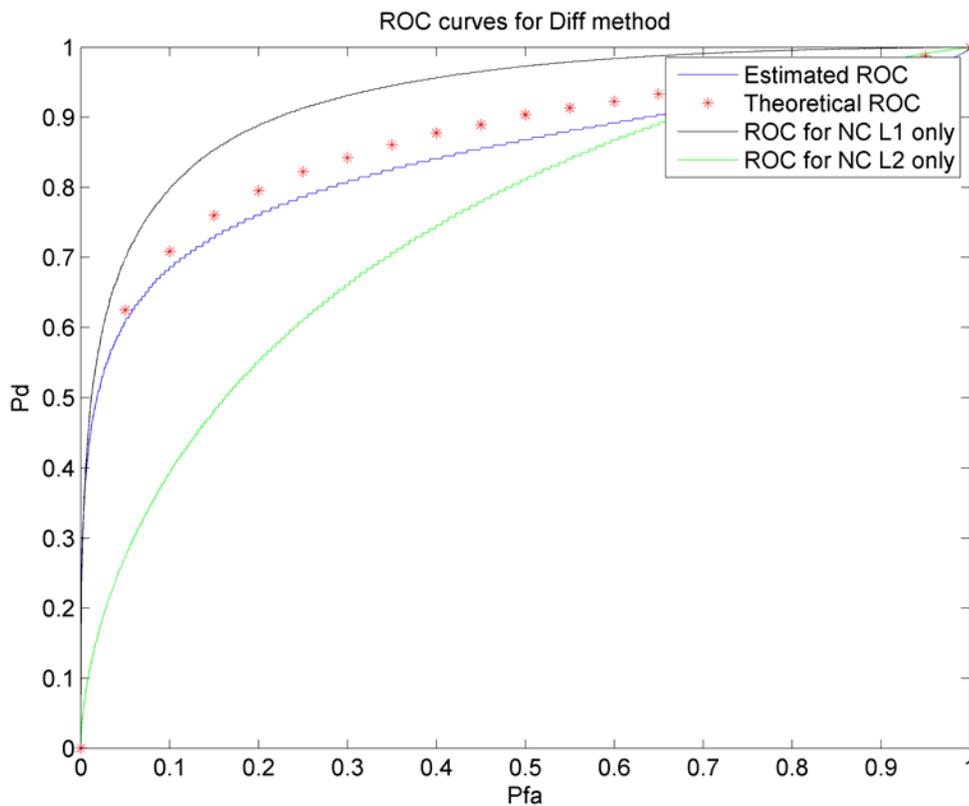
Figure 4-13 : Theoretical and simulation estimated ROC curves for the Diff$_{L1L2}$ for residual Doppler values ranging from -333.33 Hz to 333.33 Hz
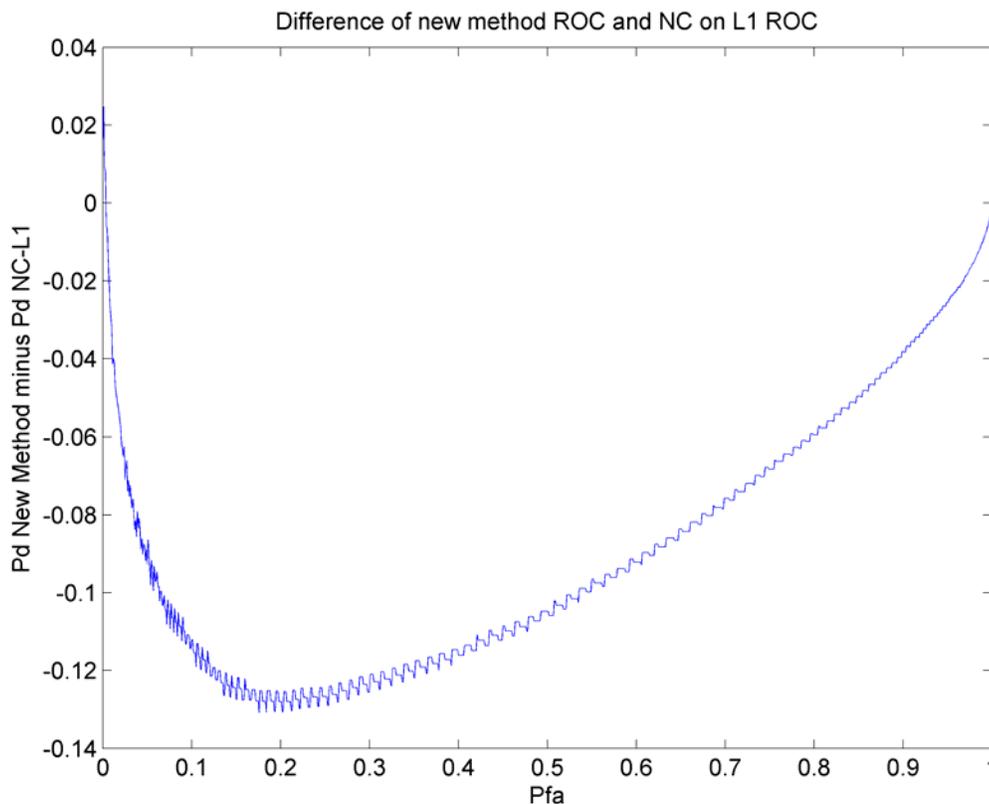
Figure 4-14 : Difference between the Diff$_{L1L2}$ ROC and the ROC obtained for a non-coherent acquisition on L1 only while limiting the Doppler error to +/- 333.33 Hz using simulated data

However, by limiting the residual Doppler frequency to 100 Hz, both problems are solved at once. In this case, the theoretical ROC curve matches the simulated ROC curve and the Diff$_{L1L2}$ method outperforms the non-coherent acquisition done on L1 only. This last point is illustrated in Figure 4-15 and Figure 4-16. The ROC curve obtained for the new method is above the ROC curve of the L1 non-coherent method only for a small probability of false alarm but the whole point of detection is to maximize its probability while minimizing the probability of false alarm. As such, one can safely claim that the new combined method outperforms the non-coherent acquisition on L1 only. Note that if one needs to limit the residual Doppler frequency, the Doppler bin size needs to be

decreased. As such, one could use a longer coherent integration time. Therefore, this method is recommended for combining sets of longer coherent integration times.
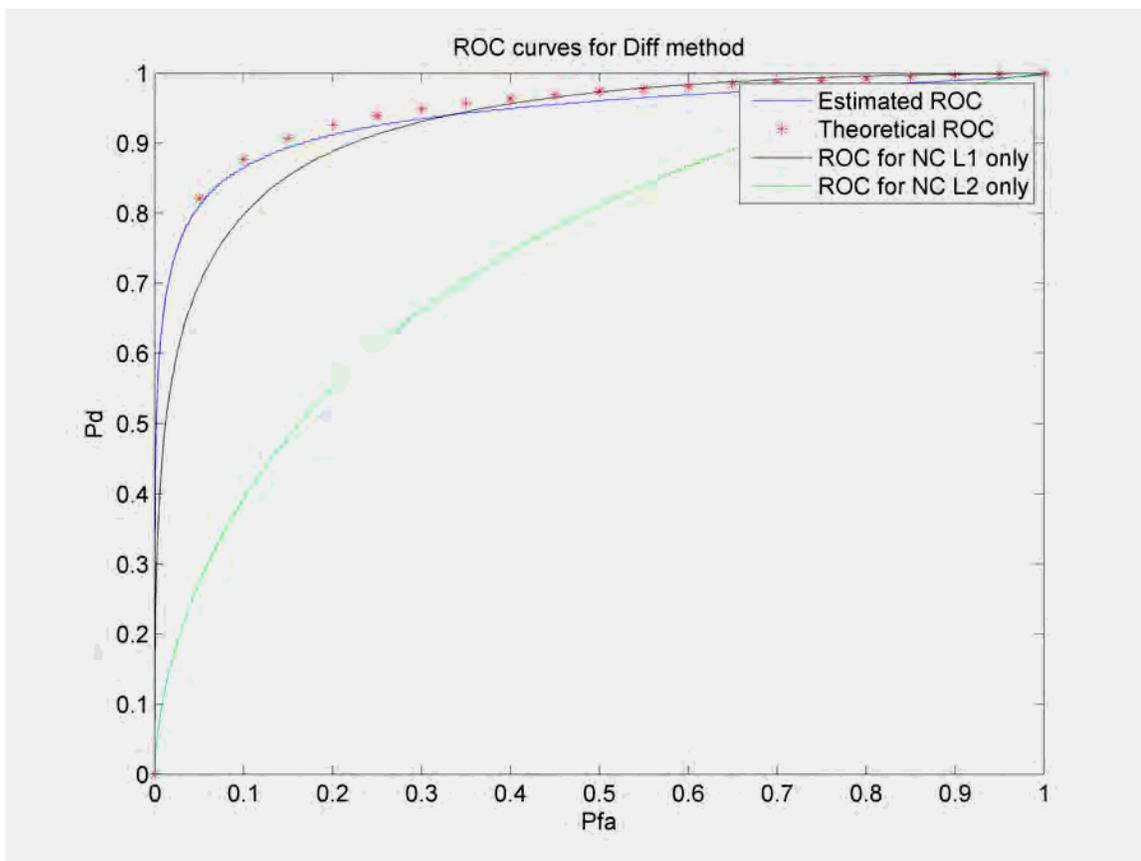
Figure 4-15 : Theoretical and simulation estimated ROC curves for the Diff$_{L1L2}$ for residual Doppler values ranging from -100 Hz to 100 Hz

Difference of new method ROC and NC on L1 ROC
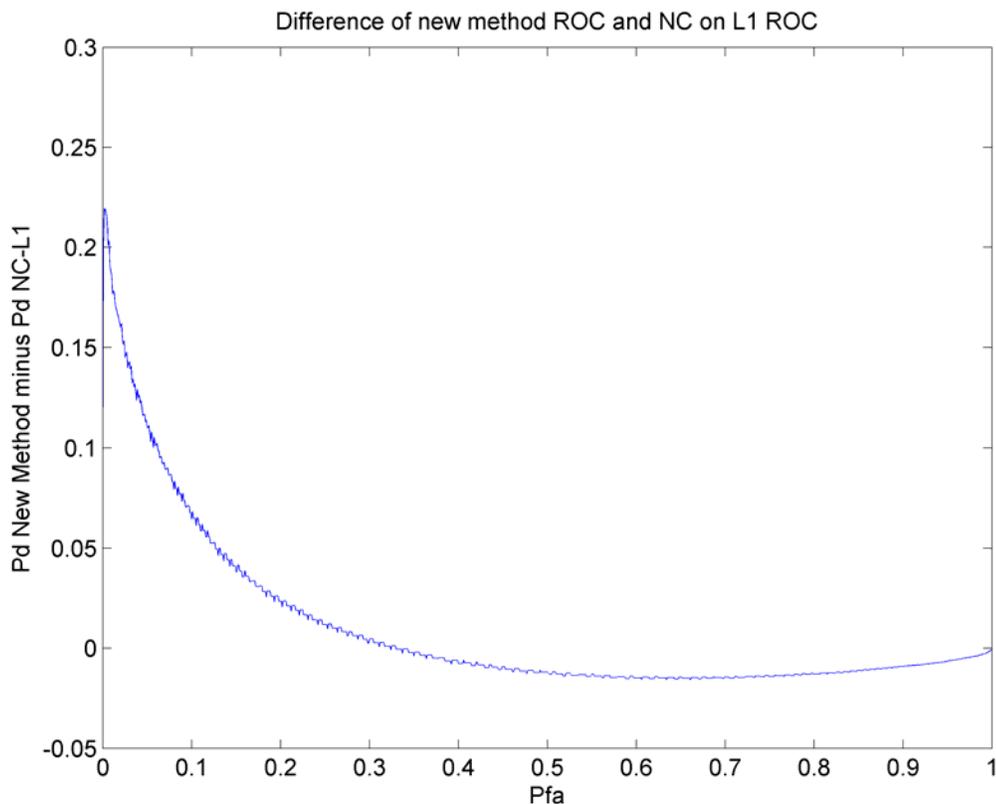
Figure 4-16 : Difference between the Diff$_{L1L2}$ ROC and the ROC obtained for a non-coherent acquisition on L1 only while limited the Doppler error to 100 Hz using simulated data

Finally, Figure 4-17 and Figure 4-18 show the results of the NCDiff$_{L1L2}$ method. Note that the small difference visible between the theoretical and estimated ROC curves is once again due to the fact that the theoretical model does not take into account the residual Doppler frequency corrupting the correlator outputs.
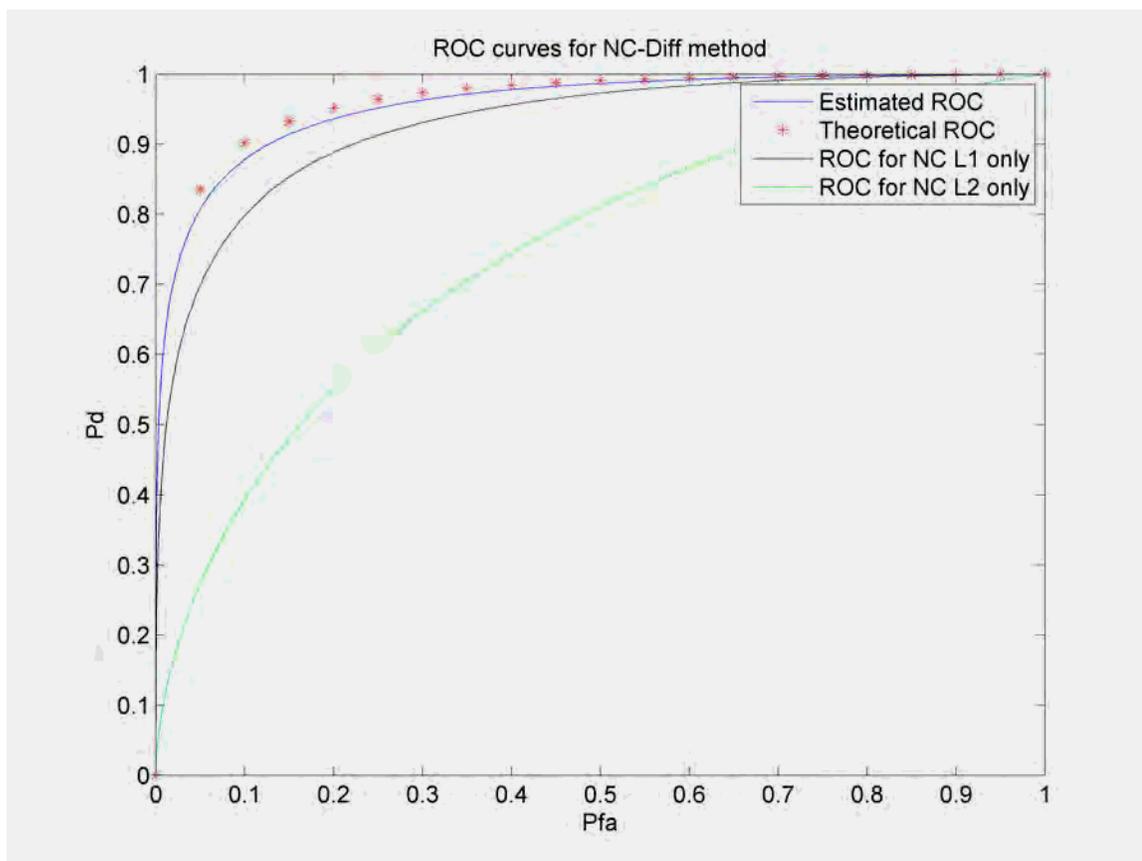
Figure 4-17 : Theoretical and simulation estimated ROC curves for the NCDiff$_{L1L2}$ method
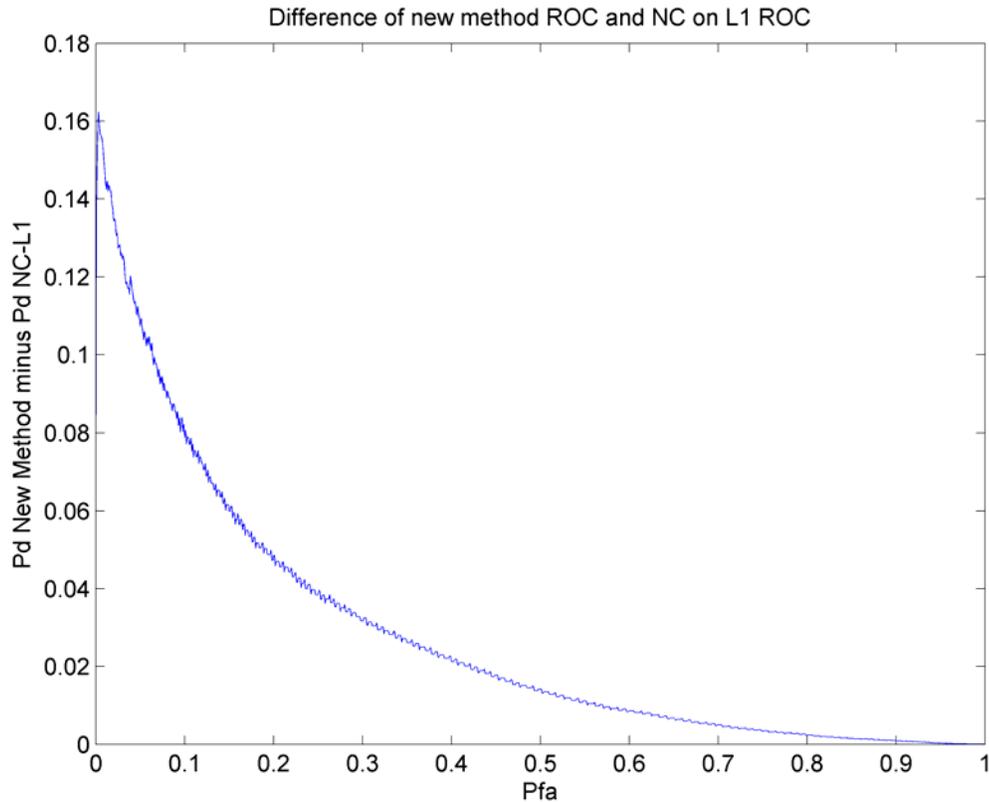
Figure 4-18 : Difference between the NCDiff$_{L1L2}$ ROC and the ROC obtained for a non-coherent acquisition on L1 only using simulated data

From the above figures, it is clear that the NCDiff$_{L1L2}$ not only outperform the non-coherent acquisition performed on L1 only but also the two other L1/L2 combining acquisition schemes proposed. This can be observed through the difference between the novel method ROC curves with the L1 non-coherent ROC curve (Figure 4-12, Figure 4-16 and Figure 4-18). Therefore, the NCDiff$_{L1L2}$ method is recommended for low C/N$_0$ conditions but, as it is more complex than the others, the NC$_{L1L2}$ methods would be preferable, depending on the computation power available.

4.4.2 Results for real data

A similar analysis to that above is performed when one uses real data to create the output of the correlators as shown in Figure 4-1. Figure 4-19 to Figure 4-24 show the ROC curves and ROC curve differences obtained for each method.
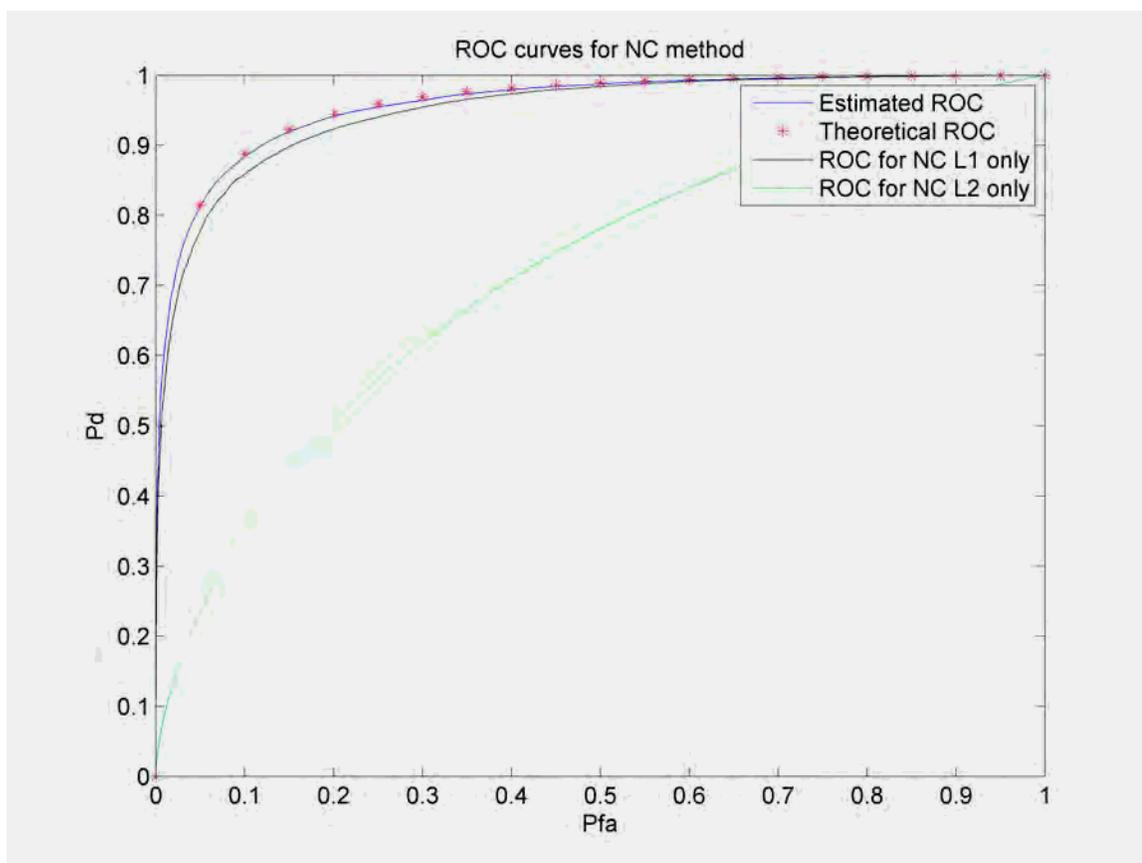
Figure 4-19 : Theoretical and "real data" estimated ROC curves for the NC$_{L1L2}$

Difference of new method ROC and NC on L1 ROC
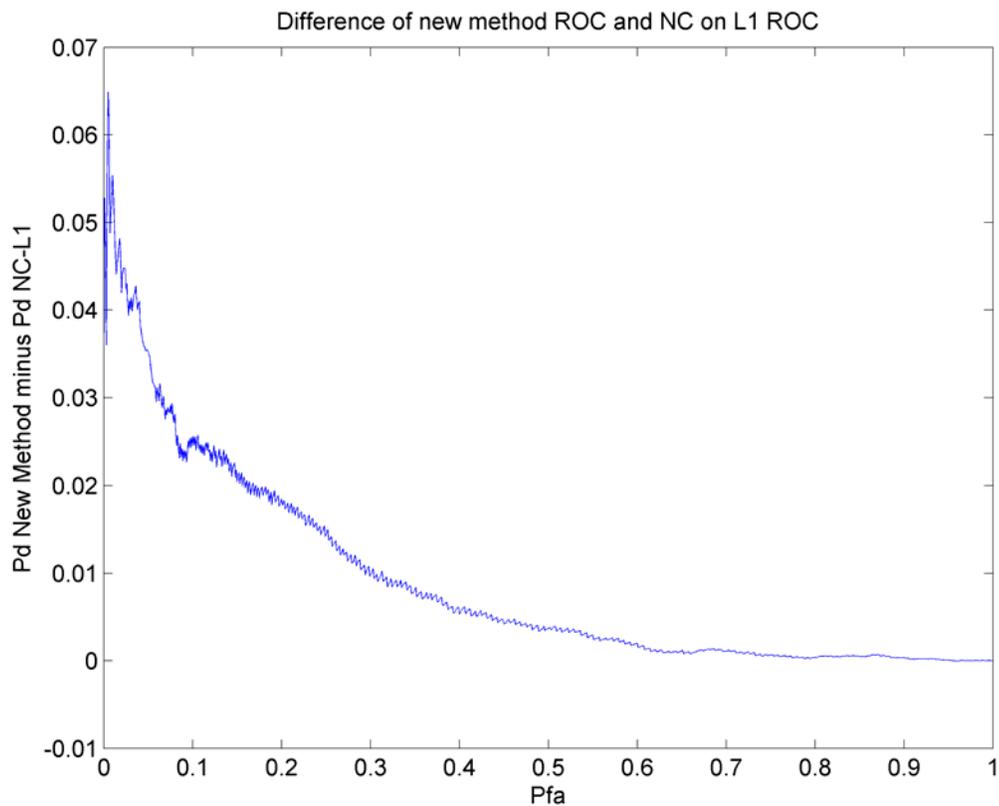
Figure 4-20 : Difference between the NC$_{L1L2}$ ROC and the ROC obtained for a non-coherent acquisition on L1 only using real data

Once again the NC$_{L1L2}$ method outperforms the L1 or L2 only non-coherent acquisition.
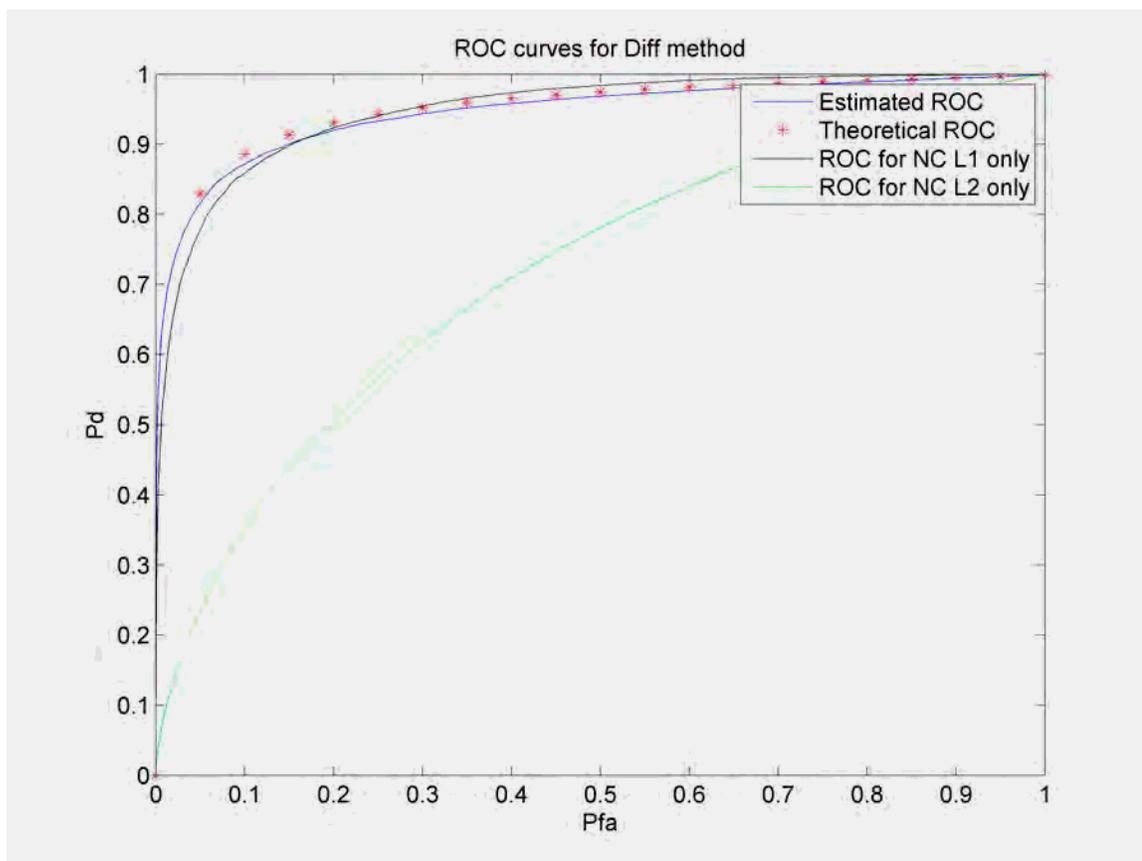
Figure 4-21 : Theoretical and "real data" estimated ROC curves for the Diff$_{L1L2}$
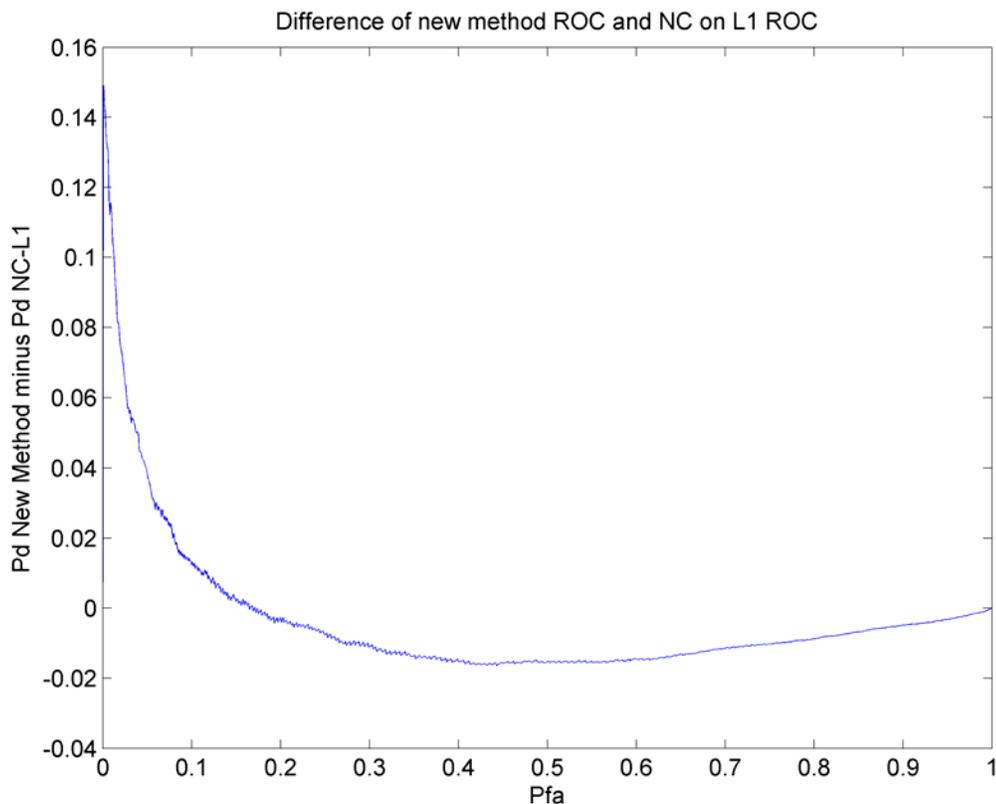
Figure 4-22 : Difference between the Diff$_{L1L2}$ ROC and the ROC obtained for a non-coherent acquisition on L1 only using real data

Note that, as the Doppler residual was kept low (about 50 Hz) during the creation of the correlator outputs, the Diff$_{L1L2}$ does not show degraded performance as it was the case for the simulation results (Figure 4-13). Once again, as one tries to maximize the probability of detection while minimizing the probability of false alarm, the fact that the ROC curve of the Diff$_{L1L2}$ method passes under the ROC curve of the L1 non-coherent acquisition has no impact on the validity of this method.
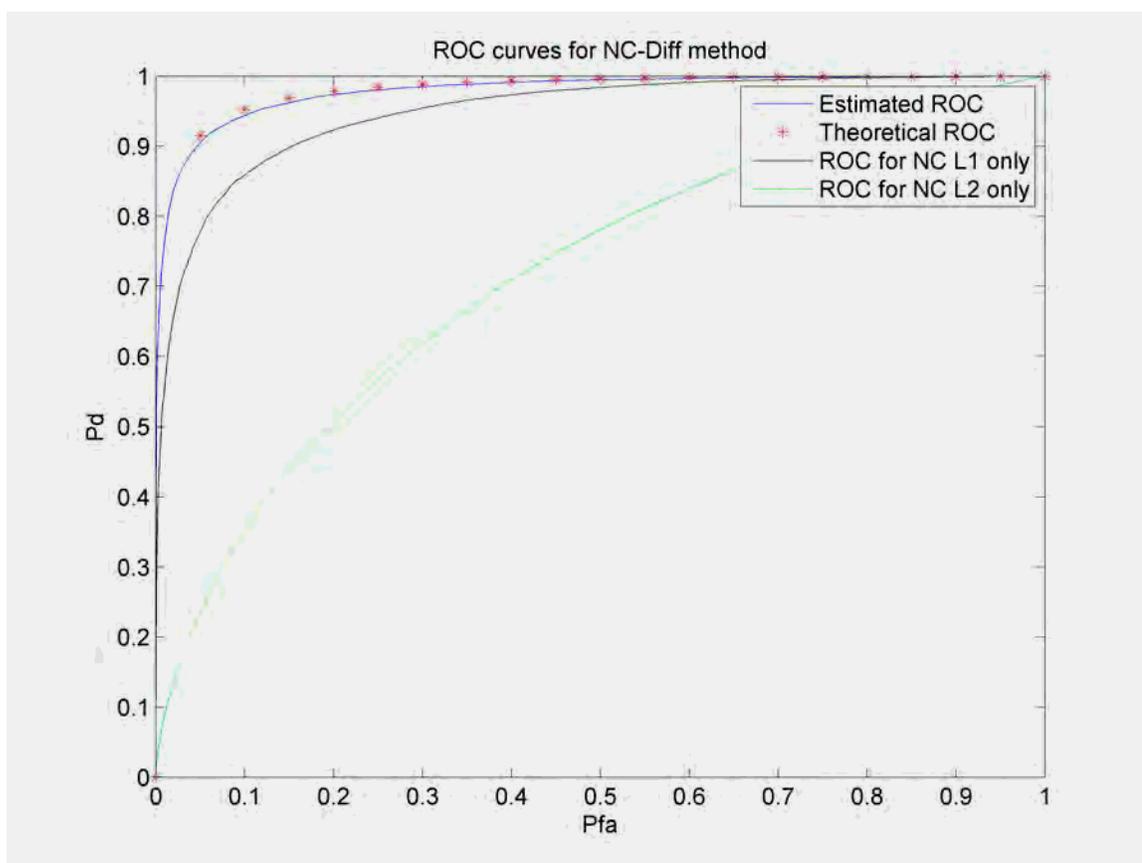
Figure 4-23 : Theoretical and "real data" estimated ROC curves for the NCDiff$_{L1L2}$ method
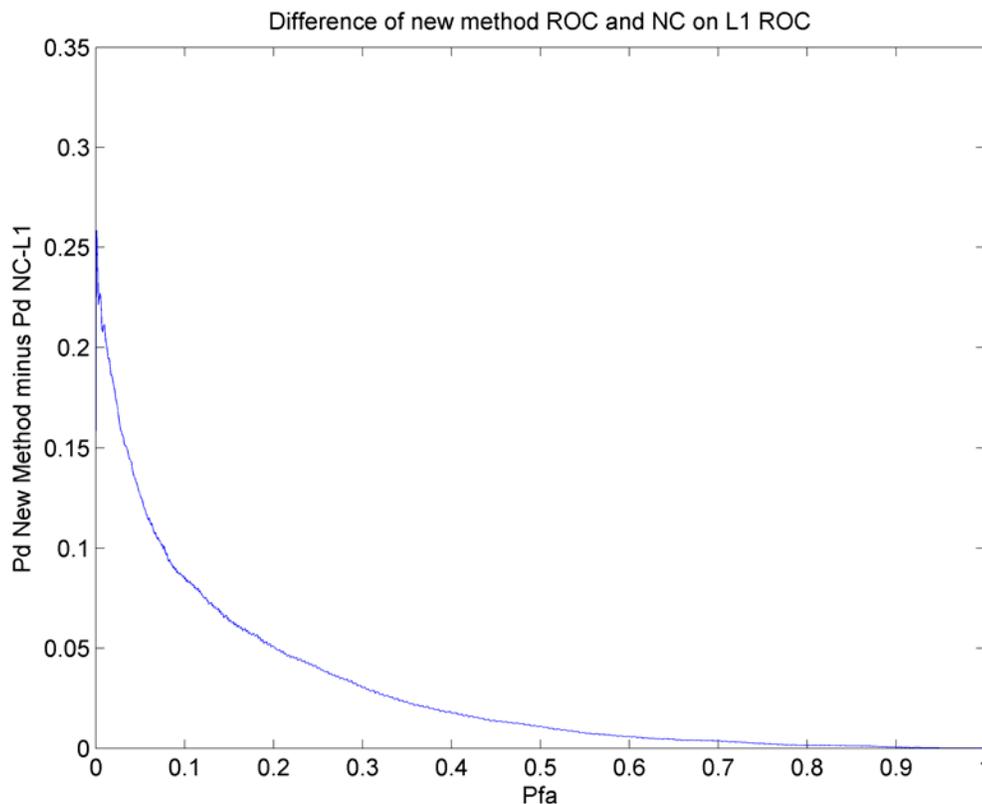
Figure 4-24 : Difference between the NCDiff$_{L1L2}$ and the ROC obtained for a non-coherent acquisition on L1 only using real data

From the above figures, it is clear that, as was the case for the simulation results the NCDiff$_{L1L2}$ method not only outperforms the non-coherent acquisition performed on L1 only but also the two other L1/L2 combining acquisitions proposed (see Figure 4-20, Figure 4-22 and Figure 4-24).

4.5 Conclusions for 1 ms coherent integration and 4 ms of incoming data

By combining the GPS signals transmitted in the L1 and L2 frequency bands, one does not only take advantage of L1 (higher signal power) and L2 (no need for data bit synchronization) but also improves the overall detection capability compared to using

only one signal. Of the three methods proposed to combine the L1 C/A and L2C signals at the acquisition level, two proved to systematically outperform the legacy L1 C/A non-coherent acquisition. The first method (NC_{L1L2}) combining the non-coherent acquisition on L1 and L2 showed promising performance with the proper weight applied on L2. Similarly, the $NCDiff_{L1L2}$ method combining non-coherent and differential acquisitions on L1 and L2 significantly improves the probability of properly detecting the signals. The $Diff_{L1L2}$ method combining differential acquisitions performed on L1 and L2 is strongly dependent on the residual Doppler frequency remaining after the Doppler removal process. Poor performance was observed when the residual Doppler error varies over the whole range of half a Doppler bin size defined by a 1 ms coherent integration (-333.33 Hz to 333.33 Hz). However, by limiting the Doppler error to 100 Hz, performances are strongly improved and the $Diff_{L1L2}$ method becomes preferable to the non-coherent L1 acquisition. As limiting the Doppler bins size means the possibility to increase the coherent integration time, this method is recommended for longer coherent integration. Finally, while the $NCDiff_{L1L2}$ method outperforms the non-coherent L1 acquisition, it also shows better performance than the other two combining methods. However, due to its complexity compared to the NC_{L1L2} method, one would employ it only when sufficient computation power is available.

4.6 Effect of the coherent integration time

In order to investigate the effect of changing the coherent integration time on the proposed L1/L2 combined acquisition method, similar experiments as for 1 ms coherent integration time are performed. As such, this section shows that the theoretical model still

holds when the coherent integration time is changed. Results are first presented through simulation and then through real data collection.

4.6.1 Results drawn from simulation

Once again, the correlator outputs are simulated using a similar process to the one described in Chapter 3. Table 4-3 defines the simulation parameters used to generate the L1 correlator outputs whereas Table 4-4 defines the simulation parameters used to generate the L2 correlator outputs. Note that only the coherent integration time used is changed with respect of the simulation process used for 1 ms coherent integration. The overall acquisition time being kept to 4 ms, one now uses $M=2$ in the combined acquisition scheme.

Table 4-3: Parameters used to simulate the L1 correlator outputs

Paremeter	Value
$C/N_{0\,L1}$	30 dB-Hz
T	2 ms
$\sigma_1{}^2$	equal to σ^2
$d_1(k)$	Random 1 or -1
Code Phase Step	1 / 4 chip
dt_1	Uniformly distributed between 0 and 1 / 8 chip
ΔF_1	Uniformly distributed between -166.66 Hz and 166.66 Hz
φ_1	Uniformly distributed between 0 and 2π

Table 4-4: Parameters used to simulate the correlator outputs for L2

Paramter	Value
$C/N_{0\,L2}$	$C/N_{0\,L1} - 1.5$
T	2 ms
σ_1^2	equal to twice σ^2
$d_2(k)$	Random 1 or -1
dt_2	$dt_1 + d_{iono}$
d_{iono}	Dependent on VTEC and Map
VTEC	Uniformly distributed between 10 TECU and 60TECU
Map	Dependent on elevation angle E
E	Uniformly distributed between 0° and 90°
ΔF_2	$\Delta F_1 \times f_2 / f_1$
φ_2	Uniformly distributed between 0 and 2π

ROC curves obtained for each method are shown in Figure 4-25. Note that the non-coherent acquisition method performed on L1 C/A only or L2 CM only as means of comparison uses four incoming milliseconds and a 2 ms coherent integration time.
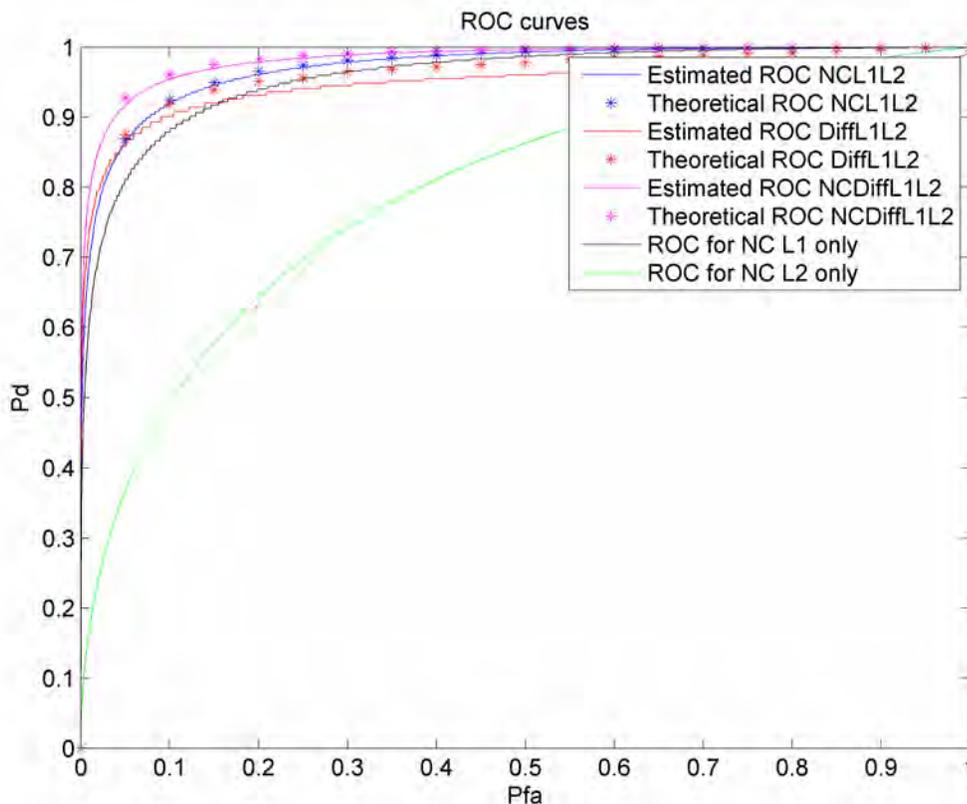
Figure 4-25: ROC curves of the combined method obtained through simulation process for a 2 ms coherent integration time

Note that the discrepancies observed for the Diff_{L1L2} are due to the fact that the theoretical model does not take into account the residual Doppler frequency error. This last point becomes even more evident through the use of real data as the Doppler error was kept at 50 Hz instead of ranging from -166.66 Hz to 166.66 Hz.

Figure 4-26 shows the difference between the estimated NC_{L1L2}, Diff_{L1L2} and NCDiff_{L1L2} ROC curves with the classic non-coherent integration acquisition on L1 only ROC curve. Analysis on the results is provided for both the simulation and real data cases in Section 4.6.3.
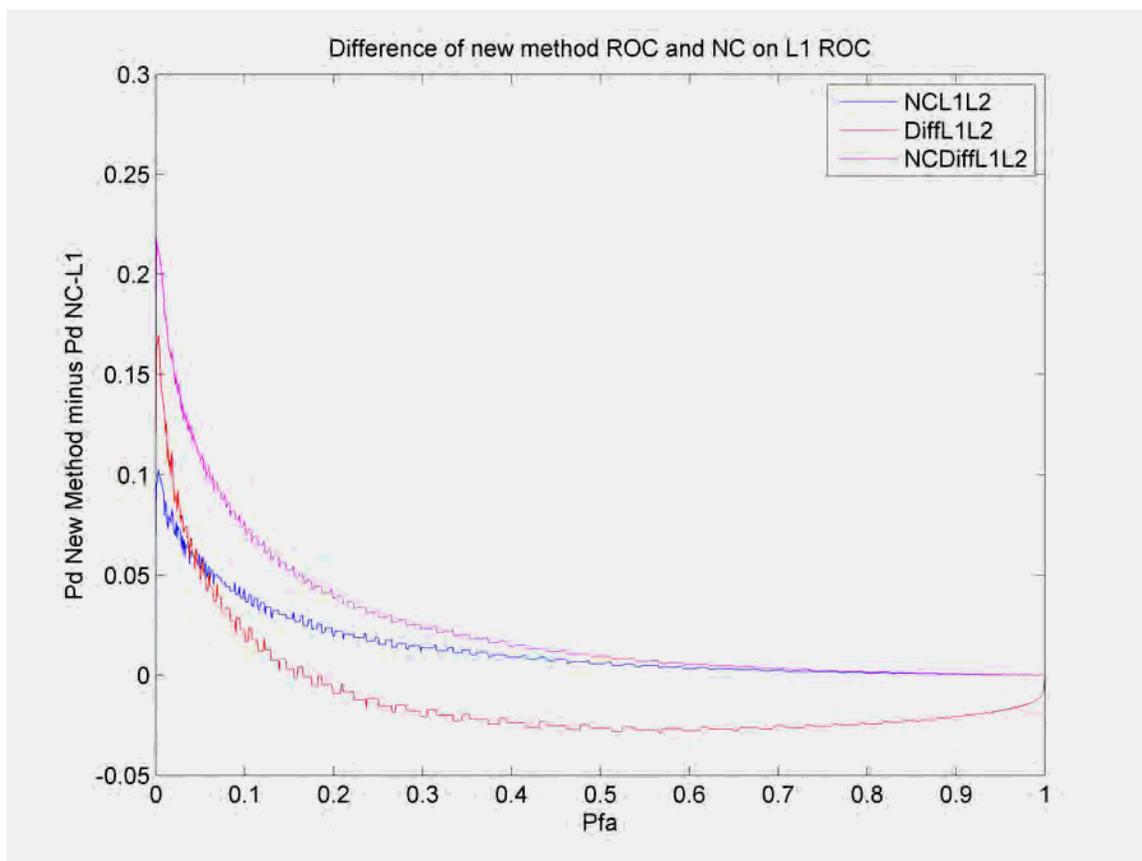
Figure 4-26: Difference between the new combined method ROC curves with the non-coherent acquisition on L1 ROC curve

4.6.2 Results from real data collection

The same set of real data used previously and obtained as shown in Figure 4-1 is used to generate the L1 and L2 correlator outputs with 2 ms coherent integration. Once again the overall acquisition time being kept at 4 ms, the post-correlation summation involved in the proposed acquisition schemes is composed of two terms ($M=2$).

As was the case for the simulation-based analysis, Figure 4-27 shows the different ROC curves obtained for each combined method. Note that the non-coherent acquisition

method performed on L1 C/A only or L2 CM only as means of comparison uses four incoming milliseconds and a 2 ms coherent integration time.
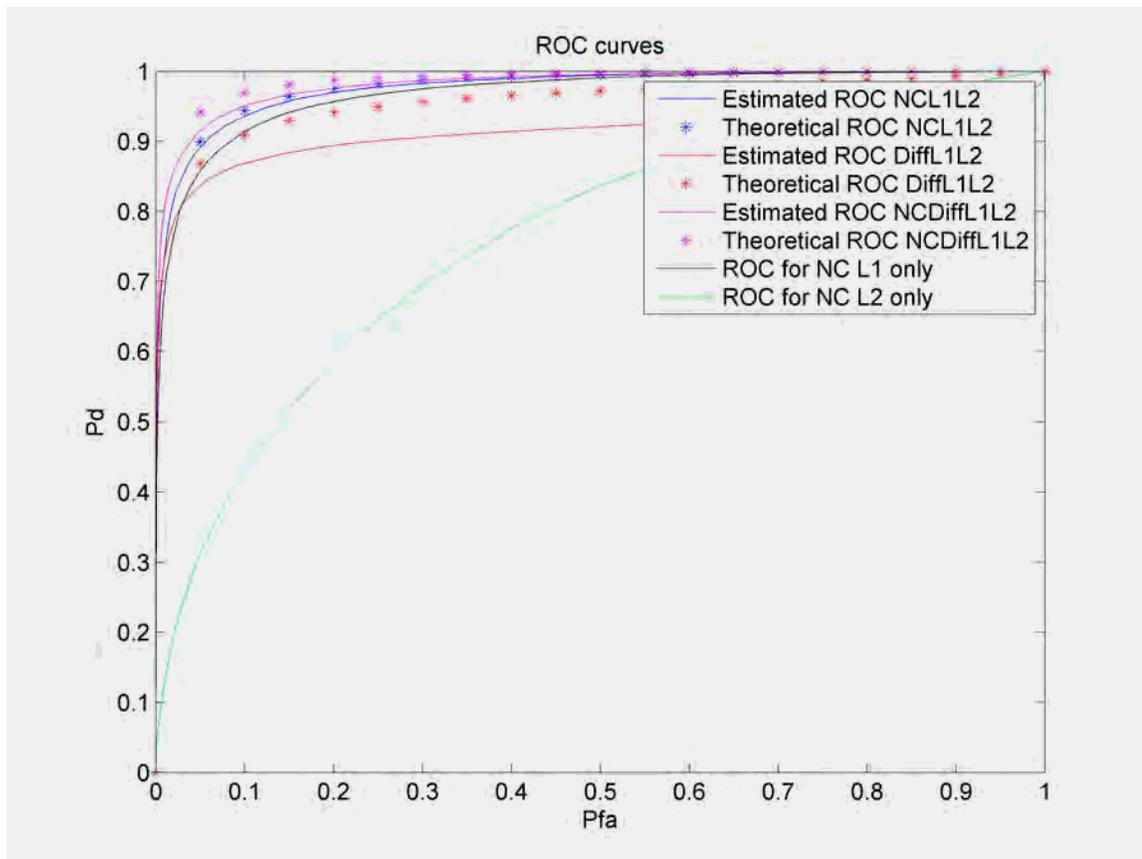
Figure 4-27: ROC curves of the combined method obtained through the use of real data for a 2 ms coherent integration time

Note that the divergence of the theoretical model ROC curves from the estimated ROC curves is due to the fact that the Doppler frequency error was not taken into account in the theory. Moreover, the divergence through the use of real data is greater than that observed with simulation. This comes from the fact that during the simulation process, the Doppler residual was uniformly distributed between -166.66 Hz and 166.66 Hz whereas it was fixed to 50 Hz while using real data.

Figure 4-28 shows the difference between the estimated NC_{L1L2}, $Diff_{L1L2}$ and $NCDiff_{L1L2}$ ROC curves with the classic non-coherent integration acquisition on L1 only ROC curve. Once again, analysis on the results is provided for both the simulation and real data cases in Section 4.6.3.
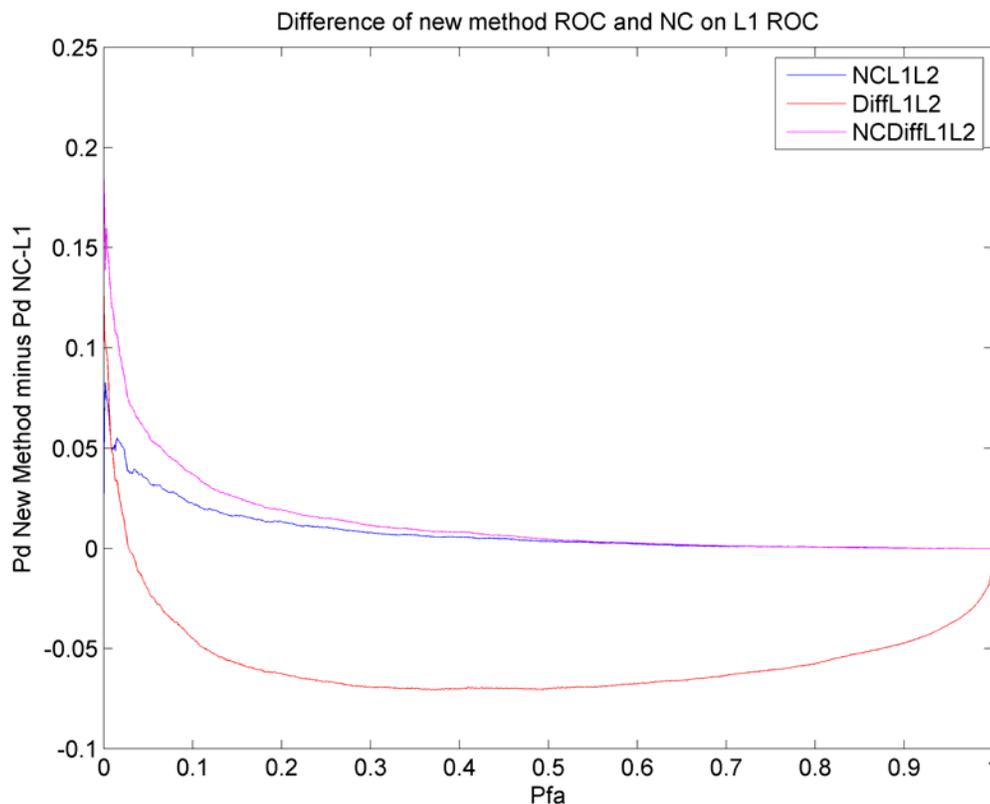
Figure 4-28: Difference between the new combined method ROC curves with the non-coherent acquisition on L1 ROC curve

4.6.3 Analysis and conclusions

As was the case with the 1 ms coherent integration case, combining the GPS signals transmitted in the L1 and L2 frequency bands allows to profit from the advantages of L1 (higher signal power) and L2 (no need for data bit synchronization), and also to improve the overall detection capability. Contrary to the 1 ms coherent integration case, the use of

2 ms coherent integration reduces the Doppler frequency error range enough such that the $Diff_{L1L2}$ method is no longer negatively affected by this error. As such, each of the three combined L1/L2 acquisition methods outperform the common non-coherent acquisition applied on L1 C/A only. The $NCDiff_{L1L2}$ method outperforms the non-coherent L1 acquisition and also shows better performance than the other two combining methods. Finally, due to the smaller range of Doppler error, the $Diff_{L1L2}$ method now outperforms the NC_{L1L2} combined acquisition scheme.

The possibility of acquiring GPS signals by combining signals transmitted at different frequencies brings an interesting improvement in the acquisition performance. The following chapters will take the matter to the next logical step and consider the possibility of L1/L2 inter-frequency combinations from a tracking point of view.

Chapter Five: Combined L1/L2 tracking scheme for weak signal environments

The next logical step following the acquisition method is to develop a method of dual frequency tracking. This chapter presents a new Kalman filter based tracking technique. First, the limitations of using a simple L1 aided L2 tracking technique are demonstrated. Then, a Kalman filter model is developed to track both L1 C/A and L2C signals concurrently while estimating a minimum number of parameters.

5.1 Motivations

GPS satellites are orbiting roughly 20,000 km above the surface of the Earth. As such, signals undergo a tremendous amount of free space loss before reaching the users. At the same time, signals have to go through the ionosphere and troposphere. Whereas all these difficulties were taken into account during the design of the system and as such the -158.5 dBW of the legacy L1 C/A signal is easily acquired and tracked by receivers under open sky conditions. Urban canyons and indoor environments add other challenges limiting the scope of the system.

Indeed, attenuation up to 25 dB or more can easily be encountered under those adverse conditions. Common solutions aiming to overcome these difficulties include a significant increase in the coherent integration time leading to the well known data bit transitions problem (Watson et al 2007). Indeed, as the L1 C/A signal carries the navigation message

at 50 Hz, one cannot use coherent integration time longer than 20 ms without using Assisted-GPS (use of external information to perform data wipe-off) or performing a data bit estimation technique. However, both techniques remain limited either by the availability of external information or the user motion and local oscillator stability.

In this research, a Kalman filter based method carrying the energy combination technique to the next stage by using both L1 C/A and L2C signals simultaneously in a combined tracking loop method to enhance performance under adverse conditions is presented.

This chapter is divided as follows:

- The ionospheric effect is described from a tracking point of view.

- The effects of the ionospheric errors described are shown through the tracking of real data. The tracking schemes presented are basic and used to highlight the ionospheric effects.

- A combined Kalman filter making used of both L1 C/A and L2 CM and CL codes is developed. This filter overcomes the ionospheric problem by estimating the TEC encountered on the signal path.

- The Kalman filter is then tested against simulated and real data, including under ionospheric scintillation.

5.2 Ionosphere and Tracking

When travelling through the ionosphere, the GPS signal is affected in two different ways. First, the code is delayed by a factor proportional to the inverse of the square of the transmitted frequency f and the total electron content (TEC, expressed in TEC units where 1 TEC unit = 10^{16} el/m^2) encountered on the signal path:

$$\tau_c = \frac{40.3}{cf^2} 10^{16} TEC \qquad \textbf{5-1}$$

with τ_c representing the code delay in seconds.

Second, an effect known as phase advance affects the carrier phase of the transmitted signal. The signal phase is advanced by the following factor in cycle (Skone 2007):

$$\varphi_p = \frac{40.3}{cf} 10^{16} TEC \qquad \textbf{5-2}$$

with c representing the speed of light.

Time differentiating Equation 5-2 directly leads to the formula of the frequency shift induced by the ionosphere:

$$f_D^i = \frac{d\phi_p}{dt} = \frac{40.3}{cf} 10^{16} \frac{dTEC}{dt}. \qquad \textbf{5-3}$$

From Equation 5-3, it is clear that the frequency shift induced by the ionosphere is related to the change of TEC encountered on the signal path. This change can come from an actual change of the TEC contained in the ionospheric layer or from the change of signal

path due to satellite motion. Under normal ionospheric conditions (no scintillation), the second effect is the most important.

It has been shown in Chapter 2 that the Doppler effect due to the relative motion on L1 f_{D1} can directly be related to the Doppler effect due to the relative motion on L2 f_{D2}:

$$f_{D1}^{motion} = \frac{f_1}{f_2} f_{D2}^{motion} \, .$$

<div align="right">5-4</div>

This is only true if one's definition of the Doppler effect only includes the relative motion between user and satellite. If one was to define the Doppler effect as the frequency shift from the transmitted frequency, this relation does not hold anymore. Indeed, the relationship between the ionosphere induced frequency shift is inverse to the above one:

$$f_{D1}^{iono} = \frac{f_2}{f_1} f_{D2}^{iono} \, .$$

<div align="right">5-5</div>

5.2.1 Tracking L1 and feeding it to L2

In order to illustrate these two effects, complex I and Q samples were collected under open sky conditions. Then the L1 C/A signal was used to track both L1 and L2 GPS signals, the principle being simply to track L1 and feeding the output parameters of the DLL and PLL tracking loop to L2 tracking. Figure 5-1 represents the equivalent PLL tracking loop used. A similar scheme could be drawn in terms of DLL tracking.
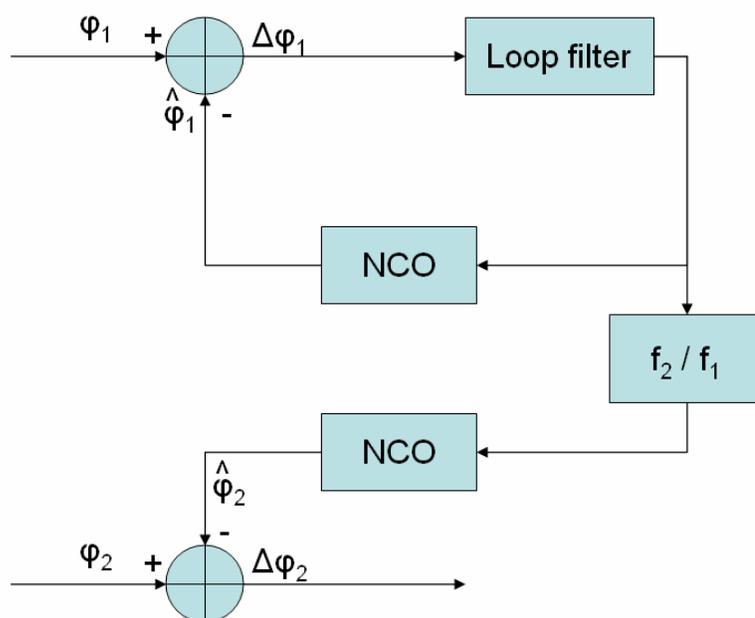
Figure 5-1: L1 PLL feeding L2 tracking

Figure 5-2 and Figure 5-3 show the results obtained using real data in terms of L1 and L2 code discriminator outputs and the L1 and L2 real parts of the prompt correlators, respectively.
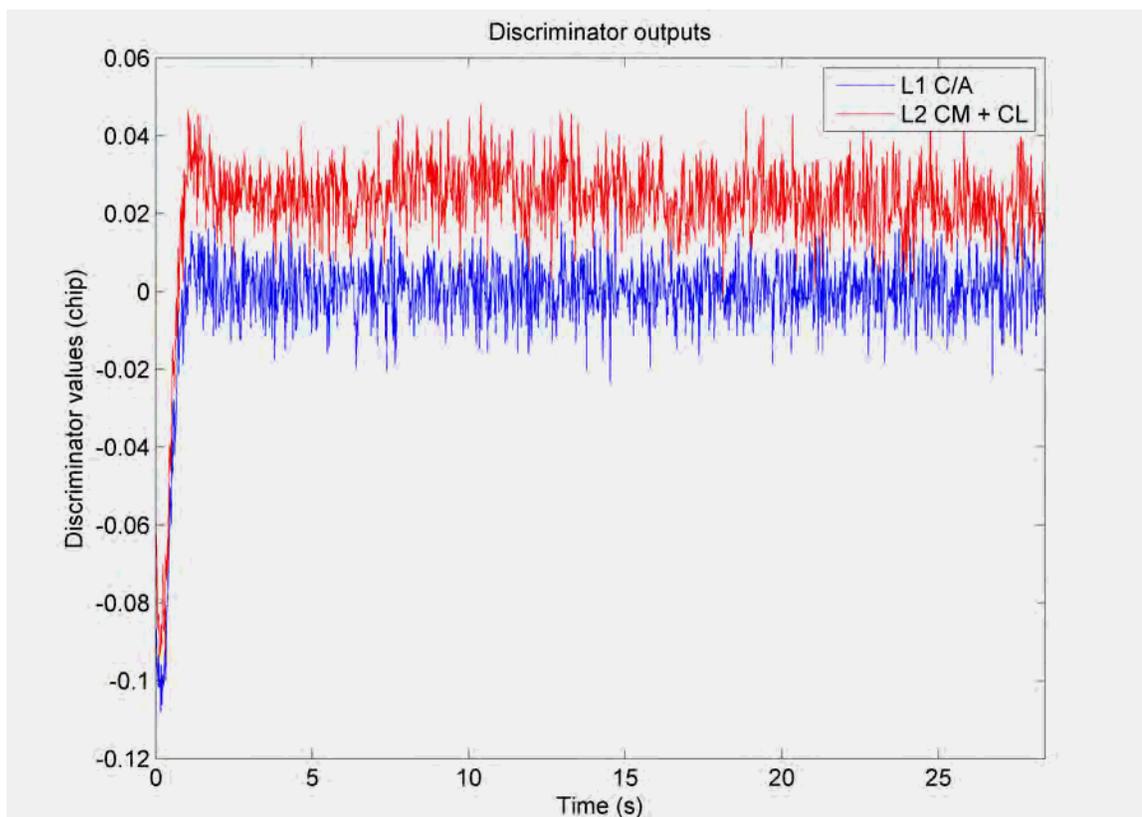
Figure 5-2: L1 and L2 code discriminator outputs

The code delay caused by the ionosphere can be easily seen in Figure 5-2 as the DLL discriminator output of the L2 signal shows an offset of about 0.02 chips. As such, in a common DLL scheme, this offset informs the DLL tracking loop that the local code used to track the signal is late compared to the incoming code and should be advanced by 0.02 chips.
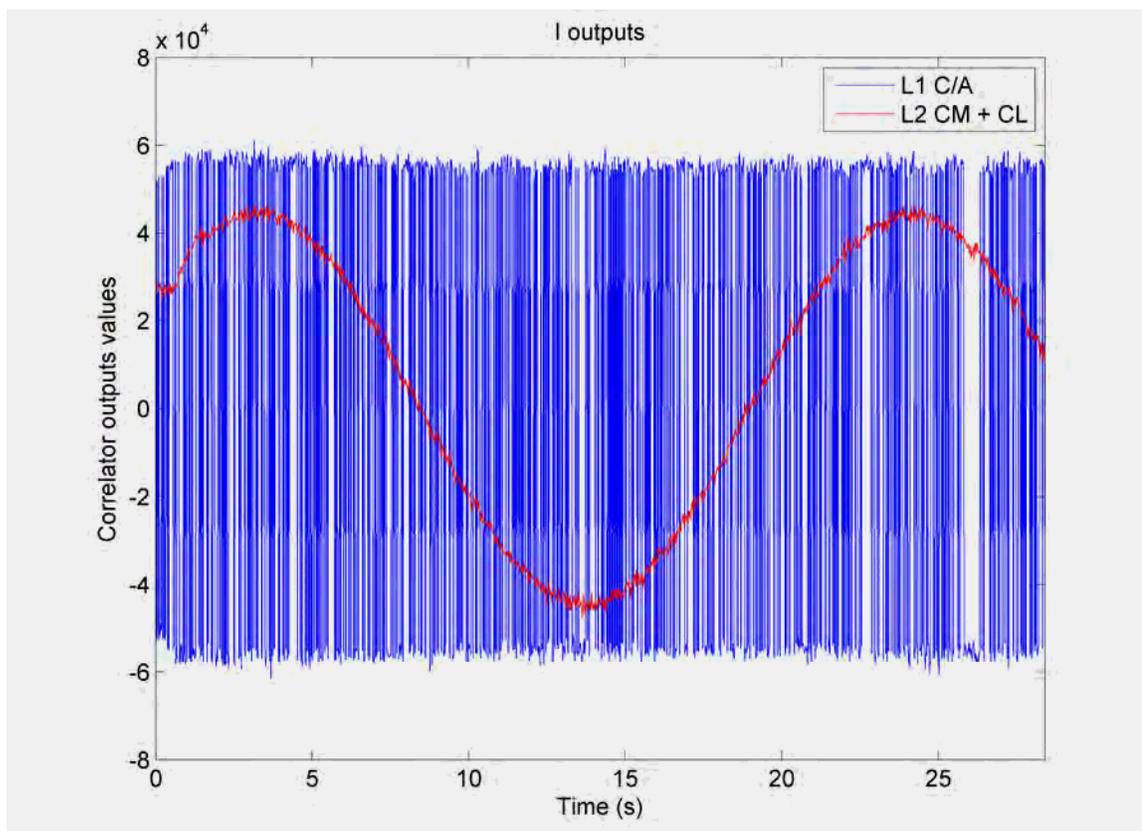
Figure 5-3: Output of the real part of the L1 and L2 prompt correlators

The phase advance phenomenon expected should be observable in Figure 5-3 as a lower amplitude for the real part of the prompt correlator on L2 compared to the one on L1. Indeed, the phase of the local carrier for L1 should be synchronized to the phase of the incoming carrier. However, due to the ionosphere induced phase difference between the L1 and L2 incoming signals, the phase of the local L2 carrier which is identical to the phase of L1, should have an offset with its incoming signal. As such, the visible effect would be that the L2 incoming signal power should be shared between the real and complex part of the L2 prompt correlator. However, the observed phenomenon is a residual carrier frequency error on the L2 signal. This last point is due to the fact that a simple phase shift would be observed only if the TEC encountered on the signal path

would not change over time. This does not hold as the satellite motion results in a change of signal path through the ionosphere. Therefore if one were to assume the ionosphere to be a layer between the satellite and the user, the TEC encountered by the signal would directly depend on the satellite elevation and change as the satellite is moving as shown in Figure 5-4. This change induces a change in the phase advance observed and as such, a frequency shift (Equation 5-3).
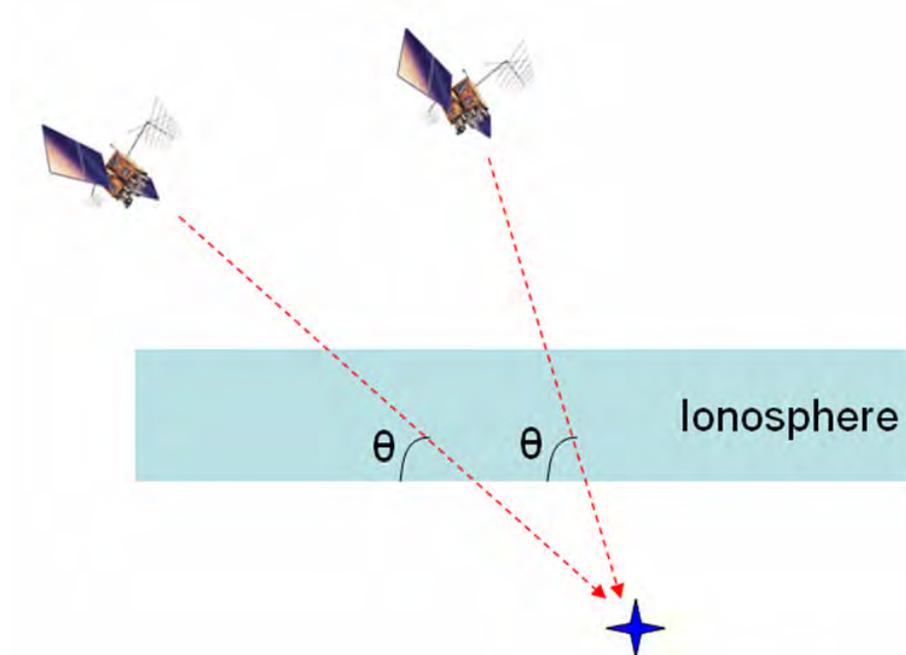
Figure 5-4: Effect of satellite motion on signal path through an ionospheric layer

5.2.2 Tracking L1 and using it as an aid to L2 tracking module

As shown in Figure 5-2 and Figure 5-3, tracking one of the two signals only and feeding the results of the tracking loop to the other deteriorates tracking performance. This effect would not be seen if one were to use a similar method for signals transmitted on the same frequency such as Galileo E1-B and E1-C.

In order to solve the ionospheric problem and be able to track both signals properly, one can either track them independently or use one to aid the other. In the following section, the possibility of using L1 C/A tracking loop to aid L2C is investigated but a similar analysis could be conducted with L2C aiding L1 C/A. The basic principle for the PLL is to track L2 while using the scaled Doppler frequency of L1 as aiding data as shown in Figure 5-5. A similar process is used for the DLL.
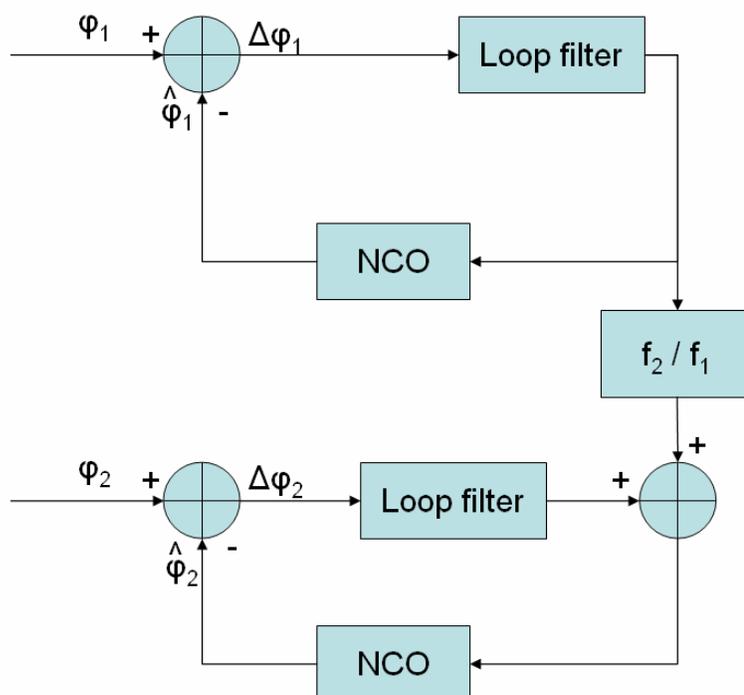
Figure 5-5: L1 PLL aiding L2 PLL
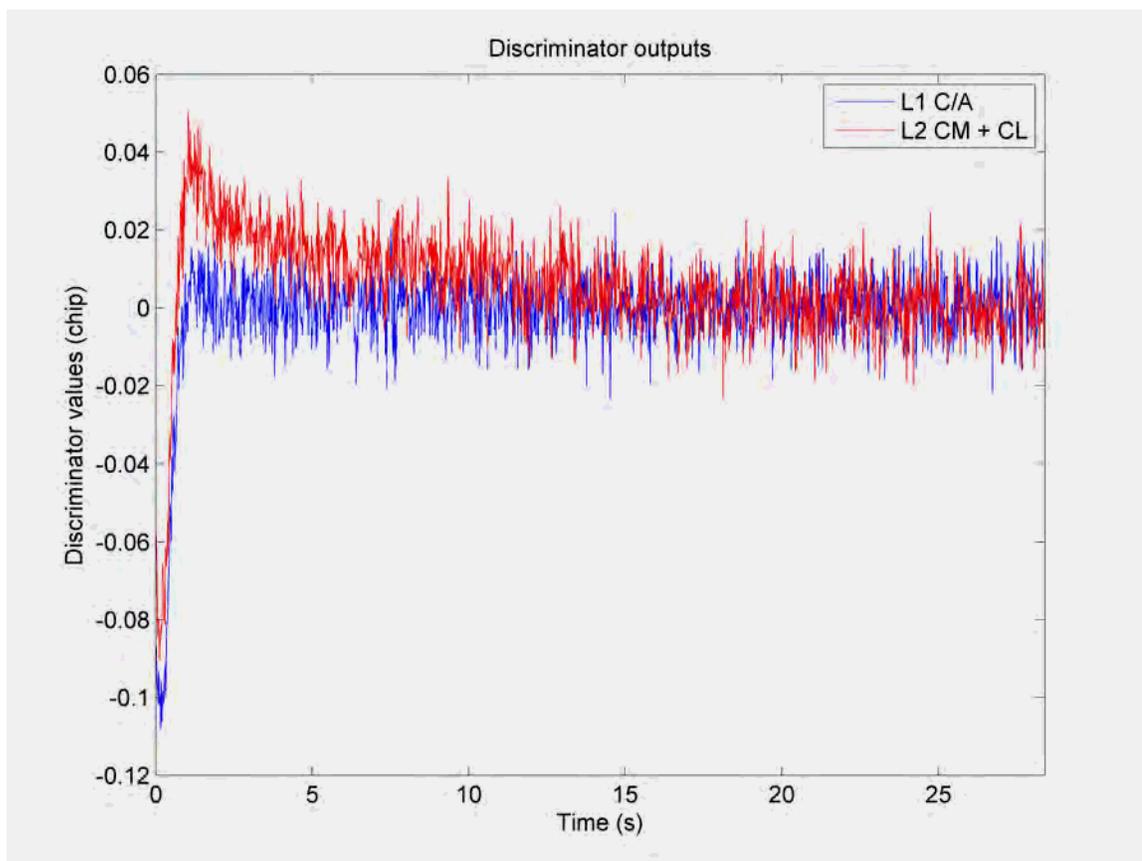
Figure 5-6: L1 aiding L2 DLL discriminator outputs

As shown in Figure 5-6, Figure 5-7 and Figure 5-8, performing aiding on L2 using the L1 signal overcomes the ionospheric phase shift and code delay problems observed previously. Indeed, the DLL discriminator of the L2 signal now converges toward zero and the real part of the prompt correlator remains constant. Note that the L2 DLL bandwidth was chosen such that the convergence period is long enough to be clearly visible on the above figure. In order to show that the ionospheric phase advance was completely removed, the real and complex parts of L2 prompt correlator are plotted in Figure 5-8 where it can be observed that the signal power is concentrated on the real part only. This last point demonstrates that the phase of the incoming L2 signal is tracked.
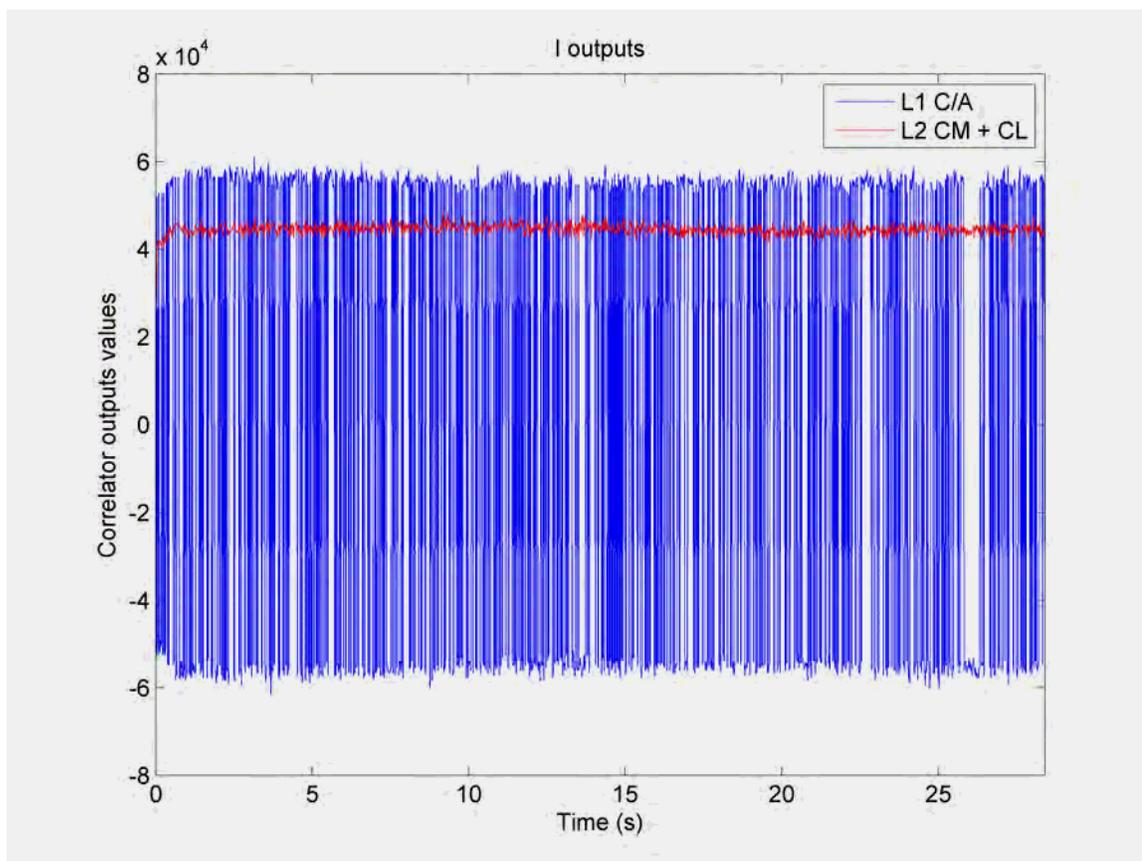
Figure 5-7: L1 aiding L2, real part of prompt correlator outputs

Unfortunately, while being able to overcome the difficulties created by the ionosphere, the aiding technique does not actually combine the two signals. Indeed, it only uses one to aid the other tracking. As such, the performance of the method is directly dependent on the signal offering the greatest power.
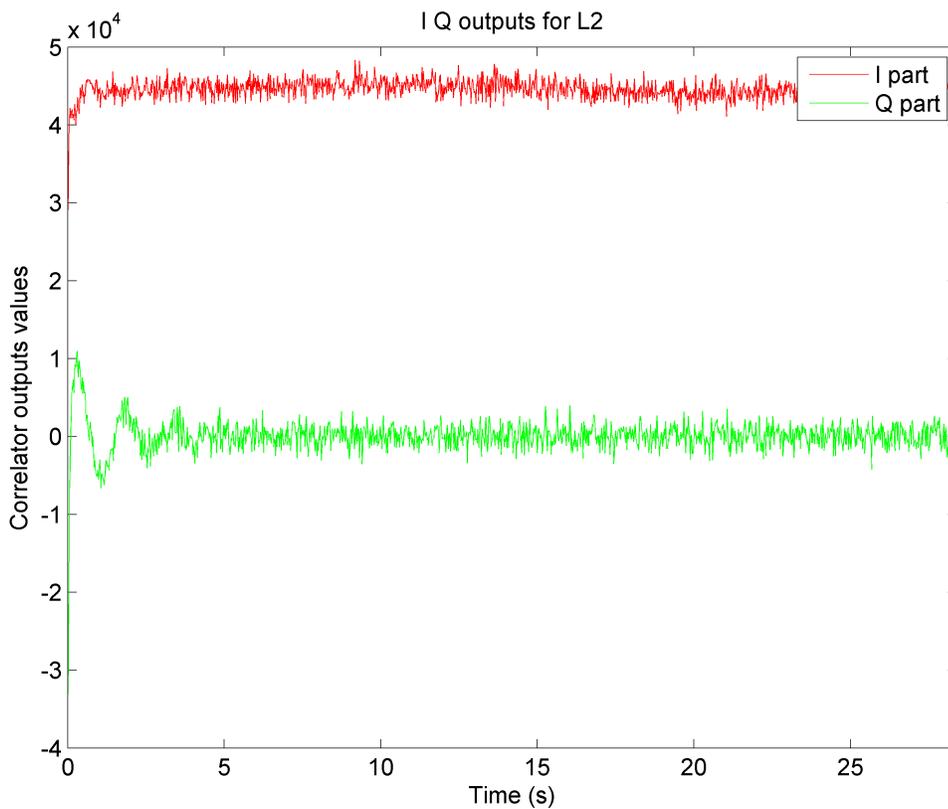
Figure 5-8: L1 aiding L2, real and complex parts of L2 prompt correlator output

A direct analogy of the aiding method would be the measurement of a distance using two different tape measures but instead of taking the mean of the measured distances, one would use the first measurement to correct the second. In the case at hand, L1 is used to aid the L2 tracking loop but the measurements of L2 are never used to aid L1. An actual combination of the two signals would use both L1 and L2 measurements to obtain a better estimate of the desired quantities.

5.3 Development of a Kalman filer based combined L1/L2 tracking

The Kalman filter developed in this research operates after the L1 and L2 code discriminator outputs and phase discriminator outputs have been computed. The goal of these discriminators is to estimate the L1 and L2 phase errors and code errors of the local signal replicas. The L1 and L2 discriminator outputs are then linked together through the designed Kalman filter to estimate the parameters needed to track both L1 and L2 signals as shown in Figure 5-9. Using the discriminator outputs as inputs of the Kalman filter was first presented by Groves et al (2007) in the context of deep integration of GPS/INS and called a non-coherent architecture.
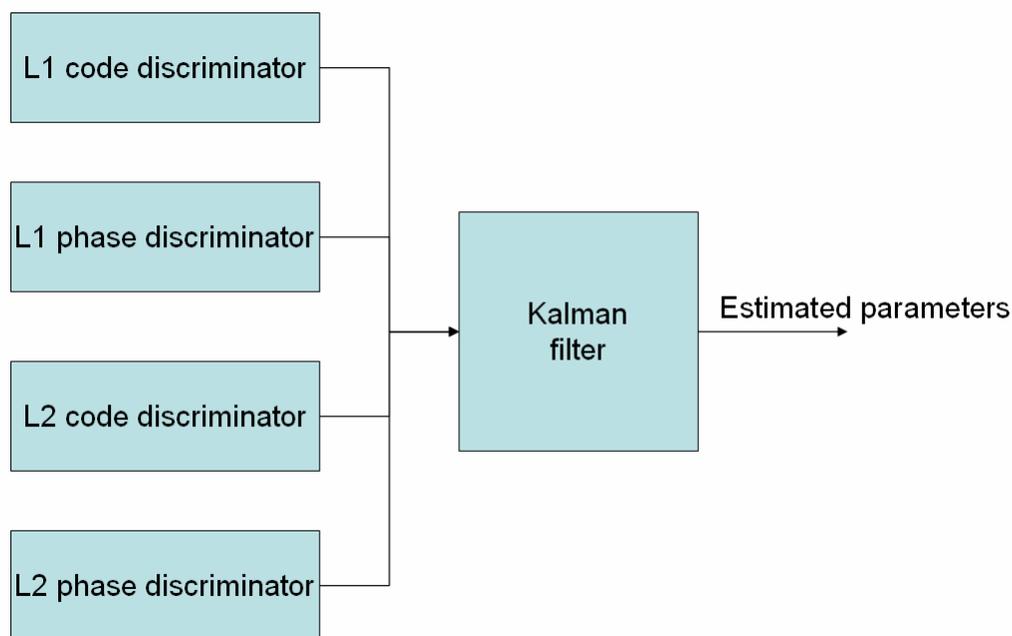
Figure 5-9: Principle of proposed Kalman filter based tracking method

5.3.1 Derivation of the observation model

5.3.1.1 Use of the phase discriminator outputs

Before describing the parameters estimated, it is important to note that the relationship between phase and TEC is:

$$\varphi = \phi + \frac{40.3}{cf}10^{16}TEC \qquad\qquad \text{5-6}$$

with φ being the total signal phase in cycles and ϕ representing the phase in cycles that would be measured if no ionospheric effect was present (i.e. the phase variation in range between the satellite and user).

As such, the total phase variation between two epochs is

$$\delta\varphi = \delta\phi + \frac{40.3}{cf_1}10^{16}\delta TEC . \qquad\qquad \text{5-7}$$

Assuming that one has achieved phase lock on the signal the quantity represented in Equation 5-7 can then be directly related to the average phase error between two coherent integrations, i.e. the output of the phase discriminator $\delta\hat{\varphi}$. Therefore if one were to use the *atan* discriminator due to its convenient auto-normalization properties, this last point can be summarized as

$$\delta\varphi = E(\delta\hat{\varphi}) = E(atan\left(\frac{Q_P}{I_P}\right))/2\pi . \qquad\qquad \text{5-8}$$

The *atan* discriminator has its output limited to the interval $[-\pi/2 \; ; \; \pi/2]$. As such, $\delta\hat{\varphi}$ being expressed in cycles is limited to $[-1/4 \; ; \; 1/4]$. However, the purpose of the discussion at hand is to keep the coherent integration time lower than 20 ms in order to avoid the need for data bit estimation or assistance data. As such, even if an error of 10 Hz in the Doppler frequency was made and a 50 vertical TEC was observed, the error created due to the Doppler frequency would be 1.25 rad and the change in phase due to the TEC would be about 3.10^{-3} rad. Therefore, the total phase error would still be within the interval $[-\pi/2 \; ; \; \pi/2]$.

Finally, by noticing that the average phase variation due to motion is directly related to the Doppler, one can write:

$$\delta\phi_1 = \frac{f_1}{f_2} \delta\phi_2 .$$

5-9

Therefore by rewriting Equations 5-7 to 5-9 for the L1 and L2 signals, the following relationship can be obtained and used as a measurement model to estimate the phase change on L2 due to motion and the variation in TEC encountered on the signal path:

$$\begin{bmatrix} \delta\hat{\varphi}_1 \\ \delta\hat{\varphi}_2{}^{CM} \\ \delta\hat{\varphi}_2{}^{CL} \end{bmatrix} = \begin{bmatrix} \dfrac{f_1}{f_2} & 1 \\ 1 & \dfrac{f_1}{f_2} \\ 1 & \dfrac{f_1}{f_2} \end{bmatrix} \begin{bmatrix} \delta\phi_2 \\ \delta iono_{L1}^{P} \end{bmatrix} \rightarrow Z = HX$$

5-10

with $\delta iono_{L1}^{P} = \dfrac{40.3}{cf_{1}} 10^{16} \delta TEC$ and $\delta\varphi_{2}$ expressed in cycles. The superscript P is used to

indicate that the estimated ionospheric effect comes from the phase discriminators

outputs and as such is limited to [-1/4 ; 1/4].

In order to use the phase discriminator outputs properly in a Kalman filter, the

corresponding covariance matrix of the measurements C must be computed. As L1 and

L2 are transmitted on different frequency bands, the noise corrupting the discriminator

output on each frequency is independent. Similarly, as the L2 CM and CL codes are

orthogonal, the noise corrupting the phase discriminator outputs for the CM and CL

codes is uncorrelated:

$$C_{Z} = \begin{bmatrix} \sigma_{\delta\hat{\varphi}_{1}}{}^{2} & 0 & 0 \\ 0 & \sigma_{\delta\hat{\varphi}_{2}{}^{CM}}{}^{2} & 0 \\ 0 & 0 & \sigma_{\delta\hat{\varphi}_{2}{}^{CL}}{}^{2} \end{bmatrix}. \qquad \textbf{5-11}$$

However, computing the variance of the *atan* discriminator proves to be challenging.

Another approach proposed is to compute the variance of the simpler *I.Q* discriminator

and compare it to the variance of the *atan* discriminator obtained through a Monte-Carlo

simulation.

As shown in Appendix A, the expected value and variance of the *I.Q* discriminator can be

expressed as

$$E(\delta\hat{\varphi}) = E(\dfrac{I_{P}Q_{P}}{2\pi}) = E(atan\left(\dfrac{Q_{P}}{I_{P}}\right)/2\pi) = \delta\varphi \qquad \textbf{5-12}$$

$$var(\delta\hat{\varphi}) = \sigma_{\delta\hat{\varphi}}^2 = \frac{1}{4\pi^2}\left(\sigma_N^2 + \sigma_N^4\right)$$

with $\sigma_N^2 = \dfrac{1}{2\dfrac{C}{N_0}T}$ and T being the coherent integration time.

Once the theoretical value of the variance of the *I.Q* discriminator was computed, a Monte-Carlo simulation was conducted and the variance of the *I.Q* and *atan* discriminators was obtained and compared to the theory as a function of the C/N_0. The results shown in Figure 5-10 demonstrate that the theoretical variance for the *I.Q* discriminator matchs perfectly the Monte-Carlo simulation.
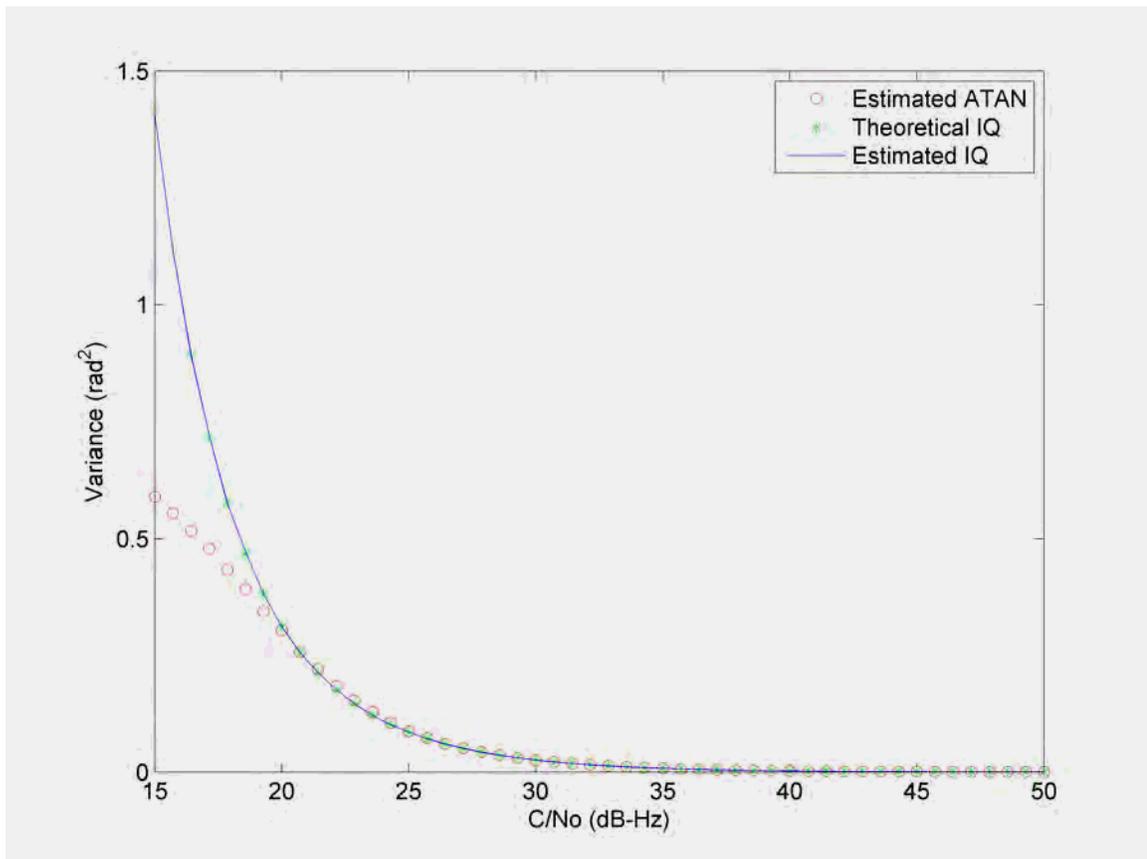
Figure 5-10: Variance of the *I.Q* and *atan* discriminator as a function of C/N₀

Moreover, Figure 5-11 shows the difference between the theoretical variance of the *I.Q*

discriminator and the simulated variance of the *atan* discriminator and illustrates that for

C/N_0 higher than 20 dB-Hz, an atan discriminator can be approximated as an I.Q

discriminator.
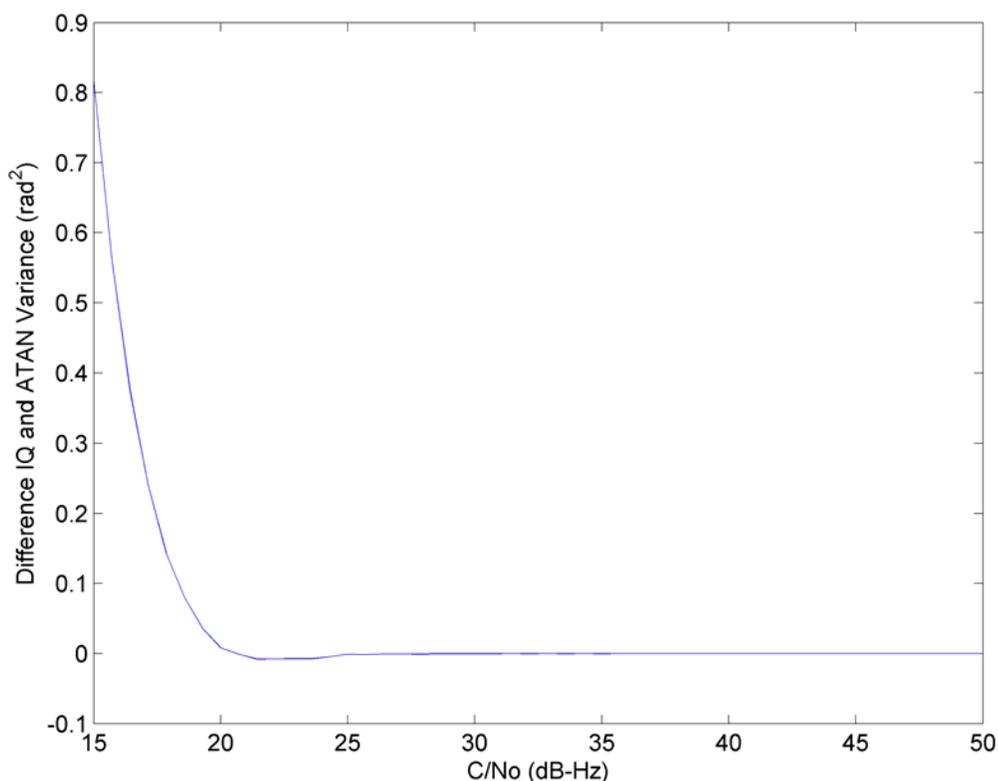
Figure 5-11: Difference between the theoretical variance of *I.Q* and Monte-Carlo variance of *atan* discriminator as a function of C/N$_0$

Finally, it is important to note that the Kalman filter is optimal for a symmetric noise

distribution (Gelb 1974). As such, an approximation of the noise corrupting the *atan*

discriminator by a Gaussian distribution of mean $\delta\hat{\varphi}$ and variance $\sigma_{\delta\hat{\varphi}}^2$ is used. In order

to verify the validity of such an approximation, the cumulative distribution functions

(CDFs) of the *atan* discriminator values, obtained through the Monte-Carlo simulation,

are plotted for different values of C/N$_0$ and compared to the corresponding Gaussian noise CDFs in Figure 5-12.
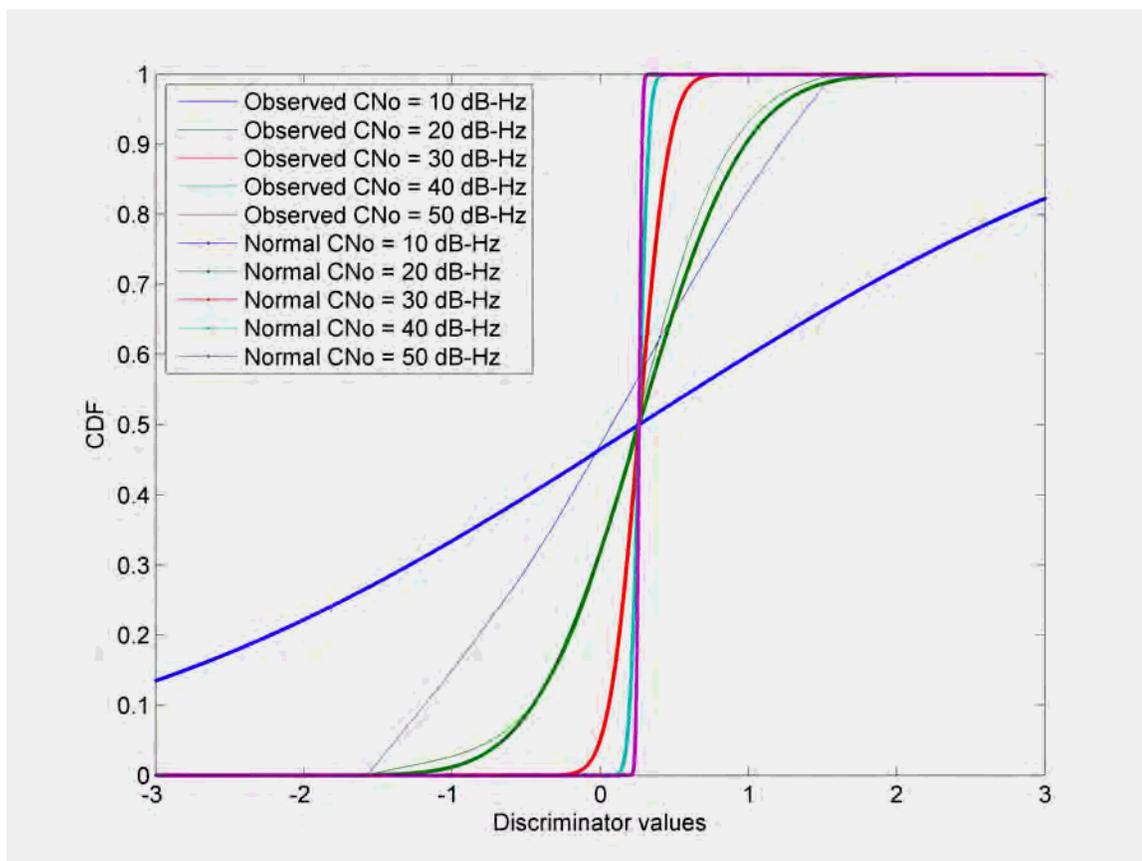
Figure 5-12: CDF of *atan* noise obtained through Monte-Carlo simulation and Gaussian noise approximation for different C/N$_0$ values

Figure 5-13 displays the difference between the CDFs obtained from the Gaussian approximation and the CDFs obtained through Monte-Carlo simulations for different C/N$_0$ values. The obtained results show that the approximation of the noise corrupting the *atan* discriminator by a Gaussian distribution holds for C/N$_0$ values above 20 dB-Hz.
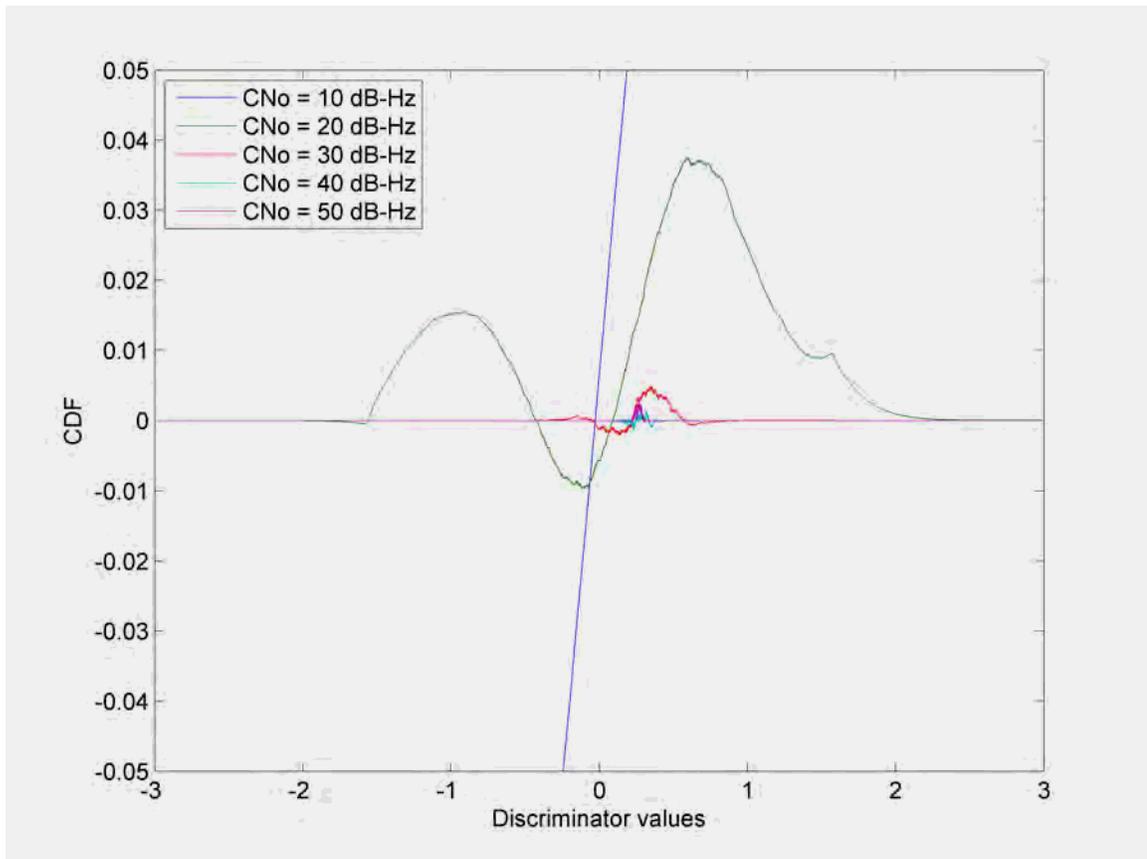
Figure 5-13: Difference between CDF of *atan* noise obtained through Monte-Carlo simulation and Gaussian noise approximation for different C/N$_0$ values

5.3.1.2 Including the code discriminator outputs

In order to track the signal, one must not only estimate the phase error through the phase discriminator output but also the code error through the code discriminator output. This section shows how the L1 and L2 code discriminator outputs can be related between themselves and the ionospheric effect. Indeed, like the phase discriminator, the code discriminator can be related to the phase error due to motion and the TEC variation.

First of all, one can express the relationship between the code delay, the range and the ionospheric variations for L1 and L2 as:

$$\delta\tau_{L1} = \delta d - \frac{f_c}{f_1}\delta iono_{L1}{}^P - \frac{f_c}{f_1}\delta iono_{L1}{}^C \qquad \text{5-14}$$

$$\delta\tau_{L2} = \delta d - \frac{f_c f_1}{f_2^{\,2}}\delta iono_{L1}{}^P - \frac{f_c f_1}{f_2^{\,2}}\delta iono_{L1}{}^C \qquad \text{5-15}$$

$\delta\tau$ being the total change in code delay between two epochs in chips, δd (chip) the change in code delay due to motion only, f_c the chipping rate. The total ionospheric effect expressed in cycles is

$$\delta iono_{L1}{}^P + \delta iono_{L1}{}^C = \frac{40.3}{cf_1}10^{16}\,\delta TEC . \qquad \text{5-16}$$

and represents the phase advance created by the ionosphere. The total effect is broken in two different parts namely $\delta iono_{L1}{}^P$ and $\delta iono_{L1}{}^C$. $\delta iono_{L1}{}^P$ represents the ionospheric effect as it can be detected by the phase discriminator. As such, $\delta iono_{L1}{}^P$ is in the interval [-1/4 ; 1/4] cycles and can only observe a fractional part of the ionospheric effect. In order for the filter to be able to observe changes in the ionospheric effect possibly larger than 1/4 cycles, the second term $\delta iono_{L1}{}^C$ is introduced. $\delta iono_{L1}{}^C$ represents the remainder of the difference of the total ionospheric effect with $\delta iono_{L1}{}^P$. As such, $\delta iono_{L1}{}^C$ permits to solve for the ambiguity in the ionospheric effect brought forth by $\delta iono_{L1}{}^P$. Unlike the phase discriminator, the code discriminator is able to observe the total effect induced by the ionosphere is not limited (it actually is limited by the correlator spacing but this parameter is large enough to contain the whole effect). Note that, even if the ionospheric effect does not change enough from one epoch to another to

leave the interval [-1/4 ; 1/4] cycles, $\delta iono_{L1}{}^C$ would still be included in order to correct for the initial relative code delay and phase advance between L1 and L2 induced by the ionosphere.

Similarly to the phase variation, the code variation can be related to the code discriminator as long as code lock was approximately achieved (i.e. after the acquisition process). Therefore, using the popular normalized early-minus-late envelope, the following equations can be written:

$$\delta\hat{\tau} = \left(1 - \Delta_{EL}/2\right)\frac{\sqrt{I_E^2 + Q_E^2} - \sqrt{I_L^2 + Q_L^2}}{\sqrt{I_E^2 + Q_E^2} + \sqrt{I_L^2 + Q_L^2}} \text{ (chip)} \qquad \textbf{5-17}$$

where Δ_{EL} is the distance between the early and late discriminator in chips also referred as early-late spacing. As such, $E(\delta\hat{\tau}) = \delta\tau$.

Therefore using Equations 5-10, 5-14, 5-15 and 5-17, a model making use of both phase and code discriminators can be derived, namely

$$
\begin{bmatrix} \delta\hat{\varphi}_1 \\ \delta\hat{\varphi}_2{}^{CM} \\ \delta\hat{\varphi}_2{}^{CL} \\ \delta\hat{\tau}_1 \\ \delta\hat{\tau}_2{}^{CM} \\ \delta\hat{\tau}_2{}^{CL} \end{bmatrix} = \begin{bmatrix} \dfrac{f_1}{f_2} & 0 & 1 & 0 \\[2mm] 1 & 0 & \dfrac{f_1}{f_2} & 0 \\[2mm] 1 & 0 & \dfrac{f_1}{f_2} & 0 \\[2mm] 0 & 1 & -\dfrac{f_c}{f_1} & -\dfrac{f_c}{f_1} \\[2mm] 0 & 1 & -\dfrac{f_c f_1}{f_2{}^2} & -\dfrac{f_c f_1}{f_2{}^2} \\[2mm] 0 & 1 & -\dfrac{f_c f_1}{f_2{}^2} & -\dfrac{f_c f_1}{f_2{}^2} \end{bmatrix} \begin{bmatrix} \delta\phi_2 \\ \delta d \\ \delta iono_{L1}^{P} \\ \delta iono_{L1}^{C} \end{bmatrix}.
$$

5-18

As the code frequency is identical on L1 and L2, the code delays differ only by the ionospheric effect (no scale factor is required).

As the measurement vector now includes the code discriminator outputs, the covariance matrix C_Z of the measurements becomes more complicated as one now needs to compute the variance of the code discriminator as well as the covariance between the code and phase discriminator in addition to the phase discriminator variance. Any covariance between L1 and L2 discriminator remains null as the noise on L1 is independent of the noise on L2. Similarly, as the CM and CL codes are orthogonal, any covariance between them is null:

$$C_Z = \begin{bmatrix} \sigma_{\delta\hat{\varphi}_1}^{\;2} & 0 & 0 & \sigma_{\delta\hat{\varphi}_1,\delta\hat{\tau}_1} & 0 & 0 \\ 0 & \sigma_{\delta\hat{\varphi}_2^{CM}}^{\;2} & 0 & 0 & \sigma_{\delta\hat{\varphi}_2^{CM},\delta\hat{\tau}_2^{CM}} & 0 \\ 0 & 0 & \sigma_{\delta\hat{\varphi}_2^{CL}}^{\;2} & 0 & 0 & \sigma_{\delta\hat{\varphi}_2^{CL},\delta\hat{\tau}_2^{CL}} \\ \sigma_{\delta\hat{\varphi}_1,\delta\hat{\tau}_1} & 0 & 0 & \sigma_{\delta\hat{\tau}_1}^{\;2} & 0 & 0 \\ 0 & \sigma_{\delta\hat{\varphi}_2^{CM},\delta\hat{\tau}_2^{CM}} & 0 & 0 & \sigma_{\delta\hat{\tau}_2^{CM}}^{\;2} & 0 \\ 0 & 0 & \sigma_{\delta\hat{\varphi}_2^{CL},\delta\hat{\tau}_2^{CL}} & 0 & 0 & \sigma_{\delta\hat{\tau}_2^{CL}}^{\;2} \end{bmatrix}. \qquad \textbf{5-19}$$

Regarding the code discriminator variance, an approach similar to that for the computation of the phase discriminator variance is taken. An approximation is made that the normalized early minus late discriminator has the same properties as the early minus late power discriminator. Then the equivalence is verified through a Monte-Carlo simulation. The early minus late power discriminator is expressed as (Ward 2006)

$$\frac{1}{2(2-\Delta_{EL})}\left[I_E^2 + Q_E^2 - \left(I_L^2 + Q_L^2\right)\right]. \qquad \textbf{5-20}$$

Through the computation described in Appendix B, it can be shown that

$$E\left[\frac{1}{2(2-\Delta_{EL})}\left[I_E^2 + Q_E^2 - \left(I_L^2 + Q_L^2\right)\right]\right]$$
$$= E\left[(1-\Delta_{EL})\frac{\sqrt{I_E^2+Q_E^2}-\sqrt{I_L^2+Q_L^2}}{\sqrt{I_E^2+Q_E^2}+\sqrt{I_L^2+Q_L^2}}\right] = E(\delta\hat{\tau}) = \delta\tau \qquad \textbf{5-21}$$

and

$$var(\delta\hat{\tau}) = \sigma_{\delta\hat{\tau}}^2$$
$$= \sigma_w^2\left[1/2 + \frac{2\delta\tau^2}{(2-\Delta_{EL})^2} - (1-\Delta_{EL})\left(1/2 - \frac{2\delta\tau^2}{(2-\Delta_{EL})^2}\right)\right] + 2\sigma_w^4\frac{\Delta_{EL}}{2-\Delta_{EL}}. \qquad \textbf{5-22}$$

By assuming that lock was achieved and $\Delta_{EL} = 0.1$ such that $\delta\tau$ is small, the following simplified expression can be obtained assuming $\delta\tau \approx 0$:

$$var(\delta\hat{\tau}) = \sigma_{\delta\hat{\tau}}^2 = \sigma_w^2 \Delta_{EL} + 2\sigma_w^4 \frac{\Delta_{EL}}{2 - \Delta_{EL}}.$$ **5-23**

Figure 5-14 shows the effect of assuming that $\delta\tau = 0$ when computing the variance when the actual error is $\delta\tau \neq 0$. It assumes the use of a one chip spacing between the early and late correlators. As such, the maximum error is 0.5 chips.
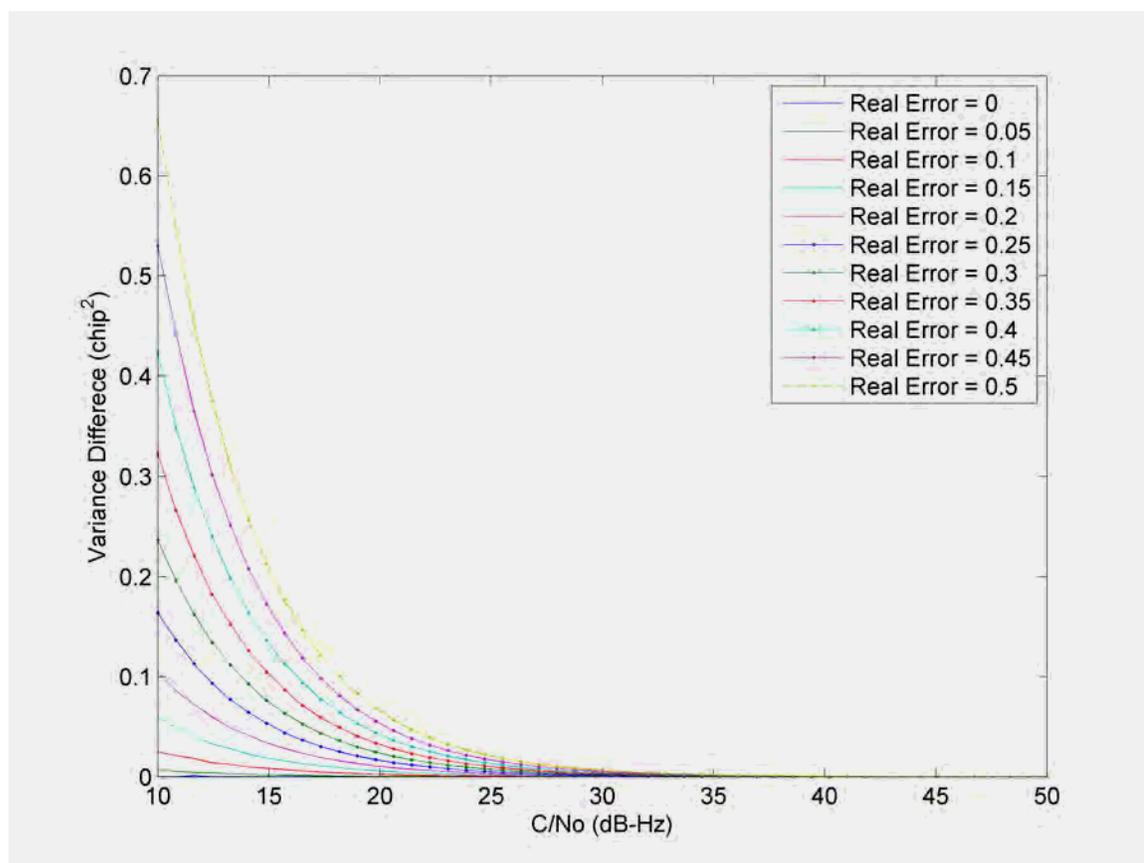
Figure 5-14: Effect of assuming that the code error is zero when estimating the variance of the early minus late power discriminator

As the real code error $\delta\tau$ becomes greater, the error affecting the estimate of the early minus late power discriminator output variance increases. However, for small values of $\delta\tau$ the error introduced in the discriminator variance is negligible. As such, if one were to use an early-late correlator spacing of 0.1 chips, the maximum error would be 0.05 chips and the resulting error on the estimated variance would become negligible. Such early-late spacing is commonly referred as narrow correlator and was developed by NovAtel in 1992. Apart from solving the problem at hand, the narrow correlator technology also results in better performance in terms of multipath mitigation (Van Dierendonck et al 1992).

In order to verify that one can approximate the variance of the normalized early minus late envelope discriminator by the early minus late power discriminator, a Monte-Carlo simulation was conducted to obtained their respective variances and compare them to the theoretical value computed as shown in Figure 5-15. Note that, whereas the code delay introduced in the simulation is 0.05 chips and the early late spacing is 0.1 chips, the code delay is assumed to be null when computing the discriminator variance using in the theoretical variance formula of Equation 5-23. As shown in Figure 5-14, even though the zero code delay approximation was made in the computation of the theoretical variance, the discrepancy with the Monte-Carlo simulation variance of the early minus late power discriminator is negligible.
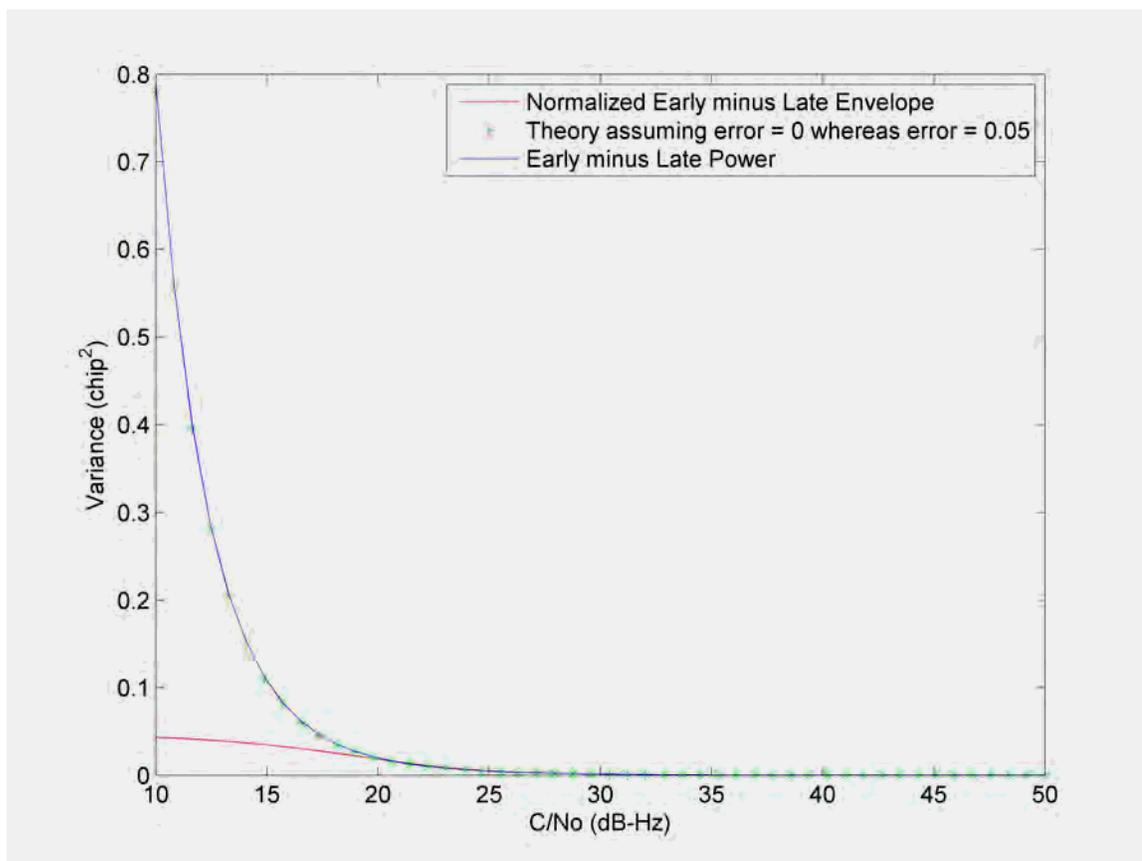
Figure 5-15: Variance of the early minus late power and normalized early minus late envelope discriminator as a function of the C/N_0

Figure 5-16 shows the difference between the theoretical variance of the early minus late power discriminator and the variance of the normalized early minus late envelope discriminator obtained through a Monte-Carlo simulation. It illustrates that for C/N_0 values greater than 20 dB-Hz, the approximation between the two discriminators holds.
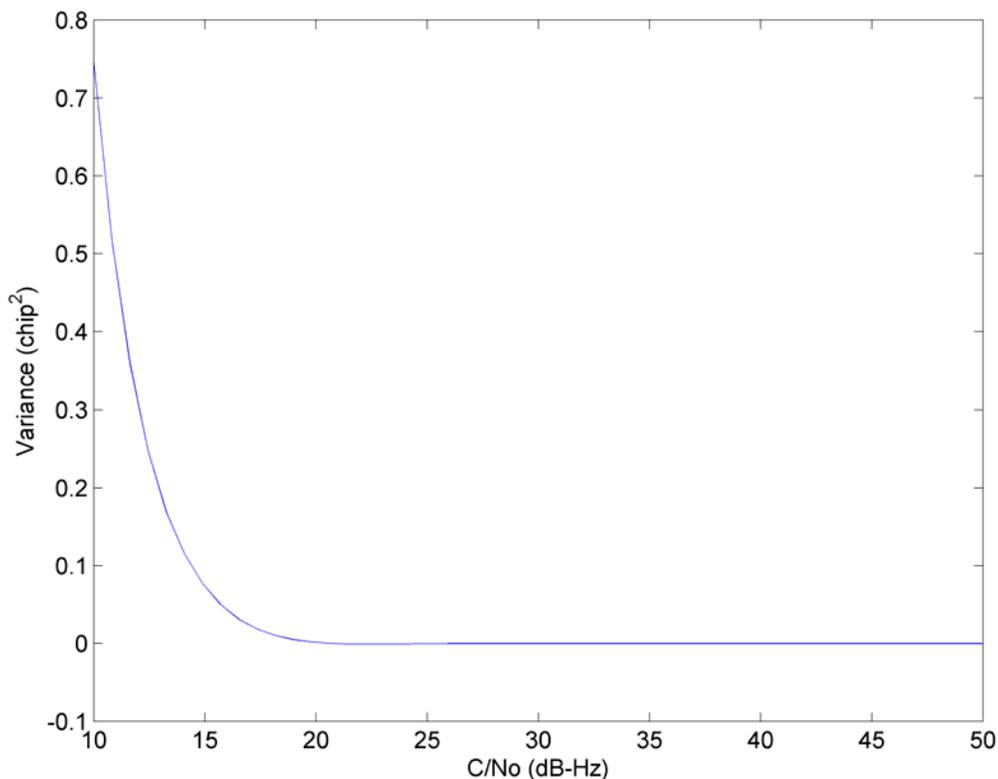
Figure 5-16: Difference between theoretical variance of the early minus late power and Monte-Carlo variance of the normalized early minus late envelope discriminator as a function of the C/N_0

Regarding the covariance of the phase *atan* discriminator and the normalized early minus late envelope discriminator, the computation of a specific theoretical value proves to be especially difficult as the approximation of these discriminators by the *I.Q* and early minus late power discriminators does not hold for the covariance. This last point is shown in Figure 5-17 where the covariance of both pairs of discriminators was determined through a Monte-Carlo simulation. However, the inability to determine a theoretical value is not of great concern as the Monte-Carlo simulation also shows that the covariance of the *atan* and normalized early minus late envelope discriminators is negligible for C/N_0 values greater than 20 dB-Hz.
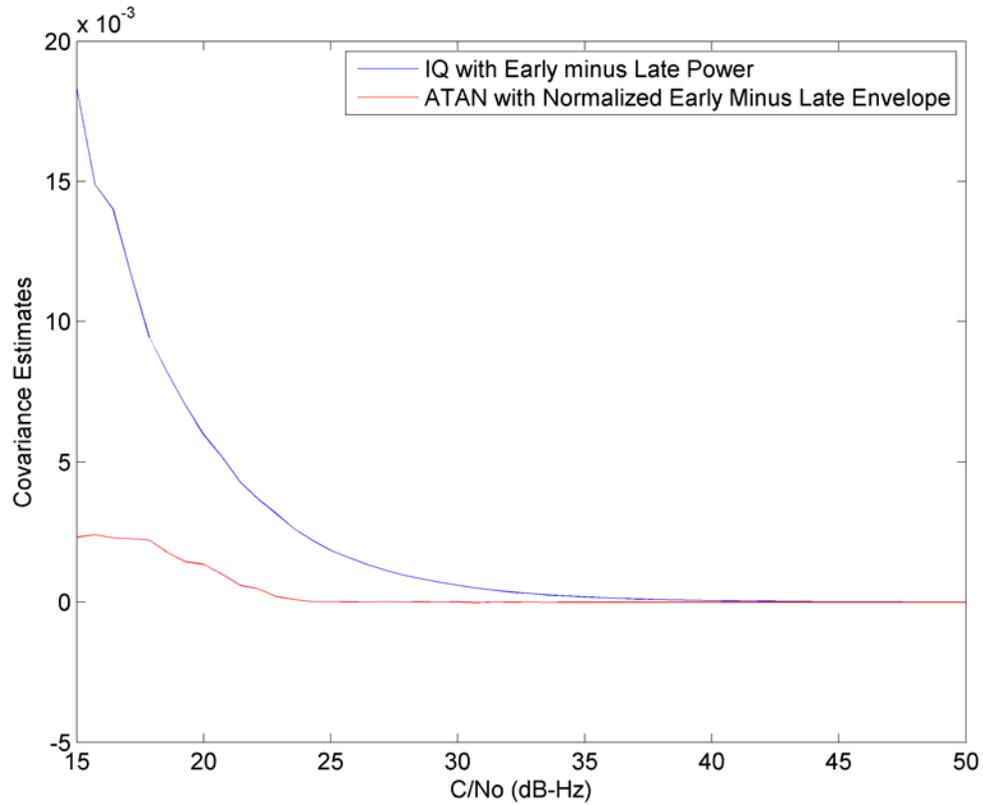
Figure 5-17: Covariance of *I.Q* and early minus late power discriminators and *atan* and normalized early minus late envelope discriminators

Therefore, the covariance matrix of the measurements can be simplified as

$$
C_Z = \begin{bmatrix}
\sigma_{\delta\hat{\varphi}_1}^2 & 0 & 0 & 0 & 0 & 0 \\
0 & \sigma_{\delta\hat{\varphi}_2^{CM}}^2 & 0 & 0 & 0 & 0 \\
0 & 0 & \sigma_{\delta\hat{\varphi}_2^{CL}}^2 & 0 & 0 & 0 \\
0 & 0 & 0 & \sigma_{\delta\hat{\tau}_1}^2 & 0 & 0 \\
0 & 0 & 0 & 0 & \sigma_{\delta\hat{\tau}_2^{CM}}^2 & 0 \\
0 & 0 & 0 & 0 & 0 & \sigma_{\delta\hat{\tau}_2^{CL}}^2
\end{bmatrix}.
\qquad \textbf{5-24}
$$

Finally, as it was the case for phase measurements, an approximation of Gaussian noise can be made. As such, a similar approximation as for the phase discriminator was

conducted on the normalized early minus late envelope discriminator. The noise is assumed to have a Gaussian distribution of mean $\delta\tau$ and variance $\sigma_{\delta\hat{\tau}}^2$. Then, the CDFs were computed for different C/N$_0$ value for both the Gaussian noise approximation and the noise obtained through the Monte-Carlo simulation, as shown in Figure 5-18. Results displayed in Figure 5-18 and Figure 5-19 show that the Gaussian noise approximation holds for C/N$_0$ greater than 20 dB-Hz.
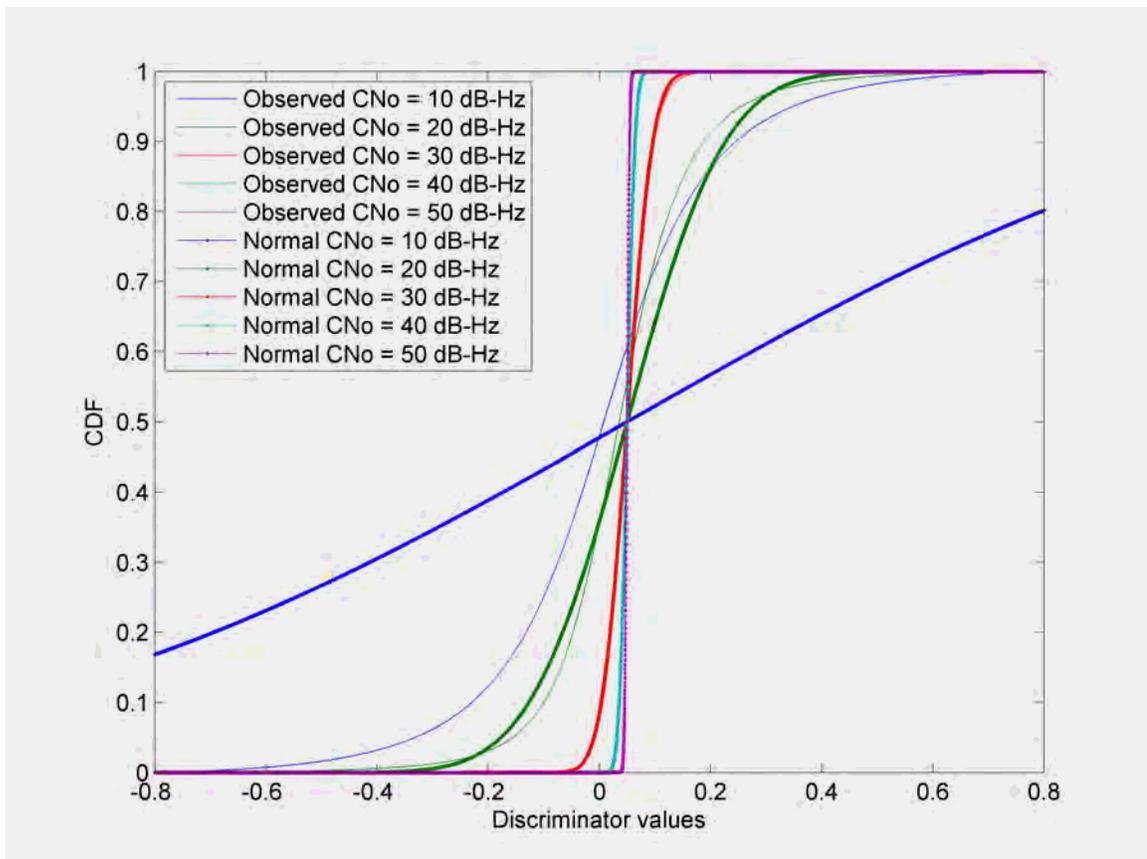
Figure 5-18: CDF of normalized early minus late envelope discriminator noise obtained through Monte-Carlo simulation and Gaussian noise approximation for different C/N$_0$ values
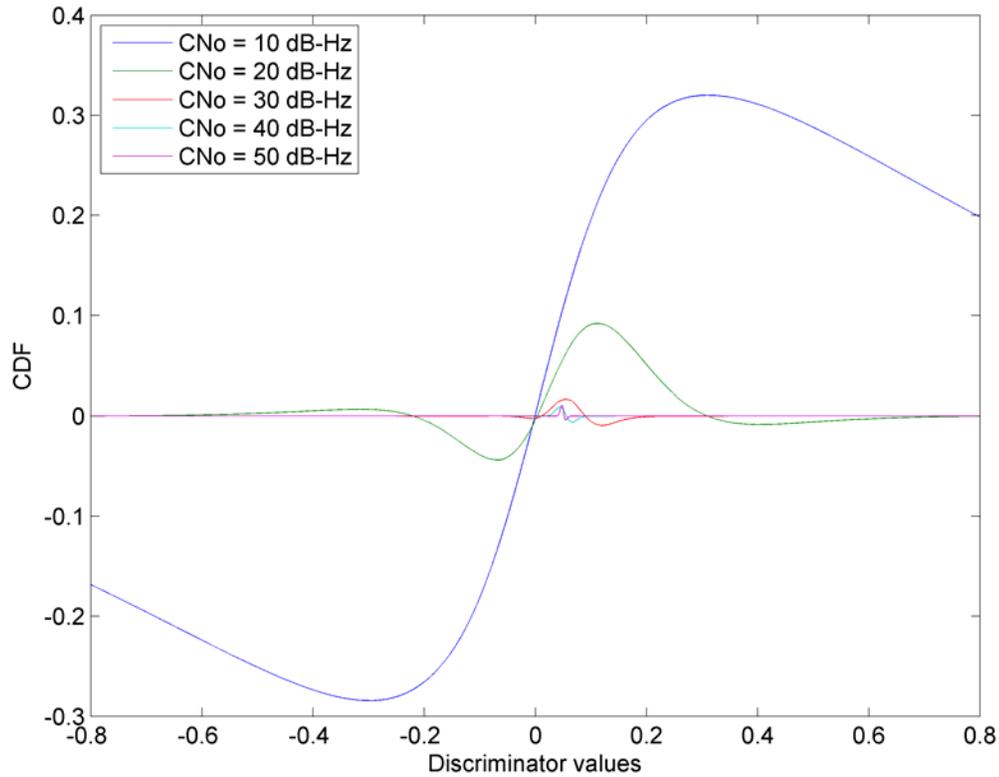
Figure 5-19: difference between CDF of normalized early minus late envelope discriminator noise obtained through Monte-Carlo simulation and Gaussian noise approximation for different C/N$_0$

5.3.2 Derivation of the dynamic model

As one's purpose is to be able to track L1 and L2 signals over time, estimating the phase error at the end of coherent integrations is not sufficient. Indeed, one actually needs the following three parameters to implement a robust Kalman filter based tracking module:

- $\delta\varphi_0$ error in the local carrier phase at the beginning of the integration interval including the ionospheric effect

- δf_0 error in the local carrier frequency at the beginning of the integration interval

- δa_0 phase acceleration error (frequency rate error) at the beginning of the

  integration interval

Note that: $\delta\varphi = \delta\varphi_0 + \dfrac{T}{2} \cdot \delta f_0 + \dfrac{T^2}{6}\delta a_0$ (Petovello & Lachapelle 2006).

The total number of elements composing the state vector derived from the observation model must then be increased from four to six in order to include the frequency error and phase acceleration error:

$$X = \begin{bmatrix} \delta\phi_{0,2} \\ \delta f_{0,2} \\ \delta a_{0,2} \\ \delta d \\ \delta iono_{L1}^{P} \\ \delta iono_{L1}^{C} \end{bmatrix}. \qquad\qquad \textbf{5-25}$$

Recall that $\delta\phi_0$ does not include the ionospheric effect.

In order to take into account the extension of the state vector, the observation model design matrix must be extended accordingly:

$$
\begin{bmatrix} \delta\hat{\varphi}_1 \\ \delta\hat{\varphi}_2{}^{CM} \\ \delta\hat{\varphi}_2{}^{CL} \\ \delta\hat{\tau}_1 \\ \delta\hat{\tau}_2{}^{CM} \\ \delta\hat{\tau}_2{}^{CL} \end{bmatrix} = \begin{bmatrix} \dfrac{f_1}{f_2} & 0 & 0 & 0 & 1 & 0 \\[2mm] 1 & 0 & 0 & 0 & \dfrac{f_1}{f_2} & 0 \\[2mm] 1 & 0 & 0 & 0 & \dfrac{f_1}{f_2} & 0 \\[2mm] 0 & 0 & 0 & 1 & -\dfrac{f_c}{f_1} & -\dfrac{f_c}{f_1} \\[2mm] 0 & 0 & 0 & 1 & -\dfrac{f_c f_1}{f_2{}^2} & -\dfrac{f_c f_1}{f_2{}^2} \\[2mm] 0 & 0 & 0 & 1 & -\dfrac{f_c f_1}{f_2{}^2} & -\dfrac{f_c f_1}{f_2{}^2} \end{bmatrix} \begin{bmatrix} \delta\phi_{0,2} \\ \delta f_{0,2} \\ \delta a_{0,2} \\ \delta d \\ \delta iono_{L1}^P \\ \delta iono_{L1}^C \end{bmatrix} \Rightarrow Z = H \cdot X . \qquad \textbf{5-26}
$$

The purpose of deriving a dynamic model is to find the relationship relating the time derivative of the state vector to the state vector itself (Gelb 1974):

$$
\dot{X} = F \cdot X + G \cdot W . \qquad \textbf{5-27}
$$

As the frequency is the time derivative of the phase and the phase acceleration is the time derivative of the frequency, the following relationships can be written where the terms w_i refer to the process noise of the model (Details on the process noise model are given later in this section):

$$
\delta\dot{\phi}_0 = \delta f_0 + w_{clock} \qquad \textbf{5-28}
$$

$$
\delta\dot{f}_0 = \delta a_0 + w_{freq} \qquad \textbf{5-29}
$$

$$
\delta\dot{a}_0 = 0 + w_{acc} . \qquad \textbf{5-30}
$$

The code Doppler error $\delta\dot{d}$ can be related to the frequency error $\delta\dot{f}$ by converting the frequency error from radians to chips through the factor β :

$$\delta \dot{d} = \beta \cdot \delta f_0 + w_d .$$

5-31

Therefore, one can express w_d as:

$$w_d = w_{code} + \beta \cdot w_{clock} .$$

5-32

β represents the ratio of the chipping rate to the carrier frequency. In the case at hand, as one estimates the L2 frequency error, the conversion is done as

$$\beta = \frac{f_c}{f_2} = \frac{1}{1200} .$$

5-33

Finally, as the time derivative of the ionosphere is not estimated, the following relationships are derived:

$$\frac{d(\delta iono_{L1}^P)}{dt} = 0 + w_{iono,p}$$

5-34

$$\frac{d(\delta iono_{L1}^C)}{dt} = 0 + w_{iono,c} .$$

5-35

The process noise on $\frac{d(\delta iono_{L1}^P)}{dt}$ is present in order to counteract possible divergences between phase and code measurements. As $\delta iono_{L1}^P$ and $\delta iono_{L1}^C$ are part of the same quantity $\delta iono_{L1}^P + \delta iono_{L1}^C$ which is in turn used to evaluate the total ionospheric effect, $w_{iono,p}$ is mainly present to stabilize the dynamic model and as such, is considered independent of $w_{iono,c}$.

The dynamic model can then be written as:

$$\dot{X} = F \cdot X + G \cdot W.$$ **5-36**

with

$$X = \begin{bmatrix} \delta\phi_{0,2} \\ \delta f_{0,2} \\ \delta a_{0,2} \\ \delta d \\ \delta iono_{L1}^{P} \\ \delta iono_{L1}^{C} \end{bmatrix}, \quad F = \begin{bmatrix} 0 & 1 & 0 & 0 & 0 & 0 \\ 0 & 0 & 1 & 0 & 0 & 0 \\ 0 & 0 & 0 & 0 & 0 & 0 \\ 0 & \dfrac{f_c}{f_2} & 0 & 0 & 0 & 0 \\ 0 & 0 & 0 & 0 & 0 & 0 \\ 0 & 0 & 0 & 0 & 0 & 0 \end{bmatrix}, \quad G = \begin{bmatrix} 1 & 0 & 0 & 0 & 0 & 0 \\ 0 & 1 & 0 & 0 & 0 & 0 \\ 0 & 0 & 1 & 0 & 0 & 0 \\ \dfrac{f_c}{f_2} & 0 & 0 & 1 & 0 & 0 \\ 0 & 0 & 0 & 0 & 1 & 0 \\ 0 & 0 & 0 & 0 & 0 & 1 \end{bmatrix}$$ and

$$W = \begin{bmatrix} w_{clock} \\ w_{freq} \\ w_{acc} \\ w_{code} \\ w_{iono,p} \\ w_{iono,c} \end{bmatrix}.$$

It becomes necessary to determine the covariance matrix Q of the process noise defined by W:

$$Q = E\left[W \cdot W^T\right] = \begin{bmatrix} S_{clock} & 0 & 0 & 0 & 0 & 0 \\ 0 & S_{freq} & 0 & 0 & 0 & 0 \\ 0 & 0 & S_{acc} & 0 & 0 & 0 \\ 0 & 0 & 0 & S_{code} & 0 & 0 \\ 0 & 0 & 0 & 0 & S_{iono,p} & 0 \\ 0 & 0 & 0 & 0 & 0 & S_{iono,c} \end{bmatrix}.$$ **5-37**

The derivation of the values of the variances of the noise associated to the dynamic model is done as follows:

- S_{clock} and S_{freq} depend on the oscillator parameters as they correspond to the expected error on the phase and frequency that can occur between updates from the observation model. From Brown & Hwang (1992), if one were to assume the general two states model presented in Figure 5-20, the clock errors of the receiver could be created from white noise components.
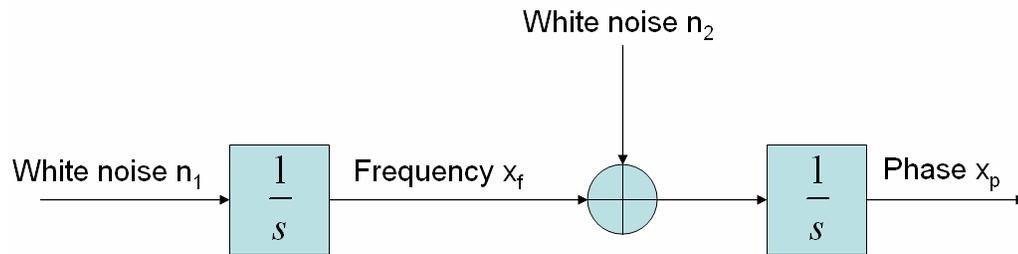
Figure 5-20: General two state model describing the clock errors (Brown & Hwang 1992)

Assuming that the spectral amplitudes of n_1 and n_2 are S_{freq} and S_{clock}, Brown & Hwang (1992) show that an accurate clock model matching Van Dierendonck et al (1984) occurs when

$$S_{clock} = \frac{h_0}{2} \cdot f_{L2}^2 \text{ cycles}^2 . \text{s}^{-1} \text{ and } S_{freq} = 2 \cdot \pi^2 \cdot h_{-2} \cdot f_{L2}^2 \text{ cycles}^2 . \text{s}^{-3},$$

provided that x_p is expressed in cycles, x_f is expressed in cycles.s^{-1} and one is tracking the L2 signal. As one tries to estimate similar parameters, the same values are used in the problem at hand.

The parameters h_0 and h_{-2} are dependent on the oscillator used as shown in Table 5-1.

Table 5-1 : *h*-parameters for different types of oscillator (Julien 2005)

	Oscillator parameters		
	h_0 (s)	h_{-1}	h_{-2} (Hz)
Quartz	$2e^{-19}$	$7e^{-21}$	$2e^{-20}$
TCXO	$1e^{-21}$	$1e^{-20}$	$2e^{-20}$
OCXO	$8e^{-20}$	$2e^{-21}$	$4e^{-23}$
Rubidium	$2e^{-20}$	$7e^{-24}$	$1e^{-29}$
Caesium	$1e^{-19}$	$1e^{-25}$	$2e^{-23}$

- S_{acc} depends on the rate of change of the LOS range variation, or the change in Doppler. Neglecting user motion, the Doppler for L2 is approximately 4000 Hz at the horizon and 0 Hz at the zenith. Moreover, the satellite takes approximately two hours from the horizon to the zenith. Thus, the average variation is 0.5 Hz/s and is used as the 3σ point. Thus, a value of $S_{acc} = 3.5 \cdot 10^{-2}$ cycles^2.s^{-5} is chosen.

- S_{code} corresponds to the expected divergence between the variation of the delay for the code and the phase over time (the common change over time being already accounted for by S_{clock} through G) . The only divergence between the code and phase comes from the ionosphere and is already taken into account. Therefore, the value of this parameter is kept $S_{code} = 5 \cdot 10^{-9}$ chip^2.s^{-1}.

- $S_{iono,c}$ corresponds to the ionospheric effect variation over time. As a satellite takes approximately four hours from the horizon to horizon, the variation of TEC encountered on the signal path is mainly due to the satellite motion (assuming no scintillation). Assuming a vertical TEC value of 60 TECU, the delay experienced by the L2 signal transmitted by a satellite at the horizon is about 48 m whereas the delay for a satellite at the zenith is about 16 m. Therefore, the variation is 32 m in 7200 s, thus around $5 \cdot 10^{-3}$ m in 1 s. The final value of $S_{iono,c}$ is then set to $S_{iono,c} = 7 \cdot 10^{-4}$ cycles^2.s^{-1}. Regarding $S_{iono,p}$, it is set to the same values as $S_{iono,c}$ in order to stabilize the dynamic model.

5.3.3 From the continuous to the discrete time domain

As the Kalman filter takes place after the code and phase discriminator outputs and so after the coherent integration (hereby kept at 20 ms) has been performed, the continuous time domain model does not apply. In order to apply the Kalman filter design to discrete time signals, one must convert the dynamic model to the discrete domain. The equation relating the instant k to the instant $k+1$ is as follows (Gelb 1974):

$$X_{k+1} = \Phi_k \cdot X_k + w_k \text{ with } E\left(w_k \cdot w_k^T\right) = Q_k.$$

Φ_k is called the state transition matrix and Q_k is the covariance matrix of the w_k the discrete noise corresponding w.

From Grewal and Andrews (2001), the state transition matrix Φ_k transforming the state vector at the instant k to the state vector at the instant $k+1$ can be easily computed for time invariant systems from the dynamic matrix F and the time between the two epochs:

$$\Phi_k = e^{F \cdot T} \qquad\qquad \textbf{5-38}$$

$$T = t_{k+1} - t_k . \qquad\qquad \textbf{5-39}$$

In the case at hand T is the coherent integration time used during the tracking module and is kept at 0.02 s. As T is small, one can use a Taylor series expansion for Equation 5-38:

$$\Phi_k = \sum_{i=0}^{\infty} \frac{T^i}{i!} F^i \qquad\qquad \textbf{5-40}$$

where the symbol "!" denotes factorial.

Given the structure of F as defined above, one can readily show that $F^3 = 0$. Therefore, the expression of Φ_k can be simplified to

$$\Phi_k = I + F \cdot T + \frac{F^2 \cdot T^2}{2} . \qquad\qquad \textbf{5-41}$$

At this point, the following expression for Φ_k can easily be derived:

$$\Phi_k = \begin{bmatrix} 1 & T & \dfrac{T^2}{2} & 0 & 0 & 0 \\ 0 & 1 & T & 0 & 0 & 0 \\ 0 & 0 & 1 & 0 & 0 & 0 \\ 0 & T\beta & \dfrac{\beta T^2}{2} & 1 & 0 & 0 \\ 0 & 0 & 0 & 0 & 1 & 0 \\ 0 & 0 & 0 & 0 & 0 & 1 \end{bmatrix}$$

5-42

with $\beta = \dfrac{f_c}{f_2} = \dfrac{1}{1200}$.

A last step is necessary to convert the dynamic model from the continuous to the discrete domain. One needs to convert the covariance matrix $G \cdot Q \cdot G^T$ of the "continuous case" process noise $G \cdot W$ to the covariance matrix Q_k of the "discrete case" process noise expressed by w_k. This step is done according to a simple formula provided by Grewal & Andrews (2001):

$$Q_k = \int_k^{k+1} \Phi(t, t+\tau) \cdot G(\tau) \cdot Q(\tau) \cdot G^T(\tau) \cdot \Phi^T(t, t+\tau) \cdot d\tau .$$

5-43

In the above formula, $\Phi(t, t+\tau)$ is the discrete time domain transition matrix transforming the state vector at t to the state vector at $t+\tau$ and τ represents the time elapsed between the instants k and $k+1$. In the problem at hand, as the state transition matrix is time invariant, it was named Φ_k and is used to transform the state vector at the instant k to the instant $k+1$. Similarly, Q and G are time invariant in the model developed earlier. Therefore the formula proposed by Grewal & Andrews (2001) reduces to:

$$Q_k = \int_k^{k+1} \Phi_k \cdot G \cdot Q \cdot G^T \cdot \Phi_k{}^T \cdot d\tau \qquad \textbf{5-44}$$

and Q_k can be written as

$$Q_k = \begin{bmatrix}
S_{clock}T + \dfrac{T^3 S_{freq}}{3} + \dfrac{T^5 S_{acc}}{20} & \dfrac{T^2 S_{freq}}{2} + \dfrac{T^4 S_{acc}}{8} & \dfrac{T^3 S_{acc}}{6} \\[2ex]
\dfrac{T^2 S_{freq}}{2} + \dfrac{T^4 S_{acc}}{8} & TS_{freq} + \dfrac{T^3 S_{acc}}{3} & \dfrac{T^2 S_{acc}}{2} \\[2ex]
\dfrac{T^3 S_{acc}}{6} & \dfrac{T^2 S_{acc}}{2} & TS_{acc} \quad \cdots \\[2ex]
\dfrac{T^3 S_{freq}\beta}{3} + \dfrac{T^5 S_{acc}\beta}{20} + TS_{clock}\beta & \dfrac{T^2 S_{freq}\beta}{2} + \dfrac{T^4 S_{acc}\beta}{8} & \dfrac{T^3 S_{acc}\beta}{6} \\[2ex]
0 & 0 & 0 \\[2ex]
0 & 0 & 0
\end{bmatrix}$$

$$\begin{bmatrix}
\dfrac{T^3 S_{freq}\beta}{3} + \dfrac{T^5 S_{acc}\beta}{20} + TS_{clock}\beta & 0 & 0 \\[2ex]
\dfrac{T^4 S_{freq}\beta}{2} + \dfrac{T^4 S_{acc}\beta}{8} & 0 & 0 \\[2ex]
\cdots \qquad \dfrac{T^3 S_{acc}\beta}{6} & 0 & 0 \\[2ex]
\dfrac{T^3 S_{freq}\beta^2}{3} + \dfrac{T^5 S_{acc}\beta^2}{20} + TS_{clock}\beta^2 + TS_{code} & 0 & 0 \\[2ex]
0 & TS_{iono,p} & 0 \\[2ex]
0 & 0 & TS_{iono,c}
\end{bmatrix}.$$

Finally, the measurement model is repeated here for convenience:

$$Z_k = H_k \cdot X_k + v_k$$

with
$$Z_k = \begin{bmatrix} \delta\hat{\varphi}_1 \\ \delta\hat{\varphi}_2^{CM} \\ \delta\hat{\varphi}_2^{CL} \\ \delta\hat{\tau}_1 \\ \delta\hat{\tau}_2^{CM} \\ \delta\hat{\tau}_2^{CL} \end{bmatrix}, \quad H_k = \begin{bmatrix} \dfrac{f_1}{f_2} & 0 & 0 & 0 & 1 & 0 \\ 1 & 0 & 0 & 0 & \dfrac{f_1}{f_2} & 0 \\ 1 & 0 & 0 & 0 & \dfrac{f_1}{f_2} & 0 \\ 0 & 0 & 0 & 1 & -\dfrac{f_c}{f_1} & -\dfrac{f_c}{f_1} \\ 0 & 0 & 0 & 1 & -\dfrac{f_c f_1}{f_2^2} & -\dfrac{f_c f_1}{f_2^2} \\ 0 & 0 & 0 & 1 & -\dfrac{f_c f_1}{f_2^2} & -\dfrac{f_c f_1}{f_2^2} \end{bmatrix}, \quad X_k = \begin{bmatrix} \delta\phi_{0,2} \\ \delta f_{0,2} \\ \delta a_{0,2} \\ \delta d \\ \delta iono_{L1}^P \\ \delta iono_{L1}^C \end{bmatrix} \quad \text{and}$$

$$R_k = E\left(v_k \cdot v_k^T\right) = \begin{bmatrix} \sigma_{\delta\hat{\varphi}_1}^2 & 0 & 0 & 0 & 0 & 0 \\ 0 & \sigma_{\delta\hat{\varphi}_2^{CM}}^2 & 0 & 0 & 0 & 0 \\ 0 & 0 & \sigma_{\delta\hat{\varphi}_2^{CL}}^2 & 0 & 0 & 0 \\ 0 & 0 & 0 & \sigma_{\delta\hat{\tau}_1}^2 & 0 & 0 \\ 0 & 0 & 0 & 0 & \sigma_{\delta\hat{\tau}_2^{CM}}^2 & 0 \\ 0 & 0 & 0 & 0 & 0 & \sigma_{\delta\hat{\tau}_2^{CL}}^2 \end{bmatrix}.$$

5.3.4 Kalman filter equations

For the reader's convenience, the author has repeated the equations used by a linear Kalman filter as provided by Grewal & Andrews (2001). In the following, $\hat{X}_k$ represents the estimated state vector.

- System dynamic model:

$$X_k = \Phi_{k-1} \cdot X_{k-1} + w_{k-1}$$

$$w_k \quad N\left(0, Q_k\right).$$

- Measurement model:

$$Z_k = H_k \cdot X_k + v_k$$

$$v_k \quad N(0, R_k).$$

- Initial conditions:

$$E(X_0) = \hat{X}_0$$

$$E(\tilde{X}_0 \cdot \tilde{X}_0^T) = P_0.$$

- Independence assumptions:

$$E(v_k \cdot w_i^T) = 0 \text{ for all } k \text{ and } i.$$

- State estimate extrapolation:

$$\hat{X}_k(-) = \Phi_{k-1} \cdot \hat{X}_{k-1}(+).$$

- Error covariance extrapolation:

$$P_k(-) = \Phi_{k-1} \cdot P_{k-1}(+) \cdot \Phi_{k-1}^T + Q_{k-1}.$$

- State estimate observational update:

$$\hat{X}_k(+) = \hat{X}_k(-) + K_k \cdot \left[Z_k - H_k \cdot \hat{X}_k(-) \right].$$

- Error covariance update:

$$P_k\left(+\right)=\left[I-K_k\cdot H_k\right]\cdot P_k\left(-\right).$$

- Kalman gain matrix:

$$K_k = P_k\left(-\right)\cdot H_k{}^T\left[H_k\cdot P_k\left(-\right)\cdot H_k{}^T + R_k\right]^{-1}.$$

In the above equation P_k represents the covariance matrix of the error $\tilde{X}_k\left(-\right)$ $\hat{X}_k\left(-\right)-X_k$:

$$P_k\left(-\right)=E\left(\tilde{X}_k\left(-\right)\cdot\tilde{X}_k\left(-\right)^T\right).$$

Finally, the initial conditions need to be defined by the Kalman filter designer. As such, $\hat{X}_0$ represents the estimate of the initial state vector to the best knowledge possible and P_0 represents the uncertainty that the designer has over the defined initial estimate of the state vector $\hat{X}_0$. As one has no information on the initial phase error, Doppler frequency error, phase acceleration error and range error, these elements of $\hat{X}_0$ are set to zero. However, the initial error of the ionosphere can reasonably be estimated as the mean value that one can encounter at a given latitude. Therefore, for the case at hand (North America), this value was fixed to 30 cycles which corresponds to 35 TECU. Regarding P_0, as the initial phase error could be on the order of a cycle, the variance of the initial phase error is fixed to 1 cycle^2. The uncertainty on the Doppler error is function of the coherent acquisition time used. In the case at hand, a 20 ms coherent acquisition was

used. As such the maximum error is 16.5 Hz and the element of P_0 is set to 270 Hz^2. The uncertainty on the phase acceleration error is kept at 4 cycles^2.s^{-4} given that one targets low dynamics vehicle of about 0.5 m.s^{-2} (the environment being urban canyon conditions). The uncertainty on the range error is set depending on the code phase step used during the acquisition process. In the case at hand, the corresponding value of P_0 is set to 0.01 chip^2. Finally, as one does not know the actual value of the ionosphere but can estimate its initial error around 20 TECU, the corresponding value of P_0 is set to 500 cycles^2. Regarding the estimated ionospheric effect on the phase, the value is set to 1 cycles^2 in order for the phase estimate to converge. Therefore :

$$
\hat{X}_0 = \begin{bmatrix} 0 \\ 0 \\ 0 \\ 0 \\ 0 \\ 30 \end{bmatrix} \text{ and } P_0 \begin{bmatrix} 1 & 0 & 0 & 0 & 0 & 0 \\ 0 & 270 & 0 & 0 & 0 & 0 \\ 0 & 0 & 4 & 0 & 0 & 0 \\ 0 & 0 & 0 & 0.01 & 0 & 0 \\ 0 & 0 & 0 & 0 & 1 & 0 \\ 0 & 0 & 0 & 0 & 0 & 500 \end{bmatrix}.
$$

The following chapter presents the results obtained using the Kalman filter based combined tracking developed above. Results are shown compared to the standard single frequency tracking technique. Data sets with attenuated signals and mild ionospheric scintillation are presented.

Chapter Six: Results of the L1 / L2 combined Kalman filter based tracking method

This chapter presents the results of the Kalman filter based combined tracking method developed in the previous chapter. Results are provided by comparing the Kalman filter tracking to the standard single frequency technique. Finally, the proposed method is also tested during mild ionospheric scintillations.

6.1 Results and Analysis

As a first step toward the validation of the proposed combined L1 / L2 Kalman filter based tracking method, a simple simulation process is set up. The purpose of this simulation is to verify that the combined tracking is indeed capable of correctly tracking and estimating the desired parameters under ideal conditions. Once this necessary verification is done, real data tracking is attempted. Results from two real data scenarios are presented. First, signals that have been artificially attenuated using a variable attenuator are tracked to demonstrate the performance of the new filter as a function of signal strength. Second, real data collected during low ionospheric scintillation is tracked to demonstrate the ability of the new method to track relative delay changes between the L1 and L2C signals.

6.1.1 Using simulation process

In order to verify the proposed tracking method, a simple L1/L2 signal simulator was developed. As one wants to test the tracking module presented under ideal conditions, errors such as orbital errors, instrumental errors, tropospheric delay, oscillator errors and multipath were not implemented. Similarly, the simulator developed is only simulating one satellite and does not make use of ephemeris to compute true data bits but considers these random. However, the ionospheric errors (phase advance and code delay), Doppler effect and realistic C/N_0 are considered. The ionospheric error is modeled as a constant code delay or phase advance computed from the input TEC value. The Doppler frequency is not considered fixed but can change linearly over time and is adapted sample per sample. Table 6-1 presents the parameters used to simulate L1 C/A and L2C complex samples.

Table 6-1 : L1 C/A and L2C Simulation parameters

General parameters	
PRN	7
Simulation time	50 s
Sampling frequency	3 MHz
TEC	30 TECU
L1 parameters	
C/N_0	45 dB-Hz
Intermediate frequency	0.12 MHz
Initial Doppler	1000 Hz
Doppler rate	-0.2 Hz.s^{-1}
L2 parameters	
C/N_0	1.5 dB under L1 C/N_0
Intermediate frequency	0.12 MHz
Doppler	L1 Doppler times F_2 / F_1
Doppler rate	L1 Doppler rate times F_2 / F_1

Four parameters were considered in order to validate the combined tracking proposed.

First of all, the tracking capabilities of the Kalman filter are verified through the Doppler error, defined as the estimated Doppler frequency minus the true Doppler frequency (Figure 6-1).
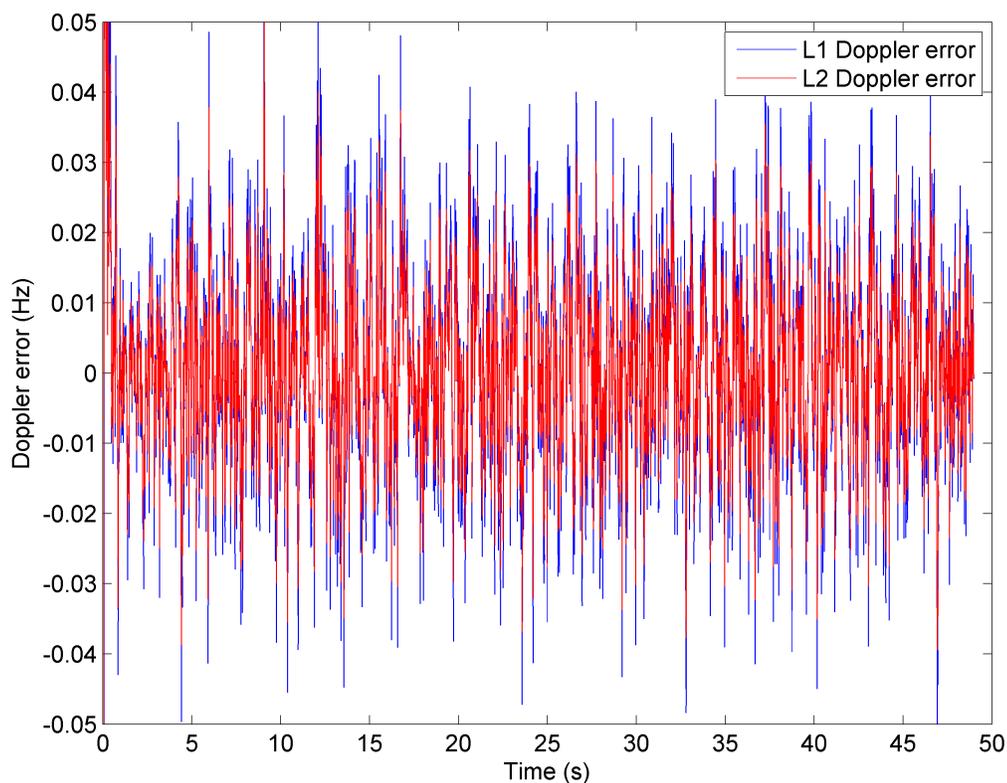
Figure 6-1: Observed Doppler frequency error for L1 and L2

Another parameter of interest when testing the behaviour of the combined tracking method is the code error defined as the estimated code delay output by the Kalman filter minus the true code delay given by the simulator. As the code delay is then used to estimate the pseudorange between the GPS satellite and the receiver, the code error is shown in Figure 6-2 in centimetres.
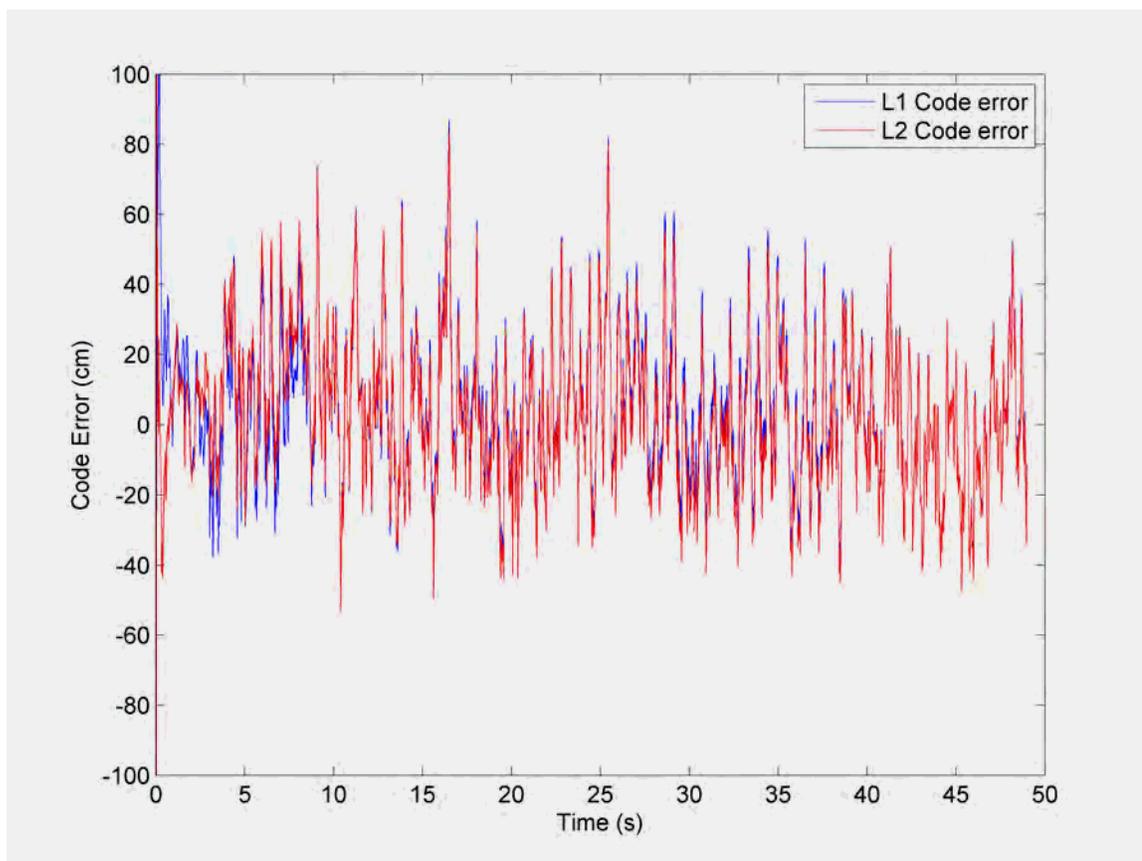
Figure 6-2: Observed code errors in centimetres for L1 and L2

The third parameter of interest toward the validation of the proposed method and its performance is the carrier phase error. Once again, as the final purpose of a GPS receiver is to provide possible users with their positions, the phase error is provided in centimetres (Figure 6-3).
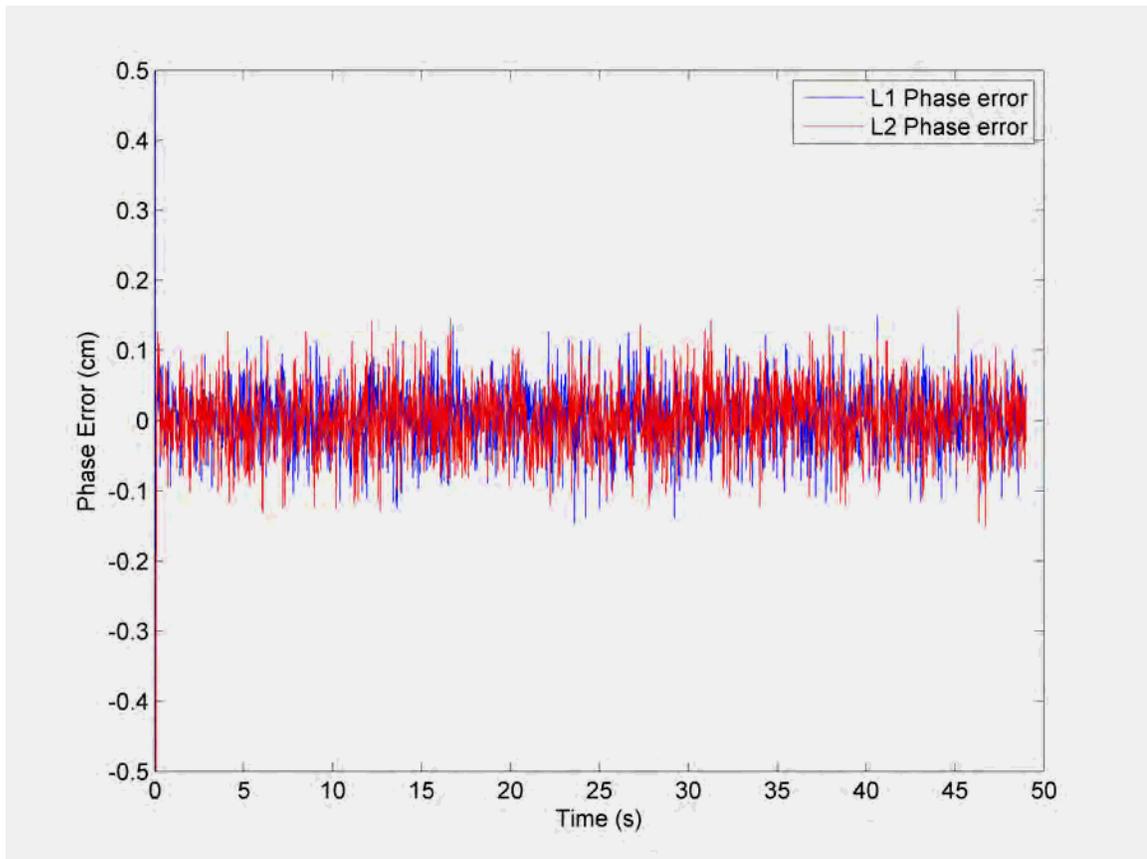
Figure 6-3 : Observed carrier phase errors for L1 and L2

As illustrated by Figure 6-1 to Figure 6-3, the Kalman filter based combined tracking method is able to track both L1 and L2 signals. The Doppler error being close to zero shows that the proposed method properly tracked the Doppler frequency of L1 and L2. Similarly, the code and carrier phase errors being close to zero proves that the combined tracking properly follows the code delay and carrier phase parameters over time. Therefore, the proposed method is capable of providing the pseudorange and phase measurements for both L1 and L2, necessary for high accuracy positioning.

Finally, as the proposed method also estimates the ionospheric effect, one can deduce the resulting TEC values. In order to verify that the output TEC values of the Kalman filter is

correct, the TEC error defined as the difference between the estimated TEC and true TEC

values is plotted in Figure 6-4.
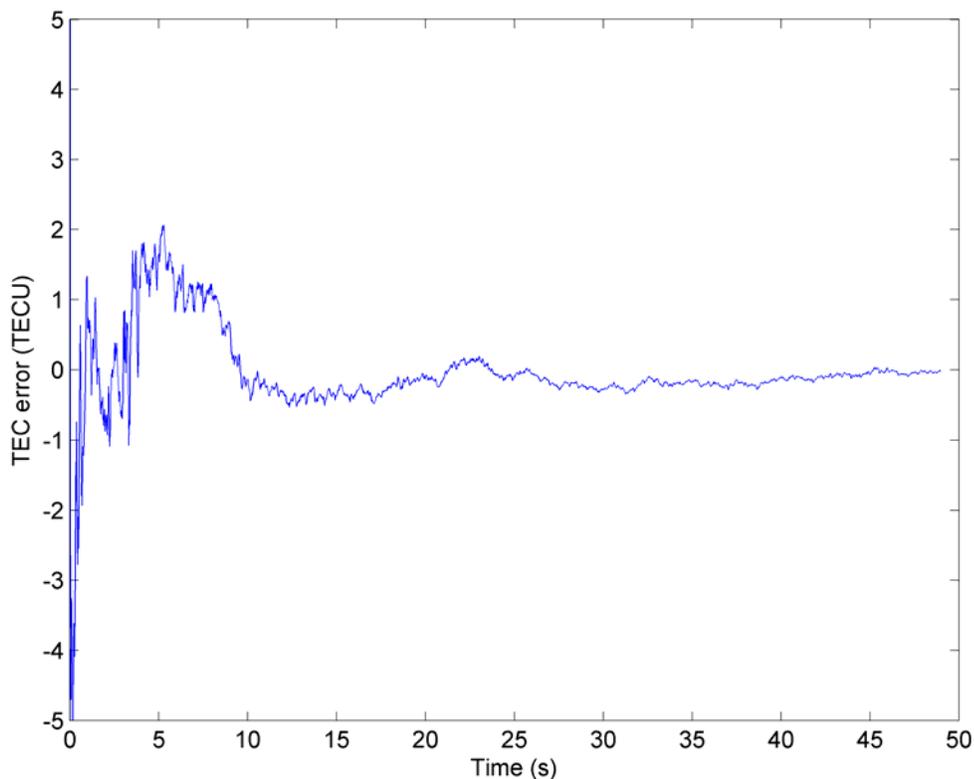
Figure 6-4 : Observed TEC errors

The estimated TEC error rapidly converges toward the simulated value of 30 TECUs and

the error converges toward zero (the Kalman filter was initialized with a value of 10

TECU). As such, the proposed combined tracking method not only doubles the number

of observations with respect to common L1 tracking only but also provides the user with

accurate and rapid estimates of the total electron content encountered on the signal path.

6.1.2 Using real data with attenuation

In order to properly validate the proposed tracking method, the use of simulations is not enough. Indeed, as the simulations are usually created by the method's developer, it is common that the model used during the simulation process is also the one in the Kalman filter developed. As such, simulation model, measurements and dynamic models match and the Kalman filter developed would obviously work.

To avoid this effect, the use of real data becomes necessary. The data used in the case at hand was taken under opened sky conditions and a variable attenuator was used to degrade the C/N_0 at a rate of 1 dB per second. The data collection scheme is shown in Figure 6-5. The L1 and L2 signals are first collected using a dual frequency antenna, then passed through the variable attenuator and finally collected by a L1/L2 front-end externally clocked by an OCXO oscillator. The oscillator h-parameters are then used in the Kalman filter model as mentioned in the previous chapter. Finally, the collected data is transferred to a computer executing the Kalman filter based tracking program.
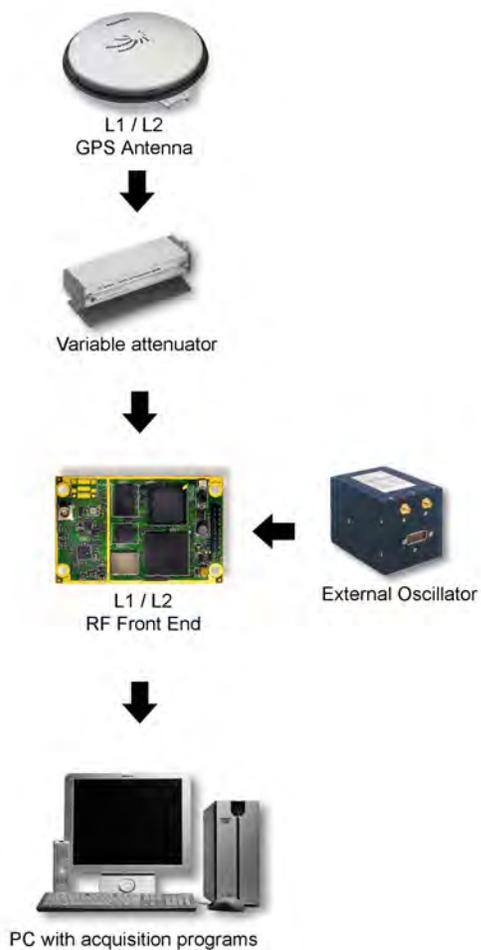
Figure 6-5 : Real data collection scheme

The variable attenuator is set to 0 dB attenuation during the first 30 s and then increased by 1 dB/s. The resulting C/N_0 profile for L1 C/A over time is shown in Figure 6-6.
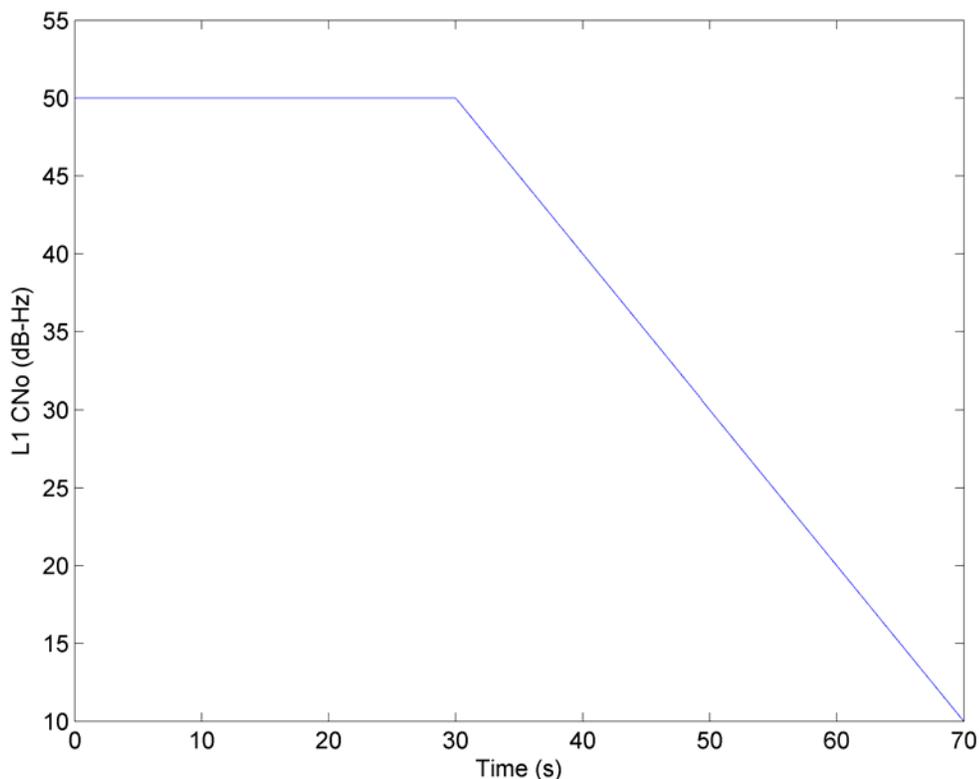
Figure 6-6: L1 C/N$_0$ profile over time as estimated by an external commercial receiver

In order to evaluate and compare the performance of the proposed Kalman filter based tracking, the L1 and L2 signals are also tracked using a standard tracking module as presented in Ward (2006). The L1 and L2 single frequency standard tracking modules make use of a third order PLL and second order DLL with carrier aiding. The bandwidths implemented are 5 Hz for the PLL and 0.05 Hz for the DLL as it is aided by the PLL. A narrow correlator spacing of 0.1 chips was used. The coherent integration time was 20 ms. Regarding L2 standard tracking, both the CM and CL code were merged into one code to compute the correlator output. This was easily done as the CM code did not transmit data at the time of the experiments. Therefore, the L2 standard tracking module

behaves like only one code corresponding to the sum of the CM and CL code. The developed Kalman filter tracking does not make use of this but assumes that the CM code does transmit data.

Figure 6-7 and Figure 6-8 show the Doppler frequency as measured by the Kalman filter method and the standard tracking method for both L1 and L2.
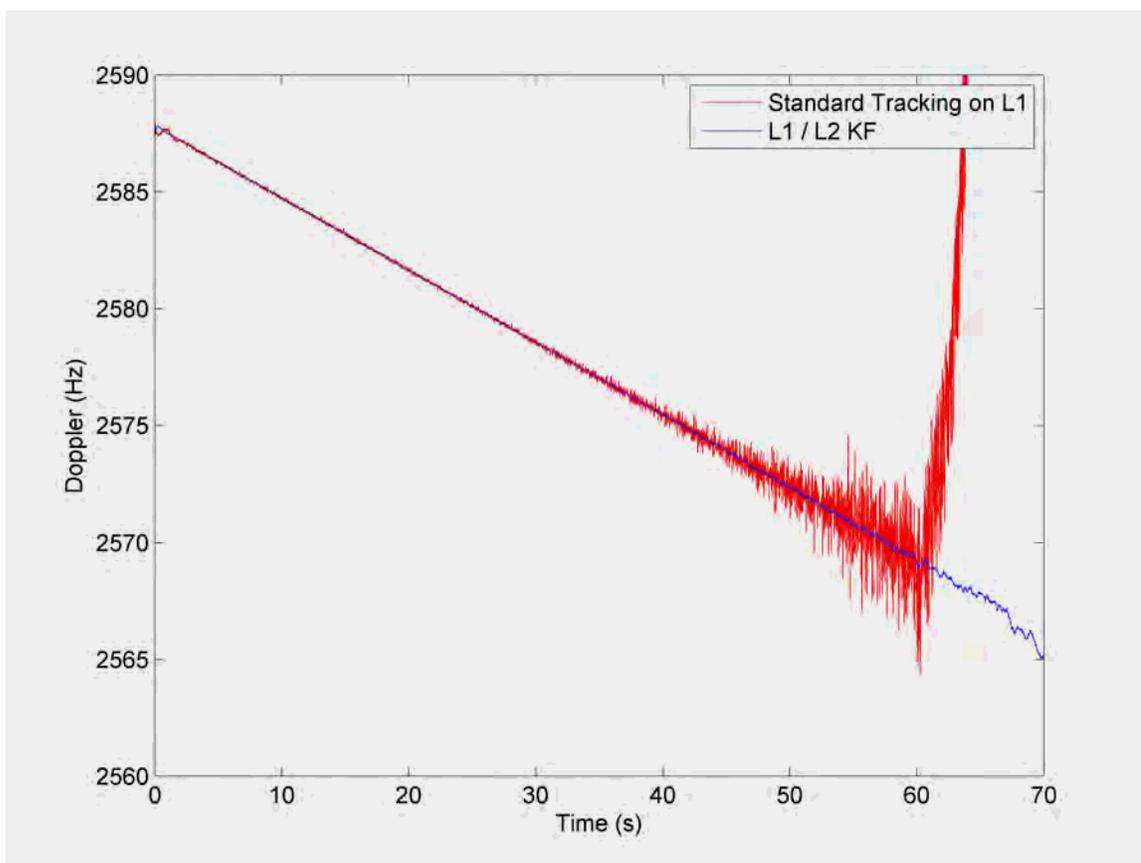
Figure 6-7 : L1 Doppler as measured by the standard L1 only tracking module and the L1/L2 Kalman filter based tracking module
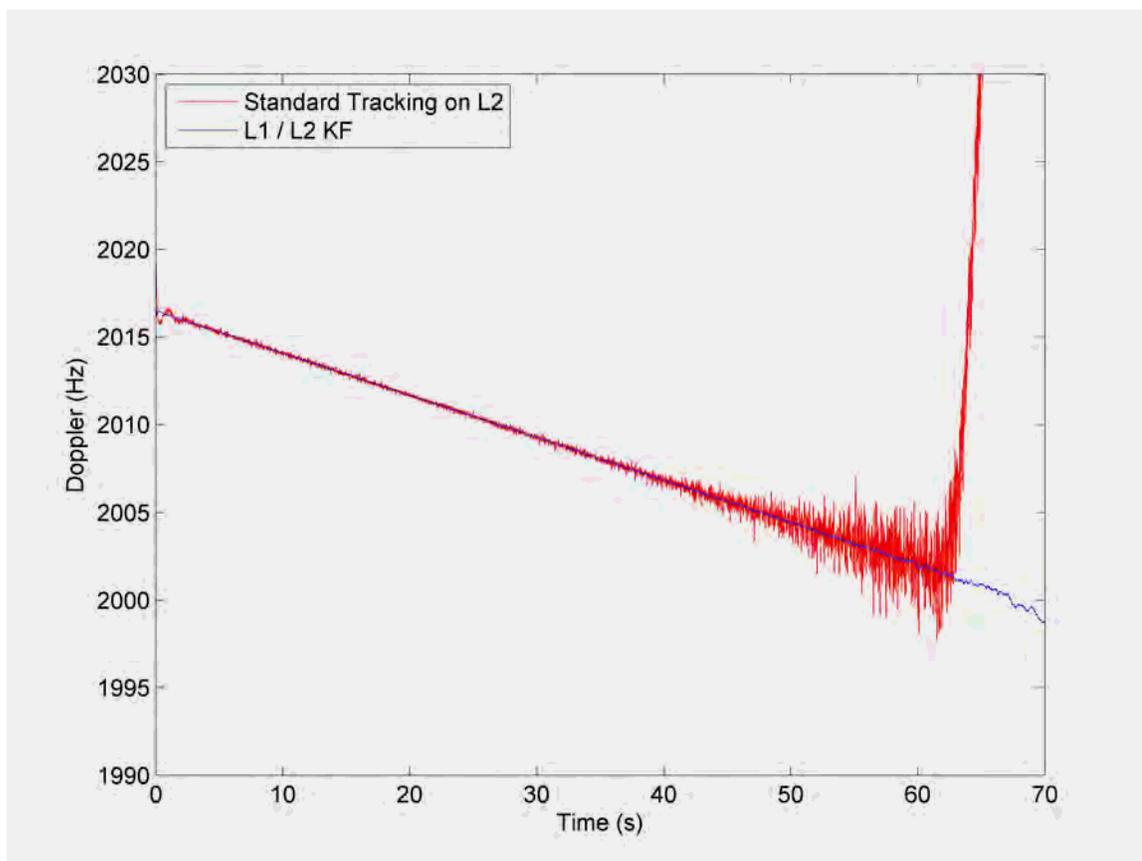
Figure 6-8: L2 Doppler as measured by the standard L2 only tracking module and the L1/L2 Kalman filter based tracking module

The Doppler frequencies output by the Kalman filter are smoother than the ones output by the single frequency tracking module. The L2 standard tracking module is obviously noisier than the L1 tracking module as the resulting L2 CM plus CL code tracked remains 1.5 dB below the L1 C/A code.

From the Doppler frequencies, the L1 only standard tracking module seems to track longer than the L2 only standard tracking module. This is once again explained by the power difference between the two signals. However, the proposed Kalman filter seems to be able to keep track of the signals even longer than the L1 single frequency tracking module. In order to confirm this impression and quantify the sensitivity of the combined

tracking technique with respect to the single frequency tracking technique, the phase lock indicators defined by Van Dierendonck (1996) are computed and shown in Figure 6-9 and Figure 6-10. The phase lock indicators for L1 and L2 for the Kalman filter based tracking are derived from the real and imaginary parts of the L1 and L2 correlator outputs respectively using the following formula:

$$PLI(t) = \frac{\left(\sum_{i=1}^{M} I_P(t+i)\right)^2 - \left(\sum_{i=1}^{M} Q_P(t+i)\right)^2}{\left(\sum_{i=1}^{M} I_P(t+i)\right)^2 + \left(\sum_{i=1}^{M} Q_P(t+i)\right)} . \qquad \textbf{6-1}$$

As such, the phase lock indicators derived from the proposed combined tracking are different for L1 and L2 since the noise and the phase errors on L1 are different from the noise and phase errors on L2.
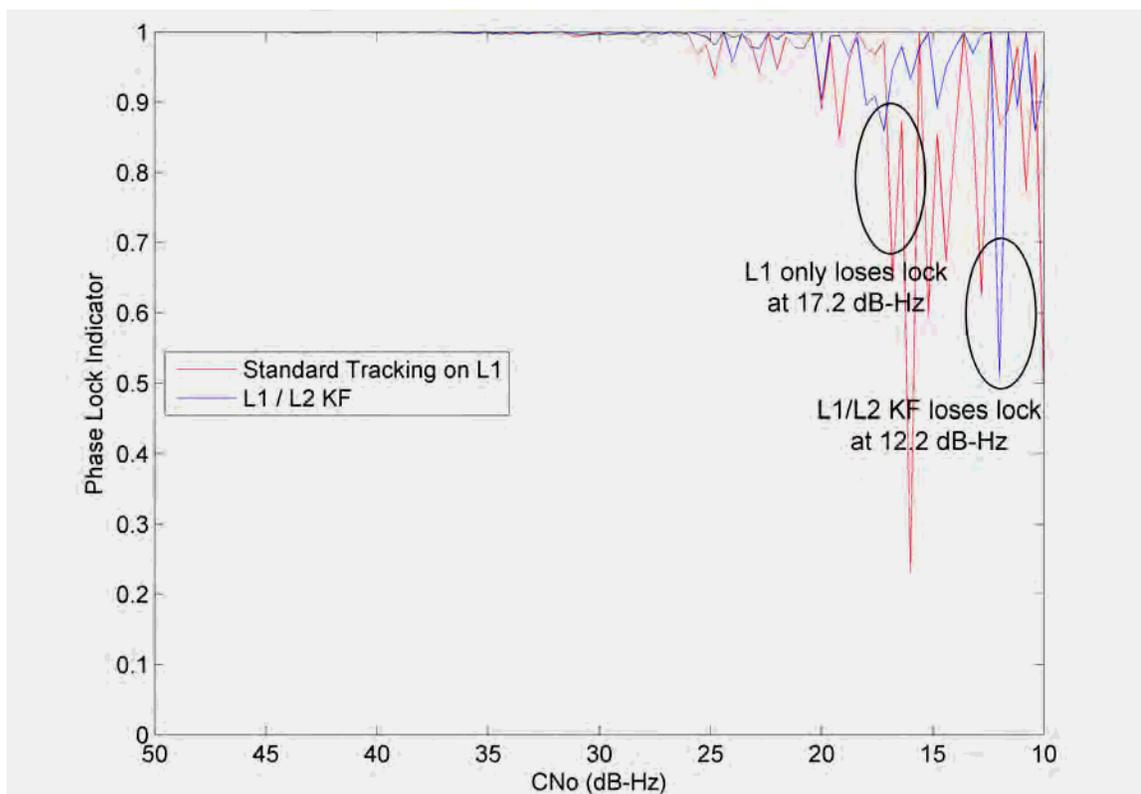
Figure 6-9 : Phase lock indicator computed on the L1 C/A signal for the L1 only standard tracking module and the Kalman filter based tracking
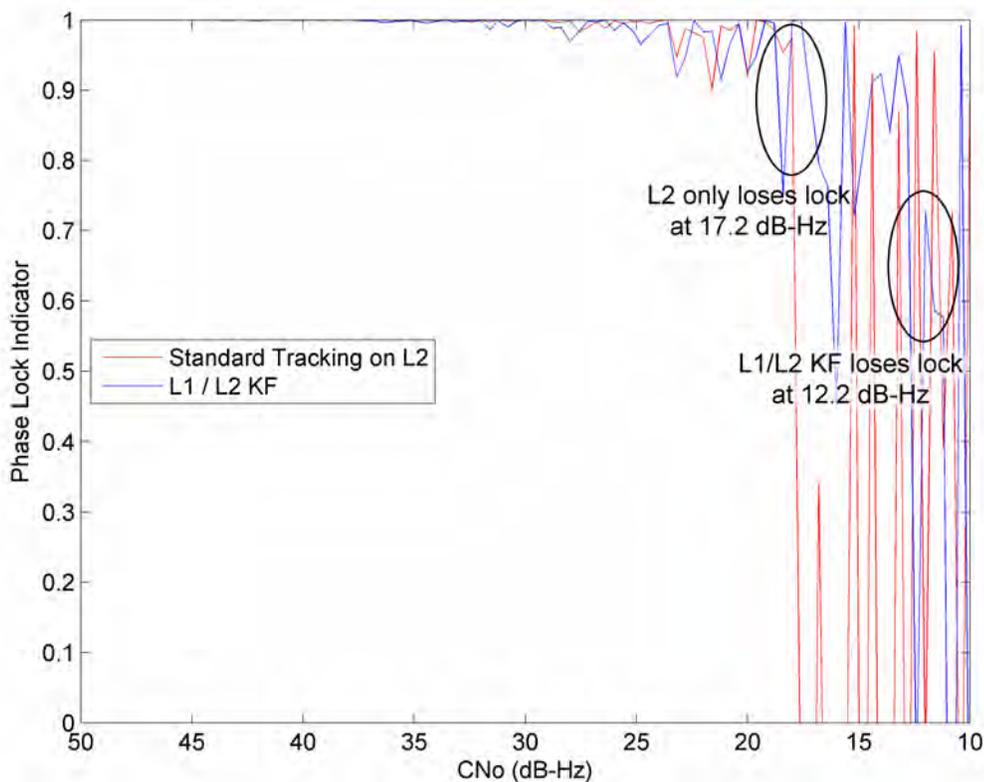
Figure 6-10 : Phase lock indicator computed on the L2 CM + CL signal for the L2 only standard tracking module and the Kalman filter based tracking

As shown through the computation of the phase lock indicators, the proposed Kalman filter based combining method has a sensitivity 5 dB greater than the L1 single frequency tracking module and 5.8 dB greater than the L2 single frequency tracking module. This means that by using the combination of both L1 and L2 signals and not L1 aiding L2, one is able to increase the sensitivity of its tracking loops. The above results are consistent with previous studies (Psiaki 2001, Psiaki & Jung 2002, Humphreys et al 2005, Petovello & Lachapelle 2006, Yu et al 2006). For instance the tests performed by Petovello et al (2008) show that a L1 C/A single frequency Kalman filter based tracking brings 4 dB sensitivity improvement compared to the standard tracking module (using the same PLL and DLL loops parameters as here). As such, the benefit of combining L1 C/A with L2C

is underlined by an additional 1 dB sensitivity improvement compared to a single frequency Kalman filter based tracking module.

Moreover, the proposed method not only permits tracking of both signals at once with a greater sensitivity than standard single frequency tracking loops but also outputs an estimated value of the TEC encountered on the signal path. The estimated TEC is shown in Figure 6-11 as a function of time. As a means of comparison, the estimated TEC obtained from GSNRx$^{\text{TM}}$ (GNSS Software Navigation Receiver), a software receiver developed by the PLAN (Position Location And Navigation) group (Petovello et al 2008), and from a NovAtel OEMV-3 (both L2C capable) are presented. The TEC values are derived from carrier smoothed pseudoranges for both GSNRx$^{\text{TM}}$ and the NovAtel receiver.
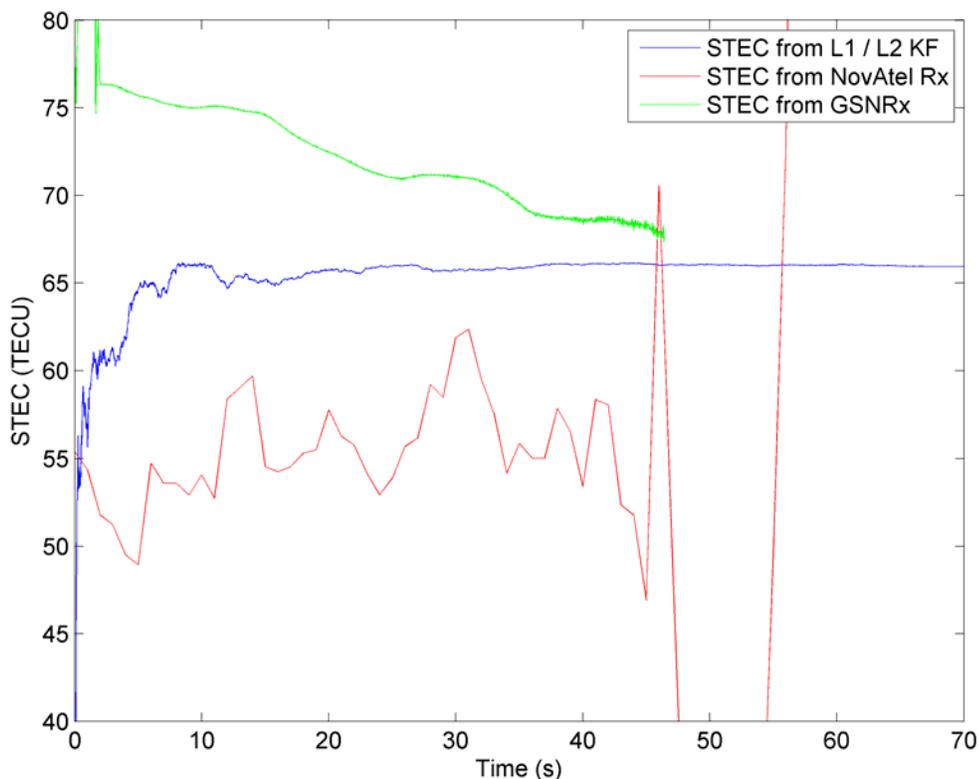
Figure 6-11 : Estimated TEC values encountered on the signal path as a function of time

However, even if the above values are in accordance with each other, they do not match the vertical TEC value of 8.9 TECU generated by the International GNSS Service (IGS). Indeed, the TEC values generated by the NovAtel receiver, GSNRx^{TM} receiver or Kalman filter based tracking method are corrupted by the satellite and receiver instrumental biases. Appendix C shows how it is possible to correct for the satellite bias using the TGD parameter provided in the broadcast ephemeris and how one can estimate the receiver instrumental bias and ionospheric effect if two or more L2C satellites are tracked. An estimate of the receiver instrumental bias of 12.8 nanoseconds, derived in Appendix C using data collected two weeks before the above data collection with

attenuation was computed. Since the instrumental biases are almost constant over time, the same value was used for correcting the TEC values shown in Figure 6-11. The satellite elevation was then computed to determine the vertical TEC and compare it to the IGS generated value, as shown in Figure 6-12.
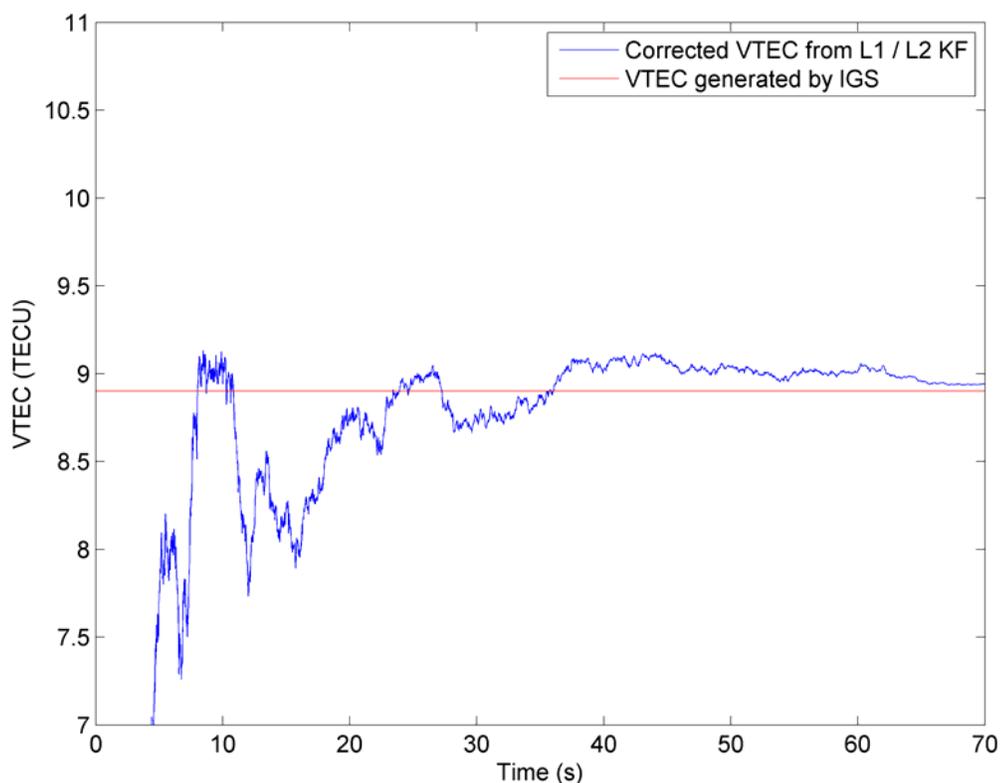
Figure 6-12: Satellite and receiver bias free vertical TEC values derived from the Kalman filter based tracking and compared to the IGS generated values

As this data set was collected under quiet ionospheric conditions, the ionospheric effects disturbing the L1 and L2 signals are also constant over time. As such, the TEC encountered on the signal path is also almost constant (barely changing due to satellite motion) which represents ideal conditions for the method developed herein. However, it

is well known that the TEC can vary quickly during iosnopheric scintillation events. This is discussed in the following section.

6.1.3 Kalman filter based tracking under scintillations

6.1.3.1 Presentation of the scintillation effect

Solar activity is not constant in time, but varies according to a cycle of eleven years. As the sun's activity increases, it is said to enter a period of solar maximum. During this period of high activity, the Earth's ionosphere becomes denser and thicker as it reacts to the intensified far ultraviolet spectrum of the sun. The sun ejects billion of tons of plasma through the solar flare phenomenon which in turn produces magnetic storms and ionospheric storms in the Earth's ionosphere. During such events, the ionosphere's TEC does not remain constant but changes according to the incoming plasma creating irregularities in the TEC (Klobuchar 1996). These irregularities can cause diffraction and scattering of radio signals when passing through the ionosphere. The resulting signals present random temporal fluctuations in amplitude and phase when they are captured by a receiver antenna on the surface of the Earth. It is these random amplitude and phase fluctuations which are collectively known as ionospheric scintillation (Klobuchar1996).

6.1.3.2 Obtaining real data containing ionospheric scintillation

Whereas the sun's activity was not in a period of solar maximum at the time of writing of this thesis, it was slowly drifting toward it and should reach this state in two to four years time. However, intense solar outbursts have been known to occur during below average solar cycles and especially on the up-side slope of solar activity.

The data used herein were collected by Aiden Morrison, PhD candidate in the PLAN group at the time of writing. The data were collected at Eureka, Nunavut, Canada located at latitude 79°58′59″N and longitude 85°56′59″W between October 6 and November 28, 2008. Scintillation events were confirmed by an Ionospheric Scintillation Monitor Receiver (Beach & Kintner 2001). Since the data were not collected during a solar maximum, it is not expected to contain fast varying strong scintillation.

6.1.3.3 Processing the data using the Kalman filter based tracking

In the following, the combined L1 / L2 Kalman filter based tracking module is used to process the above data.

First the estimated TEC values as output by the Kalman filter and the GSNRx^{TM} software receiver are shown in Figure 6-13. Once again, the TEC values derived from GSNRx^{TM} make use of carrier smoothed pseudoranges.
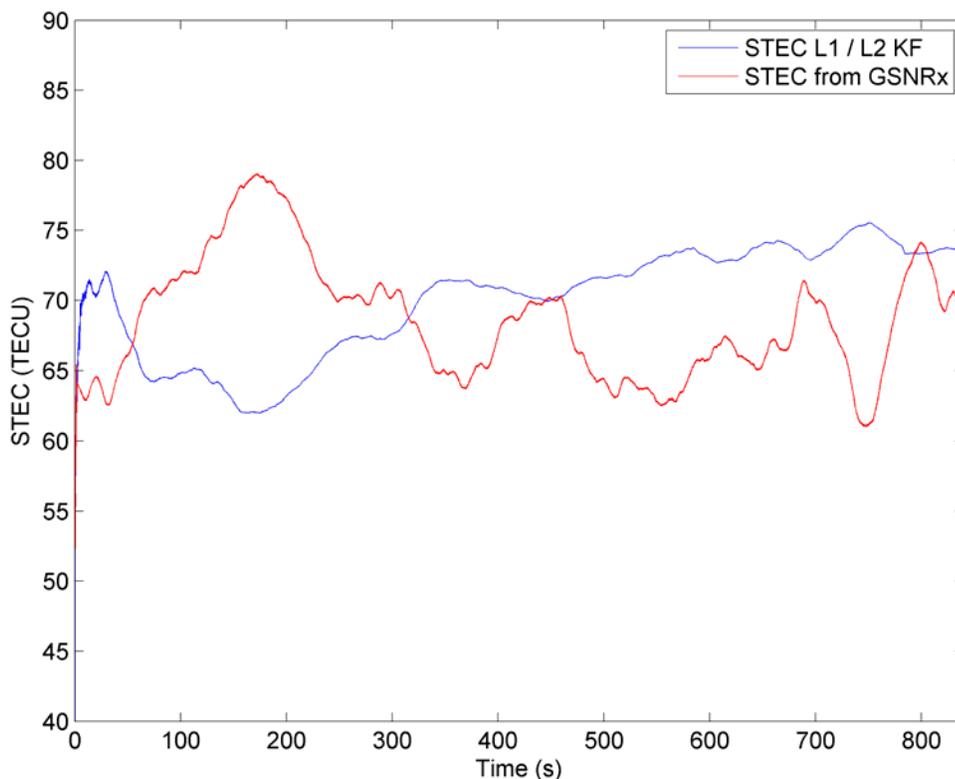
Figure 6-13 : TEC values output by the Kalman filter tracking and GSNRx™ smooth pseudorange during scintillation

The TECs encountered along the signal path do not remain constant as it was the case for real data collected during a quiet day. On the contrary, the TEC values vary slowly as the signals pass through large irregularities in the ionosphere.

Once again, even if the TEC encountered on the signal path matched for GSNRx™ and the Kalman based tracking, they are far from the IGS generated value of 5.3 TECU, as shown in Figure 6-14. The latter is smooth and more than likely a poor estimate of the real ionosphere over Eureka due to the lack of data in the proximity of Eureka used in the IGS model. As such, the computed TEC values are corrected according to Appendix C and results are shown in Figure 6-14. Note that the same receiver delay was used even if

the above data was taken almost two months later. Indeed, only one L2C satellite was present in the Eureka data set. Therefore, it is possible that a receiver bias is still present in the so-called corrected vertical TEC values.
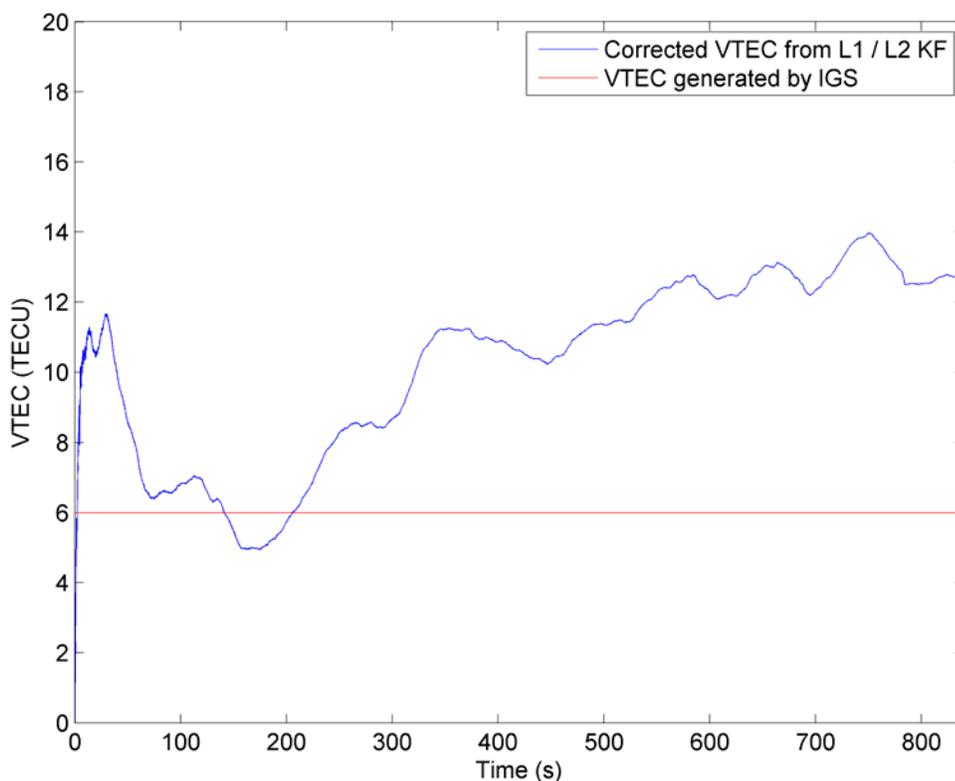
Figure 6-14: Satellite and receiver biases free vertical TEC values derived from the Kalman filter based tracking and compared to the IGS generated values

One of the effects of the fast ionospheric scintillation being temporal fluctuations in the signal amplitude, the C/N_0 for L1 is estimated and shown as a function of time in Figure 6.15. The L1 C/N_0 does not stay constant over time but varies according to the satellite motion. As the satellite slowly drifts away from zenith, the C/N_0 decreases. However, an odd spike in the C/N_0 can be seen at about 784 s. This spike could be the result of a fast varying irregularity, resulting in an increase in the amplitude of the L1 signal. Indeed, the

L1 was probably diffracted and recombined additively. In order to confirm this effect, a zoom around the 784 s is done on the graph of the TEC values. Figure 6-16 presents the slant TEC values estimated as well as the L1 C/N_0 estimated at epoch 784 s.
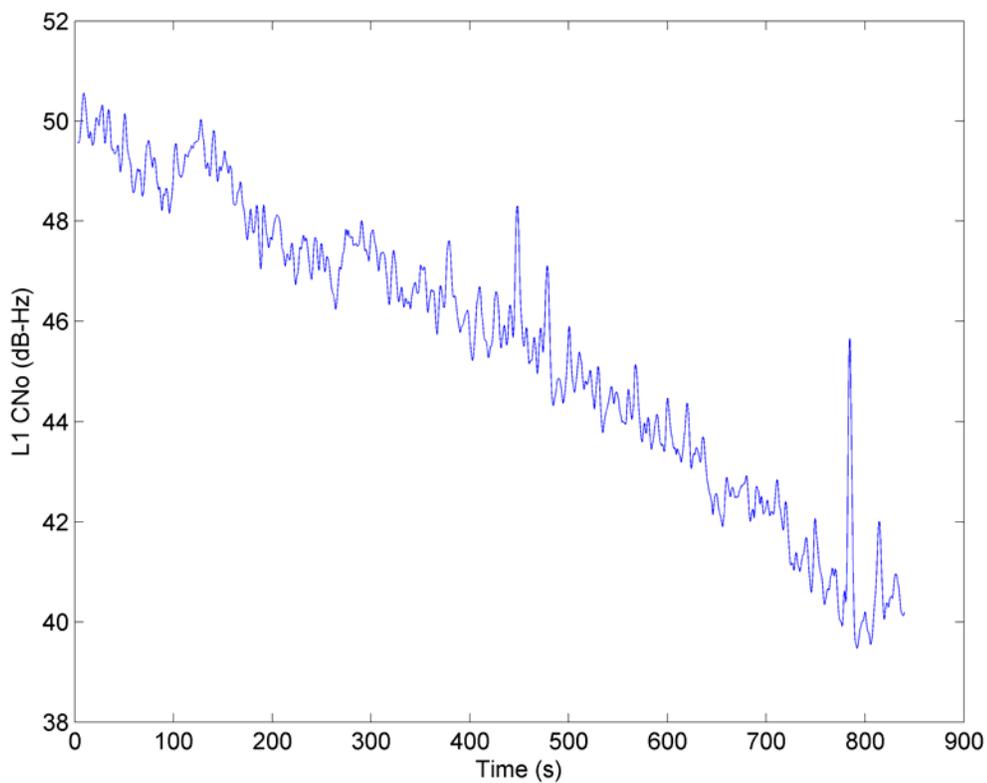
Figure 6-15 : Estimated L1 C/N_0 values as a function of time
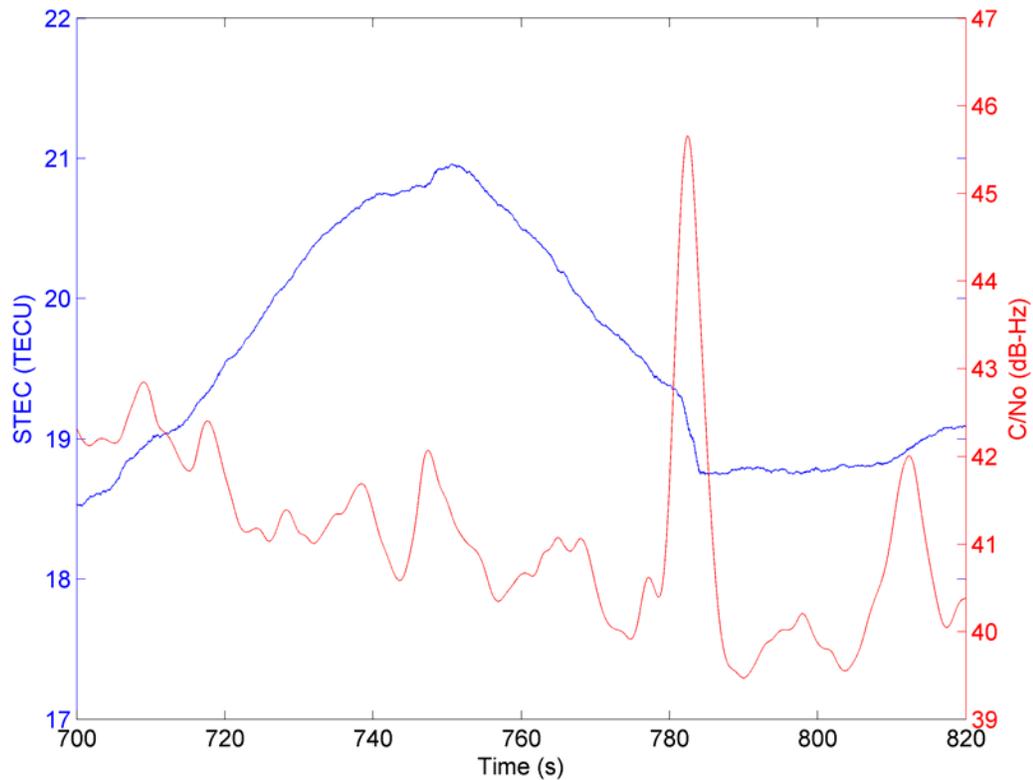
Figure 6-16: Estimated TEC values and C/N$_0$ during rapidly varying scintillation

The observed increase in the estimated C/N$_0$ is synchronized with a rapid decrease in the TEC encountered on the signal path. This corresponds to a boundary of one of the ionospheric irregularities with a rapid change in TEC. As such, the developed Kalman filter based tracking is capable of tracking during slow and rapid changes of TEC values encountered along the signal path, and, as such through at least minor scintillations events.

6.2 Conclusions

In this chapter, the possibility of combined tracking of signals transmitted on different frequencies was discussed. The main problem with inter-frequency combination lays in

the frequency dependent effects induced by the ionosphere, resulting in an additional code delay and phase advance different for each signal. As such, it has been shown that using one signal only to track both L1 C/A and L2C is not possible as it results in a residual Doppler frequency error and a bad synchronization of the local code. In order to solve these difficulties, one can either track each signal independently or use one signal to aid the other. However, neither of these solutions actually combines the signals as they do not make use of both signals to obtain better estimates of the desired parameters and as such, the tracking performance is limited to the signal of greatest power. Therefore, a Kalman filter based tracking method combining the outputs of the phase and code discriminators and aiming to estimate the TEC variation on the signal path was proposed. Moreover, as this method uses the outputs of the discriminators, a complete derivation of the statistical properties of the $I.Q$ and early minus late power discriminators was done and presented in Appendices A and B. The obtained mean and variance were used to approximate the popular auto-normalizing *atan* discriminator and normalized early minus late envelope. The fact that one can approximate the noise corrupting the discriminators as Gaussian was demonstrated. The implemented Kalman filter based tracking is able to outperform the single frequency tracking on L1 and L2. The sensitivity of the novel method is 3 dB above L1 standard tracking and 4.5 dB above L2 standard tracking provided that the single frequency tracking modules have a PLL bandwidth of 15 Hz and a DLL bandwidth of 0.5 Hz with carrier aiding for a static receiver under attenuation. As a by-product of the combined tracking, the TEC encountered along the signal path is also estimated. As such, it was shown that the Kalman filter tracking also provides a fast and accurate estimate of the TEC when corrected for the satellite and receiver instrumental

biases. Finally, the proposed Kalman filter based tracking method is able to track through at least minor scintillations.

Chapter Seven: Conclusions, recommendations and future work

7.1 Conclusions and recommendations

7.1.1 Combined acquisition

By combining the GPS signals transmitted on the L1 and L2 frequency bands, one can not only profit from the advantages of L1 (higher signal power) and L2 (no need for data bit synchronization) but also improve overall detection capability compared to using only one signal. Of all the different methods proposed to combine L1 C/A and L2C signals at the acquisition level, three proved to outperform the legacy L1 C/A non-coherent acquisition. Two are independent of the residual Doppler frequency errors and relative phase between L1 and L2 correlator outputs whereas the last one has performance related to residual Doppler frequency error. For the first method, namely NC_{L1L2}, combining the non-coherent acquisition on L1 and L2 showed promising performance when the proper weight is applied on L2. An improvement of 8 % in terms of probability of detection compared to the standard non-coherent acquisition on L1 only was observed. Similarly, for the $NCDiff_{L1L2}$ method, combining non-coherent and differential acquisitions on L1 and L2 significantly improved the probability of properly detecting the signals. An improvement of 16 % is expected for the $NCDiff_{L1L2}$ method. The $Diff_{L1L2}$ method of combining differential acquisitions performed on L1 and L2 is strongly dependent on the residual Doppler frequency remaining after the Doppler removal process. Poor

performance was observed when the residual Doppler error varies over the whole range of half a Doppler bin size defined by a 1 ms coherent integration (0 Hz to 333.33 Hz). However, by limiting the Doppler error to 100 Hz, performance is greatly improved and the Diff_{L1L2} method showed an improvement of 20 % compared to the non-coherent L1 acquisition. Similar conclusions can be drawn for the case where integration times longer than one millisecond were used. Because limiting the Doppler bin size allows for increased coherent integration times, the Diff_{L1L2} is recommended for longer coherent integration. Indeed, two milliseconds of coherent integration proved to reduce the range of the residual Doppler error such that the Diff_{L1L2} method is no longer negatively affected by this error. Finally, while the NCDiff_{L1L2} method outperforms the non-coherent L1 acquisition, it also shows better performance than the other two combining methods. However, due to its complexity compared to the NC_{L1L2} method, one would employ it only when appropriate computational power is available.

7.1.2 Combined tracking

Combining tracking of signals transmitted on different frequencies was demonstrated. The main problem in inter-frequency combination lies in the frequency dependent effects induced by the ionosphere resulting in code delay and phase advance. Using one signal only to track both L1 C/A and L2C is not possible as it results in a residual Doppler frequency error and a bad synchronization of the local code. In order to solve for these difficulties, one can either track each signal independently or use one signal to aid the other. However, neither of these solutions actually combine the signals as they do not make use of both signals to obtain better estimate of the desired parameters. Therefore, a

Kalman filter based tracking method combining the outputs of the phase and code discriminators and aimed at estimating the TEC variation on the signal path was proposed, implemented and tested. The *I.Q* and early minus late power discriminator means and variances were used to approximate the means and variances of the *atan* and normalized early minus late envelope discriminators. It was shown that one can safely approximate the noise corrupting the discriminators as Gaussian for C/N_0 above 20 dB-Hz. The sensitivity of the novel method is about 3 dB above L1 standard tracking and 4.5 dB above L2 standard tracking provided that the single frequency tracking modules have a PLL bandwidth of 15 Hz and a DLL bandwidth of 0.5 Hz with carrier aiding. As a by-product of the combined tracking, the TEC encountered on the signal path is also estimated. However, the TEC values estimated by the Kalman filter remain corrupted by the satellite and receiver instrumental biases. To counteract this problem, it was shown that by tracking two or more Block IIR-M satellites at once using the Kalman filter based tracking algorithm, it was possible to correct for the satellite instrumental bias through the navigation message parameters and then estimate the receiver instrumental bias and vertical TEC. As such, the Kalman filter based tracking can also provide a fast and accurate estimate of the TEC if two or more satellites are tracked (provided that the two satellites tracked experience different levels of ionosphere effect). Finally, it was shown that the proposed Kalman filter combined based tracking method is able to track through at least minor scintillation.

7.2 Future work

7.2.1 Combined acquisition

The combined acquisition methods proposed in this research were applied on similar signals in terms of chipping rate and modulation. Indeed, both signals used a 1.023 MHz code frequency and a BPSK modulation. With the development and modernization of new GNSS signals, new horizons are opening in terms of signal combinations at the same frequency and at different frequencies. For instance, GPS is currently undergoing the implementation of another signal on the L5 frequency band. This new signal has a transmitted power and a chipping rate higher than the L1 C/A signal. Moreover, it is composed of a data channel on the in-phase component and a pilot channel on the quadra-phase component through a QPSK modulation. Therefore, the possibility of combining L1 C/A, L2C, L5 data and L5 pilot could be considered through both inter-frequency and intra-frequency combinations. Another example is Galileo, which is predicted to be operational in 2013. This system will be made of signals transmitted over three frequency bands. With the arrival of new frequencies, the combined acquisition technique proposed in this research could be extended to include more than two frequencies. However, most of the new signals include new modulations changing the shape of the auto-correlation function. As such, the methods developed during this research would need to be adapted and investigated.

7.2.2 Combined tracking

The proposed Kalman filter based combined tracking algorithm presented in this research makes use of the L1 C/A, L2 CM and L2 CL signals. For instance, the phase discriminator used herein is a Costas discriminator as it is insensitive to 180° phase reversal in the signal, which occurs as the data bit sign changes. The use of a Costas discriminator is required for signals with data bits, but it lowers the PLL tracking threshold by 6 dB compared to a pure PLL. However, as L2 CL is a pilot channel, it does not contain data bits and a pure (four quadrants) discriminator such as *atan2*, as presented in Julien (2005) or Macabiau et al (2003), could be applied to this channel. Moreover, the coherent integration time does not need to be limited to the data bit length for a pilot channel. In light of the above, the proposed Kalman filter could be improved to include the use of a pure discriminator and longer coherent integration time for the L2C pilot channel. This assumes the possibility of using asynchronous observations on L2 CL, L1 C/A and L2 CM.

The proposed Kalman filter based tracking should then be used to obtain pseudorange and phase measurements and compute the receiver position. Once again, results should be expressed in terms of improvement compared to standard single frequency tracking. As was the case for the combined acquisitions, the possibility of tracking signals on more than two frequencies at once needs to be considered. In particular, the use of three frequencies (L1, L2, L5 for GPS and L1, E5a, E5b for Galileo) would deliver more observations to process with the Kalman filter. Therefore, it is expected to reach better performance than that observed during this work while providing a better estimate of the

inter-frequency delays which can in turn be used to estimate the ionosphere and receiver instrumental biases.

REFERENCES

Abramowitz, M. and I. A. Stegun, (1964) *Handbook of mathematical functions*, Dover Publications, Inc., New York

Avellone, G., M. Frazzetto, and E. Messina (2007) "A New Waveform Family for Secondary Peaks Rejection in Code Tracking Discriminators for Galileo BOC(n,n) Modulated Signals", in *Proceedings of the 2007 National Technical Meeting of the Institute of Navigation*, 22 - 24 January, The Catamaran Resort Hotel, San Diego, California

Avila-Rodriguez J.-A., V. Heiries , T. Pany, B. Eissfeller, (2005) "Theory on Acquisition Algorithms for Indoor Positioning", in *Proceedings of 12th Saint Petersburg International Conference on integrated navigation systems*, 23-25 May, Saint Petersburg, Russia

Beach, T. and P. Kintner, (2001) "Development and Use of a GPS Ionospheric Scintillation Monitor", *IEEE Transactions on Geoscience and Remote Sensing*, vol 39, no 5, May

Betz J.W. (2002) "Binary Offset Carrier Modulations for Radionavigation, Navigation", *Journal of the Institute of Navigation*, vol 48, no 4, Winter 2001-2002, pp.227-246

Borio, D. (2008) *A Statistical Theory for GNSS Signal Acquisition*, Doctoral Thesis, Dipartimento di Elettronica, Politecnico di Torino, Italy

Borio, D., C. Gernot, F. Macchi and G. Lachapelle (2008) *The Output SNR and its Role in Quantifying GNSS Signal Acquisition Performance*, ENC GNSS 08, 23-25 April 2008, Toulouse, France

Braasch, M. (1997) "Multipath Effects", [Chapter 14] in *Global Positioning System: Theory and Applications Volume I*, B.W. Parkinson, B.W. and J.J. Spilker, Ed., American Institute of Aeronautics and Astronautics Inc., Washington, pp. 547-568

Brown, R.G, and P.Y.C. Hwang (1992), *Introduction to Random Signals and Applied Kalman Filtering*, 2nd ed, John Wiley & Sons, Inc., 1992

Cannon, M.E. (2005) *Satellite Positioning*, ENGO 561 Lecture Notes, Department of Geomatics Engineering, University of Calgary, Canada

Coco, D.S., C. Coker, S.R. Dahlke, J.R. Clynch (1991) "Variability of GPS satellite differential group delay biases", *IEEE Transactions on Aerospace and Electronic Systems*, vol 27, no 6, pp. 931-938.

Crews, C.L. (2008) *Long-Term Future of GPS*, Proceedings of ION NTM 2008, San Diego, CA

Dong, S, X. Li and H. Wu (2007) "About Compass Time and Its Coordination with other GNSSs", in *Proceedings of the 39th Annual Precise Time and Time Interval (PTTI) Meeting*, 26-29 November 26-29, Long Beach, California, US

Fedrizzi, M., E.R. de Paula, I.J. Kantor, R.B. Langley, A. Komjathy, E.A. Araujo-Pradere, and T.J. Fuller-Rowell (2004) "Ionospheric Response to Severe Magnetic Storms Using GPS Total Electron Content Measurements" in *Proceedings of the International Beacon Satellite Symposium 2004*, 18-22 October, Trieste, Italy

Fontana, R.D., W. Cheung, P.M. Novak, T.A. Stansell, JR. (2001) "The new L2 civil signal" in *Proceedings ION GNSS 2001*, Salt Lake City, USA, pp. 617-631

Gebre-Egziabher, D., A. Razavi, P. Enge, J. Gautier, S. Pullen, B.S. Pervan and D. Akos (2005) Sensitivity and Performance Analysis of Doppler-Aided GPS Carrier-Tracking Loops, NAVIGATION, 52(2), 49-60.

Gelb, A. (1974) *Applied Optimal Estimation* The M.I.T. Press, Cambridge, Massachusetts.

Gerein, N., M. Olynik and M. Clayton (2004) "Galileo BOC(1,1) Prototype Receiver Development", in *Proceedings of ION GNSS 2004*, 21-24 September, Long Beach Convention Center, Long Beach, California

Grewal, M. S. and A. P. Andrews (2001) *Kalman Filtering: Theory and Practice using Matlab*, 2nd Edition, John Wiley & Sons, New York, Chichester

Groves, P. D., and C. J. Mather and A. A. Macaulay, "Demonstration of non-coherent deep INS/GPS integration for optimized signal-to-noise performance," in *Proceedings of ION GNSS 2007*, 25-28 September, Forth Worth TX, USA

Humphreys, T.E., M.L. Psiaki, P.M. Kintner, B.M. Ledvina and P.M. Kintner Jr. (2005) "GPS Carrier Tracking Loop Performance in the Presence of Ionospheric Scintillations", in *Proceedings of ION GNSS 2005*, 13-16 September, Long Beach Convention Center, Long Beach, California

Ioannides R. T., L.E. Aguado and G. Brodin (2007) "Diverse Signals Combinations for High-Sensitivity GNSS", *Journal of Navigation*, vol 60, no 3, Cambridge University Press, pp. 497-515

Julien, O. (2005), *Design of Galileo L1F Tracking Loops*, PhD Thesis, Department of Geomatics Engineering, University of Calgary, UGCE Report 20227

Kaplan, E.D., J.L. Leva and M.S. Pavloff (2006) "Fundamentals of Satellite Navigation", [Chapter 2] in *Understanding GPS: Principles and Applications*, E.D. Kaplan, Artech House Publishers, Boston, London

Keegan, R.G. (1990) P-*code Aided Global Positioning System Receiver*, U.S. Patent No. 4,972,431.

Klobuchar, J.A. (1996) "Ionospheric effects on GPS", [Chapter 12] in *Global Positioning System: Theory and Applications Volume 1*, B.W. Parkinson, B.W. and J.J. Spilker, Ed., American Institute of Aeronautics and Astronautics Inc., Washington, pp. 485-515

Lachapelle, G. (2006) *GPS Theory and Applications*, ENGO 625 Lecture Notes, Department of Geomatics Engineering, University of Calgary, Canada

Landis, D., T. Thorvaldsen, B. Fink, P. Sherman and S.Holmes (2006) A Deep Integration Estimator for Urban Ground Navigation, ION Annual Meeting/IEEE PLANS, San Diego, CA, Institute of Navigation and IEEE, 927-932.

Lim, D.W., S.W. Moon, C. Park, S.J. Lee (2006) "L1/L2CS GPS Receiver Implementation with Fast Acquisition Scheme," in *Proceedings of Position, Location, And Navigation Symposium*, *IEEE/ION*, 25-27 April, pp 840- 844

Macchi, F. (2009) *Development and Testing of an L1 Combined GPS-Galileo Software Receiver*, PhD Thesis, Department of Geomatics Engineering, University of Calgary, Canada (Available at http://plan.geomatics.ucalgary.ca)

MacDoran, P.F., R.B. Miller, L.A. Buennagel, J.H. Whitcomb (1985) "Codeless System for Positioning with NAVSTAR-GPS," in *Proceedings of the 1std International Symposium on Precise Positioning with the Global Positioning System*, Vol.1, Rockville, Maryland.

Megahed, D., C. O'Driscoll and G. Lachapelle (2009) "Performance Evaluation of Combined L1/L5 Kalman Filter-Based Tracking versus Standalone L1/L5 Tracking in Challenging Environments", in *Proceedings of ION GNSS 2009*, 22-25 September, Savannah GA, USA

Mongrédien, C., M.E. Cannon and G. Lachapelle (2007) "Performance Evaluation of Kalman Filter Based Tracking for the New GPS L5 Signal", in *Proceedings of ION GNSS 2007*, 25-28 September, Forth Worth TX, USA

Mongrédien, C. (2008) *GPS L5 Software Receiver Development for High-Accuracy Applications,* PhD Thesis, Department of Geomatics Engineering, University of Calgary, UGCE Report 20268

Muthuraman, K., S.K. Shanmugam and G. Lachapelle (2007) "Evaluation of Data/Pilot Tracking Algorithms for GPS L2C Signals Using Software Receiver," in *Proceedings of ION GNSS 2007*, 25-28 September, Fort Worth TX, USA

Muthuraman, K., R. Klukas and G. Lachapelle (2008) "Performance Evaluation of L2C Data/Pilot Combined Carrier Tracking", in *Proceedings of ION GNSS 2008*, 16-19 September, Savannah, GA, USA

Nunes, F., F. M. G. Sousa, J. M.N. Leitao (2005) "Improving Multipath Mitigation in GPS/Galileo BOC Signals with Gating Functions", in *Proceedings of the 61st Annual Meeting*, June 27 - 29, Royal Sonesta Hotel, Cambridge, Massachusetts

Ohlmeyer, E.J. (2006) Analysis of an Ultra-Tightly Coupled GPS/INS System in Jamming, ION Annual Meeting/IEEE PLANS, San Diego, CA, Institute of Navigation and IEEE, 44-53.

Pany, T., M. Irsigler and B. Eissfeller (2005) "S-Curve Shaping: A New Method for Optimum Discriminator Based Code Multipath Mitigation", in *Proceedings of ION GNSS 2005*, 13-16 September, Long Beach Convention Center, Long Beach, California

Petovello, M. and G. Lachapelle (2006) "Comparison of Vector-Based Software Receiver Implementation with Applications to Ultra-Tight GPS/INS Integration", in *Proceedings of ION GNSS 2006*, 26-29 September, Forth Worth TX, USA, pp. 1790-1800

Petovello, M., C. O'Driscoll and G. Lachapelle (2008) "Carrier Phase Tracking of Weak Signals Using Different Receiver Architectures", in *Proceedings of ION NTM08*, 28-30 January, San Diego CA, USA.

Petovello, M., C.O'Driscoll, G. Lachapelle, D. Borio and H. Murtaza (2008) "Architecture and Benefits of an Advanced GNSS Software Receiver", *Journal of Global Positioning Systems*, vol 7, no 2, pp 156-168.

Psiaki, M.L. (2001) "Smoother-Based GPS Signal Tracking in a Software Receiver", in *Proceedings of ION GPS 2001*, 11-14 September, Salt Lake City UT, USA, pp 2900-2913.

Psiaki, M.L. and H. Jung (2002) "Extended Kalman Filter Methods for Tracking Weak GPS Signals", in *Proceedings of ION GPS 2002*, 24-27 September, Portland OR, USA, pp 2539-2553

Psiaki, M. L., L. Winternitz, M. Moreau (2004) "FFT-Based Acquisition of GPS L2 Civilian CM and CL Signals," in *Proceedings of the ION GNSS 2004*, 21-24 September, Long Beach CA, USA, pp 457-473

Requicha, A., (1970) "Direct computation of distribution functions from characteristic functions using the fast fourier transform" in *Proceedings of the IEEE*, vol. 58, no. 7, pp. 1154-1155

Ries, L., F. Legrand, L. Lestarquit, W. Vigneau, J-L. Issler (2003) "Tracking and Multipath Performance Assessments of BOC Signals Using a Bit-Level Signal Processing Simulator", in of ION GNSS 2003, 9 – 12 September, Oregon Convention Center, Portland OR, USA

Sasibhushana Rao, G., (2007) "GPS satellite and receiver instrumental biases estimation using least squares method for accurate ionosphere modeling", *Journal of earth system science*, vol. 116, n°5, pp. 407-411.

Skone, S. (2007) *Atmospheric Effects on Satellite Navigation Systems*, ENGO 633 Lectures Notes, Department of Geomatics Engineering, University of Calgary, Canada

Simon, Marvin K., (2006) *Probability Distributions Involving Gaussian Random Variables: A Handbook for Engineers, Scientists and Mathematicians*, Springer-Verlag New York, Inc., Secaucus, NJ

Van Dierendonck, A.J., J.B. McGraw, and R.G. Brown (1984) "Relationship between Allan variances and Kalman filter parameters" in *Proceedings of the 16th Annual Precise Time and Time Interval (PTTI) Applications and Planning Meeting*, NASA Goddard Space Flight Center, pp 273–293

Van Dierendonck, A. J., P. Fenton and T. Ford (1992) "Theory and Performance of Narrow Correlator Spacing in a GPS Receiver", *Journal of the Institute of Navigation*, vol. 39, no. 3, Fall 1992

Van Dierendonck, A. J., (1996) "GPS Receivers", [Chapter 8] in *Global Positioning System: Theory and Applications Volume 1*, B.W. Parkinson, B.W. and J.J. Spilker, Ed., American Institute of Aeronautics and Astronautics Inc., Washington, pp. 329-405

Ward, P. (2006) "GPS Satellite Signal Characteristics", [Chapter 4] in *Understanding GPS: Principles and Applications*, E.D. Kaplan, Artech House Publishers, Boston, London

Ward, P. (2006) "Satellite Signal Acquisition and Tracking", [Chapter 5] in *Understanding GPS: Principles and Applications*, E.D. Kaplan, Artech House Publishers, Boston, London

Watson, R., G. Lachapelle, R. Klukas, S. Turunen, S. Pietilä and I. Halivaara (2006) "Investigating GPS Signals Indoors with Extreme High-Sensitivity Detection Techniques", *Journal of the Institute of Navigation*, vol 52, no 4, pp. 199-213.

Wiederholt, L.F., and E.D. Kaplan (2006) "GPS System Segments", [Chapter 3] in *Understanding GPS: Principles and Applications*, E.D. Kaplan, Artech House Publishers, Boston, London

Woo, K.T. (1999) "Optimum semi-codeless carrier phase tracking of L2," in *Proceedings of. ION GPS 1999*, Nashville, TN, USA, pp 289-306.

Yang, C., C. Hegarty, and M. Tran (2004) "Acquisition of the GPS L5 Signal Using Coherent Combining of I5 and Q5", in *Proceedings of ION GNSS 2004*, 21-24 September, Long Beach CA, USA

Yang, C. (2005) "Joint Acquisition of CM and CL Codes for GPS L2C", in *Proceedings of the 61st Annual Meeting*, June 27 - 29, Royal Sonesta Hotel, Cambridge, Massachusetts

Yu, W., G. Lachapelle and S. Skone (2006) "PLL Performance for Signals in the Presence of Thermal Noise, Phase Noise, and Ionospheric Scintillation", in *Proceedings of ION GNSS 2006*, 26-29 September, Forth Worth TX, USA

Appendix A: Derivation of *I.Q* phase discriminator expected value and variance

From Van Dierendonck (1996), the real and complex part of the prompt correlator can be expressed as

$$I_P = sinc(\pi \Delta fT)D\sqrt{2\frac{C}{N_0}T}R(\tau)cos(\delta\phi) + n_I \qquad \textbf{A-1}$$

$$Q_P = sinc(\pi \Delta fT)D\sqrt{2\frac{C}{N_0}T}R(\tau)sin(\delta\phi) + n_Q \qquad \textbf{A-2}$$

Δf being the frequency error, T the coherent integration time, D the data bit, R the auto-correlation function, τ the code error and $\delta\phi$ the phase error.

$n_{I/Q}$ represents the Gaussian noise corrupting the real and complex part of the correlator respectively and has the following properties:

$$var(n_I) = var(n_Q) = 1 \qquad \textbf{A-3}$$

$$E(n_I) = E(n_Q) = E(n_I n_Q) = 0 \qquad \textbf{A-4}$$

Note that the I and Q parts of the noise are not independent but can be considered uncorrelated due to the carrier removal process which multiplied it by the *sin* and *cos* which are orthogonal functions.

As the final purpose is to use the statistical properties of the *I.Q* discriminator as an approximation of the auto-normalizing *atan* discriminator, one has to normalize Equations A-1 and A-2 by dividing by

$$\sqrt{2\frac{C}{N_0}T} \ .$$

$$\text{A-5}$$

Then, assuming that the Doppler error Δf and code error τ are small and that one integrates over one data bit only, Equations A-1 and A-2 can be rewritten (after normalization) as

$$I_P = cos(\delta\phi) + N_I \tag{A-6}$$

$$Q_P = sin(\delta\phi) + N_Q \tag{A-7}$$

with $N_I = \dfrac{n_I}{\sqrt{2\dfrac{C}{N_0}T}}$ and $N_Q = \dfrac{n_Q}{\sqrt{2\dfrac{C}{N_0}T}}$.

As such, the statistics of N_I and N_Q are

$$var(N_I) = var(N_Q) = \sigma_N^{\ 2} = \frac{1}{2\dfrac{C}{N_0}T} \tag{A-8}$$

$$E(N_I) = E(N_Q) = E(N_I N_Q) = 0. \tag{A-9}$$

Finally, using Equations A-6 and A-7, one can access the statistical properties of the *I.Q* discriminator.

Calling $\delta\hat{\phi} = I_P Q_P$, its expected value is

$$E(\delta\hat{\phi}) = E(I_P Q_P)$$

$$= E\left[(cos(\delta\varphi) + N_I)(sin(\delta\varphi) + N_Q) \right]$$

$$= E\left[cos(\delta\varphi) sin(\delta\varphi) \right]$$

$$= \frac{1}{2} sin(2\delta\varphi)$$

A-10

Therefore, for small values of the phase error, the expected value reduces to the actual phase error:

$$E(\delta\hat{\phi}) = E(I_P Q_P) = \delta\phi$$

A-11

Regarding the computation of the discriminator variance, the following formula is derived:

$$\sigma_{\delta\varphi}^2 = E(\delta\hat{\varphi}^2) - E(\delta\hat{\varphi})^2$$

$$= E(I_P^2 Q_P^2) - E(I_P Q_P)^2$$

$$= E\left[cos(\delta\hat{\varphi}) sin(\delta\hat{\varphi}) \right]^2 + 2E\left[cos(\delta\hat{\varphi})^2 sin(\delta\hat{\varphi}) \right] E\left[N_Q \right] + E\left[cos(\delta\hat{\varphi})^2 \right] E\left[N_Q^2 \right]$$

$$+2E\left[cos(\delta\hat{\varphi}) sin(\delta\hat{\varphi})^2 \right] E[N_I] + 4E\left[cos(\delta\hat{\varphi}) sin(\delta\hat{\varphi}) \right] E\left[N_I N_Q \right]$$

$$+2E\left[cos(\delta\hat{\varphi}) \right] E\left[N_I N_Q^2 \right] + E\left[sin(\delta\hat{\varphi})^2 \right] E\left[N_I^2 \right] + 2E\left[sin(\delta\hat{\varphi}) \right] E\left[N_I^2 N_Q \right]$$

$$+E\left[N_I^2 N_Q^2 \right] - E\left[cos(\delta\hat{\varphi}) sin(\delta\hat{\varphi}) \right]^2$$

Remembering the noise properties, this expression reduces to:

$$\sigma_{\delta\varphi}^{2} = E\left[\cos(\delta\hat{\varphi})^{2}\right]E\left[N_{Q}^{2}\right] + E\left[\sin(\delta\hat{\varphi})^{2}\right]E\left[N_{I}^{2}\right] + E\left[N_{I}^{2}N_{Q}^{2}\right] \qquad \textbf{A-12}$$

$$\sigma_{\delta\phi}^{2} = \sigma_{N}^{2} + \sigma_{N}^{4} \qquad \textbf{A-13}$$

Appendix B: Derivation of the early minus late power code discriminator expected value and variance

From Equations A-1 and A-2 and through applying the normalization factor, the output of the early and late correlator can be expressed as (assuming a small frequency error and an integration period smaller than or equal to one data bit length)

$$I_E = R\left(\tau - \frac{\Delta}{2}\right)cos(\delta\phi) + N_{IE}$$ **B-1**

$$Q_E = R\left(\tau - \frac{\Delta}{2}\right)sin(\delta\phi) + N_{QE}$$ **B-2**

$$I_L = R\left(\tau + \frac{\Delta}{2}\right)cos(\delta\phi) + N_{IL}$$ **B-3**

$$Q_L = R\left(\tau + \frac{\Delta}{2}\right)sin(\delta\phi) + N_{QL}$$ **B-4**

Δ being the correlator spacing that is the number of chip between the early and late correlators.

However, before one begins the actual derivation of the early minus late power statistical properties, it is important to note that the noise corrupting the early and late discriminators is not completely uncorrelated. Indeed, even if one were to assume that the auto-correlation properties of the PRN code were perfect (hypothesis adopted herein), the output noise of the early and late correlators would be uncorrelated only if the correlator spacing Δ were more or equal to 1 chip. As such, if Δ is smaller than 1 as it is the case

for narrow correlator, the noise corrupting the early and late correlators can then be divided in two parts:
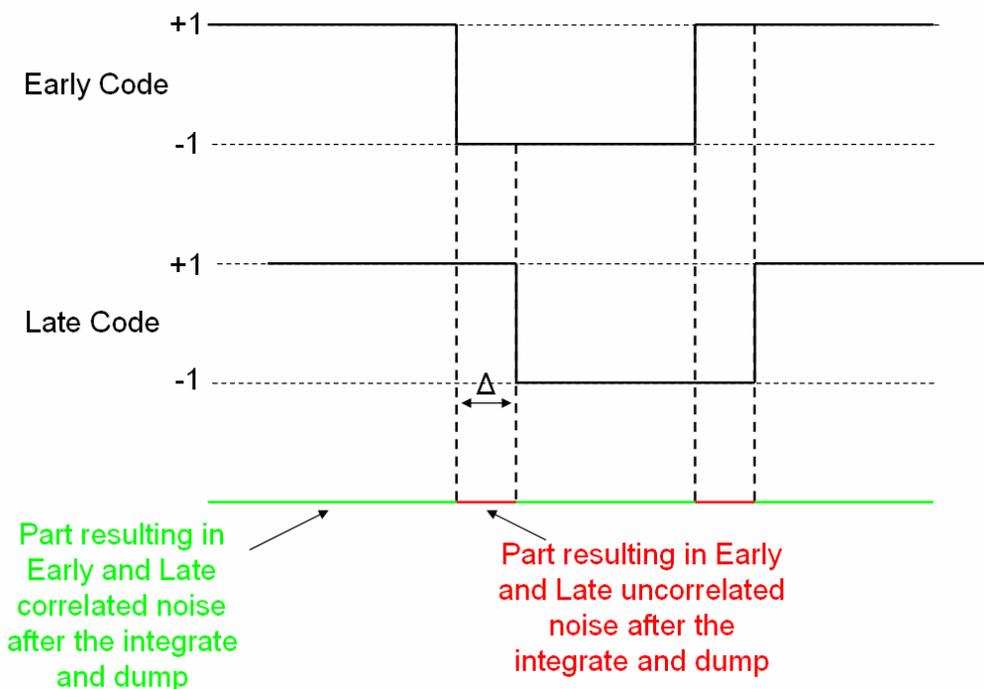
The first part called *W* represents the identical noise component shared between early and late correlators. The second part called *w* is the noise component uncorrelated (assuming perfect PRN code) for early and late correlators. These can be expressed as

$$N_{IE} = W_{IEL} + w_{IE}$$ **B-5**

$$N_{IL} = W_{IEL} + w_{IL}$$ **B-6**

$$N_{QE} = W_{QEL} + w_{QE}$$ **B-7**

$$N_{QL} = W_{QEL} + w_{QL}.$$ **B-8**

Note that the noise on the I and Q channels is uncorrelated and that

$$E(W_{IEL}) = E(w_{IE}) = E(w_{IL}) = 0$$

$$E(W_{QEL}) = E(w_{QE}) = E(w_{QL}) = 0$$

$$E(w_{IE}w_{IL}) = E(w_{QE}w_{QL}) = 0$$

$$E(W_{IEL}{}^2) = E(W_{QEL}{}^2) = (1-\Delta)\sigma_N{}^2$$

$$E(w_{IE}{}^2) = E(w_{IL}{}^2) = \Delta\sigma_N{}^2$$

$$E(w_{QE}{}^2) = E(w_{QL}{}^2) = \Delta\sigma_N{}^2.$$

The definition proposed herein for the early minus late power discriminator is the following:

$$\hat{\tau} = \frac{1}{2(2-\Delta)}\left[I_E{}^2 + Q_E{}^2 - (I_L{}^2 + Q_L{}^2)\right]. \tag{B-9}$$

For sake of simplicity, one also defines:

$$\bar{I}_E = R\left(\tau - \frac{\Delta}{2}\right)\cos(\delta\phi) \tag{B-10}$$

$$\bar{Q}_E = R\left(\tau - \frac{\Delta}{2}\right)\sin(\delta\phi) \tag{B-11}$$

$$\bar{I}_L = R\left(\tau + \frac{\Delta}{2}\right)\cos(\delta\phi) \tag{B-12}$$

$$\bar{Q}_L = R\left(\tau + \frac{\Delta}{2}\right)\sin(\delta\phi). \tag{B-13}$$

Using the previous definition and Equations B-1, B-2, B-3 and B-4, one can compute the expected value of $\hat{\tau}$ as

$$E\left[I_E^{\ 2} + Q_E^{\ 2} - (I_L^{\ 2} + Q_L^{\ 2})\right]$$

$$= \bar{I}_E^{\ 2} + \bar{Q}_E^{\ 2} - (\bar{I}_L^{\ 2} + \bar{Q}_L^{\ 2}) + E(N_{IE}^{\ 2}) + E(N_{QE}^{\ 2}) - E(N_{IL}^{\ 2}) - E(N_{QL}^{\ 2}).$$

However,

$$E(N_{IE}^{\ 2}) = E(N_{QE}^{\ 2}) = E(N_{IL}^{\ 2}) = E(N_{QL}^{\ 2})$$

and

$$E\left[I_E^{\ 2} + Q_E^{\ 2} - (I_L^{\ 2} + Q_L^{\ 2})\right]$$

$$= \left[R(\tau - \frac{\Delta}{2})\right]^2 - \left[R(\tau + \frac{\Delta}{2})\right]^2$$

$$= 2\tau(2 - \Delta).$$

Therefore,

$$E(\hat{\tau}) = \tau. \qquad\qquad \textbf{B-14}$$

The variance of the discriminator can be expressed as:

$$\sigma_{\hat{\tau}}^{\ 2} = \left(\frac{1}{2(2-\Delta)}\right)^2 [A - B]$$

with

$$A = E\left[\left(I_E^{\ 2} + Q_E^{\ 2} - (I_L^{\ 2} + Q_L^{\ 2})\right)^2\right]$$

and

$$B = E\left[\left(I_E^{\ 2} + Q_E^{\ 2} - (I_L^{\ 2} + Q_L^{\ 2})\right)\right]^2.$$

Then, developing the expression for A as

$$A = E\left[(I_E^{\ 2} + Q_E^{\ 2})^2\right] - 2E\left[(I_E^{\ 2} + Q_E^{\ 2})(I_L^{\ 2} + Q_L^{\ 2})\right]$$
$$+ E\left[(I_L^{\ 2} + Q_L^{\ 2})^2\right]$$

which can be expressed as

$$A = A_1 - 2A_2 + A_3$$

with

$$A_1 = E\left[(I_E^{\ 2} + Q_E^{\ 2})^2\right]$$

$$A_2 = E\left[(I_E^{\ 2} + Q_E^{\ 2})(I_L^{\ 2} + Q_L^{\ 2})\right]$$

$$A_3 = E\left[(I_L^{\ 2} + Q_L^{\ 2})^2\right].$$

Similarly,

$$A_1 = E\left[(\bar{I}_E + N_{IE})^4\right] + 2E\left[(\bar{I}_E + N_{IE})^2(\bar{Q}_E + N_{QE})^2\right] + E\left[(\bar{Q}_E + N_{QE})^4\right]$$
$$= A_{11} + 2A_{12} + A_{13}$$

with

$$A_{11} = E\left[(\bar{I}_E + N_{IE})^4\right]$$

$$A_{12} = E\left[(\bar{I}_E + N_{IE})^2(\bar{Q}_E + N_{QE})^2\right]$$

$$A_{13} = E\left[(\bar{Q}_E + N_{QE})^4\right].$$

One can also express A_{11} as

$$A_{11} = \bar{I}_E^4 + 6\bar{I}_E^2 E(N_{IE}^2) + 4\bar{I}_E E(N_{IE}^3) + E(N_{IE}^4).$$

Note that N_{IE} is Gaussian zero-mean and of variance σ_N^2. As such, it has a probability

density function of

$$f(x) = \frac{1}{\sqrt{2\pi\sigma_N^2}} e^{\frac{-x^2}{2\sigma_N^2}}.$$

Therefore

$$E(N_{IE}^3) = \int_{-\infty}^{+\infty} \frac{x^3}{\sqrt{2\pi\sigma_N^2}} e^{\frac{-x^2}{2\sigma_N^2}} dx$$

$$= \int_{-\infty}^{0} \frac{x^3}{\sqrt{2\pi\sigma_N^2}} e^{\frac{-x^2}{2\sigma_N^2}} dx + \int_{0}^{+\infty} \frac{x^3}{\sqrt{2\pi\sigma_N^2}} e^{\frac{-x^2}{2\sigma_N^2}} dx$$

$$= -\int_{0}^{+\infty} \frac{x^3}{\sqrt{2\pi\sigma_N^2}} e^{\frac{-x^2}{2\sigma_N^2}} dx + \int_{0}^{+\infty} \frac{x^3}{\sqrt{2\pi\sigma_N^2}} e^{\frac{-x^2}{2\sigma_N^2}} dx$$

$$= 0.$$

Similarly, one can show that

$$E(N_{IE}{}^4) = 2\int_0^{+\infty} \frac{x^4}{\sqrt{2\pi\sigma_N{}^2}} e^{\frac{-x^2}{2\sigma_N{}^2}} dx .$$

However,

$$\int_0^{+\infty} x^n e^{-ax^2} dx = \begin{cases} \dfrac{\Gamma\left(\dfrac{n+1}{2}\right)}{2a^{\frac{n+1}{2}}} & n > -1, a > 0 \\[4mm] \dfrac{(2k-1)!!}{2^{k+1}a^k}\sqrt{\dfrac{\pi}{a}} & n = 2k, k \quad integer, a > 0 . \\[4mm] \dfrac{k!}{2a^{k+1}} & n = 2k+1, k \quad integer, a > 0 \end{cases}$$

Note that Γ represents the Gamma function and the operator !! is the double factorial.

Using this integral for the problem at hand, one can show that

$$E(N_{IE}{}^4) = 3\sigma_N{}^4 .$$

Therefore, the expression of A_{11} reduces to

$$A_{11} = \bar{I}_E{}^4 + 6\bar{I}_E{}^2\sigma_N{}^2 + 3\sigma_N{}^4 .$$

Similarly, it can be shown that:

$$A_{12} = \bar{I}_E{}^2\overline{Q}_E{}^2 + \bar{I}_E{}^2\sigma_N{}^2 + \overline{Q}_E{}^2\sigma_N{}^2 + \sigma_N{}^4$$

and

$$A_{13} = \overline{Q}_E{}^4 + 6\overline{Q}_E{}^2\sigma_N{}^2 + 3\sigma_N{}^4$$

which reduces the expression of A_1 to

$$A_1 = (\bar{I}_E^{\,2} + \bar{Q}_E^{\,2})^2 + 8\sigma_N^{\,2}(\bar{I}_E^{\,2} + \bar{Q}_E^{\,2}) + 8\sigma_N^{\,4}.$$

Moreover, by noticing the strong similarities between the expressions of A_1 and A_3, one can readily determine that

$$A_3 = (\bar{I}_L^{\,2} + \bar{Q}_L^{\,2})^2 + 8\sigma_N^{\,2}(\bar{I}_L^{\,2} + \bar{Q}_L^{\,2}) + 8\sigma_N^{\,4}.$$

From this point forward, only A_2 is required to finalize the computation of A:

$$A_2 = E\left[(I_E^{\,2} + Q_E^{\,2})(I_L^{\,2} + Q_L^{\,2})\right]$$

$$= E(I_E^{\,2}I_L^{\,2}) + E(I_E^{\,2}Q_L^{\,2}) + E(Q_E^{\,2}I_L^{\,2}) + E(Q_E^{\,2}Q_L^{\,2})$$

$$= A_{21} + A_{22} + A_{23} + A_{24}$$

with

$$A_{21} = E(I_E^{\,2}I_L^{\,2})$$

$$A_{22} = E(I_E^{\,2}Q_L^{\,2})$$

$$A_{23} = E(Q_E^{\,2}I_L^{\,2})$$

$$A_{24} = E(Q_E^{\,2}Q_L^{\,2})$$

Deriving A_{21} gives

$$A_{21} = \bar{I}_E^2\bar{I}_L^2 + \bar{I}_E^2 E(N_{IL}^2) + 4\bar{I}_E\bar{I}_L E(N_{IE}N_{IL}) + 2\bar{I}_E E(N_{IE}N_{IL}^2) + \bar{I}_L^2 E(N_{IE}^2)$$

$$+ 2\bar{I}_L E(N_{IE}^2 N_{IL}) + E(N_{IE}^2 N_{IL}^2).$$

However, by using the interpretation of the noise corrupting the early and late correlators given earlier, one can show that:

$$E(N_{IL}^2) = E(N_{IE}^2) = \sigma_N^2$$

$$E(N_{IE}N_{IL}^2) = (N_{IE}^2 N_{IL}) = 0$$

$$E(N_{IE}N_{IL}) = (1-\Delta)\sigma_N^2$$

$$E(N_{IE}^2 N_{IL}^2) = \left[2(1-\Delta)^2 + 1\right]\sigma_N^4.$$

Therefore,

$$A_{21} = \bar{I}_E^2\bar{I}_L^2 + \bar{I}_E^2\sigma_N^2 + 4\bar{I}_E\bar{I}_L(1-\Delta)\sigma_N^2 + \bar{I}_L^2\sigma_N^2 + \left[2(1-\Delta)^2 + 1\right]\sigma_N^4.$$

The expressions for A_{22}, A_{23} and A_{24} can be similarly determined as

$$A_{22} = \bar{I}_E^2\bar{Q}_L^2 + \bar{I}_E^2\sigma_N^2 + \bar{Q}_L^2\sigma_N^2 + \sigma_N^4$$

$$A_{23} = \bar{Q}_E^2\bar{I}_L^2 + \bar{Q}_E^2\sigma_N^2 + \bar{I}_L^2\sigma_N^2 + \sigma_N^4$$

$$A_{24} = \bar{Q}_E^2\bar{Q}_L^2 + \bar{Q}_E^2\sigma_N^2 + 4\bar{Q}_E\bar{Q}_L(1-\Delta)\sigma_N^2 + \bar{Q}_L^2\sigma_N^2 + \left[2(1-\Delta)^2 + 1\right]\sigma_N^4.$$

Then using A_{21}, A_{22}, A_{23} and A_{24}, A_2 can be expressed as

$$A_2 = (\overline{I}_E^{\;2} + \overline{Q}_E^{\;2})(\overline{I}_L^{\;2} + \overline{Q}_L^{\;2}) + 2(\overline{I}_E^{\;2} + \overline{Q}_E^{\;2} + \overline{I}_L^{\;2} + \overline{Q}_L^{\;2})\sigma_N^{\;2} + 4(\overline{I}_E \overline{I}_L + \overline{Q}_E \overline{Q}_L)(1-\Delta)\sigma_N^{\;2}$$
$$+ 2\left[2(1-\Delta)^2 + 2 \right]\sigma_N^{\;4}.$$

Finally, combining A_1, A_2 and A_3 yields the expression of A:

$$A = A_1 - 2A_2 + A_3$$
$$= \left[(\overline{I}_E^{\;2} + \overline{Q}_E^{\;2}) - (\overline{I}_L^{\;2} + \overline{Q}_L^{\;2}) \right]^2 + 4(\overline{I}_E^{\;2} + \overline{Q}_E^{\;2} + \overline{I}_L^{\;2} + \overline{Q}_L^{\;2})\sigma_N^{\;2} - 8(\overline{I}_E \overline{I}_L + \overline{Q}_E \overline{Q}_L)(1-\Delta)\sigma_N^{\;2}$$
$$+ 8\Delta(2-\Delta)\sigma_N^{\;2}.$$

Note that B is equal to

$$B = \left[(\overline{I}_E^{\;2} + \overline{Q}_E^{\;2}) - (\overline{I}_L^{\;2} + \overline{Q}_L^{\;2}) \right]^2.$$

Therefore

$$A - B = 4(\overline{I}_E^{\;2} + \overline{Q}_E^{\;2} + \overline{I}_L^{\;2} + \overline{Q}_L^{\;2})\sigma_N^{\;2} - 8(\overline{I}_E \overline{I}_L + \overline{Q}_E \overline{Q}_L)(1-\Delta)\sigma_N^{\;2} + 8\Delta(2-\Delta)\sigma_N^{\;2}$$

and

$$\sigma_{\hat{\tau}}^{\;2} = \left(\frac{1}{2(2-\Delta)} \right)^2 [A - B]$$

can finally be expressed as

$$\sigma_{\hat{\tau}}^2 = \sigma_N^{\;2}\left[1/2 + \frac{2\tau^2}{(2-\Delta)^2} - (1-\Delta)\left(1/2 - \frac{2\tau^2}{(2-\Delta)^2} \right) \right] + 2\sigma_N^{\;4} \frac{\Delta}{2-\Delta}.$$

Appendix C: Computation of the receiver instrumental bias from the Kalman filter based combined tracking outputs and broadcast ephemeris data

According to the IS-GPS 200 Revision D, the differential group delay between L1 and L2 signals can be corrected with the L1/L2 correction term T_{GD} transmitted with the satellites ephemeris. The T_{GD} is computed by the Control Segment (CS) from measurements provided by the satellite contractor during its manufacture. The L1/L2 inter-frequency instrumental bias due to the satellite hardware can then be computed as

$$\delta t_{SV}^{L2-L1} = (1 - \gamma) \cdot T_{GD} \qquad \qquad \textbf{C-1}$$

$$\gamma = \left(\frac{F_1}{F_2}\right)^2 . \qquad \qquad \textbf{C-2}$$

The relative L1/L2 time delay induced by the ionosphere is different for each satellite as long as each one has a different elevation angle. Indeed, the TEC encountered on the signal path can be related to the vertical TEC through the mapping function defined in Equation 2-14 which is dependent on the satellite elevation angle. On the other hand, the receiver instrumental bias is the same for all channels but is unknown to the user. As such, the relative time delay between L1 and L2 can be expressed as

$$\Delta t_i^{L2-L1} = \left(\frac{40.3}{c \cdot F_2^{\ 2}} - \frac{40.3}{c \cdot F_1^{\ 2}}\right) \cdot \Psi(\theta_i) \cdot VTEC + \delta t_{SV,i}^{L2-L1} + \delta t_{Rx}^{L2-L1} \qquad \qquad \textbf{C-3}$$

with Δt_i^{L2-L1} being the relative delay between L2 and L1 for the satellite i, c being the speed of light, Ψ being the mapping function, θ_i being the satellite i elevation angle, $\delta t_{SV,i}^{L2-L1}$ being the instrumental bias of the satellite i and δt_{Rx}^{L2-L1} being the receiver instrumental bias.

From Equation C-3, if two L1 C/A and L2C satellites or more were tracked, the receiver instrumental bias and the ionosphere vertical TEC could be determined. Note that the user needs to know approximately his position and the satellite ephemeris in order to obtain the satellite elevation angle.

In the case at hand, real data collected two weeks before the attenuated data collection in Chapter 6 are used. This set of data and the one used in Chapter 6 were collected using the same equipment. However, no attenuation was used and two Block IIR-M satellites, namely PRN 17 and 31, were in view.

PRN 17 and 31 were tracked using the Kalman filter based combined tracking presented in Chapter 5. The results in terms of slant TEC are shown in Figure C-1.
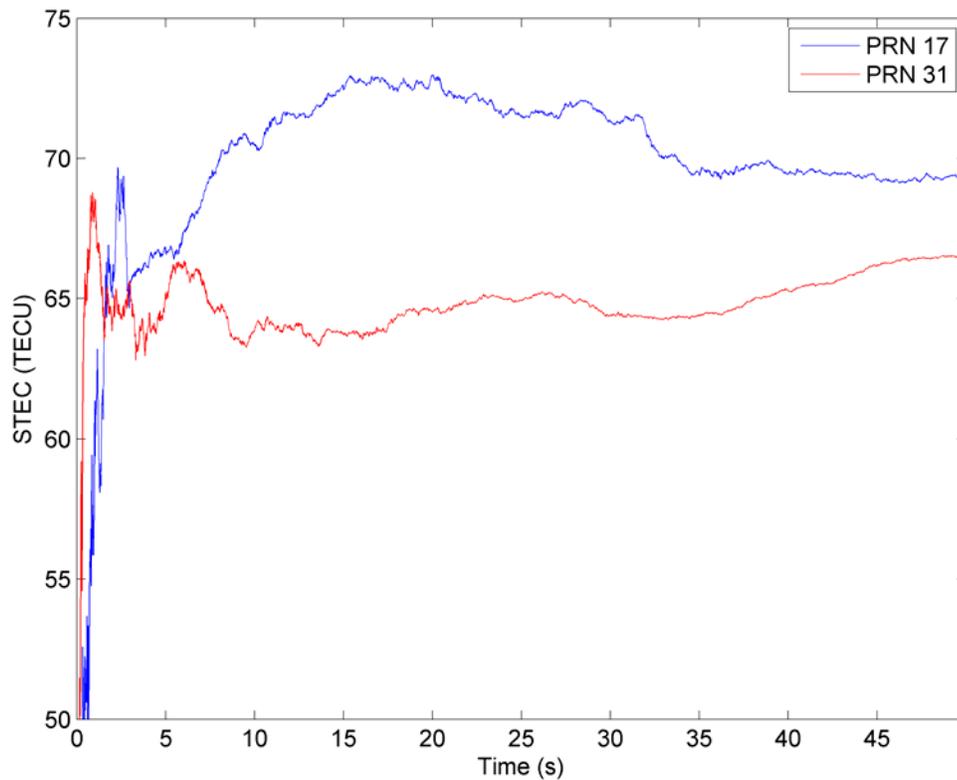
Figure C-1: TEC encountered on the signal path for PRN 17 and PRN 31 as computed by the Kalman filter based combined tracking

As PRN 17 and 31 were tracked by the Kalman filter, the data bits of the navigation message were decoded and the satellite instrumental biases and elevation angles were computed. Using Equation C-3, the TEC values encountered on the signal path were corrected for the satellite instrumental biases and used to compute the vertical TEC and receiver instrumental biases using a least-squares method. Note that, in the case at hand, the least-squares method would not be required but was developed to be used with two or more satellites. The least-squares model used is

$$\begin{bmatrix} \Delta t_1^{L2-L1} \\ \Delta t_2^{L2-L1} \\ \vdots \\ \Delta t_i^{L2-L1} \end{bmatrix} = \begin{bmatrix} \left(\dfrac{40.3}{c \cdot F_2^2} - \dfrac{40.3}{c \cdot F_1^2} \right) \cdot \Psi(\theta_1) & 1 \\ \left(\dfrac{40.3}{c \cdot F_2^2} - \dfrac{40.3}{c \cdot F_1^2} \right) \cdot \Psi(\theta_2) & 1 \\ \vdots & \vdots \\ \left(\dfrac{40.3}{c \cdot F_2^2} - \dfrac{40.3}{c \cdot F_1^2} \right) \cdot \Psi(\theta_i) & 1 \end{bmatrix} \cdot \begin{bmatrix} VTEC \\ \delta t_{Rx}^{L2-L1} \end{bmatrix} + \begin{bmatrix} w_1 \\ w_2 \\ \vdots \\ w_i \end{bmatrix}. \qquad \textbf{C-4}$$

Note that the noise components w_i are uncorrelated as they correspond to the noise corrupting different PRNs tracked by the receiver. The covariance matrix of the noise is based on the covariance matrix of the state vector as output by the Kalman filter based combined tracking method.

Using the developed least-squares model, the vertical TEC and receiver bias are computed. As a mean of verification, the value found for the VTEC is compared to the value provided by the International GNSS Service (IGS) for the given day. The results of this method are provided in Figure C-2 and Figure C-3. As the vertical TEC estimated matches the vertical TEC generated by IGS, the receiver instrumental bias found to be 12.8 nanoseconds was declared validated and used as a correction when only one satellite was available as it was the case in Chapter 6.
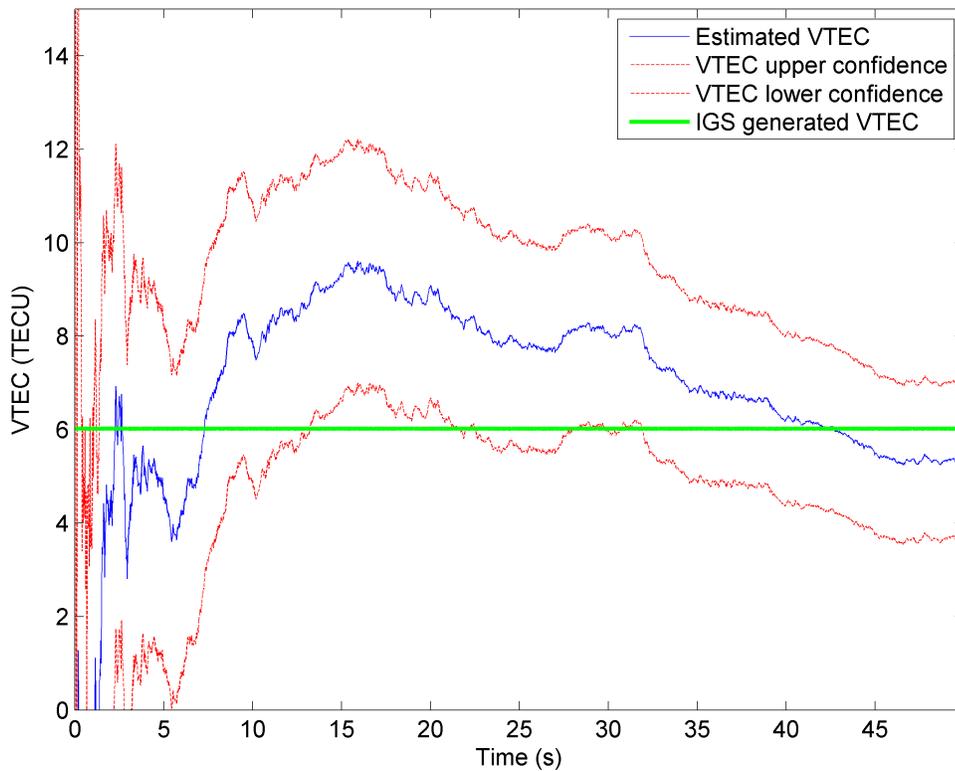
Figure C-2: Estimated VTEC from the least-squares method using the Kalman filter based combined tracking outputs and IGS generated VTEC as well as he 1σ confidence
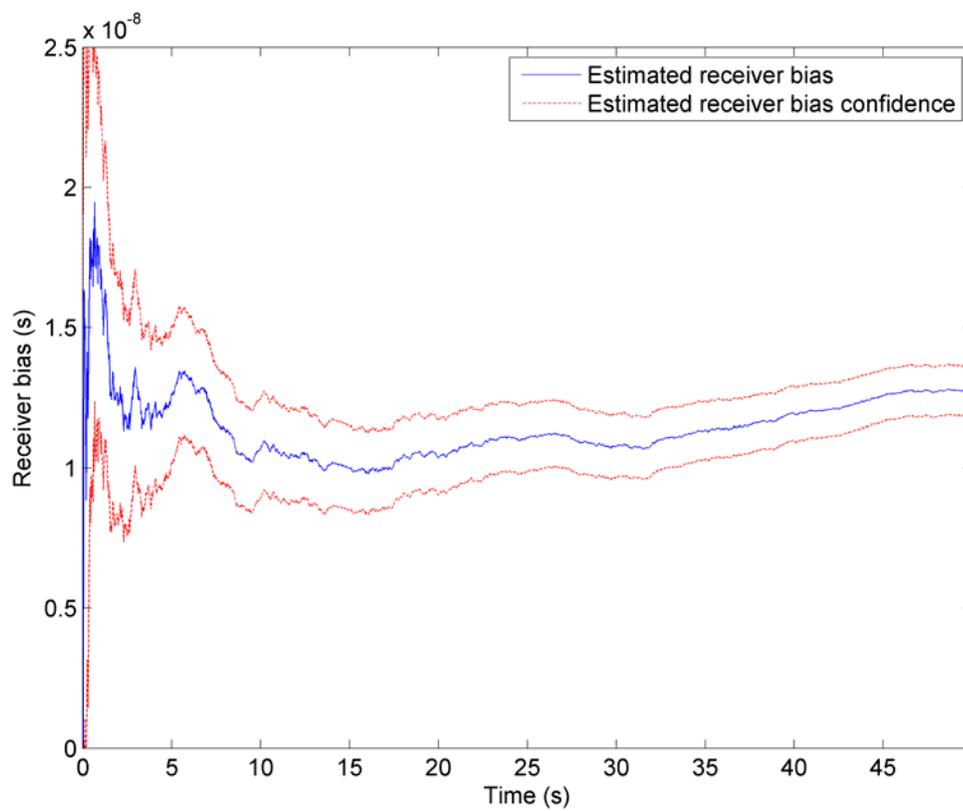
Figure C-3: Estimated receiver bias from the least-squares method using the Kalman filter based combined tracking outputs as well as the 1σ confidence